Analysis of Novel Techniques of Drag Reduction and Stability Increase for Sport Utility Vehicles using Computational Fluid Dynamics

Ahmed Ali Shakir Al-Saadi

Submitted in accordance with the requirements for the degree of
Doctor of Philosophy

The University of Leeds
School of Chemical and Process Engineering

February, 2019

Declaration

The candidate confirms that the work submitted is his own, except where work which has formed part of jointly authored publications has been included. The contribution of the candidate and the other authors to this work has been explicitly indicated below. The candidate confirms that appropriate credit has been given within the thesis where reference has been made to the work of others.

Some of the results in this thesis have already been published as shown below. The analyses, simulations, discussions and conclusions were all done by Ahmed Al-Saadi. Other authors of these publications provided feedback and guidance.

Al-Saadi, A., Hassanpour, A. & Mahmud, T. (2016). Simulations of Aerodynamic Behaviour of a Super Utility Vehicle Using Computational Fluid Dynamics. *Adv Automob Eng*, *5*(134), 2.

Al-Saadi, A., Hassanpour, A., Motlagh, Y. G. & Mahmud, T. (2017, April). Simulation of Aerodynamic Behaviour of a Road Vehicle in Turbulent Flow. In *Proceedings of the 25th UKACM Conference on Computational Mechanics* (Vol. 12, p. 13).

Acknowledgements

I am thankful to my wife (Dhelal) for her love, patience and support that have always been my strength. Also, I am thankful for my children, Zahraa and Mohammed, you bring joy to my life and I have found my smile with you in all difficult times throughout my study. Furthermore, I would like to express my deepest gratitude to all my family members for their love and support.

A special thanks to my caring father and loving mother. Words cannot express how grateful I am to you. It is really difficult for me to be away from you all these years. Whatever I am now is because of you.

I would like to thank my supervisors (Dr Ali Hassanpour and Dr Tariq Mahmud). A special word of thanks is given to David G Kibble for his kind help regarding English language in chapters one and four. Also, I would like to thank Adrian Gaylard from Jaguar Land Rover Limited for his kindness in providing me with valuable information about the experimental measurements of the Land Rover Discovery (4-SDV6 GS) and the MIRA wind tunnel. Great acknowledgment is given to all my colleagues.

I must here express my thanks my sponsor (The Ministry of Higher Education and Scientific Research in Iraq/ University of Al-Qadisiyah) for granting me the opportunity to carry out my PhD at the University of Leeds.

Abstract

The main objective of this study is to investigate ways to reduce the aerodynamic drag coefficient and to increase the stability of road vehicles using three-dimensional Computational Fluid Dynamics (CFD) simulation. Two baseline models, the Ahmed body and the Land Rover Discovery 4, were used in these simulations. The effects of model scale and slant angle were investigated for the Ahmed body in addition to a new technique to measure the drag coefficient used in the experiments has been investigated numerically in this study. Many new aerodynamic devices and external design modifications were used for the Land Rover Discovery 4. ANSYS Meshing was used to create a variety of mesh cases for mesh optimization and ANSYS Fluent software was used to simulate all models. Different sizes of computational domain were used in order to study the effect of the blockage ratio on the aerodynamic behaviour. The range of Reynolds numbers used in this study for the Ahmed body was between 3×10^5 and 30×10^5 similar to the experimental studies. The uniform free stream velocity of air at the inlet ranging from 100km/h to 140km/h was used for the Land Rover Discovery 4. Reynolds-averaged Navier–Stokes equations (RANS) and Large Eddy Simulation (LES) turbulence models were used to establish the most appropriate turbulence model for the Ahmed body geometry. Only RANS was used for the Land Rover Discovery 4. In general, the trend of drag coefficient as a function of the Reynolds number for the Ahmed body was in good agreement with the experiments, whereas LES simulation results were closer to the experimental data. The drag and lift coefficients obtained from ANSYS Fluent for the baseline of the Land Rover Discovery 4 were validated with experimental data. It is found that the use of modern aerodynamic add-on devices and modifications has a significant effect in reducing the aerodynamic drag coefficient.

Keywords: Modelling; Aerodynamics; Ahmed body; SUV; Turbulent Flow.

Contents

List of Abbreviations

2D	Two-dimensional
3D	Three-dimensional
AIAA	American Institute of Aeronautics and Astronautics
CAD	Computer-Aided Design
CFD	Computational Fluid Dynamics
Discovery 4	Fourth Generation of this Model of Vehicle (Discovery)
FV	Finite Volume
GM	General Motors
LES	Large Eddy Simulation
Ni-Cr	Nickel-Chrome alloy
PIV	Particle Image Velocimetry
RANS	Reynolds Averaged Navier-Stokes
RSM	Reynolds Stress Model
SGS	Sub-Grid Scale
SST	Shear Stress Transport
SUV	Sport Utility Vehicle
SVV	Spectral Vanishing Viscosity
URANS	Unsteady Reynolds Averaged Navier-Stokes
VCR	Volumetric Control Region
VG	Vortex Generator
VLES	Very Large Eddy Simulation
VMF	Vehicle Modelling Function
V&V	Verification and Validation
WALE	Wall Adapting Local Eddy-viscosity

List of Symbols

A	Frontal area of the vehicle
A_v	Frontal area of the vehicle
A_w	Frontal area of the wind tunnel
B	Blockage ratio
$C_{1\varepsilon}$	Adjustable constant
$C_{2\varepsilon}$	Adjustable constant
C_D	Drag coefficient
C_{dc}	Corrected drag coefficient
C_{dm}	Measured drag coefficient
C_{ij}	Convective term
C_L	Lift coefficient
C_p	Pressure coefficient
C_{wale}	Model constant (LES-WALE)
C_μ	Adjustable constant
d	Diameter
d_h	Hydraulic diameter
D_{ij}	Diffusion term
e_{ijk}	Alternating symbol
F	Force
F_{Ahmed}	Drag force of the Ahmed body
$F_{Ahmed+Plate}$	Drag force of the Ahmed body and plate
F_D	Drag force
F_L	Lift force
F_{Plate}	Drag force of the plate
H	Height of the vehicle
H_1	Height of the volumetric control region number 1

H_2	Height of the volumetric control region number 2
H_3	Height of the volumetric control region number 3
H_4	Height of the computational domain
h	Hour
$\mathbf{I}$	Identity matrix
L	Length of the vehicle
L_1	Length of the volumetric control region number 1
L_2	Length of the volumetric control region number 2
L_3	Length of the volumetric control region number 3
L_4	Length of the computational domain
O_H	Distance between computational domain ceiling and vehicle model
O_L	Distance between computational domain inlet and vehicle model
O_W	Distance between computational domain side wall and vehicle model
p	Pressure
$\bar{p}$	Filtered pressure
P_{ij}	Production term
P_k	Rate of production of turbulent kinetic energy
Re	Reynolds number
R_{ij}	Reynolds stress
$\bar{S}$	Rate of strain tensor
S_{ij}	Mean rate of strain
t	Time
u, v, w	Velocity components
$\bar{u}, \bar{v}, \bar{w}$	Filtered velocity components
$\acute{u}, \acute{v}, \acute{w}$	Fluctuating velocity components

u	Velocity vector components
u_*	Friction velocity
u_∞	Velocity of the oncoming flow
U_∞	Velocity of the oncoming flow
V	Velocity
W	Width of the vehicle
W_1	Width of the volumetric control region number 1
W_2	Width of the volumetric control region number 2
W_3	Width of the volumetric control region number 3
W_4	Width of the computational domain
$\mathcal{W}$	Correction factor
x, y, z	Cartesian coordinates
y	Vertical distance from the wall
y^+	Dimensionless wall distance
α	Slant angle
β	Slantwise angle of the back windscreen
β_1	Revised model constant
β_2	Revised model constant
β^*	Revised model constant
Δ	Difference
δ	Boundary layer thickness
δ_{ij}	Kronecker delta
σ_k	Revised model constant
σ_ω	Revised model constant
$\sigma_{\omega,1}$	Revised model constant
$\sigma_{\omega,2}$	Revised model constant
σ_ϵ	Adjustable constant

ε	Dissipation rate
ε_{ij}	Rate of dissipation
μ	Dynamic viscosity
μ_t	Eddy viscosity
ν	Kinematic viscosity
ν_{SGS}	Sub-grid viscosity
ρ	Density
τ	Sub-grid-scale stress tensor
τ	Shear stress
$\tau_{i,j}$	Shear stress tensor entry
τ_w	Wall shear stress
ω	Specific dissipation rate
Ω_{ij}	Rotational term
γ_1	Revised model constant
γ_2	Revised model constant
∇	Gradient
Π_{ij}	Pressure-strain interaction

List of Figures

List of Tables

Chapter 1 Introduction

Aerodynamics is a science that deals with the movement of gaseous fluids (such as air) and with forces acting on bodies (such as cars) in motion relative to such fluids [1]. It is necessary to understand the movement of air around the body in order to calculate the forces and moments acting on it. For this purpose velocity, pressure and temperature are calculated for a flow field (air around a body) as a function of position and time. There are basically two types of aerodynamics, namely external and internal (*ibid*). The aerodynamics of aeroplanes, rockets, wind turbine blades and road vehicles are examples of external aerodynamics. On the other hand, internal aerodynamics is the study of flow through passages in solid objects. Jet engines, rocket engines and air conditioning pipes are examples of internal aerodynamics. The work described throughout this thesis concentrates on the external aerodynamics with regard to SUV.

1.1 Research background and motivation

A steady increase in global energy demand has a direct influence on fuel prices. This together with the environmental problems caused by exhaust gases of cars is the main motives behind the need to reduce the fuel consumption of road vehicles. Reducing aerodynamic drag can lead to a reduction in fuel consumption and an increase in top speed [2]. Global warming has put pressure on designers to improve vehicle designs by means of external modifications and add-on devices [3]. External car design has been improved to achieve better performance and to increase passenger comfort. Aerodynamic behaviour affects the performance of the car, especially comfort and handling [4]. Most of the improvements have focused on reducing drag coefficient to improve acceleration and fuel economy [5]. Road vehicle aerodynamics is a very complex field because of the modern irregular external design of road vehicles and their proximity to the road surface [6]. Heisler [7], Katz [8], Levin [9] and Schuetz [4] mentioned that the resistance force of car movement is significant because of aerodynamic drag and rolling resistance as shown in Figure 1.1. Aerodynamic drag increases with velocity, but rolling resistance is almost constant. At a velocity of 65km/h, aerodynamic drag is equal to rolling resistance but at less than 65km/h rolling resistance is more than aerodynamic drag. Therefore, aerodynamics is less important at low speed.

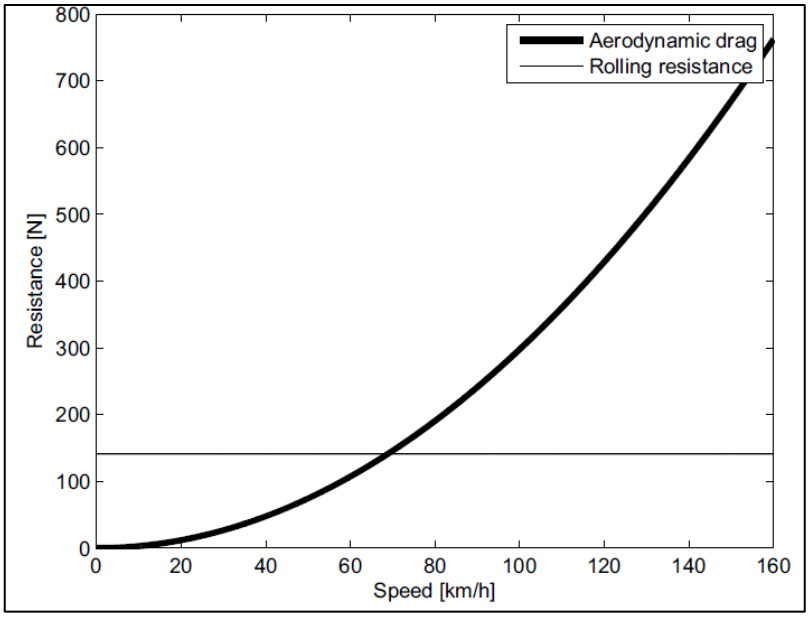

Figure 1.1: Aerodynamic drag and rolling resistance [9]

Hucho [10]; Krishnani [3] and Schuetz [4] illustrated vehicle aerodynamics comprising visibility, performance, cooling, comfort, drivability and local forces. For example, Figure 1.2 shows many features which can be affected by the aerodynamics of road vehicles. Aerodynamic behaviour is used to improve the drag coefficient, stability of the vehicle on the road especially at high speed, the engine cooling system, cooling brake system, passenger comfort, and visibility for the passenger.

Figure 1.2: Issues that are affected by road vehicle aerodynamics [3]

There are two main methods, which can be used to study automotive aerodynamics; these are Computational Fluid Dynamics (CFD) and experimental measurements. CFD is a

branch of fluid mechanics, which uses numerical analysis to solve a wide range of problems that include fluid flows. Better numerical simulation can be achieved by using high performance computers. While an experimental method is a procedure used to support, validate, or refute a hypothesis by observation. Wind tunnels have been used to experimentally study the aerodynamic behaviour of vehicles. However, there are limits to the use of the wind tunnel [4]:

1. The Reynolds number is very low in the scale model experiments.
2. It is difficult to put all the details of car design on the scale models.
3. Blockage effects occur due to the dimensions of the wind tunnel are limited.
4. Crosswind and turbulence have limited representation in the wind tunnel.
5. Full prototype testing is very expensive.

At the beginning of the automotive industry, numerical methods provided models for testing because no real cars were available. Reducing the development cycle, lowering costs and rising flexibility are the reasons for justifying the use of a numerical approach. Figure 1.3 shows the complexity of the flow around the car by smoke in the wind tunnel 1.3(a) and the streamline of air generated by computer simulation for the area near the wake as shown in Figure 1.3(b); [4]. It is clear that the movement of air over the roof of the car is separated at the end of the roof; a phenomenon is known as the wake. The wake is a low pressure zone and its location is behind the car [11]. The shape of the rear of the car is more important than the shape of the front because of the wake.

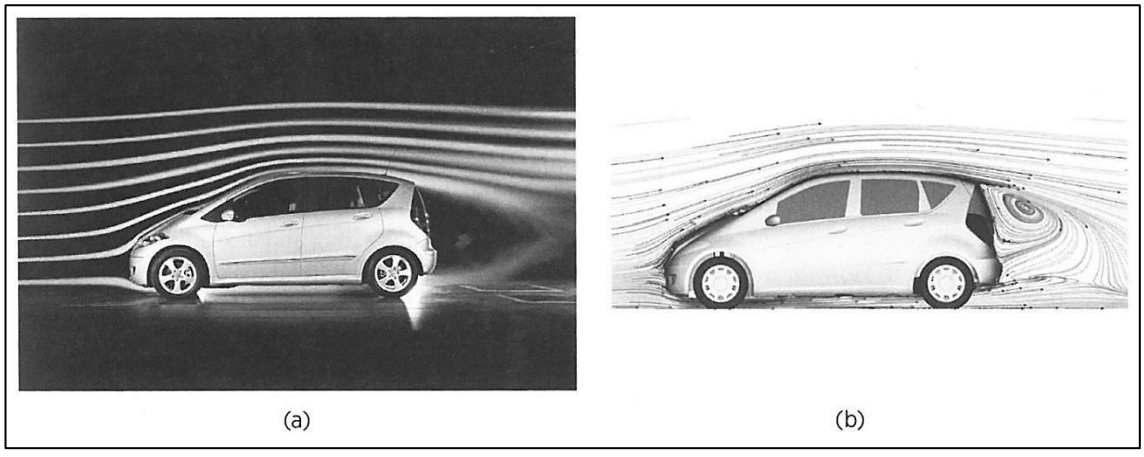

Figure 1.3: Flow visualization: (a) in a wind tunnel with smoke, (b) by computer simulation [4]

1.2 Different rear end shapes

In general, there are four types of road vehicle rear end shapes [4]. Figure 1.4 illustrates each type of road vehicle shape with measured and simulated drag coefficients. Reynolds Averaged Navier-Stokes (RANS) was used to calculate drag coefficients (*ibid*). The first type, called notchback, is the most streamlined shape as shown in Figure 1.4(a). Family cars are often designed in this way and the shape is also known as sedan. The second type is fastback as shown in Figure 1.4(b). This type is used in some saloon cars, super cars and sports cars and the wake area for this type of car design is small. Small family cars use a hatchback design as shown in Figure 1.4(c). Finally, there is the squareback or so-called box-type as shown in Figure 1.4(d). This design is used in station wagons, Sport Utility Vehicles (SUVs), vans and buses. The wake area for this type of design is large. The squareback (box-type) model is the most important design to study because it has many applications. Hucho [10], Lay [12] and Schuetz [4] illustrated the effect of the external design of vehicle on the drag coefficient. For example, Figure 1.5 shows the effect of the shape of the front and rear of the vehicle in Lay's study of 1933. Obviously, the rear end shape of the vehicle has a greater influence on the drag coefficient.

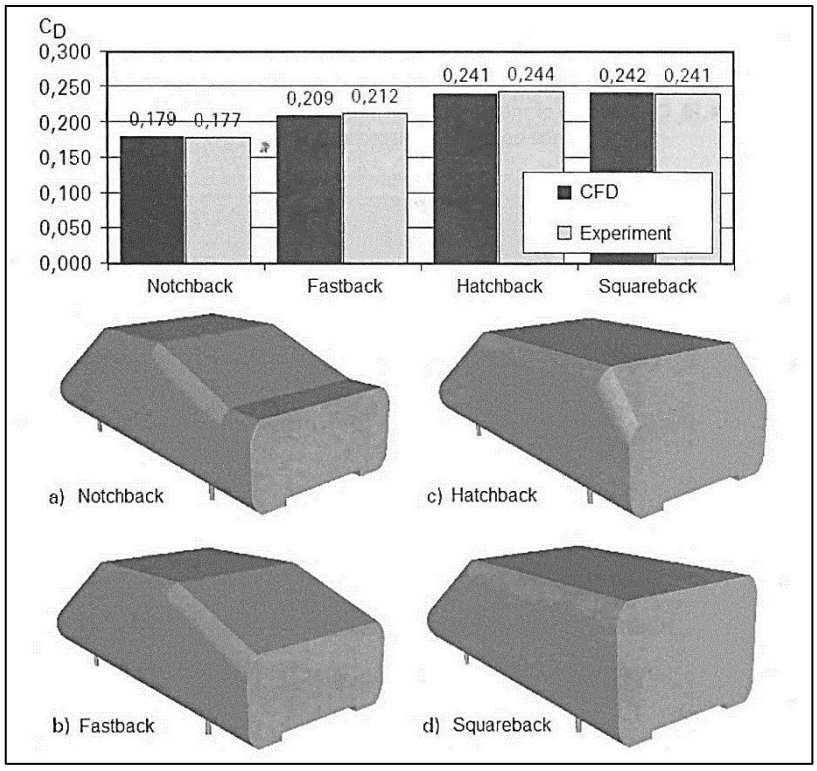

Figure 1.4: The four-types of rear end shapes of road vehicles with measured and simulated drag coefficients [4]

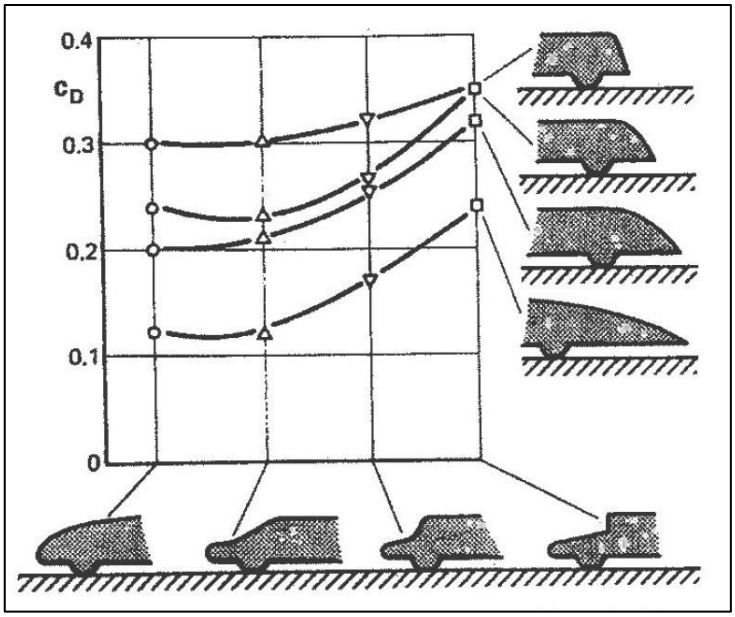

Figure 1.5: Summary of the test results by Lay [10]

This study focuses on the aerodynamic behaviour of road vehicles. Automotive aerodynamic studies started by using simplified models such as Ahmed model. Figure 1.6 illustrates the standard geometry of the Ahmed model and its dimensions. Ahmed *et al.* [13] created this geometry in 1984 and it has become a benchmark to study the main features of aerodynamic behaviour for road vehicles. The Ahmed model is also used to study the behaviour of turbulent flow around simple car geometry.

The SUV is an automotive classification, usually a type of station wagon car with off-road car features. Sales of this type of cars have been increased significantly in recent years. The present study focuses on the Land Rover Discovery 4 as a kind of the SUV since it is one of the most popular SUVs. The first generation of this model was introduced in 1989 by the British manufacturer Jaguar Land Rover. The fourth generation (the Land Rover Discovery 4) used in the present study was being produced from 2009 until 2016. The Land Rover Discovery 4 in Figure 1.7 was chosen in the present study because it has a high drag coefficient (C_D = 0.4) due to its the non-streamlined shape [14, 15]. This type of SUV consumes fuel between 9.3 *l*/100 km and 14.1 *l*/100 km depending on the engine capacity. The drag coefficient of passenger cars is usually between 0.3 and 0.5 [10].

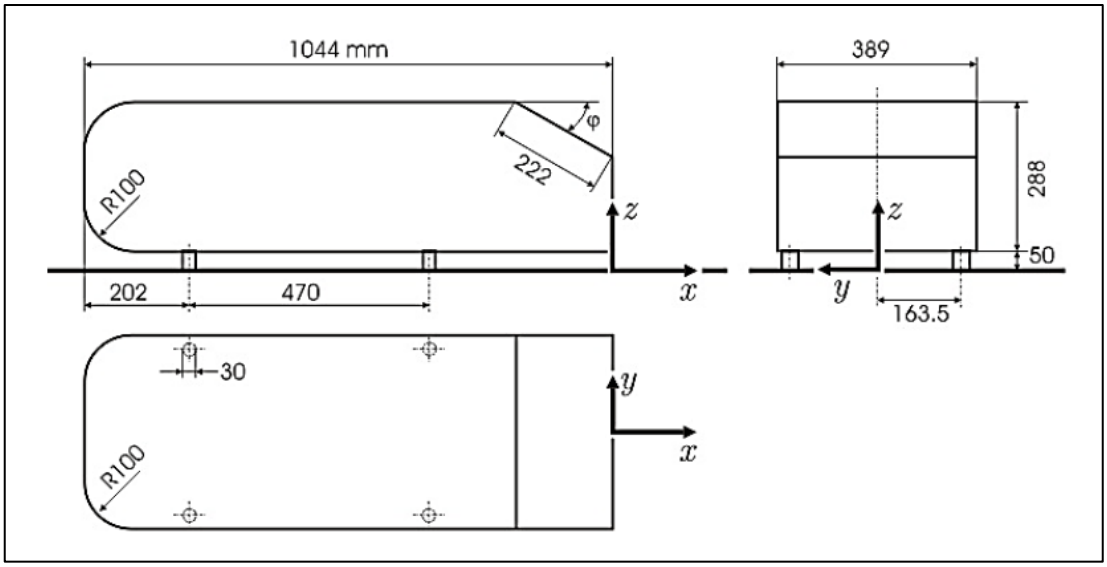

Figure 1.6: Standard geometry of the Ahmed model [13]

Figure 1.7: The Land Rover Discovery 4 [14]

1.3 Aims and objectives

The overall aim of this thesis is to study the novel techniques for the reduction of drag and increase of stability for the Land Rover Discovery 4 using CFD, through the analysis of aerodynamic forces, pressure distribution, air velocity and wakes around the surface of the vehicle. This will lead to a reduction of fuel consumption and reduce air pollution as well as improved safety. Despite previous experimental and modelling studies on the aerodynamic behaviour of this type of SUV cars, the combined effect of design modifications on both the drag and lift coefficients has not been studied in detail. Therefore, the main aim of this thesis is to optimize the design modification of the Land Rover Discovery 4 while considering both aforementioned effects.

The research objectives of this thesis are as follows:

1- To develop and validate the CFD methodologies based on a widely used Ahmed model as well as the baseline (benchmark) model of the Land Rover Discovery 4.

2- To investigate the aerodynamic characteristics of the Ahmed model for two scale sizes (55% and full scale) and the presence of a flat plat under the legs of the Ahmed model in the wind tunnel.

3- To simulate the Land Rover Discovery 4 with different modifications of external design and add-on aerodynamic devices.

4- To optimize these modifications and add-on devices through identifying the best feature for the reduction of drag coefficient and increase of the Land Rover Discovery 4 stability.

1.4 Overview of this thesis

The thesis is organised as follows:

A general introduction about automotive aerodynamics and motivation for the research are presented in Chapter 1. Furthermore, aims and objectives of the present study are defined. The purpose of this chapter is to describe the scope of the present study and provide a brief explanation of the thesis.

Chapter 2 is dedicated to the literature review of several types of vehicle design and the different types of aerodynamic devices acting upon road vehicle are described. A critical review of previous experiments and CFD modelling studies to investigate design modifications and add-on devices for the aerodynamic improvement of road vehicles are

presented. The gaps in the previous studies has been identified and summarized. The purpose of this chapter is to find out what has been studied to determine the gap that can be covered in the present study.

Chapter 3 is dedicated to the governing equations of fluid flow and their numerical solution methods. Furthermore, turbulence models, Reynolds number, boundary layer, separation, drag coefficient and lift coefficient are described. This chapter aims at identifying the governing equations and turbulence models used in the present study.

Chapter 4 describes the methods that were used in the present study. Two types of baseline (benchmark) models (Ahmed model and Land Rover Discovery 4) and all modifications are presented in this chapter. The assumptions related to these models are listed. The chapter also deals with different sizes of the computational domain, mesh refinement, and boundary conditions. Moreover, validation of the CFD models is performed via the comparison of results obtained with empirical data evident in the literature. This chapter focuses on the description of the specific methods which were used in the present study for the Ahmed model and all the Land Rover Discovery models. Pre-processor and solver will be undertaken with details in Chapter 4. Post processor will be undertaken with details in Chapter 4 and Chapter 5. Most simulations in Chapter 4 and all simulations in Chapter 5 will be used RANS models because they have acceptable accuracy and computationally cheaper. Two cases of LES will be used in Chapter 4 because it has good accuracy but computationally expensive.

Chapter 5 is dedicated to the numerical results of the baseline (benchmark) model of the Land Rover Discovery 4 and the effect of the blockage ratio on the results. The chapter also deals with the numerical results of different add-on aerodynamic devices and modifications and their optimisation, which have been added to the Land Rover Discovery 4. The purpose of this chapter is to objectively present the numerical results of all case-studies of the Land Rover Discovery 4 and determine the best model.

Chapter 6 presents the discussion of all chapters of the present study. The purpose of the discussion chapter is to describe and interpret the significance of findings.

Chapter 7 presents the conclusions and suggested future work based on the current study. The aim of this chapter is to interpret the arguments and that could determine possible future studies.

Chapter 2 Literature review

2.1 Introduction

A literature review of the aerodynamic behaviour of road vehicles is provided in this chapter. The aim is to provide a background related to two key areas of interest in road vehicle aerodynamics, which are drag reduction and stability of a vehicle on the road. Section 2.2 describes the different external designs of road vehicles. Focusing on previous studies of road vehicle models that are of relevance to the present study. The effects of external design modifications on the aerodynamic behaviour, i.e., streamlines, drag coefficient and lift coefficient are also discussed. An investigation of the effects of add-on aerodynamic devices on the road vehicle, with specific focus on the drag and lift coefficients is provided. Together with critical review of previous CFD modelling and experimental studies. An investigation of external design modifications and devices that can improve the overall aerodynamic behaviour of road vehicles in provided herein. A description of the flow around many types of car, add-on aerodynamic devices and modifications that are used on road vehicles and car body aerodynamic shape optimization are reviewed. Section 2.5 presents summary of the literature review. Section 2.6 is dedicated to the conclusions of this chapter.

2.2 Different external design of road vehicles

The external design of vehicles is many and varied as shown in Figure 2.1, and it is very complex with regard to its geometry [4, 10]. Road vehicles operate close to the ground (*ibid*). In order to optimize the performance of vehicles, it is proposed that the external design of the road vehicle is divided into three categories. Moreover, these divisions will not only depend on shape but will also take into consideration the size, speed and utilization of vehicles. For example, the stability of fast cars on the road at high speed is more important than fuel consumption, while for heavy vehicles the efficiency of fuel consumption is more important than stability [2]. Some modifications and aerodynamic devices are suitable for one category, such as cab side extender extensions which are suitable only for tractor-trailers.

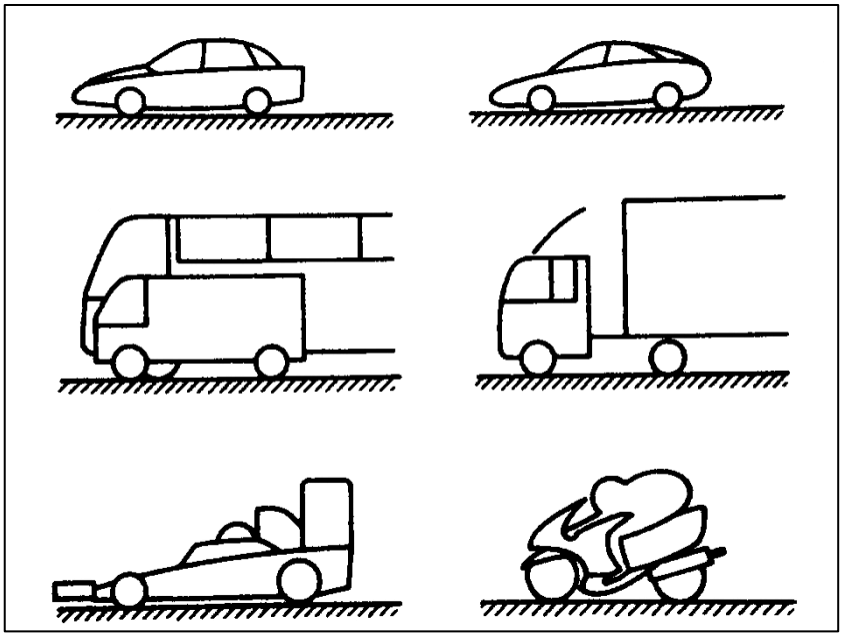

Figure 2.1: Different shapes of road vehicles [4]

2.2.1 Ahmed model

The Ahmed model [13] has been widely used in aerodynamic studies of road vehicles by numerous researchers [16, 17] The Ahmed model is simple and free from all kinds of accessories as well as wheels; nevertheless it can be used to study the aerodynamic behaviour of a road vehicle based on the main features such as the slanting surfaces. Figure 2.2 illustrates a three dimensional (3D) full scale schematic diagram of the Ahmed model, with its main dimensions. Red dotted line in top view refers to a plate under the geometry which was used by Bello-Millán *et al*. [18] as a new technique to calculate the drag coefficient. This model is primarily designed to study the affect the slant angle (α) at the end part of the model on the drag coefficient and vortices behind the vehicle [19, 20, 21]. It is also used to validate the numerical results. For the numerical simulations, it is important to ensure grid convergence and turbulent models by comparing forces acting on the geometry or values of the air velocity around the geometry [18]. An accurate simulation of the airflow around the Ahmed model is a challenge in CFD. Many turbulent models have been investigated, specifically RANS [16, 19] and LES [22, 23, 24]. The results of LES are slightly more accurate than RANS compared with experimental measurements, but the difference would not be significant enough to justify very long simulation times in LES.

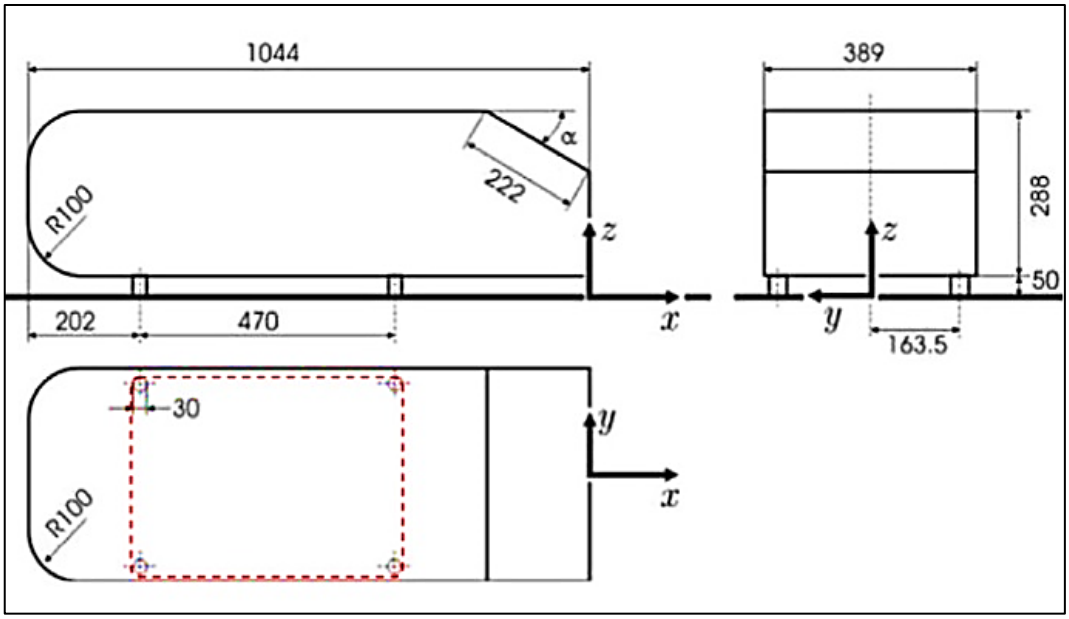

Figure 2.2: The 3D Ahmed vehicle model with dimensions in millimetres [18]

According to Verzicco *et al*. [25] the Ahmed model can be considered as a prototype for small vans, mini-buses and buses. The problem of this type of geometric shape is not limited only to the front of the Ahmed model but the biggest problem is at the rear due to the air streamlines cannot return to their original form. This is consistent with Lay's study of 1933 [12]. This is because of the sharp angles; leading to air swirls behind the vehicle. Franck *et al*. [26] numerically solved the unsteady air flow around the Ahmed model at a Reynolds number of 4.25 million. This study focused on the flow behind the Ahmed model (the wake zone). Two critical cases of the slant angle in this type of shape were 12.5° and 30°. The slant surface length was fixed at 222mm for all cases. A tetrahedral mesh was used throughout the computational domain and the wedge layers were used around the Ahmed model surfaces to get a better resolution near the body surface. This technique is used by most researchers in this field.

The LES technique was applied using the Smagorinsky Subgrid Scale Model. The flow in the wake zone can be in two different dimensions attached with a slant angle of less than 12.5° and more than 30°. But the flow in the wake zone is widely separated 3D with a slant angle between 12.5° and 30°. In general the mean drag coefficient (C_D) of this numerical study was in line with the data gathered experimentally. The percentage relative errors were -1% for the finer mesh and +6% for the coarser mesh. This means that mesh size can affect the numerical results. Guilmineau [19] numerically investigated the aerodynamic behaviour of the Ahmed model with two different slant angles which

were 25° and 35°. The width and height of the computational domain were 0.935 m and 1.4 m respectively, with half of the Ahmed model was used inside the computational domain. The blockage ratio in this study was 4.39% depending on the dimensions of the computational domain. Therefore, the drag coefficient was not accurate enough. The distance from the inlet side to the beginning of the Ahmed model was two body lengths and from the end of the Ahmed model to the outlet side was three body lengths. Two types of grid were used. The first type was without stilts and the total points were about 1.8×10^6 with 16 blocks. The second type was with stilts and the total points were 3.6×10^6 with 32 blocks. Various turbulence models were used because the Ahmed model with a slant angle of 25° can be considered as a challenge case of turbulence modelling. All simulations with different turbulence models predict massive separation at the slant angle equal to 25° whereas the experimental tests show reattachment approximately half-way down the entire length of the slant face.

Conan *et al*. [20] tested the drag coefficient of the Ahmed model with different values of slant angles and various measurement mechanisms. A 3D Ahmed model was investigated by Howard and Pourquie [21]. They found that slant angles between 12.5° and 30° caused high drag forces because low downwind pressure is created behind the model. A combination of LES with a Spectral Vanishing Viscosity (SVV) technique was used to study the bluff body by Minguez *et al*. [17]; this approach was called the LES-SVV method. Two models of Ahmed model were experimentally studied by Watkins and Vino [27] with a change in the vehicle spacing. They focused on the structure of the wake behind the vehicle because it is significant in terms of the drag force.

Meile *et al*. [28] studied the Ahmed model by using experimental and numerical approaches. Two slant angles were used 25° and 35°. They compared their experimental drag coefficient values as a function of the Reynolds number with modelling results which were achieved using the ANSYS Fluent code. They found that the drag coefficient decreased with increasing of Reynolds number; this being confirmed by other researchers [18, 29]. Most recently Bello- Millán *et al*. [18] experimentally studied a 55% scale model of the Ahmed model with a slant angle of 25°, but different yaw angles, in a wind tunnel. The frontal projected area in the experiments was calculated at zero yaw angle but used for all ranges of yaw angles throughout the study. A new technique was used to calculate the drag coefficient by placing a plate under the geometry and connecting it to a force sensor as mentioned previously (Figure 2.2). The drag coefficients obtained as a function of Reynolds number in this study were approximately 30% greater than those reported in other experimental studies. This difference is presumably as a result of the separation

generated at the edge between the end part of the roof and the beginning of the slanting surface.

It is thought that the size of the model affects the results. Therefore, it is necessary to study the effect of model size on the drag coefficient. There have been many studies of Ahmed model aerodynamics using experimental and numerical methods. Most of these studies focused on the wake behind this type of geometry and the effect of slant angle on the wake. A number of experimental and numerical techniques were used to calculate the drag coefficients. Other studies used aerodynamic devices to reduce the drag coefficient of this type of geometric shape. To the best of our knowledge, there is no reported work on the lift coefficient of the Ahmed model, especially with a scale model and using the plate under the model. A new experimental technique [18] was used to calculate the drag coefficient; however, there was no detailed analysis of the effect of the size and shape of the plates on the obtained drag and lift coefficients.

2.2.2 Trucks

Combination heavy vehicles consume a lot of fuel. Most of the power from the engine from this fuel is used to overcome aerodynamic drag at high speeds, while the remaining portion is dissipated through the tyres rolling resistance, drive train friction and the resistance slope [30]. These aerodynamic losses were first given considerable attention in an effort to improve the fuel economy of trucks. The primary focus of these efforts where aerodynamics of the tractor and the trailer. For that reason, all of these studies have treated the heavy vehicle as one entity and have not highlighted the main areas accountable for an increase in drag. According to Hilmi Safuan [31], at low speed, the mass of the truck will influence the engine load on the truck, but as the truck gathers speed to more than 80km/h, the aerodynamics of the truck will influence the engine load. This information agrees with the studies of other researchers [7, 8, 9]. Since on the motorway, trucks are speeding up to approximately 100km/h, it is essential that aerodynamic improvements are carried out to reduce operating costs.

The aerodynamics and passive ventilation behaviour of a 1/7th scale livestock trailer model was studied by Gilkeson *et al*. [32] using both experimental and numerical approaches. A combination of structured hexahedral and unstructured tetrahedral cells was used with different levels of refinement. Three different levels of mesh refinement, 2.33, 3.14 and 4.65 million, were used in order to obtain the numerical results. y^+ values were between 30 and 300 in all cases. The blockage ratio was 3.4% and it was calculated based on the average frontal area of the working section. The free-stream air velocity in

the experimental work was 19.2m/s which is equivalent to Re = 1.74×10^6 depending on the combined length of the vehicle–trailer. Gambit (version 2.3.16) was used to create the mesh within the computational domain and Fluent (6.3.26) to simulate all cases.

Three turbulence models were used in the numerical simulations which were Spalart–Allmaras, realizable k-ε and SST k-ω models. The turbulence intensity at the inlet of the wind tunnel was measured at 2.65%. The authors used the same turbulence intensity in the numerical simulations. Standard wall functions and no-slip boundary conditions for all walls were used. Six different case-studies of the towing vehicle–trailer were used with a range of normalized heights (h/H) between 0 and 0.5 as shown in Figure 2.3. Towing vehicles were different sizes of pick-up trucks and SUVs. The agreement between SST k-ω and realizable k-ε results was good. However, the drag coefficient from Spalart–Allmaras using the same number of cells was higher than other turbulent models. Drag coefficient of road vehicles can be anticipated accurately using RANS models as mentioned in this study and other studies [16, 19]. To choose the appropriate turbulence model for a specific geometry, the numerical results of different RANS models should be compared with the experimental measurements. It is worth mentioning that ventilation characteristics were similar for all different towing vehicle heights. The agreement between numerical and experimental results was good except at the rear part of the trailer. The effect of a domain length was studied based on the trailer surface pressures calculations. The effect of the distance between the vehicle and trailer was not studied. As a result of this previous study, pressure coefficient on the surfaces of the scale towing vehicle–trailer is shown in Figure 2.4.

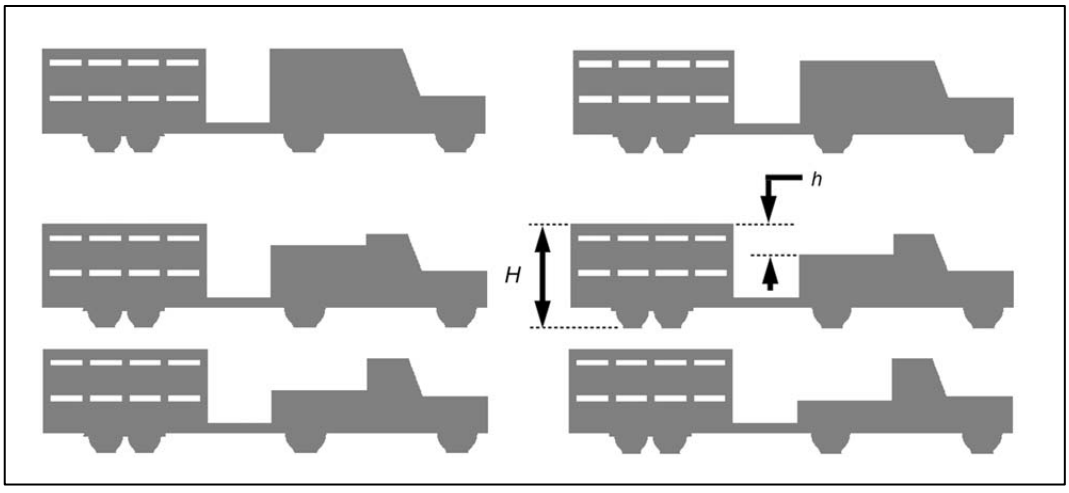

Figure 2.3: Six different case-studies of the towing vehicle–trailer [32]

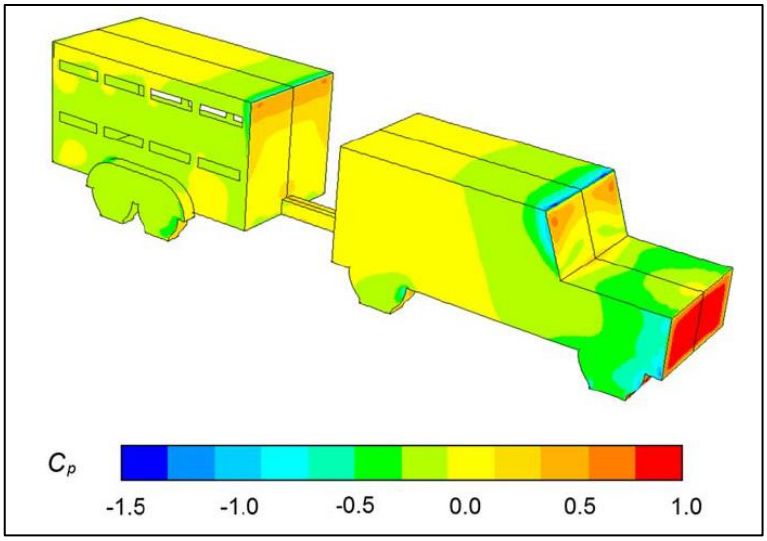

Figure 2.4: Pressure coefficient on the surfaces of the scale towing vehicle–trailer [32]

2.2.3 Passenger vehicles

There are many shapes of saloon cars. Figure 2.5 illustrates four car models with different car-tails, i.e. step-back (a), straight-back (b), fast-back (c) and distributor-installed back (d). It is clear that most differences in car design are at the back of the car as mentioned by Guo *et al*. [33]. A wagon car (squareback) has a relatively high rake angle, see Figure 2.6(a). This high rake angle makes the flow separate early so not staying attached over the rear windscreen because the flow separates at the roof end [33]. If the flow would remain attached it could create a strong downwash which causes a high degree of turbulence in the wake, this would increase the drag (in aeronautics downwash is the change in direction of air deflected by the aerodynamic action of an airfoil, wing or helicopter rotor blade in motion, as part of the process of producing lift). This type of behaviour is common in hatchbacks with a rake angle near 30^{o} and trailing vortices could be created to some extent and the induced drag will be increased. A high rake angle decreases the downwash and the induced drag but it will, on the other hand, have a negative impact on the pressure drag [9]. Sedan cars consist of three boxes in order to get more streamlined shape rather than the wagon design that consists of two boxes as illustrated in Figures 2.6 and 2.7 (*ibid*).

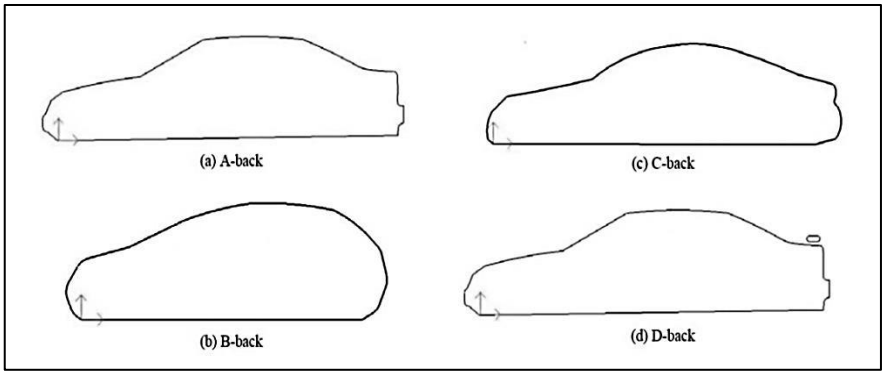

Figure 2.5: Different car bodywork shapes for car-tails. (a), (b), (c) and (d) are the models for step-back (a-back), straight-back (b-back), fast-back (c-back) and distributor-installed (d-back), respectively [33]

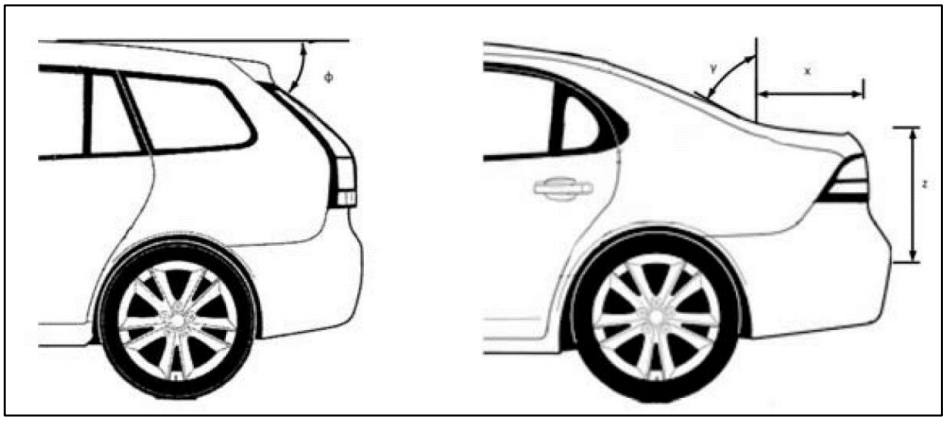

Figure 2.6: The rear-ends of the wagon and sedan [9]

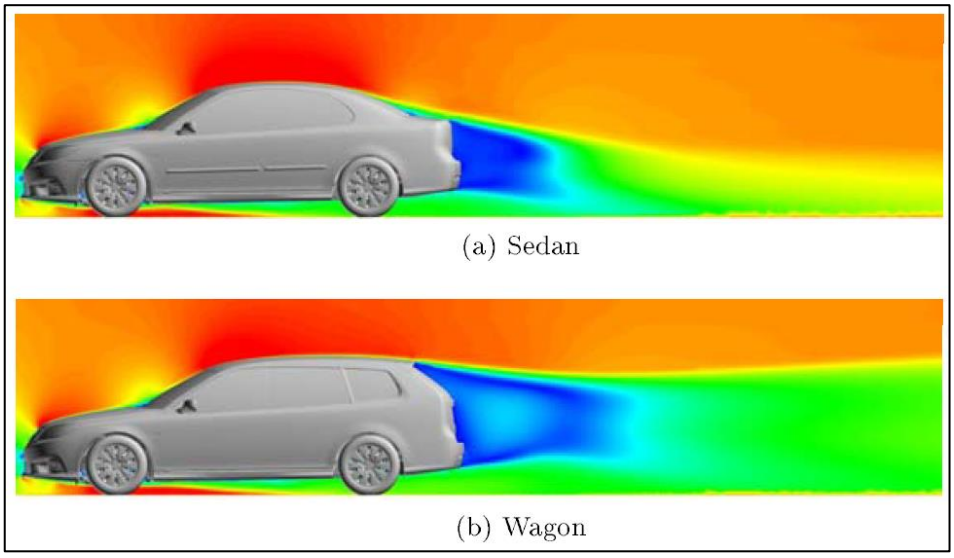

Figure 2.7: Velocity magnitude on the symmetry plane [9]

2.3 Aerodynamic modifications for road vehicles

The technique of changing the shape of the Ahmed model with sharp edges to a form with soft edges was studied numerically by Verzicco *et al*. [25] and experimentally by Thacker *et al.* [29]. A reduction in air resistance and noise was identified with the air streamline being softer than that associated with the ordinary type (the Ahmed model with sharp edges). Verzicco *et al*. [25] used the LES model to study the Ahmed model with one stilt to support this geometry as shown in Figure 2.8. One stilt similar to aerofoil instead of four-cylinder legs was used to achieve mesh quality.

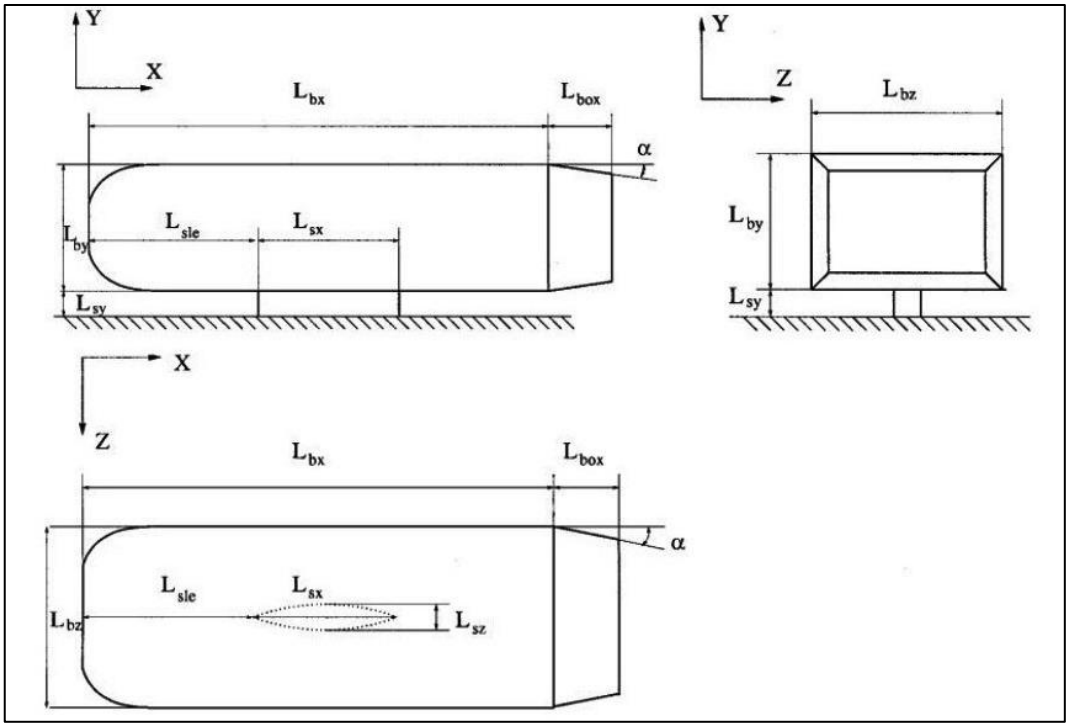

Figure 2.8: Orthogonal views of the body and dimensions [25]

Harinaldi *et al.* [34] studied two models a reversed Ahmed model (with an opposite direction of air flow), as shown in Figure 2.9. The ratio of the size of the model used in this study relative to the original Ahmed model was a quarter with a front slant angle (α) = 35^{o}. It is postulated that the results from this study cannot be compared with the standard Ahmed model results due to differences in model size and air direction. Figure 2.10 shows the computational domain that was used in this simulation. The size of the computational domain in this study is suitable for accurate results as indicated in other studies [19, 26, 35, 36]. The uniform velocity at inlet was 13.9m/s and the suction velocity was 1m/s. The first model had no flow control while the second had active flow control by means of

suction, (Figure 2.11). This technique was used to improve the drag aerodynamic efficiency. The suction was achieved using a low flow rate with the suction velocity set at 1m/s, as shown in Figures 2.9 and 2.11(b).

This research combined computational and experimental work. The commercial solver ANSYS Fluent (version 6.3) with a standard k-ε flow turbulence model computational approach was used to determine the characteristics of the flow field and drag forces. The controlled low speed wind tunnel was used in the experimental approach to validate the reduction of aerodynamic drag obtained through computations. Reducing fuel consumption and increasing the stability of the vehicle were studied. The swirls around the family van model were reduced by modifying the flow separation. The wake and the vortex formation were reduced by using this technique. In the computational approach the aerodynamic drag was reduced by about 13.86% and by approximately 16.32% experimentally. Figure 2.11 shows the pathline velocity field at the rear part of the reversed Ahmed model. The power consumption by active flow control (pump) was not studied. Therefore, the reduction in the drag coefficient was not accurate. This type of modification is somewhat similar to the base bleed.

Designers changed the shape of the boxy body with sharp edges to a form with soft edges. This technique led to reduction in air resistance and noise with the air streamline being softer than the ordinary type [25]. Figure 2.12 shows a modern design of a coach [37]. This model shows a streamlined shape from all sides: front, roof and sides of the coach.

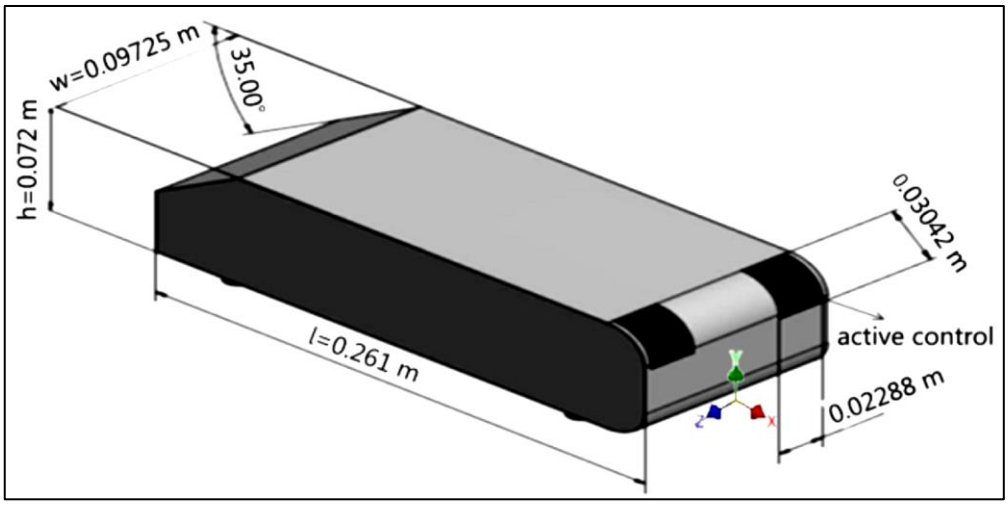

Figure 2.9: Van model of the type of a reversed Ahmed model [34]

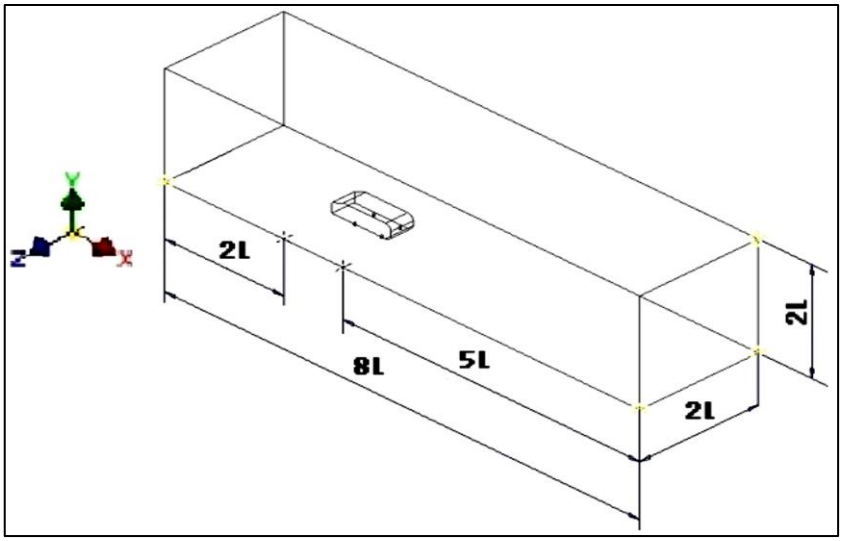

Figure 2.10: Computational Flow Domain [34]

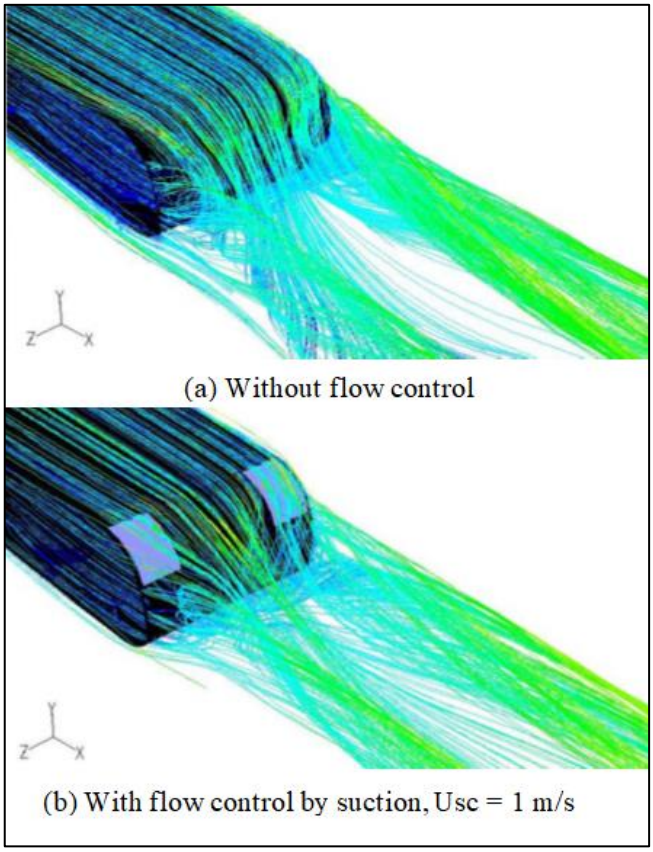

Figure 2.11: Pathline velocity field at the rear part of the reversed Ahmed model with the upstream velocity, Uo = 13.9m/s [34]

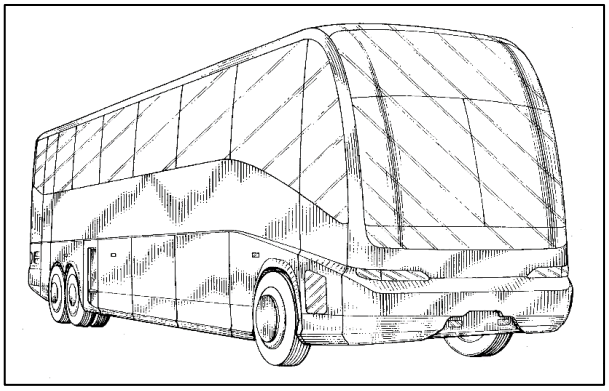

Figure 2.12: Typical tourist coach [37]

Roy and Srinivasan [38] investigated the effects of a crosswind and aerodynamic drag on the fuel consumption of trucks. The characteristics of air surrounding a truck similar to bluff body were studied with the aims of reducing roadside accidents due to wind loading and improving fuel economy. CFD was used to analyse the three-dimensional fluid flow and calculate the pressure distribution on the truck's external surface. The unsteady fluid flow distribution was calculated by solving the Navier-Stokes equation with a two-equation k-ε turbulence closure model. This study indicated the possibility of using k-ε turbulence model to simulate aerodynamics of road vehicles. There were two different designs of truck shapes studied for two different boundary conditions. The first boundary condition was with no crosswind, and the second was with moderate crosswind.

The computational domain was 40 l x 10 d, where l was the length of the truck and d was the maximum width of the truck. It is worth mentioning that the computational domain size in this study was very large compared with other numerical studies [19, 26, 35, 36]. Figure 2.13 shows truck designs A (ordinary design) and B (modified design) used for simulation. It was found that modifying the design of the truck could dramatically improve the efficiency of fuel consumption. The estimated fuel saving was approximately 35% in this study [38]. These researchers proved that the drag coefficient of vehicle can be improved by modifying the external design.

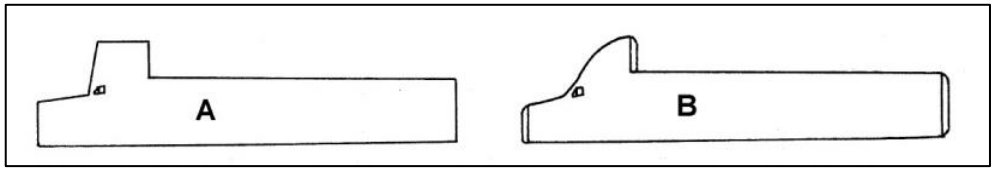

Figure 2.13: Truck designs A and B used for simulation [38]

Some researchers used a two-dimensional (2D) geometry vehicle to study the aerodynamic behaviour [33, 39, 40]. As mentioned by Ghani [40], a 2D geometry vehicle is able to predict the drag coefficient within an error of about 5%. A 2D geometry of the trailing vehicle was modelled by Amirnordin *et al*. [39] according to a hatchback type passenger car as shown along with the pressure contour in Figure 2.14. The hatchback car produced counter rotating vortices at the near end similar to that produced by the bus as shown in Figure 2.15. The wake structures behind the body were influenced by high pressure that occurs in front of the body. This study gives the initial impression for aerodynamic behaviour.

The airflow over the road vehicle is more significant than the underbody [41]. Therefore, the affect of the slant angle of the rear part of the vehicle on drag coefficient has been extensively investigated during the past years [13, 20, 21]. The airflow behaviour in the rear part of the 3D Ahmed model is illustrated in Figures 2.16 [41] and 2.17 [42]. Trailing vortices, shown in Figure 2.16, were created at its lateral edges (rear pillars) which are drag producing due to inclined the rear part of the roof of the Ahmed model from the squareback baseline. The longitudinal vortices resulting from lateral edges at the rear part of the vehicle cannot be seen in the 2D geometry studies, due to the neglect of the third dimension that shows the lateral edges. Figure 2.17 shows the effect of the side edges on the wake structure of the 3D Ahmed model. Thus, the wake structure of the 2D geometry (as in Figure 2.15) is not similar to the 3D geometry (as in Figures 2.16 and 2.17). It is postulated that the results from 2D vehicle are similar to the results of 3D vehicle on the symmetry plane.

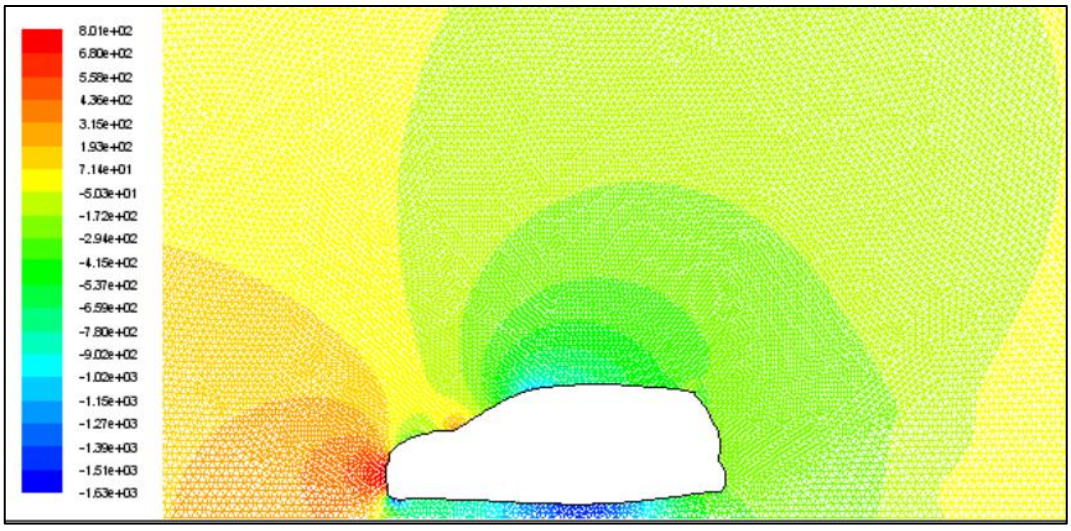

Figure 2.14: Contour of static pressure [39]

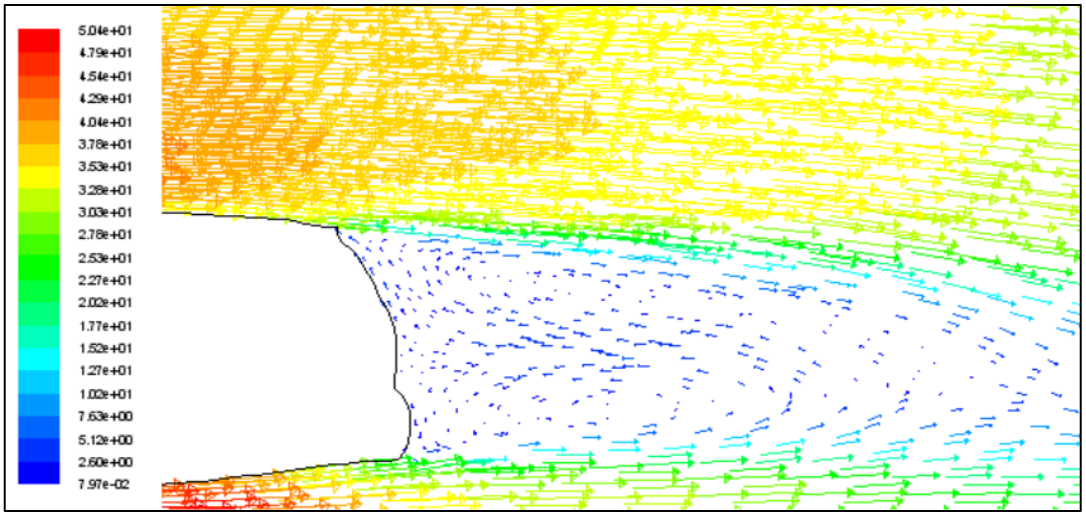

Figure 2.15: Velocity vectors behind the passenger car [39]

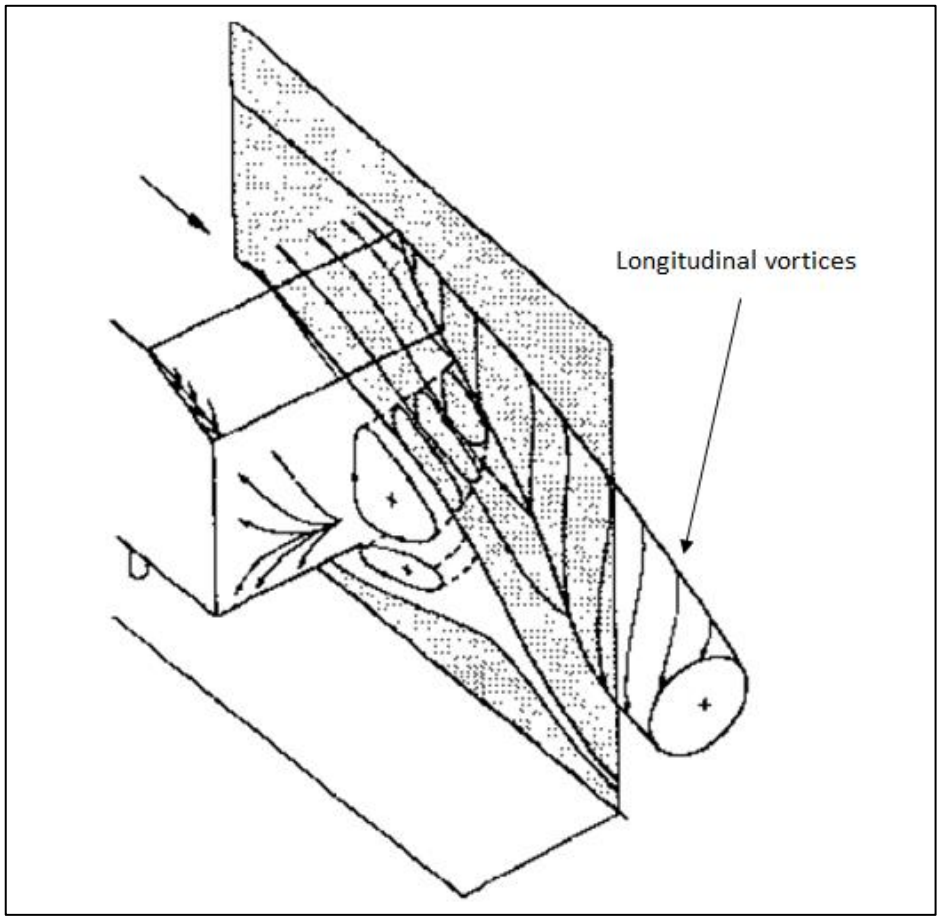

Figure 2.16: Wake flow pattern of the Ahmed model [41]

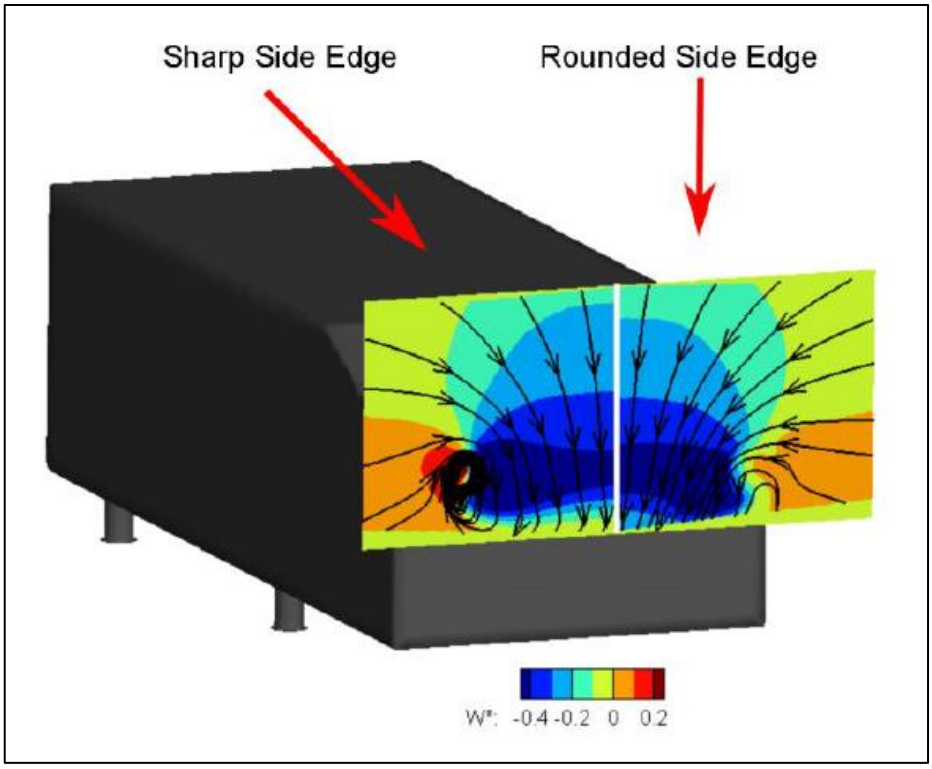

Figure 2.17: Wake visualization [42]

The 2D finite element model was used by Guo *et al*. [33] to analyse the aerodynamic behaviour of a saloon car. ANSYS software was used for modelling and analysis of the saloon car model. The potential fluid theory equations and Navier-Stokes equations were used to describe the aerodynamic behaviour of the saloon car. A simple car model was achieved with modifications to the front surfaces as shown in Figure 2.18. The bottom of the saloon car body was assumed to be a flat surface. The wheels, wind gaps and rear view mirrors were neglected in modelling of the finite element model to simplify the solution. The initial air velocity was 32m/s. This analysis was based on three different slantwise angles of the back windscreen for $\beta = 17°$, $\beta = 23°$ and $\beta = 30°$, respectively as shown in Figure 2.19. Also there were four saloon car models with different car-tails: step-back, straight-back, fast-back and distributor-installed back.

This study and other studies [25, 29, 38] confirmed that the external design modifications can improve the drag coefficient. For turbulent flow computation, the k-ε turbulence model was adopted. As mentioned in this study and other studies (Amirnordin *et al*. [39]; Guo *et al*. [33]; Harinaldi *et al*. [34]; Levin and Rigdal [9]; Miralbes [43]; Roy and Srinivasan [38]), k-ε turbulence model can be used to simulate the aerodynamic of road vehicles. The velocity profile and pressure distribution of air around the saloon car were

studied. The results illustrated that the car top and bottom surfaces were exposed to high pressure. Wind swirling occurred behind the car and it was dependent on the shape of the car. The inclination angle of the rear of the windscreen affects drag and lift force. An increase in the inclination angle of the back windscreen led to increased air resistance but decreased lift force.

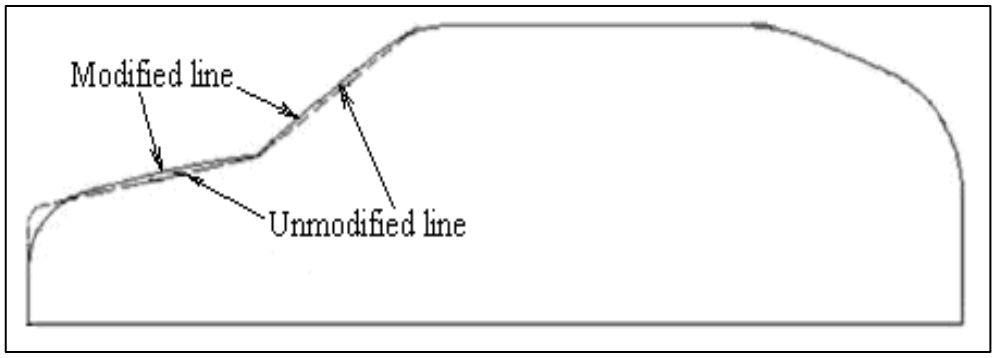

Figure 2.18: The bodywork shape of the automobile in the longitudinal middle section [33]

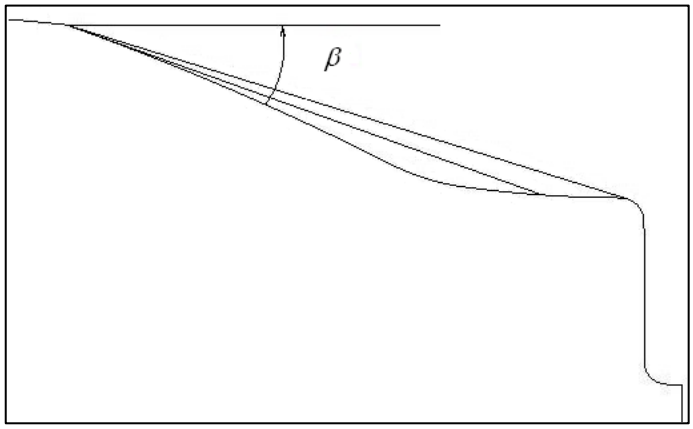

Figure 2.19: Sketch map of the slantwise angle variation of back windscreen [33]

Barbut and Negrus [44] studied the influence of the lower part design of sedan cars on the air resistance as shown in Figure 2.20. Re-design of the lower part of the sedan car could reduce the aerodynamic drag equivalent to approximately 20% because of the viscous effects and the fluid interaction under the saloon car with the typical bluff body flow pattern behind. Computational fluid dynamics for the optimization of the design of the lower part of the sedan car was used. The parallel version of DxUNSp was used as a CFD code.

The re-design of the sedan car was studied with the overall size, a fixed geometry of the interior parts, and frozen geometry of the wheels track. In addition, their aim was also to improve the aerodynamic drag whilst at the same time maintaining other dynamic characteristics such as stability. The authors considered a set of global data as a basic reference. It was as follows: Reference speed was 25m/s, the reference Reynolds number was 2.5×10^6, length was 1.5 m, total reference drag was 0.2411, and reference lift was 0.5662. The MeTHIs software was used to divide the computational domain into eight domains. The code runs in the URANS version of an explicit time integration algorithm.

TecPlot software was used to display the results of the velocity and streamlines are shown in Figure 2.21. Analysis of the flow under the sedan car was carried out using CFD as it was difficult to find real conditions even in the wind tunnels. As a result, the CFD was the used as a tool to analyses the flow under the sedan car with the potential to introduce important changes mainly for the optimal strategy in the car industry. Simulations showed aerodynamic drag reduced from 0.2411 to 0.2105 (almost 12.7%) by re-design of the under body of the sedan car [44].

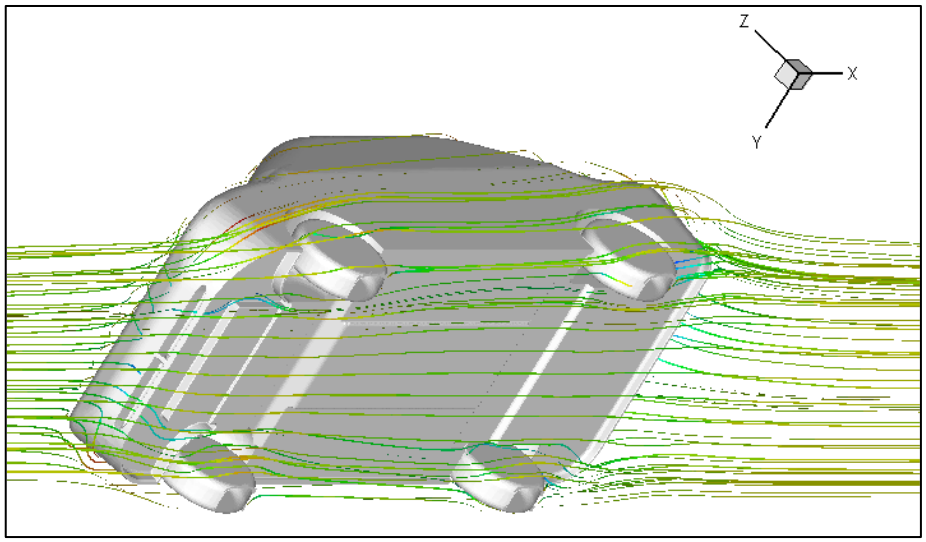

Figure 2.20: Typical CFD flow analysis for the lower part of a sedan car [44]

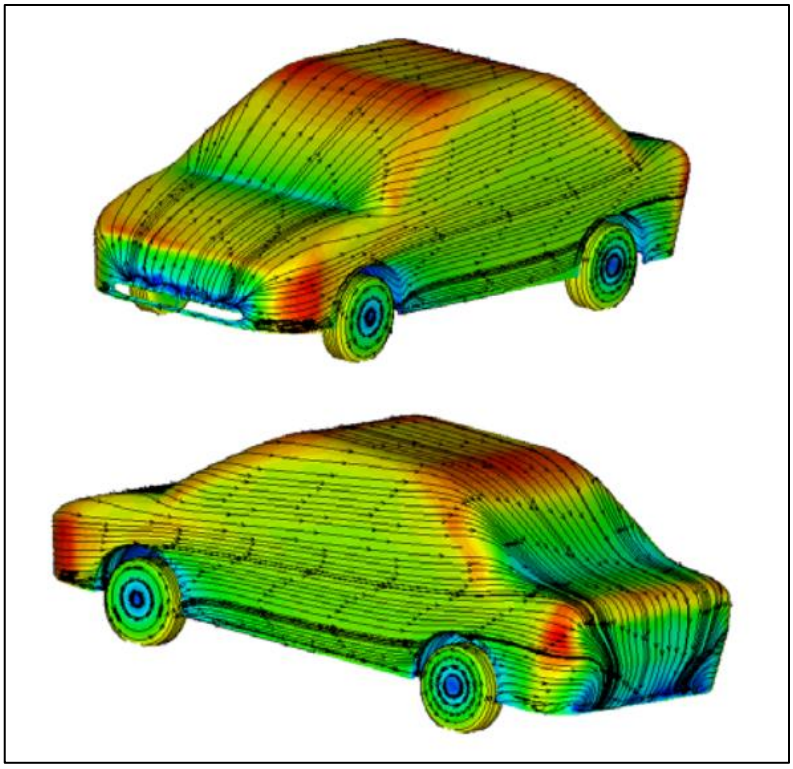

Figure 2.21: Velocity and streamlines distribution on the car surface [44]

An optimized external design of a sedan car by using an Artificial Neural Network was studied by Song *et al*. [45]. The authors focused on modifying the rear external design of the sedan car by using a modification to the boot, the rear side and the rear undercover to optimized rear shape of the YF SONATA model being shown in Figure 2.22. There were two modifications for each part: the length and angle, with limitations to avoid deviations very far from the original design of the car as shown in Figure 2.23. The objective was to minimize the drag coefficient (C_D) value and the lift coefficient (C_L) to less than that of the baseline. Unsteady fluid flow around the automobile driving at high speeds was analysed by CFD.

The study also calculated the pressure around the sedan car and the changes in the drag coefficient. The realizable k-ε model-based DES model was used because it had the highest accuracy compared to the experimental data [45]. A half geometry shape of the YF SONATA was analysed to reduce the time of simulation. GAMBIT and Tgrid were used to generate the meshes. Three boundary conditions were considered: (i) airflow of 100km/h from the front of the car, (ii) the wheels of the car rotating with a rotational speed of 84.175 rad/s corresponding to 100km/h and (iii) moving ground conditions with a velocity of 100km/h. The results show that DES is better than RANS and LES. Figure

2.24 shows an example of the CFD simulation result of-case 46 (equal to the baseline model). On the experimental side the 1/4th scale model of YF SONATA has been tested in a wind tunnel experiment at the Korean Air Force Academy.

The full-size model of the YF SONATA was tested in the Hyundai Motors Corporation wind tunnel to confirm the active affect of an air flap on the aerodynamic performance. The full-sized experimental study showed that the aerodynamic performance was improved by approximately 7.1% if the intake of the engine room was closed by an air flap. The theoretical and experimental studies for a normal design show that the YF SONATA's C_D was 0.31 at 100km/h but for the intake-closed model reduced the C_D to 0.263~0.279. The authors [45] showed very important information about the C_D which were as follows: the average of C_D over five seconds was 0.266 which was taken as the base value in this research. Immediately after the moving car, fluctuations in the C_D occur until about 2.3 s. Therefore, an unsteady phenomenon can be observed.

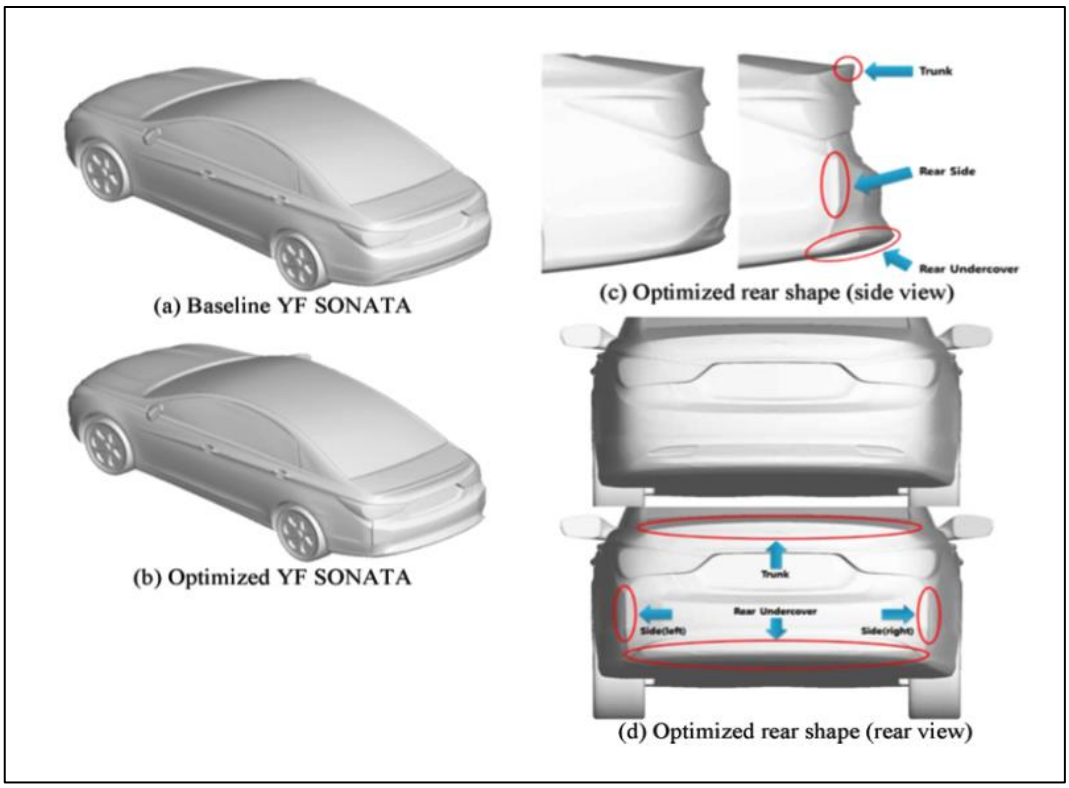

Figure 2.22: Optimized YF SONATA shape [45]

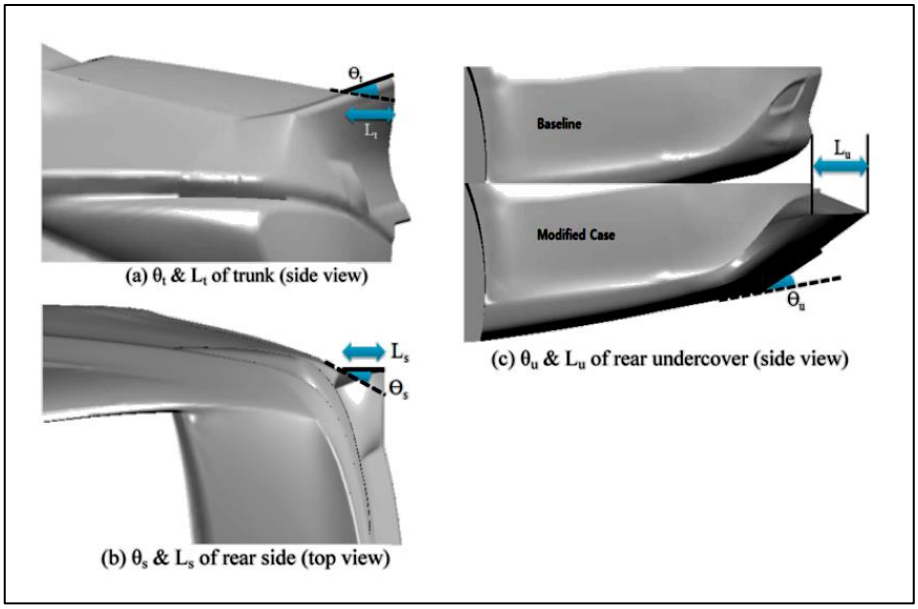

Figure 2.23: Concept of design variables [45]

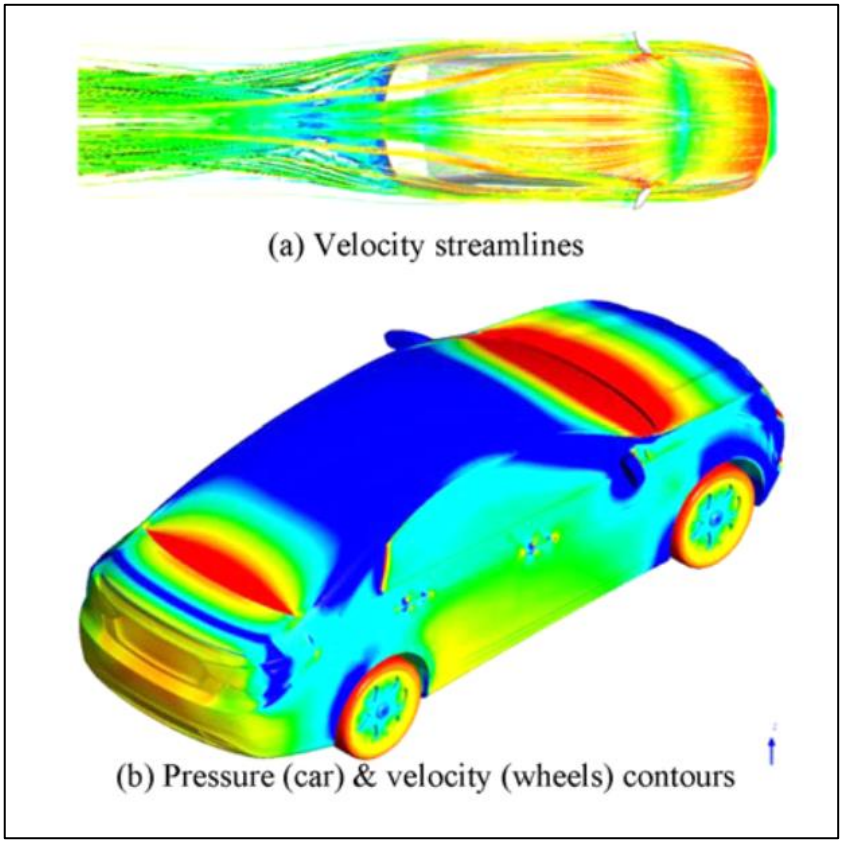

Figure 2.24: Example of CFD simulation result-case 46 [45]

2.4 Sport Utility Vehicles

The aerodynamic development of the full scale model of the Land Rover Discovery 5 was studied numerically by Chaligné *et al*. [46] in the first development stages to optimize the external design, then a full scale of this SUV was tested in the MIRA wind tunnel to reduce the drag coefficient as shown in Figure 2.25. Then a combination between numerical and experimental studies was done to enable a better understanding of the aerodynamic behaviour. Commercial CFD code, EXA PowerFLOW, was used in the numerical simulations. This code provides a Very Large Eddy Simulation turbulence model, which is based on a Lattice Boltzmann solver. Good agreement between numerical and experimental results was achieved except the results of cooling drag. As a result of this previous study, the overall drag coefficient can be reduced by improving the design of the wheels. The drag coefficient of the Land Rover Discovery 5 with a perfect design for the wheels is about 0.33.

Aerodynamic behaviour around a Range Rover with open and closed cooling apertures was investigated experimentally by Pitman and Gaylard [47]. The FKFS Aero-acoustic wind tunnel in Germany was used with different case-studies of this SUV. The speed of the inlet airflow in a wind tunnel was 100km/h for all cases. The study focused on the possibility of reducing the drag coefficient by using multi-case-studies of Range Rover as shown in Figure 2.26. Sixty-five sensors of the surface pressure were placed in different places within Land Rover Discovery such as inside the cooling ducts, around the internal combustion engine and on the surfaces of the vehicle as shown in Figure 2.27. The effect of wheel rotation on aerodynamics, open and closed cooling, was studied in detail. CFD was shown to be invaluable for visualising the airflow around the vehicle because of its predictive capability.

Figure 2.25: Land Rover Discovery 5 inside MIRA wind tunnel [46]

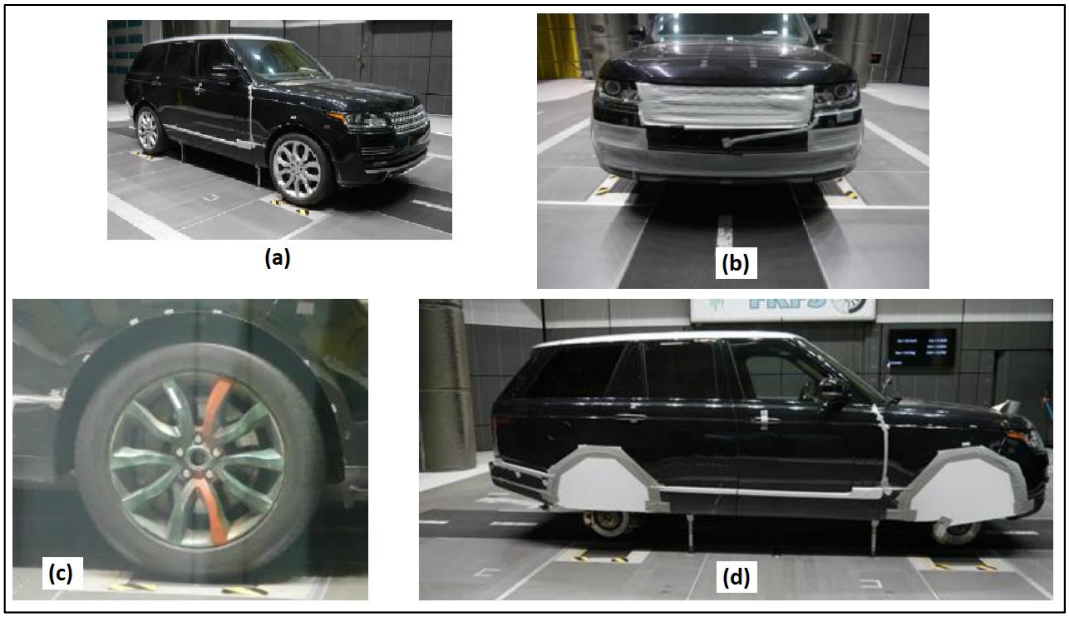

Figure 2.26: Range Rover case-studies: (a) Baseline model with 22” wheels. (b) Closed cooling case-study (c) 20” wheel style (d) No-wheels case-study [47]

Figure 2.27: Surface pressure measurements on tailgate and rear screen [47]

Two aerodynamic modifications, base bleed and a rear cavity, were investigated by Brown *et al*. [48] to determine their effectiveness in drag reduction. A full-scale wind tunnel was used to test different case-studies which were rear cavity, base bleed and several combinations as shown in Figure 2.28. For more clarity about simplifying passive

base bleed see Figure 2.29. These modifications lead to reducing the drag coefficient by restructuring the pressure behind the vehicle. A variety of *d/h* ratios were used where the external cavity was between 0.17 and 0.83 while body cavity was between 0 and 0.83. Figure 2.28 shows all case-studies and dimensions of these aerodynamic modifications. As mentioned by Brown *et al*. [48], external cavities lead to an increase in aerodynamic drag. This may be due to an increase in the surface area, which led to an increase in viscous force. A maximum reduction in the drag coefficient of 3.3% was achieved by using a body cavity while for base bleed was between 0.3% and 1.1%.

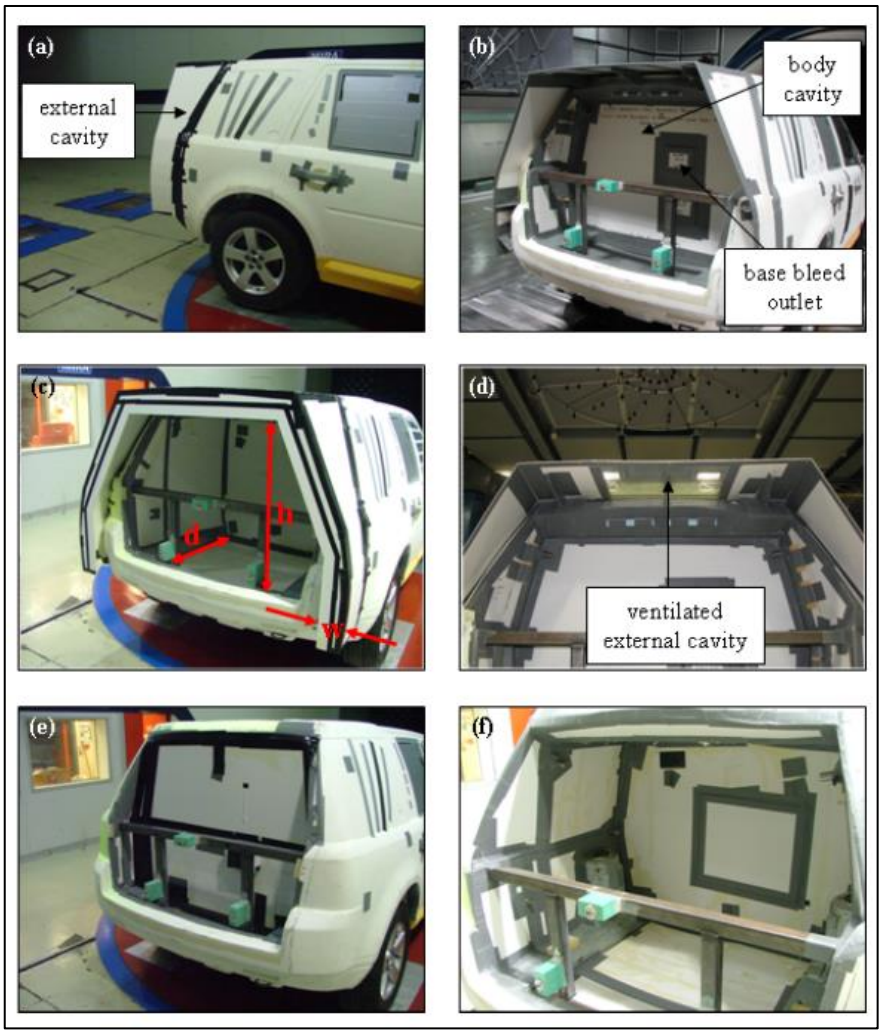

Figure 2.28: Several case-studies of SUV (a) External cavity, (b) Combination of body and external cavities, (c) Definitions of cavity dimensions, (d) External cavity with ventilated section, (e) Body cavities (f) Deep body cavities [48]

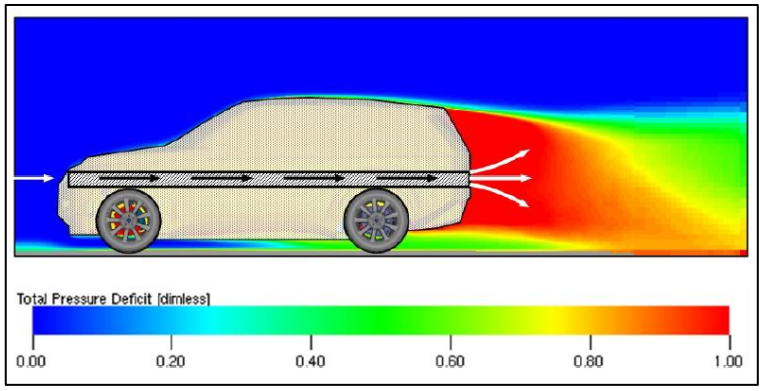

Figure 2.29: Side view of simplifying passive base bleed [48]

2.5 Add-on aerodynamic devices for road vehicles

Khalighi *et al*. [49] investigated the unsteady flow around the Ahmed model. Experimental tests and numerical simulations were carried out for this model with and without aerodynamic add-on devices. Two types of add-on devices attached to the back were used to improve the aerodynamic behaviour; these consisted of a boat-tail and a box with a cavity. Both boat-tail and cavity have the slanting surfaces similar to that in the Ahmed model. Therefore, the study of the slant angle in the Ahmed model can be used to design the boat-tail and cavity. Unsteady RANS was used for these transient numerical simulations.

All experimental tests were performed in a small sized wind tunnel. The pressure and velocity of the air inside the wind tunnel were measured. There was reasonable agreement between the numerical results and those obtained experimentally in terms of the flow structures and drag coefficient. Figure 2.30(b) shows the boxy shape with a square back body. This type of shape needs devices to reduce the resistance to the movement of the vehicle. The first device added the cavity behind the vehicle as shown in Figure 2.30(c). A cavity consists of plates surrounding the rear surface of the shape to form a ditch. This cavity works to reduce air swirls that occur behind the vehicle, especially at high speeds. The second add-on aerodynamic device to the surface of the rear of the vehicle added a boat-tail as shown in Figure 2.30(d). This type of device is better than the cavity model because the boat-tail works on the smooth lines of airflow from all directions. This leads to a reduction in the aerodynamic drag, noise and vibration [25].

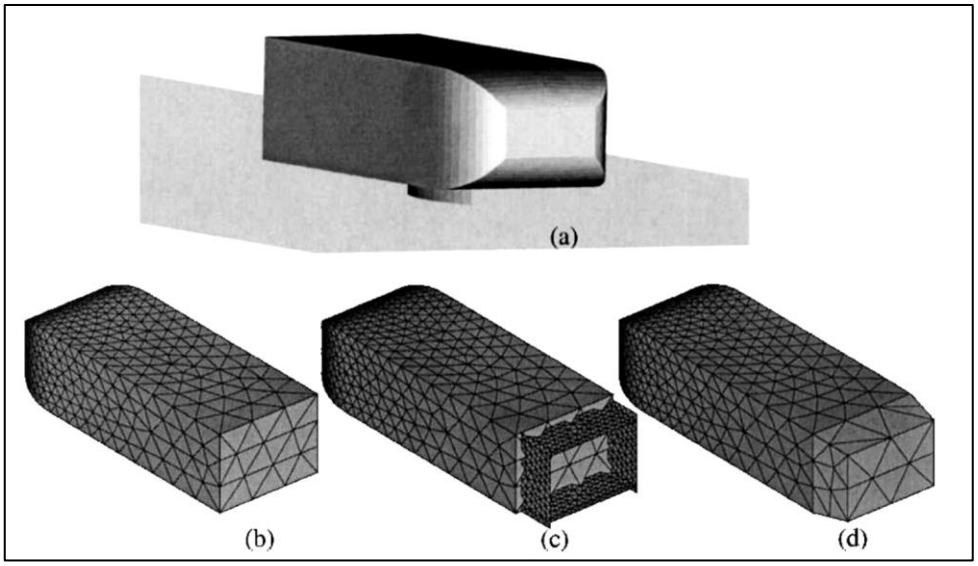

Figure 2.30: Geometrical models: (a) perspective view of the body, (b) square-back body, (c) cavity, and (d) boat-tail back [25]

Estimation of the real reduction in fuel consumption could be achieved by using a variety of commercial aerodynamic drag reducing devices for heavy duty trucks. Fourteen model tests with different drag reduction devices were used by Du Buisson and Erens [50] in addition to the original model which was unmodified. Computer simulation was used to calculate reduction in fuel consumption. The calculations depend on reliable information obtained from a 1/20th scale tractor-trailer wind tunnel model, (Figure 2.31). All the different collected information were for devices available as a function of wind angle of incidence for the model. This truck was 32000 kg, with the frontal area of a tractor-trailer combination equal to 9.5m^2 with a C_D of 0.95, and transmission system efficiency equal to 0.86.

Drag resistance of a tractor-trailer at 80km/h represents about 50% of the total resistance. This is confirmed by other researchers [7, 8, 9, 31]. Large savings of fuel consumption can be achieved by improving the aerodynamic drag. However, taking into consideration all factors above-mentioned a reduction in drag coefficient does not necessarily lead to a reduction in fuel consumption. The small-scale tractor-trailer model was used and that can lead to inaccurate results. For more accurate results the investigation required a full-scale model test or at least asymptotically the full size of the original model, however, these were not used in this case study. The scale tractor-trailer wind tunnel model tests were carried out using a low speed wind tunnel that has a 1 × 1.4 m cross-sectional area. Models with a trailer-mounted device and with a cab-mounted device were tested in this

study. The experimental investigation revealed that the drag coefficient varied little with Reynolds number. This could agree with other researchers [18, 29]. As a theoretical result, the total drag can be reduced up to 15% [50].

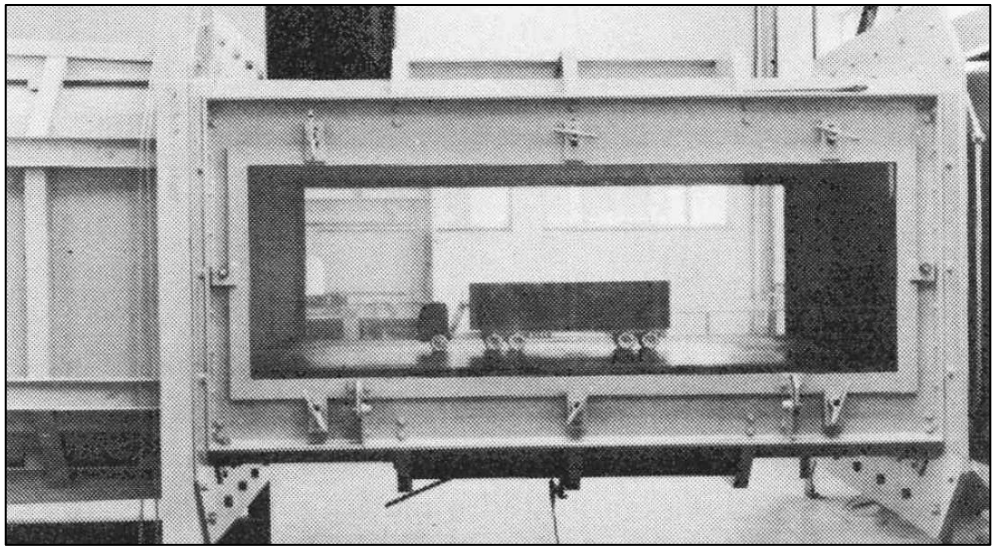

Figure 2.31: 1/20th Scale tractor-trailer model in wind tunnel test section [50]

As mentioned by Leuschen and Cooper [51], add-on aerodynamic components have been used to improve the efficiency of aerodynamic drag. Full-scale wind tunnel tests on a Class-8 tractor-trailer were studied. The dimensions of the wind tunnel were 9.14m high, 9.14m wide and 22.5m long, as shown in Figure 2.32. The maximum speed of the air in the wind tunnel was 200km/h and a turbulence level of 0.5%. A Volvo VN 660 was used as a test model. Figure 2.33 shows common components whose drag effects were measured. The truck model frontal area was $10.9m^2$, which was 13.3% of the wind tunnel section. It is worth noting that a blockage ratio in this case study was very high and the drag coefficient should be corrected.

As mentioned by Altinisik *et al*. [35], the measured drag coefficient of the blockage ratios higher than 7.5% should be corrected. An inlet velocity of 29.6m/s was used in all the tests that carried out by Leuschen and Cooper [51]. Many kinds of vehicle case-studies and components were studied in addition to the new drag reducing hardware as shown in Figure 2.34. This was done in order to understand the influence of common components on aerodynamic drag. Some of these aerodynamic devices can be used for SUV with suitable modifications (such as roof deflector, inflatable boat-tail and VGs on the roof). The deflector and mirrors caused an increase in fuel consumption. Side mirrors lead to increase the frontal area and that causes an increase in drag force. This study indicated

the possibility of using modern video cameras to eliminate mirror drag as the means of providing rearward vision.

All external additional parts except the mirrors and the deflector were useful parts to reduce the aerodynamic drag. In many full and model scale tests of modified tractors, covering the front grill to eliminate the cooling flow had a negligible effect on aerodynamic drag. Also the same effect occurred with the lower intake at the front bumper. Wheel rotation effects were unknown because these tests were performed with fixed wheels. To reduce the aerodynamic drag, the tractor-trailer gap was reduced from 1.14m to 0.89m. This technique can reduce the vortices between tractor and trailer by covering some of this area. As a result, the fuel consumption was reduced almost 6,667 litres a year, based on 130,000km travelled per tractor at a speed of 100km/h.

Figure 2.32: Class-8 tractor-trailer in the National Research Council of Canada. Full-scale wind tunnel [51]

Figure 2.33: Common components of aerodynamic reduction techniques which were used in the tractor-trailer [51]

Figure 2.34: New add-on aerodynamic devices [51]

Many aerodynamic devices for the underbody of a tractor-trailer combination lead to reducing the aerodynamic drag. These aerodynamic add-ons were tested by Van Raemdonck and Van Tooren [52] in the low turbulence tunnel at Delft University of Technology in The Netherlands. The cross-sectional area of the wind tunnel was 2.07m^2 (width of 1.8 m; height of 1.25 m) and the maximum speed was 120m/s. The speed of the air in the wind tunnel was set at 60m/s because of the high aerodynamic forces at higher wind tunnel speeds and the low sensitivity of Reynolds effects of the truck model. A 1/14th scaled truck model (TAMIYA Mercedes Benz 1838LS truck 1/14 and TAMIYA Container-trailer) was tested in a wind tunnel with many aerodynamic devices for the underbody as shown in Figure 2.35. The initial tractor-trailer combination model had sharp edges. These edges were modified to prevent flow separation at the front edges and initiate a turbulent boundary layer before it reached the back edges of the tractor.

The cooling and fan system were not in use for the scaled truck model because of the location of the balance system. The frontal area of the truck model was 10.34m^2 and the driving velocity of truck model was 25m/s. In the experimental tests more than 93 various aerodynamic add-ons were studied on the tractor-trailer combination. Adding the mud flaps to the truck model increased the aerodynamic drag by almost 5%. As a result of this research, the modification which was based on the cover of the wheels was always useful for the drag coefficient. Full underbody that covered the support legs, pallet box and the axles of the wheels was not performing as well as the straight side-skirts which comprise two single panels along the lower side of the trailer in a longitudinal direction. All these modifications to side-skirts reduced the aerodynamic drag up to 14%. Just a few modifications were studied for the flow in the underbody of the tractor-trailer combination [52].

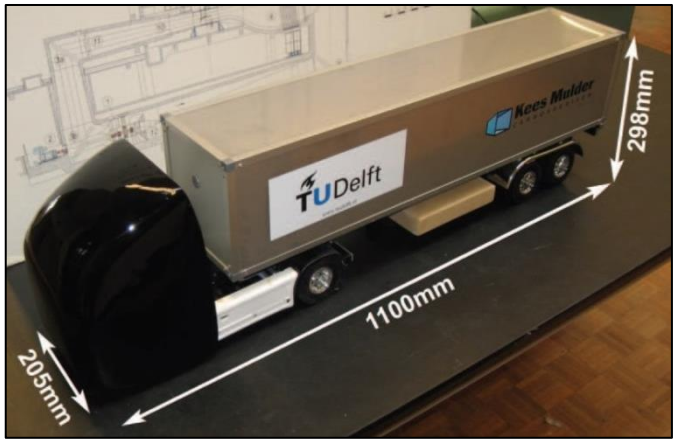

Figure 2.35: A 1/14th scaled truck model [52]

The application of the new design of devices was used to improve the aerodynamic performance for the trailer base as shown in Figure 2.36. Boat-tail, base flaps and tail devices were used by Salari and Ortega [53] to improve fuel consumption. The trailer base devices consisted of four flat plates that were attached together on the rear edges of the trailer. It forms a closed cavity at the end of the trailer. This system was used in many different forms, for example, inflatable and non-inflatable, three and four-sided, closed and opens cavity, plus other forms. The primary factors were deflection angle, boat-tail length, sealing of edges and corners, three versus four-sided, boat-tail vertical extension, and closed versus open cavity. The aerodynamic drag reduced because the typical design of the boat-tail devices (straight frame) led to a rise in the pressure on the trailer base area. Boat-tail side plates should be extended to cover the drop-frame trailers. The authors [53] have used information gathered from the literature and their own experimental investigations to create a full model of the truck.

Figure 2.36: Six different combinations of devices on the semi-trailer truck model [53]

Various topics were investigated in the literature including aerodynamic drag, advanced technology, component spacing, driver behaviour, proper maintenance and route management as investigated for example by Farkas [54]. Moreover, improving vehicle fuel consumption efficiency by using new technologies was also reported. There are a large number of factors that affect the fuel consumption rate in a vehicle. Almost half the energy of the heavy truck engine is consumed to overcome the air resistance at 55 MPH,

but two-thirds of the energy of the engine is lost to overcome the air resistance if the speed increases to 65 MPH. Four methods were used to investigate possible ways of reducing fuel consumption: Computational Fluid Dynamics, PACCAR Technical Centre testing, real-world highway testing, and wind tunnel tests. It is worth mentioning that the Computational Fluid Dynamics simulation is a combination of real world and wind tunnel conditions on the computer screen.

The use of computer simulation is better than simple wind tunnel data. The nature of the CFD analysis techniques means that full-sized models can be simulated directly, avoiding the Reynolds number matching and the wall problems faced when using a wind tunnel (proper wind tunnel facilities are rare). In addition, it is possible to simulate large models with many modifications (a wind tunnel simulation requires a priori and is often expensive). Different wind yaw angles, moving ground plane, rolling tyres, and the effects of the under hood and under body airflow with a full sized heavy truck were investigated by Farkas [54] using CFD.

Figure 2.37 shows virtual aerodynamic testing. The model used in the wind tunnel was 20% of the original size. Programs of wind tunnel tests usually run during a one week period with individual tests going on for five minutes or less to collect the data for aerodynamic drag. The experimental tests with smoke were used in this study because it has the possibility to clarify the flow characteristics of the heavy truck clearly as shown in Figure 2.38. Additional parts of the main body, such as the cab extenders, the exterior mirrors and sun visors were not investigated and their impacts on the aerodynamic performance were neglected. The deviation between measured and simulated values of fuel consumption can be less than 5%. Heat transfer which occurs under the hood was also studied. The results of this study allowed for creating a smooth flow of air which reduced air noise (*ibid*).

Figure 2.37: Virtual aerodynamic testing [54]

Figure 2.38: Tests that utilize smoke [54]

The effect of some improvements designed on the aerodynamic behaviour for semi-trailer tankers were analysed by Miralbes [43]. These improvements and modifications reduced the fuel consumption almost 11%. A commercial CFD program was used to analyse these techniques. A simplified form of the semi-trailer tanker was used in the analysis. Some external parts were neglected such as rear-view mirrors. The following assumptions were used: the velocity of the air was 30m/s and a smooth surface that moves with the same velocity of air. Heavy vehicles without improvements were studied first to ascertain the areas that contain the vortices and the highest flux detachment to act in these areas and with two models of tanker case-studies. Three kinds of aerodynamic devices were used: a nose cone, an underskirt and a boat-tail as shown in Figures 2.39, 2.40 and 2.41 respectively.

The boat-tail worked to avoid the detachment of the limit layer in the later area at the end of the truck. This model reduced the drag coefficient by almost 5% by eliminating the pressure difference that causes vortices. The nose cone was used in the front top zone of the semi-trailer as a second technique to avoid the swirl in the gap between the tractor and trailer. These devices improved the aerodynamic drag efficiency by more than 3%. The undercarriage skirt was used to prevent the air flow going into the lower area of the semi-trailer tankers to reduce air swirls resulting from the rotation of the wheels and this led to improvement in the aerodynamic behaviour by about 7%. All of these improvements were analysed separately and together. The addition of these devices led to weight gain, which means an increase in fuel consumption, but the total resistance decreased due to lower air resistance. The final outcome of this analysis showed that the aerodynamic drag reduced by almost 23% as mentioned by Miralbes [43].

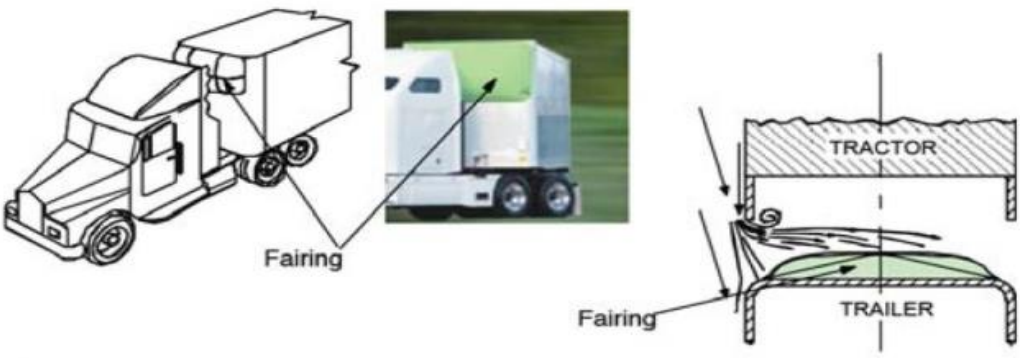

Figure 2.39: Nose cone [43]

Figure 2.40: Undercarriadge Skirt [43]

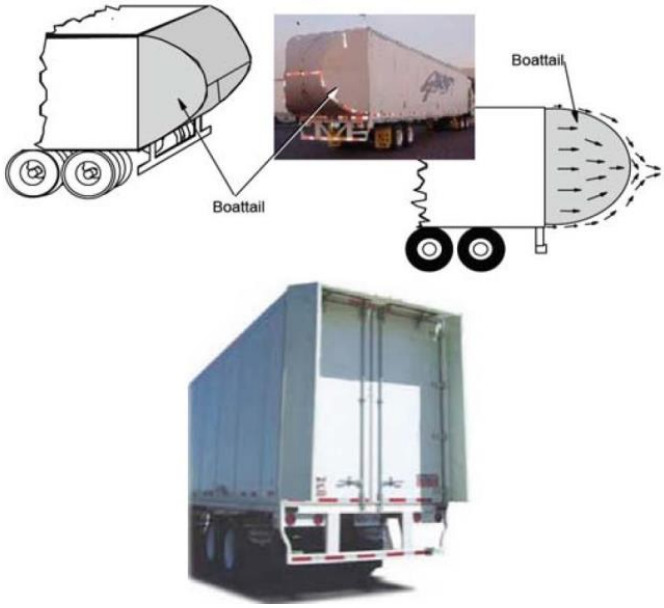

Figure 2.41: Boat-tails [43]

The effect of changing the external shape of a tractor-trailer truck and using some modification devices on aerodynamic drag were studied theoretically and experimentally by Shukri and Akram [55]. The 1/30th scale model was used in experimental work using a small wind tunnel with a 10^6 Reynolds number. A wooden model was tested in a wind tunnel with 29m/s velocity as shown in Figure 2.42. The wind tunnel section dimensions were 45 cm × 45 cm and the overall length was 120 cm. The model was based on a Mercedes-Benz 1844 ACTROS container-trailer.

The researchers focused on combining the base flap and splitter to reduce the aerodynamic drag. The modification devices that have been added to the back of truck were a base flap and a base flap with separator using four angles 0˚, 10˚, 20˚ and 30˚. Aerodynamic drag has been reduced by about 18% in experimental work when using the incline angle for the base flap with a separator equal to 10˚. The after base body length ratio was studied for four cases, for example the ratio of device length over the base body to trailer length equals 0.065 when $\beta = 0^{\circ}$. Trailer after body length ratio is defined as the length of an aft body treatment device divided by trailer length. The CFD package (ANSYS FLOTRAN 12.1) was used for the theoretical study. The theoretical part solved by using an ANSYS package with FLOTRAN CFD analysis on two-dimensional solid model was constructed on a semi-trailer truck with k–ε turbulence model. Theoretical results were velocity and pressure contour in addition to the streamline on the truck with and without modification devices at $\theta = 0^{\circ}$ only.

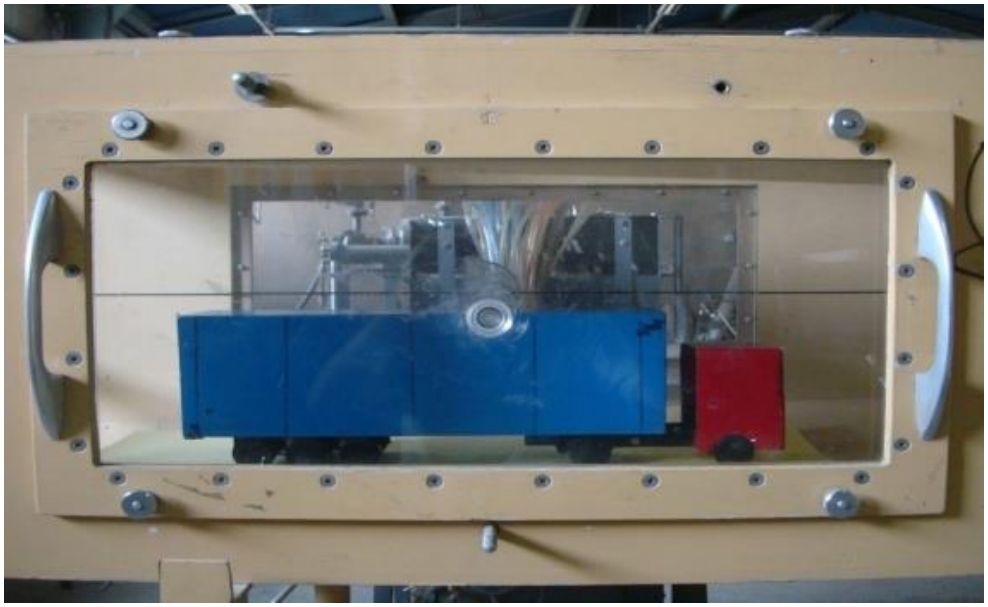

Figure 2.42: photo of test section [55]

According to Chowdhury *et al*. [56] there are many add-on devices that help to reduce fuel consumption as shown in Figure 2.43. A 1/10th scale model of a semi-trailer truck model was used in a wind tunnel as shown in Figure 2.44. The aerodynamic drag was measured for the baseline model and modification models with a variety of external devices. These add-on devices work to reduce the vortices. Front fairing, side skirting and gap filling were used as external attachments. The baseline model and modification models were measured for a wide range of speeds and yaw angles. Adding a front fairing (cab) above the roof of the truck was very useful to reduce the drag of air because this device will guide the air to the top and that helps to build a soft layer of air through the surface of the trailer 2.43(a).

In Figure 2.43(b) the design covers the gap between tractor and trailer by using a curved shape (gap filling). This design was better than the previous design because it prevents the occurrence of any vortex between the tractor and trailer. The design shown in Figure 2.43(b) treats airflow from the top and sides also. The third design covered the distance between the trailer wheels in addition to the cab on the roof of the tractor as shown in Figure 2.43(c). Reducing air swirls between the wheels of the trailer contributes effectively to reduce aerodynamic resistance and noise. Side skirts are vertical plates which are mounted in the longitudinal direction of the trailer.

The main idea of the side skirts is preventing the flow to go under the trailer with all its disturbances like support legs, storage boxes, suspension, axles and wheels, see Figure 2.43(c), (d), (e) and (f). The next design covers the distance between the wheels of the trailer and all the tyres of the trailer as shown in Figure 2.43(d). This modification was very useful to eliminate the noise and aerodynamic drag. The design shown in Figure 2.43(e) was a mixture between design 2.43(b) and design 2.43(c) and it has the benefits of both types. The final modification shown in Figure 2.43(f) is a hybrid of the designs 2.43(b) and 2.43(d) and this model was considered the best of all modifications. The results reveal that modifications by adding external attachments can reduce up to almost 26% air resistance over the reference model depending on the effects of cross winds.

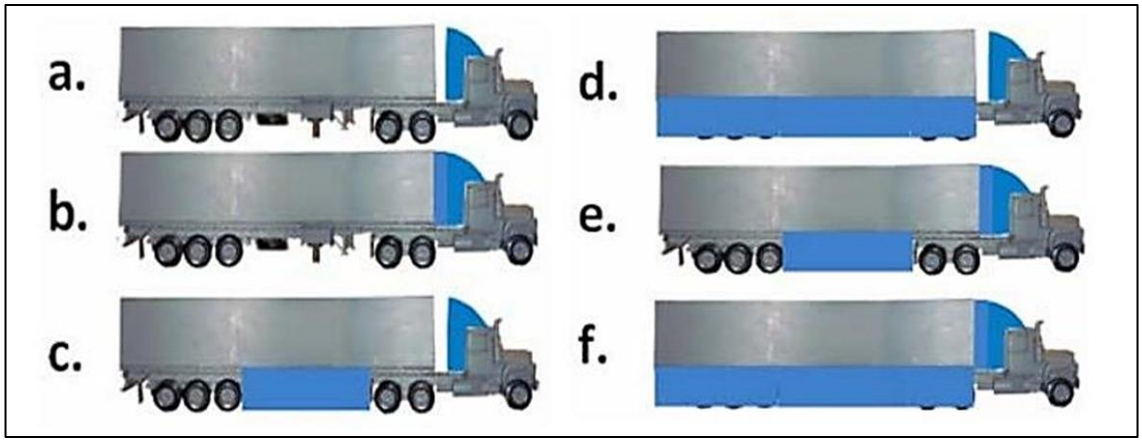

Figure 2.43: Different combinations of fairing on the baseline semi-trailer truck model [56]

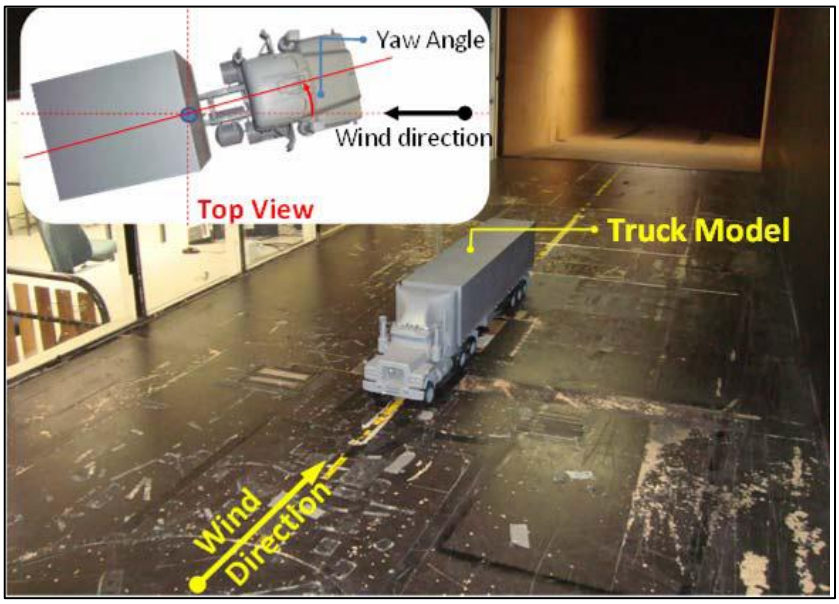

Figure 2.44: Experimental arrangement in the test section of RMIT Wind Tunnel [56]

Vortex generators (VGs) were used in the saloon car by Koike *et al*. [57] to reduce air resistance. VGs were used to minimize the separation of flow near the vehicle's rear end as shown in Figure 2.45. These pieces were installed on the rear of the saloon car roof as shown in Figure 2.46. VGs create drag, but they also reduce drag by preventing flow separation downstream. The external design of vortex generators affects aerodynamic behaviour. Experimental and theoretical methods were used to calculate velocity and pressure distributions. A full-scale model of a Mitsubishi Lancer Evolution VIII was

tested in a wind tunnel at 50m/s and the flow field around the saloon car was analysed in detail by using CFD; three different designs of vortex generators being examined.

All these types were similar in shape, but different in height (15, 20, 25mm) respectively, (Figure 2.47). The optimum design of vortex generators was in the range of height between 20 to 25mm because the drag coefficient was the smallest. This technique led to a decrease in the drag coefficient of about 0.3%. The delta-wing-shaped vortex generator's effectiveness was also examined. Figure 2.48 shows the dimensions of delta-wing-shaped vortex generators. As a result, the optimum height of the vortex generators was almost equivalent to the boundary layer thickness and the optimum position was arranging them in a row in the lateral direction 100mm upstream of the roof end at intervals of 100mm. The optimum design of vortex generators showed a reduction in both the drag and lift coefficients by about 0.006. That means it can reduce fuel consumption and provides more stability of cars on the road. The purpose of reducing the lift coefficient is to increase the downforce on the vehicle tyres, thus creating more grip.

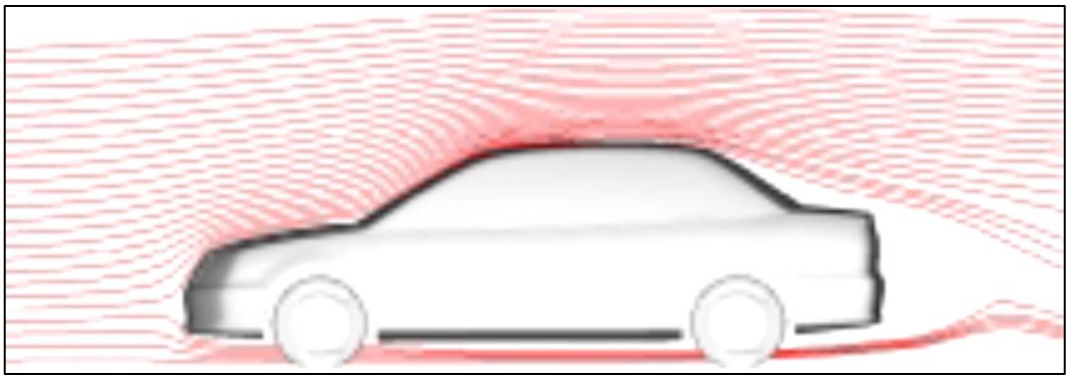

Figure 2.45: Flow around a sedan with vortex generators [57]

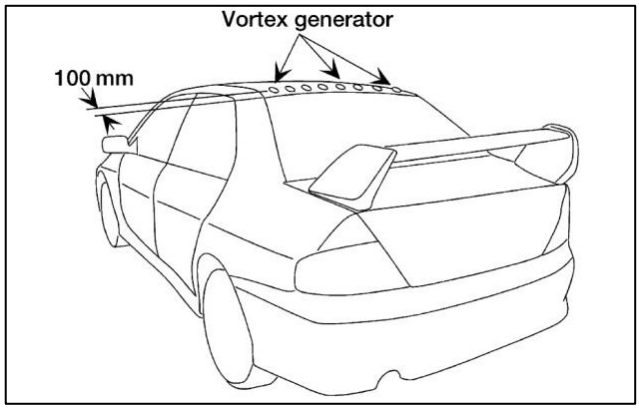

Figure 2.46: Location of vortex generators [57]

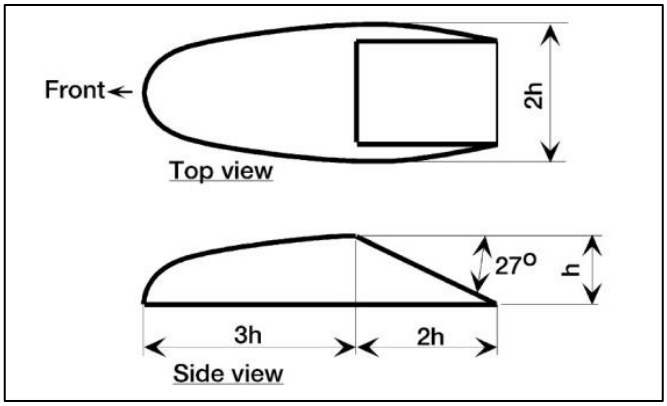

Figure 2.47: Dimensions of vortex generators used for analysis [57]

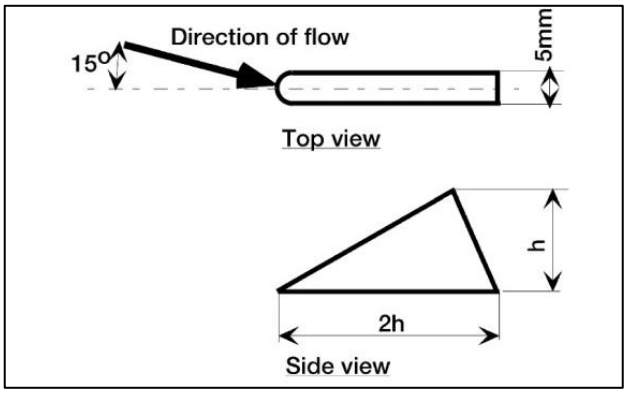

Figure 2.48: Dimensions of delta-wing-shaped vortex generators [57]

The effect of the spoiler on the sedan car was numerically studied by Hu and Wong [58]. Figure 2.49 shows the simplified 3D sedan car model. The design of the new rear-spoiler was aimed at reducing both the drag force and the lift force. Airflow was influenced by the design of the spoiler. Modifying the design of the spoiler leads to a decrease in the lift force of the sedan car and this means an increase in the stability of the sedan car on the road. The standard k-ε model was used by Hu and Wong [58] to simulate the aerodynamic of the simplified three dimensional Camry model. Two different models were used, one with a rear-spoiler and the other without a rear-spoiler.

Airfoil and plate shapes were used as the geometry of the rear spoiler as shown in Figure 2.50. Figure 2.51 shows the three-dimensional vehicle model with a rear spoiler. Twenty four cases were investigated and the differences were in the position and the angle of the spoiler. Three parameters were studied for the rear spoiler: the external shape, the position and the clearance between spoiler and boot surface. As a result, most of the sedan cars

with a spoiler have a higher drag force than those without a spoiler. The plate like spoiler with an attachment angle of 5 degrees was the best case in drag force reduction.

The new design of spoiler made a diffuser with the upper boot surface and that led to an increase in the pressure at the end of the car compared to the sedan car without a spoiler. There were two separation points of flow; the first one was at the front of the windscreen and the second one was in the middle of the rear window. To decrease the air resistance and lift force two designs of rear spoiler were made by Hu and Wong [58]. The drag force of the sedan car with the new spoiler was reduced by about 1.7% and the negative lift force increased in a high speed test.

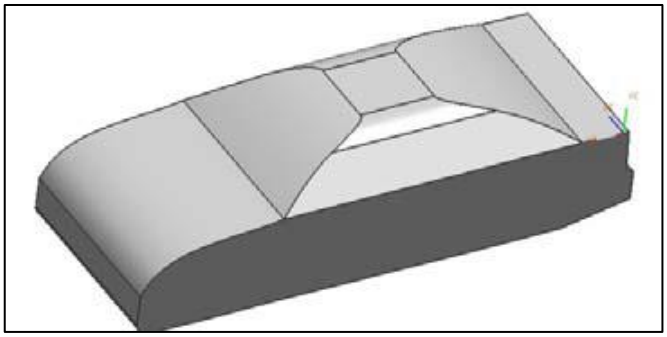

Figure 2.49: Simplified 3D sedan car model [58]

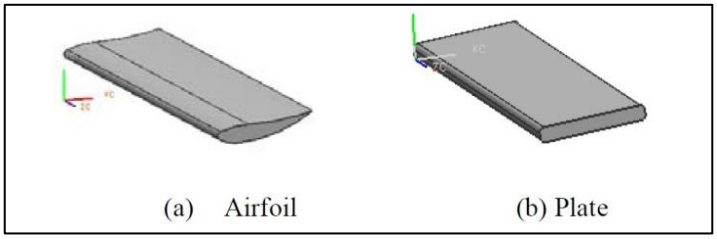

Figure 2.50: Two types of rear spoiler considered [58]

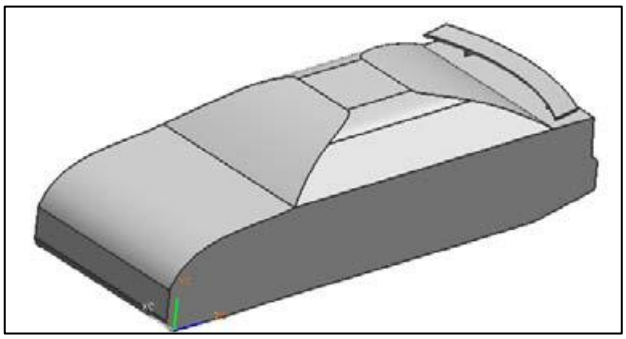

Figure 2.51: 3D vehicle model with rear spoiler [58]

Reduction in the aerodynamic drag of the saloon car by using a movable arc-shaped semi-diffuser device was studied by Kang *et al*. [59]. This aerodynamic device was installed on the rear bumper of the sedan, (Figure 2.52). The advantage of this device is that it disappears under the rear bumper, but it reappears only at high speeds (70km/h ~ 160km/h). The effect of positions and protrusive lengths and widths of rear diffuser devices were studied for seven types, but the same basic shape, as shown in Figure 2.53.

The rear diffuser device led to an increase in the base pressure of the saloon car and then prevents the low-pressure air coming through the underbody from directly soaring up to the rear surface of the boot. While the pressure of the underbody flow increases, the velocity of air flow decreases by a diffusing process which is generated from a diffuser device (under the rear bumper) and this leads to a reduction in air resistance. Using this technique, the air resistance reduced by more than 4%, this also leads to improvement in the constant speed fuel efficiency by almost 2% at 70km/h speed. The Vehicle Modelling Function (VMF) was used to realize a three-dimensional virtual saloon car case-study.

To simulate a saloon car similar to the real conditions, the computational domain was set up as: length was equal to four times the length of the car, width was equal to four and a half times the width of the saloon car, and the height was equal to three times the height, as shown in Figure 2.54. The computational domain size in this study is small as compared to other research. The dimensions of the computational domain have a significant impact on the numerical results as indicated by many researchers [19, 26, 32, 35, 36]. Fully developed flow at the inlet and outlet of the computational domain should be achieved by using suitable downstream and upstream distances. The length of the computational domain should be chosen in sufficient length so that the calculated surface pressures on the vehicle does not change significantly as mentioned by Gilkeson *et al*. [32].

The commercial CFD solver ANSYS FLUENT was used together with Detached Eddy Simulation to predicting massively separated flows. The automotive aerodynamic simulation was under fully turbulent conditions and the magnitude of Reynolds number was more than 8×10^6. The maximum length of the rear diffuser device was 500mm because of the storage limit. This technique led to a reduction in the aerodynamic drag of almost 4.12% at 130km/h, compared with the baseline model. The results show the difference between three areas of pressure, the upper flow, the side flow and the under flow respectively from high to low.

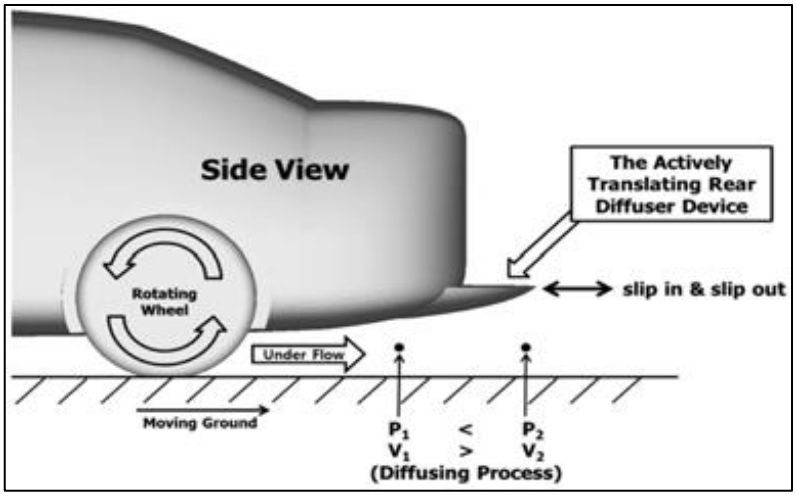

Figure 2.52: Basic concept of the actively translating rear diffuser device [59]

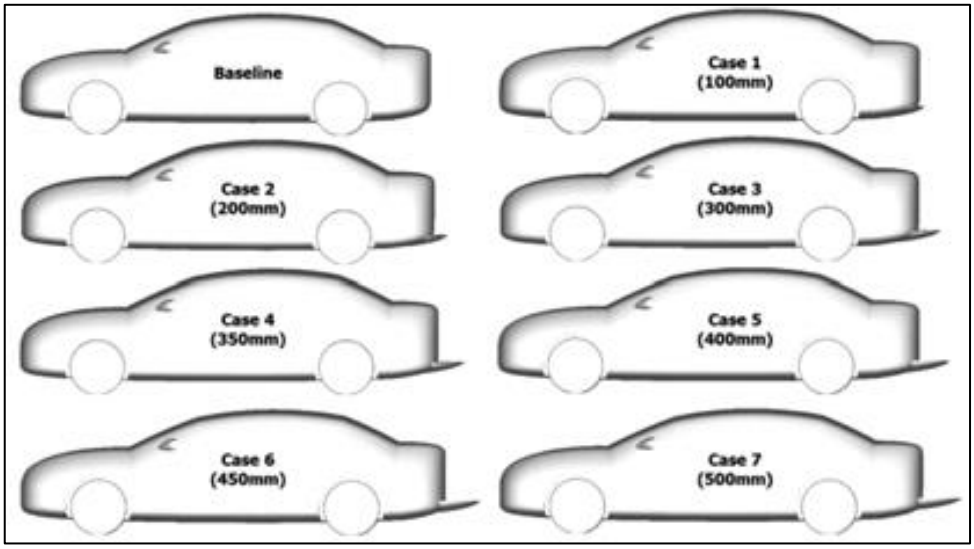

Figure 2.53: Seven rear diffuser cases-side view [59]

2.6 Aerodynamic devices

The study of adding a new aerodynamic device in the rear part of the car, see Figure 2.55, was done by Raju *et al*. [60] to reduce the air resistance and that led to a decrease in the fuel consumption. This attachment was moved into outer or inner sections depending on the conditions for controlling the pressure difference. A hydraulic system was used to control the movement of this attachment which was under driver control. This device can be closed at low speed and when stationary, but when the car was moving at high speed, the attachment was opened. By adding the device to the rear part of the car, the wind

friction drag coefficient can be reduced from approximately 0.4 to 0.2. The dimensions of this model of car were as follows: the overall width of the car with wind friction reduction attachment was 1.67 m, the overall height of the car with and without attachments was 1.49 m and the ground clearance of the vehicle was 0.17 m.

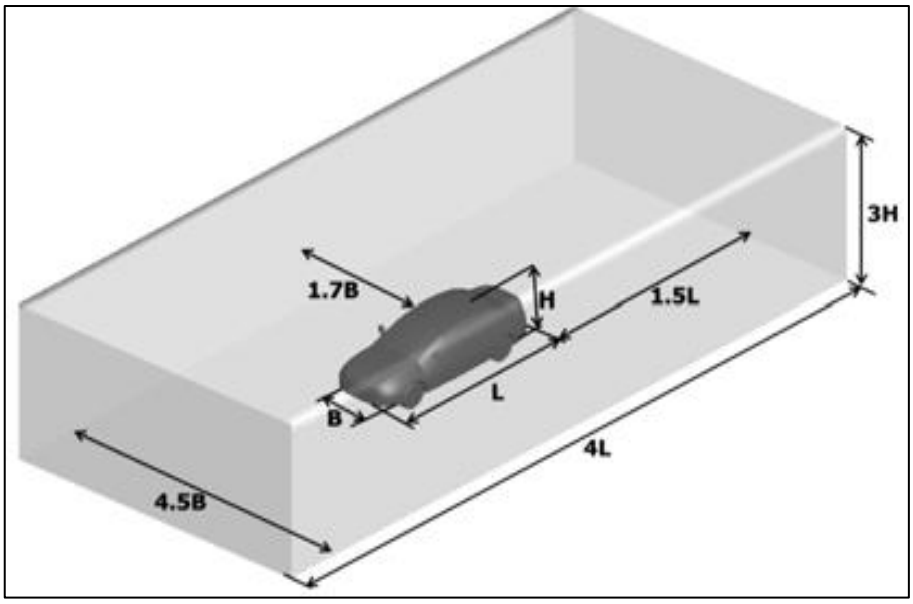

Figure 2.54: Dimensions of the computational domain [59]

The boundary conditions for this case study were as follows: the payload was 410 kg. The dead weight of the car was 1080 kg. The velocity of the car was 15m/s to 45m/s in steps of 5m/s increments. The negative aspect of this type of device was that it increased the length of the vehicle at high speeds as a result of the open device and the driver should be very careful to avoid touching the other vehicles behind the car. A disadvantage identified for this type of device was the effect on the luggage compartment capacity. This happens to the closure of this part at low speeds or when stopped. When this attachment was added, the vehicle weight increased up to 100 kg and this affected the rate of fuel consumption. On the other hand, this attachment helped to protect the car during at collision at the rear of the car.

This type of attachment was better than the fixed fairing provided at the rear of the car when parking and in traffic problems. The modification increased the maximum speed to about 1.3 of the maximum speed in the conventional car without increasing the car's engine speed. The overdrive gearbox was used to modify the maximum speed of the car. That leads to a decrease in the fuel consumption and emissions. Figure 2.55 shows a small

end car with collapsible wind friction reduction attachments at the rear portion in open condition:

- Small end car body.
- Rear end door in open condition.
- A bottom wind friction reduction attachment hinged at the bottom of the rear end door.
- Side wind friction reduction attachments hinged on either side of the rear end door.

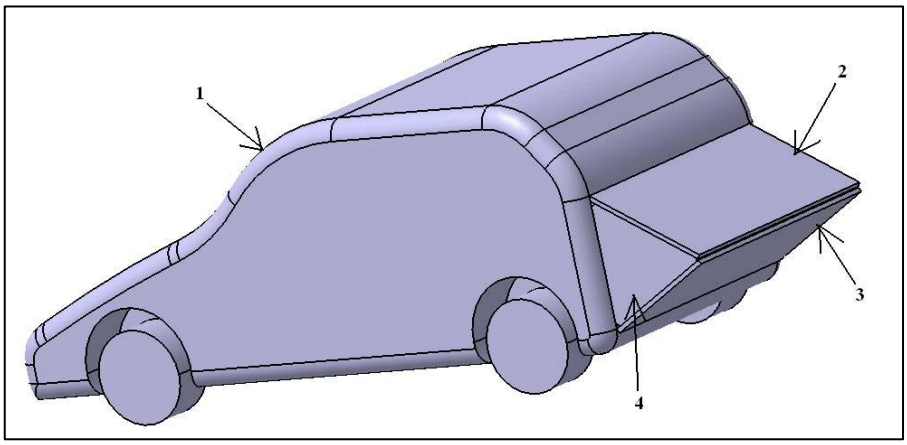

Figure 2.55: A small end car with collapsible wind friction reduction attachments at the rear portion in the open condition [60]

The base bleed was studied by Sivaraj and Raj [61] to improve the aerodynamic drag. The full-scale model was simulated using the ANSYS FLUENT software. The dimensions of the car being: overall length was 3.099 m, overall height was 1.652 m, the wheelbase was 2.230 m, width in front was 1.325 m and width at the rear was 1.315 m (Figure 2.56). The two converging ditch tubes were added above the bottom of this model of car as a base bleed system as shown in Figure 2.57. The diameter of these tubes was not homogeneous, the end of the tube in front was larger than the end of the tube in the rear. The higher air fluctuation was in the injection zone. A CFD technique was used to optimize a variety of cross sections of base bleed and interaction of the internal flows before wind tunnel testing.

There were three types of base bleed cross sectional area. These types had different frontal cross-sectional areas, but the same ending cross section. The first type was started with a circular cross section and the radius of it was 4.068mm. The second type was started with an elliptical cross section and the maximum and minimum radius of it was 6mm and 2.75mm respectively. The final type was started with a rectangular cross section. The width was 13mm and the height was 4mm. The ending cross section was the same for all

the three types and it was a circle with 1.5mm of radius. The end of the base bleed was located in the front and rear bumpers.

Figure 2.58 shows the location of base bleed in the car model. It is made up of a rubber material which was flexible. Dimensions of the domain were as follows: height 20 m, length 35 m and width 20 m. The authors considered the car as a wind tunnel model. The velocity of air in the simulation was 25m/s. As a result, the elliptical cross section had higher fluctuations compared with other types. Three-dimensional car models with base bleed had higher fluctuations compared to those without base bleed. The coefficient of drag on car model at the air velocity of 13.6m/s was 0.3521 without base bleed model and it decreased to 0.2321 with base bleed model.

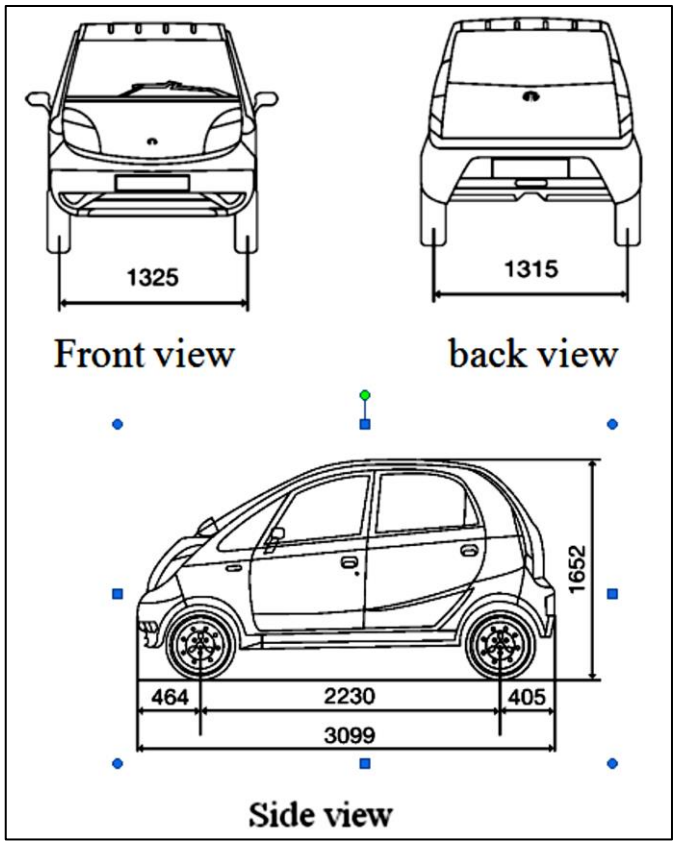

Figure 2.56: Dimensions of car with base bleed [61]

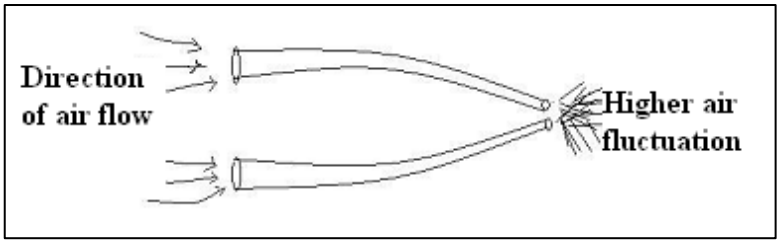

Figure 2.57: Air flows of base bleed [61]

Figure 2.58: Location of base bleed in the car model [61]

The aerodynamic forces of the saloon car and their effect on efficiency of fuel consumption and stability of the car on the road were studied by Bijlani *et al*. [62]. The study shows that approximately 75-80% of the movement resistance was from air resistance when the vehicle's speed was about 100km/h. The drag coefficient for the sedan was between 0.2 and 0.5 which depended on the external design of the car. There are two important elements in influencing the drag coefficient of a bluff body: the roundness of its front corners and the degree of taper at its rear end. External attachment devices like NACA duct, spoiler, and vortex generator were useful in decreasing the air resistance in all types of vehicles. For the low turbulence wind tunnel, 1/25th scale model of the vehicle was tested in ground plane.

Most researchers follow simplified models in tests at 30m/s. The wind tunnel and CFD were favourite tools in this type of science and combining between these two types led to a better aerodynamic design. Any change in external design can affect the fuel consumption, for example the fuel consumption can be decreased by a suitable change in slant angle for the vehicle body. Aerodynamic drag could be reduced through the use of streamlined shapes or external attachment devices, but careful checking was important to avoid lifting forces. The air flows for hatchback types detached from the surface of the car earlier than the sedan type because the sedan car was more streamlined than the hatchback type.

As mentioned by Dubey *et al*. [63], the size and the thickness of the boundary layer was measured based on the assumption that the optimum height of the vortex generator would be nearly equal to the boundary layer thickness. The boundary layer thickness at the roof end immediately in front of the flow separation point was about 30mm. Therefore, the optimum height of the vortex generator was found to be up to approximately 30mm. The shape of the vortex generator selected for the analysis was a bump shaped piece with a rear slope angle of 25° to 30°. As to the location of vortex generators, a point immediately upstream of the flow separation point exists and a point at an optimum distance of 100mm in front of the roof end was selected, as shown in Figure 2.59.

Figure 2.59: Position of vortex generators at the rear end of the roof [63]

The base pressure of a generic SUV was investigated experimentally by Wood *et al*. [64] because it is a major contributor to the drag coefficient. As mentioned by the authors, about 50% of the overall drag coefficient comes from the pressure on the base of a vehicle. It is thought that the height of the vehicle on the ground is of great importance in this ratio. All experimental tests were done in the Loughborough University wind tunnel.

Figure 2.60 shows this scale wind tunnel and it can be used for testing vehicle models up to about 0.25 of the original scale. The blockage ratio of this wind tunnel is about 5% for 1/4 scale models. Different heights of the SUV on the ground and underfloor roughness strips were tested as shown in Figure 2.61. A height of vehicles on the road has a significant effect on the pressure on the base. The study proved that roughness strips on the underbody have a very small effect on the overall aerodynamic behaviour of the SUV.

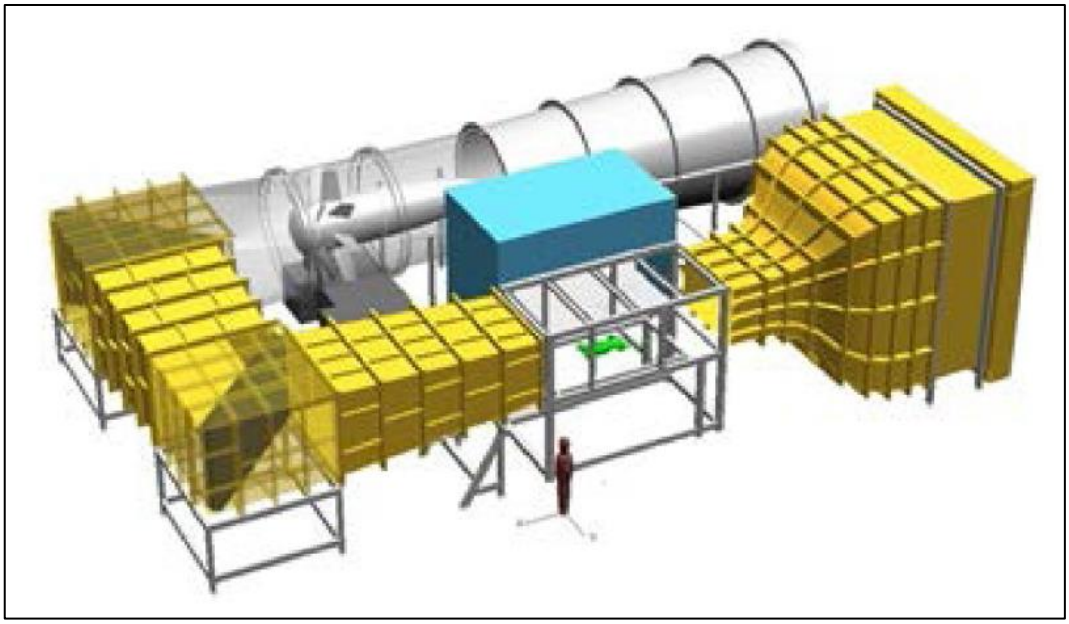

Figure 2.60: Loughborough University wind tunnel [64]

Scale models with several aerodynamic devices were built and tested by Rohatgi [65] in the wind tunnel. The baseline model was a GM SUV and the overall length of it was 1.71 m. Changes in the aerodynamics due to the inclusion of a rear screen on the back door of the SUV was investigated (Figure 2.62) in addition to a rear fairing (Figure 2.63). Three different designs of vortex generators, Figure 2.64, in addition to the front screen, Figure 2.65, were investigated inside the wind tunnel. These models of SUV were tested in different wind conditions. These authors show that the rear screen device reduces the drag coefficient up to 6.5%, while the rear fairing reduces the drag coefficient by 26%. It is postulated that a reduction in the drag coefficient up to 26%, is very difficult to achieve, especially in comparison to the other studies.

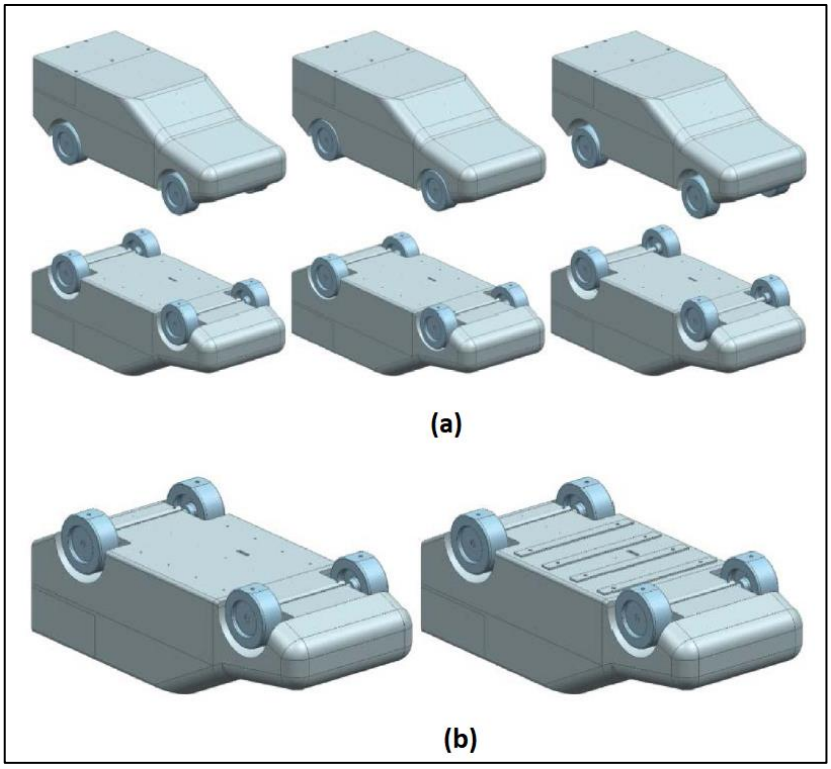

Figure 2.61: SUV case-studies (a) Ride height variations (b) Underfloor roughness strips [64]

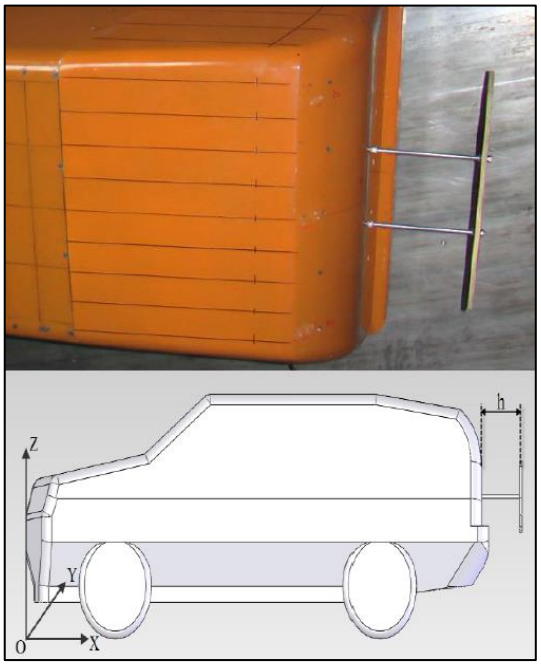

Figure 2.62: Rear Screen device [65]

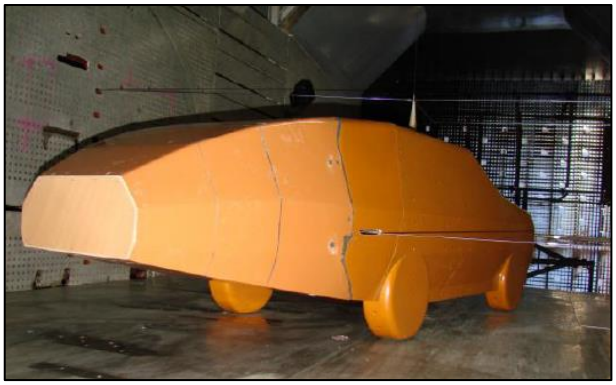

Figure 2.63: Vehicle model with rear fairing [65]

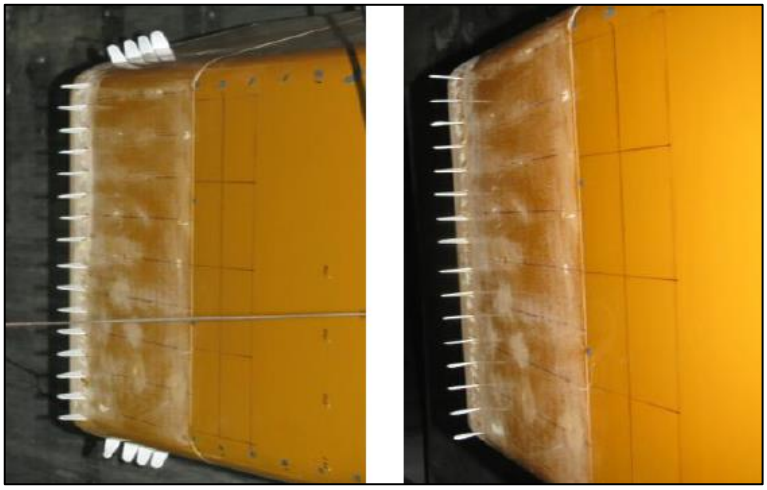

Figure 2.64: Vortex generators [65]

Figure 2.65: Vehicle model with front fairing [65]

2.7 Summary of literature review

There are numerous studies on the aerodynamic behaviour around the road vehicles using CFD simulations [9, 33, 44, 58, 59, 60] and experimental measurements [13, 18, 47, 48, 64, 65]. It should be noted that some studies used both numerical and experimental methods to study the aerodynamic behaviour around road vehicles [32, 45, 46, 57, 62]. Many turbulence models were investigated by previous researchers [20, 21, 44].

Some of the previous researchers have shown that RANS can be used to study the aerodynamic behaviour of road vehicles [16, 19, 32]. While other previous researchers have confirmed that LES can be used to achieve more accurate results [22, 25, 26], but a much higher computational expense for this case should be justified. The effect of the computational domain size on the numerical results was studied by many of the previous researchers [19, 26, 35, 36]. The affect of the blockage ratio on the numerical results was investigated by Tsubokura *et al*. [36]. The drag coefficient decreases with increasing of computational domain size especially the distance in front and behind the vehicle. Most studies focused on drag reduction without considering car stability [13, 16, 19, 20, 21, 22, 23, 24, 29, 46, 57].

A simple geometry, Ahmed model, is primarily prepared to investigate the effect of the slant angle on the drag coefficient and wake [19, 20, 21]. Modification of the external design of the Ahmed model by using soft edges was studied numerically by Verzicco *et al*. [25] and experimentally by Thacker *et al*. [29]. Bello-Millán *et al*. [18] carried out a comprehensive experimental study on Ahmed model. They used a new experimental technique based on placing a flat plate under the Ahmed model to measure the drag coefficient but without investigation of lift coefficient. However, they proposed numerical study of their work for an in depth analysis of effect of flat plate and model scale which will be one of the research work described throughout the remainder of the thesis.

SUV models were investigated by a number of recent studies. All of these studies focus on reducing the drag coefficient without considering the lift coefficient while this is an important factor for the SUV as it affects the car stability. Chaligné *et al*. [46] used both experimental and numerical approaches for reducing the drag coefficient of the full scale model of the Land Rover Discovery 5 by optimizing the external design. Pitman and Gaylard [47] focused on the possibility of reducing the drag coefficient by using multi-case-studies of Range Rover. Some of the modifications proposed by researchers [47, 48] are not practical such as no-wheels case-study (all wheels were covered by using plates).

Base bleed and rear cavity were investigated by Brown *et al*. [48] to determine their effectiveness to reduce the drag coefficient on the full scale model of the SUV. These modifications affect the comfort and visibility of the passengers. Roughness strips on the 1/4th scale models of the generic SUV were tested experimentally by Wood *et al*. [64]. This study proved so called roughness strips on the underbody have a very small effect on the overall aerodynamic behaviour.

Cavity and boat-tail for the Ahmed model were studied numerically and experimentally by Khalighi *et al*. [49]. Leuschen and Cooper [51] used an experimental approach to improve the efficiency of aerodynamic drag by using new add-on devices of a truck (such as rear trailer deflector). Salari and Ortega [53] used an experimental approach to improve the aerodynamic performance for the trailer base by using six different combinations of devices (such as boat-tail). Miralbes [43] used a numerical approach to reduce the fuel consumption almost 11% by using nose cone, boat tails and skirt. However, these add-on devices can lead to increase the overall length of the trailer which may not be desirable for road safety. Raju *et al*. [60] reduced the air resistance of sedan car by using a collapsible wind friction reduction. Several aerodynamic devices for the scale model of the GM SUV (such as rear screen device and fairing) were built and tested experimentally by Rohatgi [65] thereby reducing the drag force. These devices affect the visibility, weight and the overall length of the vehicle.

Further, Koike *et al*. [57] and Dubey *et al*. [63] used vortex generators in the saloon car to reduce air resistance. Hu and Wong [58] studied the effect of the airfoil spoiler and plate spoiler on the sedan car. Kang *et al*. [59] worked to reduce the aerodynamic drag by using a movable arc-shaped under the rear bumper of the sedan car. Barbut and Negrus [44] used some modification to the underbody of the sedan model to reduce the aerodynamic drag. Base bleed and rear cavity were investigated by Brown *et al*. [48] to determine their effectiveness in drag reduction of SUVs. Sivaraj and Raj [61] used the base bleed to improve the aerodynamic drag. The ending cross section of base bleed was a circle with 1.5mm of radius and this diameter is very small to vent. It should be noted that these modifications usually affect the comfort and visibility of the passengers and may have cost implications.

There are numerous studies on the reduction of aerodynamic drag on the cars using CFD simulations based on simple geometries and traditional aerodynamic devices as well as actual car geometries. Some studies focused on drag reduction without considering car stability. Other studies used very simple three-dimensional geometries including two-dimensional shapes; most models in these studies were not full-scale. Many types of

aerodynamic devices have an effect on the capacity of vehicles, increasing their height and possibly noise generation. The devices that can dynamically vary the overall length (e.g. change by speed) could have an influence on road traffic safety and create risks to other moving vehicles. Finally, all these modifications are not be suitable for all types of cars.

Therefore, there is a need to investigate new aerodynamic drag reduction techniques to improve the performance of road vehicles by reducing the drag coefficient and increasing their stability on the road via an increase in pressure over the car by modifications to the vehicle aerodynamics, particularly for SUVs.

Chapter 3 Theory

The analysis of engineering systems involving fluid flow, heat transfer and associated phenomena such as chemical reactions is known Computational Fluid Dynamics (CFD) [66]. This approach uses numerical analysis and simulation to solve problems that include fluid flows (*ibid*). Therefore, the CFD approach is used for modelling the airflow around a road vehicle in the work described in this thesis.

3.1 Fundamentals

A CFD approach is used to solve the governing equations that represent the fluid flow motion. These equations are based on the conservation of mass, momentum and energy (Navier Stokes equations).

3.1.1 Governing equations

The continuity equation, mass conservation, in the present study is a three-dimensional, steady flow of an incompressible flow as shown in the following [4, 67, 68]:

$$\frac{\partial u}{\partial x}+\frac{\partial v}{\partial y}+\frac{\partial w}{\partial z}=0 \tag{3.1}$$

where *u*, *v* and *w* are components of the velocity in the *x*, *y* and *z*-directions respectively.

Most road vehicles run at speeds which are less than 0.3 of the sound speed. The pressure in the flow field in this range of speed varies slightly and therefore the changes in fluid density can be neglected. Thus, the fluid in this case can be regarded as incompressible.

The momentum equations (conservation of momentum) in the present study are three-dimensional, steady flows of an incompressible flow as shown in the following [4, 67, 68]:

$$u\frac{\partial u}{\partial x}+v\frac{\partial u}{\partial y}+w\frac{\partial u}{\partial z}=-\frac{1}{\rho}\frac{\partial p}{\partial x}+\nu\left(\frac{\partial^2 u}{\partial x^2}+\frac{\partial^2 u}{\partial y^2}+\frac{\partial^2 u}{\partial z^2}\right) \tag{3.2}$$

$$u\frac{\partial v}{\partial x}+v\frac{\partial v}{\partial y}+w\frac{\partial v}{\partial z}=-\frac{1}{\rho}\frac{\partial p}{\partial x}+\nu\left(\frac{\partial^2 v}{\partial x^2}+\frac{\partial^2 v}{\partial y^2}+\frac{\partial^2 v}{\partial z^2}\right) \tag{3.3}$$

$$u\frac{\partial w}{\partial x}+v\frac{\partial w}{\partial y}+w\frac{\partial w}{\partial z}=-\frac{1}{\rho}\frac{\partial p}{\partial x}+\nu\left(\frac{\partial^2 w}{\partial x^2}+\frac{\partial^2 w}{\partial y^2}+\frac{\partial^2 w}{\partial z^2}\right) \tag{3.4}$$

where *u*, *v* and *w* are components of the velocity in the *x*, *y* and *z*-directions respectively. *p* is the pressure and *v* is the kinematic viscosity.

3.1.2 Reynolds number

The Reynolds number, Equation 3.5, is used to recognize the type of flow by measuring the ratio of inertia forces to viscous forces [68, 69, 70].

$$R_e = \frac{\rho\, v\, L}{\mu} \tag{3.5}$$

where R_e is Reynolds number; ρ is the air density (kg/m^3); v is the velocity of the oncoming flow (m/s); L is a typical length scale in the system; μ is the dynamic viscosity (kg/m.s).

The Reynolds number is used to categorize the flow behaviour into three types which are laminar, transitional and turbulent flow, see Figure 3.1 for more details about these three types of flow [71] (It should be noted that Figure 3.1(b) represents transition conditions as described in the reference [71]). It is found experimentally that the turbulent flow occurs at Reynolds number higher than its critical value as shown in Table 3.1 [66]. Table 3.1 shows all critical numbers of the Reynolds number in different types of flow [68, 72].

Types of flow		
External		**Internal**
Along surface	Around an obstacle	
$Re_x \geq 500{,}000$	$Re_d \geq 20{,}000$	$Re_{dh} \geq 2{,}300$

Table 3-1: Critical Reynolds Number

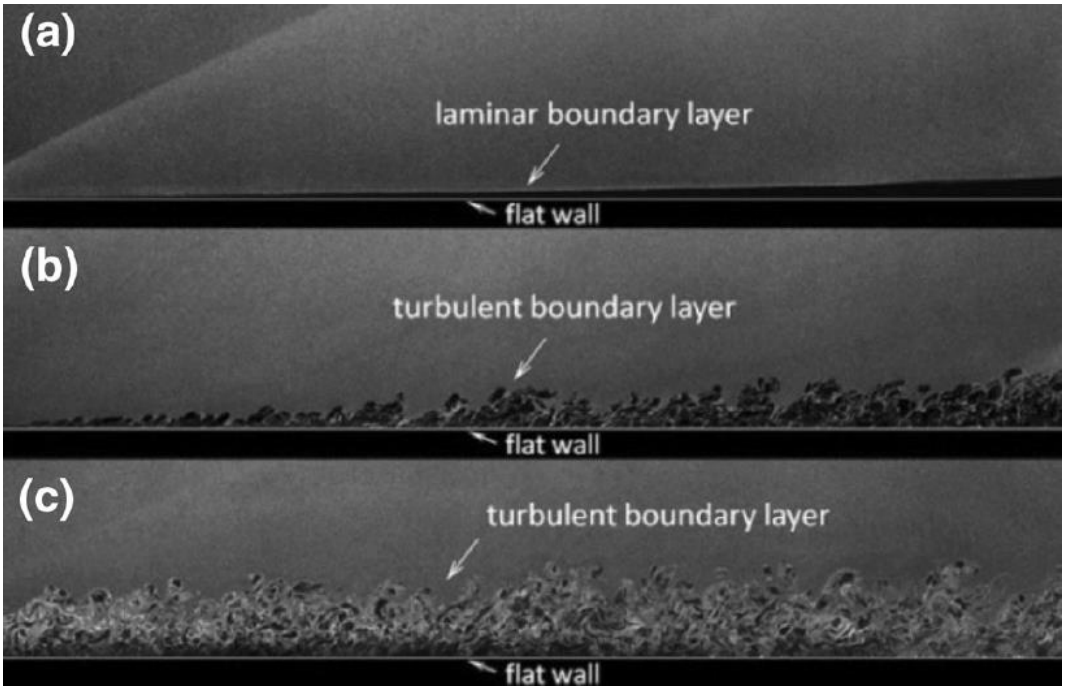

Figure 3.1: Images of boundary layers (a) laminar (b) transition (c) turbulent [71]

3.1.3 Boundary layer

Figure 3.2 illustrates a boundary layer formed in the flow along upper side of a horizontal thin smooth flat plate with the incoming fluid parallel to plate [70]. The flow velocity within the boundary layer has a gradient due to the viscosity near the plate surface. The boundary layer starts from the leading edge of the flat plate. In general, its thickness may be taken as that distance from the plate surface at which the flow velocity reaches 99% of the free stream velocity. The velocity of flow at the solid surface of the plate is zero, regardless of how quickly the fluid flows over it, the so-called no-slip condition. The flow near the leading edge of the flat plate (the first part of the boundary layer) is completely laminar. As the boundary layer thickness grows the laminar boundary layer becomes unstable, and the motion of flow within it becomes disturbed. Then the flow develops into turbulence displaying irregularities and the layer thickness increases more rapidly. There is a short length in which flow changes from laminar to turbulent, this region is known as the transition region [68, 70].

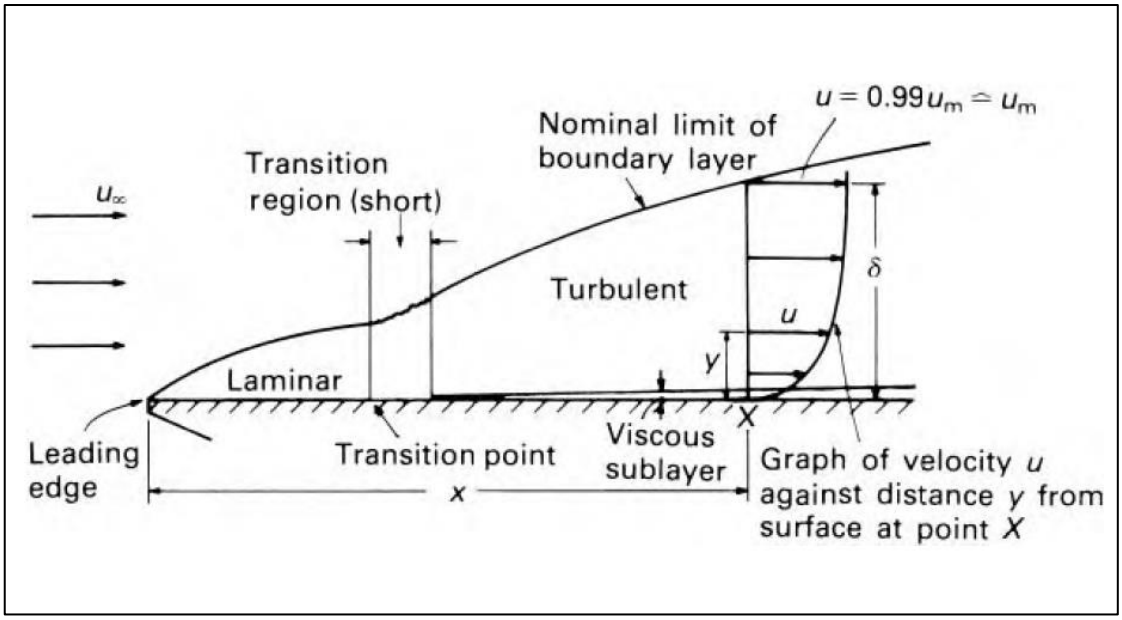

Figure 3.2: The structure of the boundary layer [70]

3.1.4 Pressure gradient and flow separation

In general, the velocity of a fluid flow varies from a position to another position. According to Newton's First Law, a change of velocity is accompanied by a change in force. Pressure is therefore expected to change from one location to another [70, 73]. An increase in the fluid velocity causes a decrease in pressure or a decrease in the fluid's potential energy. This principle is known as Bernoulli's equation and it is as follows [4, 74, 75]:

$$p + \frac{\rho}{2} v^2 = const. \tag{3.6}$$

where p is pressure (N/m^2); ρ is the air density (kg/m^3); v is the velocity.

The pressure coefficient (*Cp*) is a dimensionless parameter for studying the flow of incompressible fluids and can be used for air with the velocity less than 0.3 times of the sound velocity. It is used in aerodynamics and hydrodynamics. The pressure coefficients can be determined at specific locations around the vehicle model to predict the fluid pressure at those locations. The relationship between the dimensionless coefficient and the dimensional numbers is:

$$C_p = \frac{p - p_\infty}{\frac{1}{2}\rho_\infty v_\infty^2} = \frac{p - p_\infty}{p_o - p_\infty} \tag{3.7}$$

where p is the static pressure (N/m^2) at the point at which pressure coefficient is being evaluated; p_∞ is the static pressure in the freestream (N/m^2); $\rho_\infty$is the freestream air density (kg/m^3); p_o is the stagnation pressure in the freestream (N/m^2); v_∞ is the freestream velocity of the air (m/s).

Flow separation is responsible for wake formation [76]. Figure 3.3 shows a 2D flow around a cylinder as an example of flow separation [72]. The fluid particles decelerate on the front of the cylinder and the pressure increases in this area. The point on the left-hand of the cylinder (forward stagnation point as in Figure 3.3) is called the stagnation point (the flow velocity of this point is locally zero) and is the point of maximum pressure [73]. The thickness of the boundary layer is smallest at the stagnation point and it increases towards flow. Figure 3.4 shows velocity profile with separation on an upper part of the cylinder. The fluid particles accelerate over the left-hand section of the cylinder, and reach the maximum velocity is in the middle section of the cylinder (point C). When the velocity is a maximum, pressure is a minimum (point C). The pressure needs to decrease as fluid velocity increases to conserve energy and vice versa, according to the Bernoulli's equation [76]. As shown in Figure 3.4 the pressure gradient is positive on the back side of the cylinder. The reduction of velocity in this area is due to viscosity and the positive gradient in pressure [70]. The boundary layer flow is retarded, particularly near the body surface, and reversed flow may happen due to a pressure increase in flow direction [77]. This phenomenon is called separation. As can be seen in Figure 3.4 a dividing streamline leaves the body surface between reverse and forward flow [70].

The condition for the separation point D is as follows:

$$\left(\frac{du}{dy}\right)_{wall} = 0 \tag{3.8}$$

The boundary layer thickness increases continuously along the plate from the stagnation point to back as increasing quantities of air become affected. The boundary layer thickness increases with increasing viscosity.

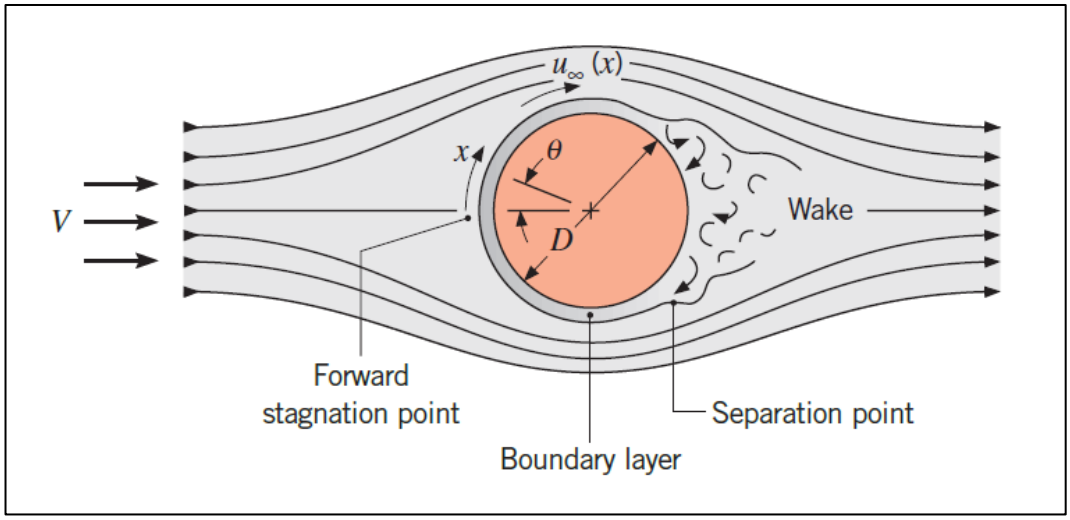

Figure 3.3: Separation on a cylinder in cross flow [72]

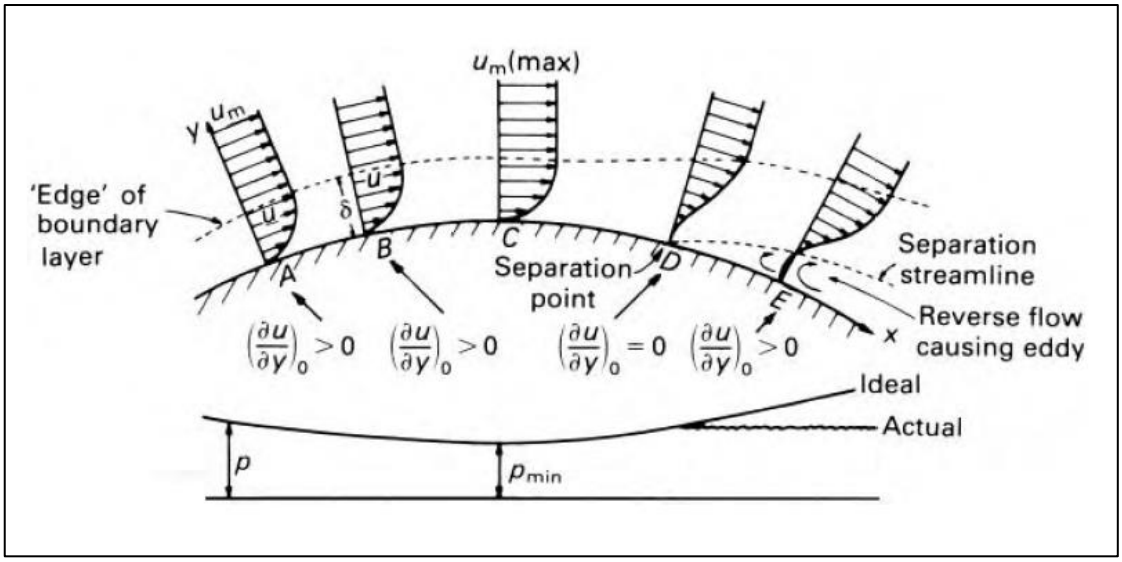

Figure 3.4: Flow in boundary layer on a cylinder before and after point of separation [70]

3.1.5 Drag and down force

There are two main forces acting on a car as it moves through air. The drag force is the force that hinders the movement of the car and the direction of this force is opposite to the direction of travel. The second force is lift force: this is perpendicular to the direction of travel. These two forces depend on the relationship between the surface smoothness of

the car, the free stream velocity, the viscosity, the air density, the frontal area and the external design of the car [2].

The drag (C_D) coefficient and lift (C_L) are calculated based on the following equations in this study [2]:

$$C_D = \frac{2F_D}{\rho\, v^2\, A} \tag{3.9}$$

$$C_L = \frac{2F_L}{\rho\, v^2\, A} \tag{3.10}$$

where C_D is the dimensionless drag coefficient; F_D is the drag force (N); ρ is the air density (kg/m^3); v is the velocity of the oncoming flow (m/s); A is the frontal area of the vehicle (m^2), as shown in Figure 3.5; C_L is the dimensionless lift coefficient and F_L is the lift force (N).

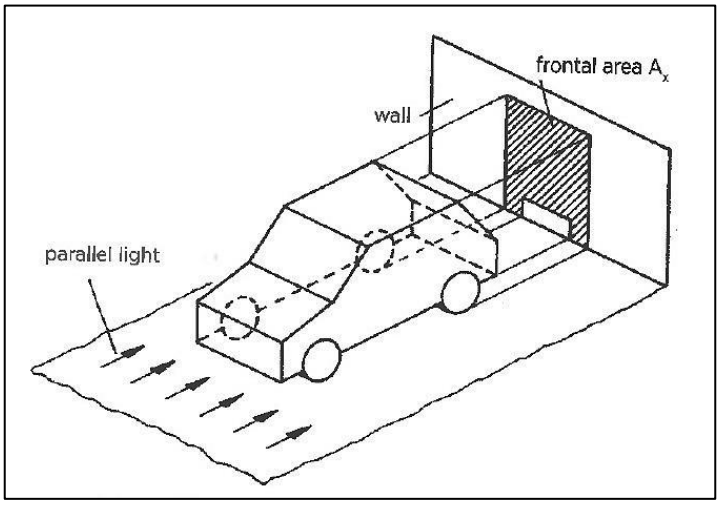

Figure 3.5: Definition of the frontal area of the vehicle [4]

As mentioned above, the Reynolds number, equation 3.5, is a function of density, velocity of the oncoming flow and other parameters. Equation 3.5 can be rewritten as follows:

$$\rho\, v = \frac{\mu\, R_e}{L} \tag{3.11}$$

If Equation 3.11 is substituted back into Equation 3.9, the following equation can obtain

$$C_D = \frac{2\,L\,F_D}{\mu\,R_e\,v\,A} = f(R_e) \tag{3.12}$$

This means that the C_D is a function of Reynolds number, and a number of studies (see Figure 4.15) confirm this. It is clear that the C_D decreases with an increase in Reynolds number.

3.2 CFD modelling of flow

A variety of CFD codes is available which contribute to the solution of a large number of engineering applications. However, most of these codes have the same structure to achieve their objectives. The structure of the CFD codes is divided into the pre-processor, solver and post-processor as shown (Figure 3.6; [78]). The pre-processor and solver are the most important stages in the structure of CFD codes. These stages have a significant influence on the accuracy of the numerical simulation results.

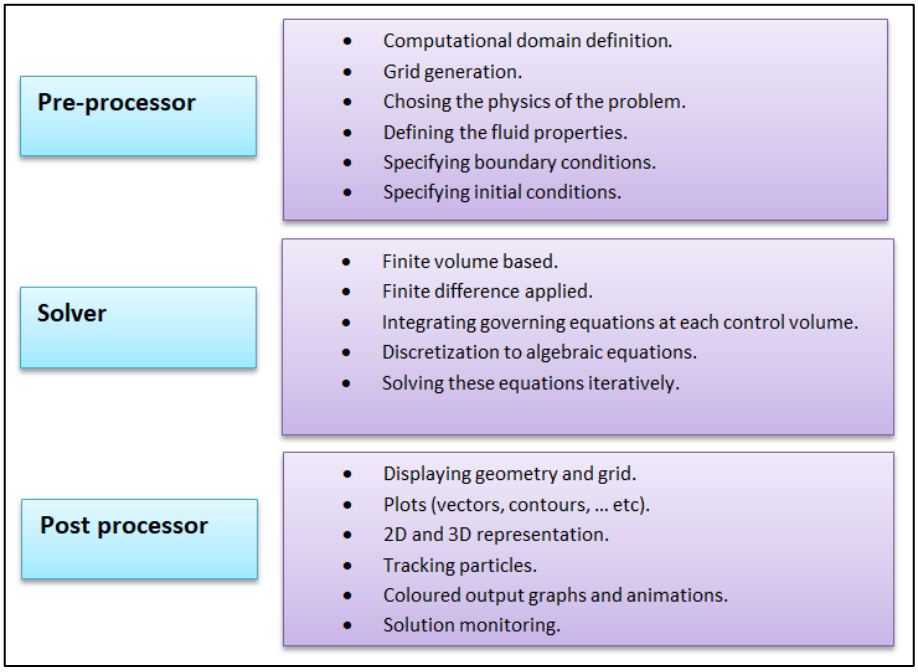

Figure 3.6: The structure of CFD codes

Creating three-dimensional geometry is the first process in this CFD modelling study. The next step is to select the dimensions of the computational domain which replaces a wind tunnel in the experimental tests. Using a number of cells in the computational model, including the objective geometry (vehicle model) can solve the governing equations. The credibility of expected numerical results is extremely sensitive to cell size.

There are no specific rules for generating a mesh for every engineering case [79]. However, it is recommended to test grid-independence until the numerical results converge (*ibid*).

The essential means used to assess reliability and accuracy in computational simulations are Verification and Validation (V&V) [80]. The verification process is the measurement of the accuracy of a computational simulation (the numerical results given by the software or code), such as published benchmark solutions [81, 80, 82] and analytical solutions [80, 82]. The procedure of the comparing the accuracy between the computational solution and the experimental data is a validation process [80]. This strategy estimates both of quantified error and uncertainty. Evaluation of the capabilities of the numerical method to correctly solve a real physical problem is the principal aim of validation. The verification process can evaluate the convergence of numerical schemes and the constitutive properties. While validation in some cases can be achieved naturally after the verification process [82]. As mentioned by Oberkampf and Trucano [80] the major strategy is the identification and quantification of errors provided by the software/code. However, it is for the individual researcher to conclude whether the computational model is validated. Ergo verification deals with mathematics and validation with physics.

It is noteworthy that there is no standard method to assess uncertainty in the CFD [83]. Physical approximation error, computer programming errors, computer round-off error, discretisation errors, iterative convergence error and usage errors are examples of some potential errors in CFD [83]. As defined by the American Institute of Aeronautics and Astronautics (AIAA), an uncertainty is a probable shortage in any stage or activity of modelling and simulation because of the lack of knowledge. Modelling of turbulence is an example of an uncertainty in implementing a CFD analysis. In general, turbulence modelling is not fully understood [83].

3.3 Turbulence models

Turbulent flow is an irregular flow behaviour which categorizes random and chaotic flow because irregular changes in the flow properties relative to place and time [66]. Turbulence models have varied in complexity, accuracy and other features to improve prediction of the flow properties [66]. Steady state Reynolds-Averaged Navier-Stokes (RANS) numerical solutions are suitable for a variety of engineering applications such as the aerodynamics of road vehicles due to the reduced computational expense [2, 4, 16, 19, 84]. Large Eddy Simulation (LES) is better than RANS in terms of accuracy when

unsteady flow data are needed or the solution of the largest eddies are important [35, 84, 85].

LES requires a high-quality mesh and this approach is computationally expensive. In addition, unsteady simulation using LES with small time steps leads to long simulation times with large quantitative data sets being produced [84, 85, 86]. A much smaller time step in LES simulation is needed for the locally refined grid system [86]. Hanjalic [87] provided a point of view for several developments on the future role of the RANS approach in the numerical calculations of turbulent flows and compared these with the LES approach. Declaring that the RANS approach will still be in use at least for the next few decades because the LES approach needs a high density of grid and higher computational loads. Altinisik et al. [35] and Hanjalic [87] expected that RANS with the k–ε turbulence model will continue to be used. Iaccarino [85] analysed the performance of three different commercial CFD codes (FLUENT, CFX and STAR-CD) for the turbulence models and confirmed that all of these CFD codes have similar characteristics in terms of accuracy and convergence. Throughout the work described in this thesis, the ANSYS FLUENT code was used for analysis and simulation in all cases. All turbulence models available in ANSYS FLUENT are shown in Figure 3.7 [88, 89].

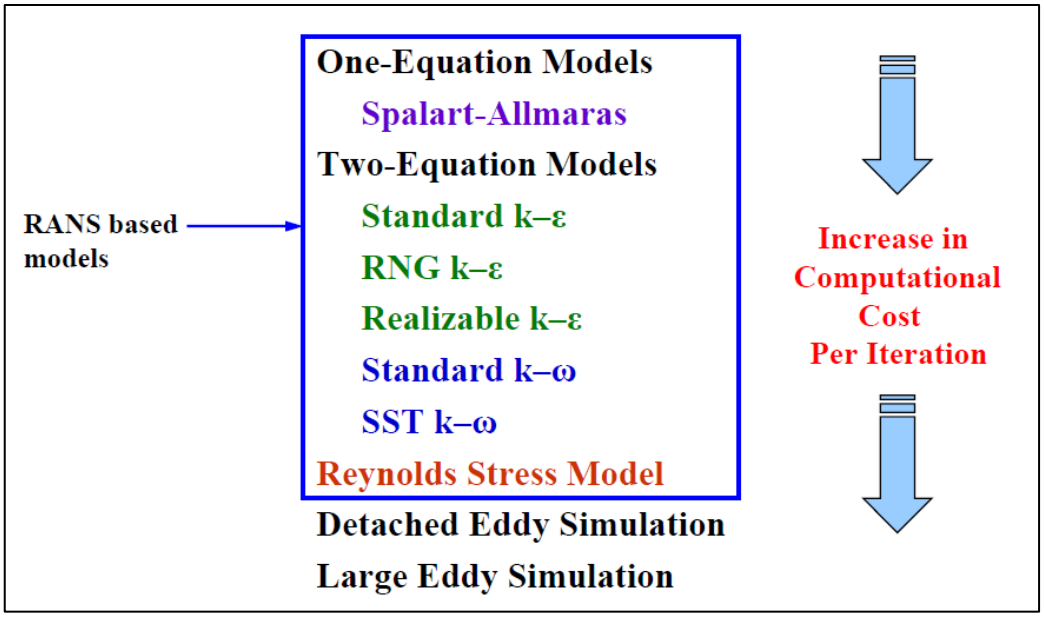

Figure 3.7: Turbulence models available in ANSYS FLUENT [88]

3.3.1 Reynolds-Averaged Navier-Stokes (RANS)

Most current CFD methods used for the analysis and simulation of external flow are based on Reynolds-averaged Navier–Stokes (RANS) equations [90]. RANS equations depend on models of turbulence-closure to provide flow field turbulent variables. RANS approaches give good predictions for attached flow but they are unsuccessful to accurately predict flow in separated flow areas. That is because these approaches solve only a part of the turbulence scales of interest (*ibid*). The RANS approaches use the following equations [4, 66]:

$$\bar{u}\frac{\partial\bar{u}}{\partial x}+\bar{v}\frac{\partial\bar{u}}{\partial y}+\bar{w}\frac{\partial\bar{u}}{\partial z}=-\frac{1}{\rho}\frac{\partial\bar{p}}{\partial x}+\nu\left(\frac{\partial^2\bar{u}}{\partial x^2}+\frac{\partial^2\bar{u}}{\partial y^2}+\frac{\partial^2\bar{u}}{\partial z^2}\right)+\left(\frac{\partial\overline{\acute{u}^2}}{\partial x}+\frac{\partial\overline{\acute{u}\acute{v}}}{\partial y}+\frac{\partial\overline{\acute{u}\acute{w}}}{\partial z}\right) \tag{3.13}$$

$$\bar{u}\frac{\partial\bar{v}}{\partial x}+\bar{v}\frac{\partial\bar{v}}{\partial y}+\bar{w}\frac{\partial\bar{v}}{\partial z}=-\frac{1}{\rho}\frac{\partial\bar{p}}{\partial y}+\nu\left(\frac{\partial^2\bar{v}}{\partial x^2}+\frac{\partial^2\bar{v}}{\partial y^2}+\frac{\partial^2\bar{v}}{\partial z^2}\right)+\left(\frac{\partial\overline{\acute{u}\acute{v}}}{\partial x}+\frac{\partial\overline{\acute{v}^2}}{\partial y}+\frac{\partial\overline{\acute{v}\acute{w}}}{\partial z}\right) \tag{3.14}$$

$$\bar{u}\frac{\partial\bar{w}}{\partial x}+\bar{v}\frac{\partial\bar{w}}{\partial y}+\bar{w}\frac{\partial\bar{w}}{\partial z}=-\frac{1}{\rho}\frac{\partial\bar{p}}{\partial z}+\nu\left(\frac{\partial^2\bar{w}}{\partial x^2}+\frac{\partial^2\bar{w}}{\partial y^2}+\frac{\partial^2\bar{w}}{\partial z^2}\right)+\left(\frac{\partial\overline{\acute{u}\acute{w}}}{\partial x}+\frac{\partial\overline{\acute{v}\acute{w}}}{\partial y}+\frac{\partial\overline{\acute{w}^2}}{\partial z}\right) \tag{3.15}$$

$$\bar{u}=\frac{1}{t_1}\int_{t_0}^{t_0+t_1}u(t)dt \quad with\ \bar{\acute{u}}=0, \qquad \bar{\bar{u}}=\bar{u} \tag{3.16}$$

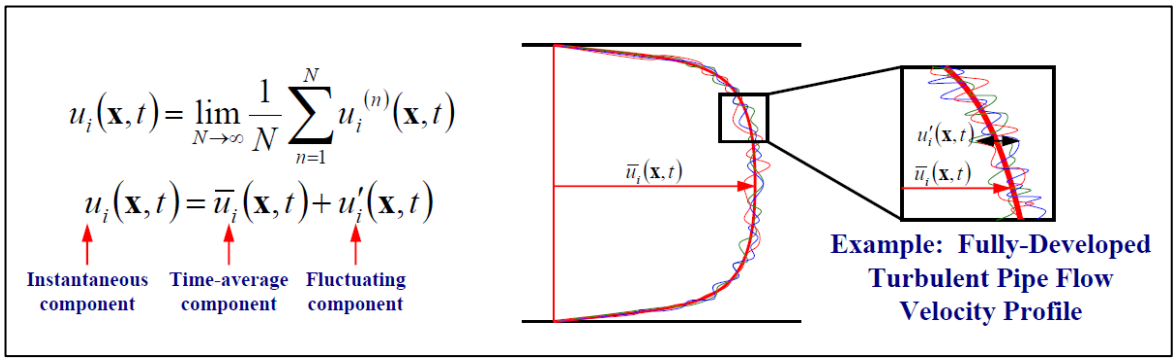

Figure 3.8: The mean flow properties in RANS modelling [88]

The *k*-*ε* turbulence model uses the following transport equations for *k* and *ε* [66]:

$$\frac{\partial(\rho k)}{\partial t} + div(\rho k \boldsymbol{U}) = div\left[\frac{\mu_t}{\sigma_k} grad\,(k)\right] + 2\mu_t S_{ij}.S_{ij} - \rho\varepsilon \tag{3.17}$$

$$\frac{\partial(\rho \varepsilon)}{\partial t} + div(\rho \varepsilon \boldsymbol{U}) = div\left[\frac{\mu_t}{\sigma_\varepsilon} grad\,(\varepsilon)\right] + C_{1\varepsilon}\frac{\varepsilon}{k}2\mu_t S_{ij}.S_{ij} - C_{2\varepsilon}\rho\frac{\varepsilon^2}{k} \tag{3.18}$$

The eddy viscosity is (*ibid*):

$$\mu_t = \rho C_\mu \frac{k^2}{\varepsilon} \tag{3.19}$$

The transport equations for *k* and *ε* in the realizable *k*-*ε* model are:

$$\frac{\partial}{\partial t}(\rho k) + \frac{\partial}{\partial x_j}(\rho k \boldsymbol{u_j}) = \frac{\partial}{\partial x_j}\left[\left(\mu + \frac{\mu_t}{\sigma_k}\right)\frac{\partial k}{\partial x_j}\right] + G_k + G_b - \rho\epsilon - Y_M + S_k \tag{3.20}$$

$$\frac{\partial}{\partial t}(\rho \varepsilon) + \frac{\partial}{\partial x_j}(\rho \varepsilon \boldsymbol{u_j}) = \frac{\partial}{\partial x_j}\left[\left(\mu + \frac{\mu_t}{\sigma_\varepsilon}\right)\frac{\partial \varepsilon}{\partial x_j}\right] + \rho C_1 S_\varepsilon - \rho C_2 \frac{\varepsilon^2}{k + \sqrt{v\varepsilon}} + C_{1\varepsilon}\frac{\varepsilon}{k}C_{3\varepsilon}G_b + S_\varepsilon \tag{3.21}$$

The difference between standard and realizable *k*-*ε* turbulence model is the viscosity coefficient and the dissipation equation. The turbulent viscosity in the realizable *k*-*ε* turbulence model is not a constant like in the standard model. A new transport equation for the realizable *k*-*ε* turbulence model is derived from an exact equation for the transport of the mean-square vorticity fluctuation.

The *k*-*ω* turbulence model was developed from the realization that most of the problems experienced by all types of *k*-*ε* turbulence model due to the modelling of the *ε* equation which is neither accurate nor easy to solve (*ε* has a local extreme close to the wall). Mathematically, this is equivalent to a change of variables $\omega \sim \varepsilon/k$. The *k*-*ω* turbulence model uses the following transport equations for *k* and *ω* [66]:

$$\frac{\partial(\rho k)}{\partial t} + div(\rho k \boldsymbol{U}) = div\left[\left(\mu + \frac{\mu_t}{\sigma_k}\right) grad\,(k)\right] + P_k - \beta^* \rho k \omega \tag{3.22}$$

where P_k is the rate of production of turbulent kinetic energy.

$$P_k = 2\mu_t S_{ij}.S_{ij} - \frac{2}{3}\rho k \frac{\partial U_i}{\partial x_j}\delta_{ij} \tag{3.23}$$

$$\frac{\partial(\rho\omega)}{\partial t} + div(\rho\omega \boldsymbol{U}) = div\left[\left(\mu + \frac{\mu_t}{\sigma_\omega}\right) grad\ (\omega)\right] + \gamma_1\left(2\rho S_{ij}.S_{ij} - \frac{2}{3}\rho\omega\frac{\partial U_i}{\partial x_j}\delta_{ij}\right) - \beta_1\rho\omega^2 \tag{3.24}$$

The SST turbulence model uses the following equations [66]:

$$\frac{\partial(\rho k)}{\partial t} + div(\rho k \boldsymbol{U}) = div\left[\left(\mu + \frac{\mu_t}{\sigma_k}\right) grad\ (k)\right] + P_k - \beta^*\rho k\omega \tag{3.25}$$

$$\frac{\partial(\rho\omega)}{\partial t} + div(\rho\omega \boldsymbol{U}) = div\left[\left(\mu + \frac{\mu_t}{\sigma_{\omega,1}}\right) grad\ (\omega)\right] + \gamma_2\left(2\rho S_{ij}.S_{ij} - \frac{2}{3}\rho\omega\frac{\partial U_i}{\partial x_j}\delta_{ij}\right) - \beta_2\rho\omega^2 + 2\frac{\rho\ \partial k\ \partial\omega}{\sigma_{\omega,2}\ \omega\ \partial x_k\ \partial x_k} \tag{3.26}$$

The other turbulence model of the RANS is the Reynolds Stress Model (RSM). The RSM computationally expensive because this type of turbulence model has six additional equations. The RSM turbulence model uses the following equations [66]:

$$\frac{D\ R_{ij}}{Dt} = \frac{\partial R_{ij}}{\partial t} + C_{ij} = P_{ij} + D_{ij} - \varepsilon_{ij} + \Pi_{ij} + \Omega_{ij} \tag{3.27}$$

The convective term is as follows (*ibid*):

$$C_{ij} = \frac{\partial\left(\rho U_k \overline{\acute{u}_i \acute{u}_j}\right)}{\partial x_k} = div\left(\rho\overline{\acute{u}_i \acute{u}_j}\ U\right) \tag{3.28}$$

The production term is (*ibid*):

$$P_{ij} = -\left(R_{im}\frac{\partial U_j}{\partial x_m} + R_{jm}\frac{\partial U_i}{\partial x_m}\right) \tag{3.29}$$

The rotational term is (*ibid*):

$$\Omega_{ij} = -2\omega_k(\overline{\acute{u}_j\acute{u}_m}\, e_{ikm} + \overline{\acute{u}_i\acute{u}_m}\, e_{jkm}) \tag{3.30}$$

All types of *k–ε* and RSM turbulence models are not valid near the wall surface while Spalart-Allmaras and all types of *k–ω* models are valid on condition the mesh is fine enough near the wall surface [66, 88]. For this reason, the wall function is used in the *k–ε* and RSM turbulence models. Wall functions allow the use of a relatively coarse mesh near in the wall region. The non-equilibrium wall function method attempts to improve the numerical results of flows with separations, higher pressure gradients, reattachment and stagnation.

The enhanced wall treatment method is suitable for flows with low Reynolds number or with complex phenomena near the wall surface. Standard wall function and non-equilibrium wall function methods are suitable for flows with high Reynolds number (*Re* > 10^6) because the viscous sub-layer [66, 88, 91] is not resolved the mean velocity of airflow reduces near a wall surface as a result of friction effects [4]. The thickness of the boundary layer depends on the Reynolds number, ergo boundary layer thickness decreases when the velocity gradient at the wall increases.

Increasing Reynolds number causes an increase in the velocity gradient at the wall surface. There are two approaches concerning turbulence modelling to treat the near-wall airflow as shown in Figure 3.9. It is generally impractical to resolve all properties of the airflow in the near-wall region due to the velocity gradient being extremely steep near the wall. Wall functions are an economical procedure to bridge the gap between the turbulent core and the true wall boundary values [92].

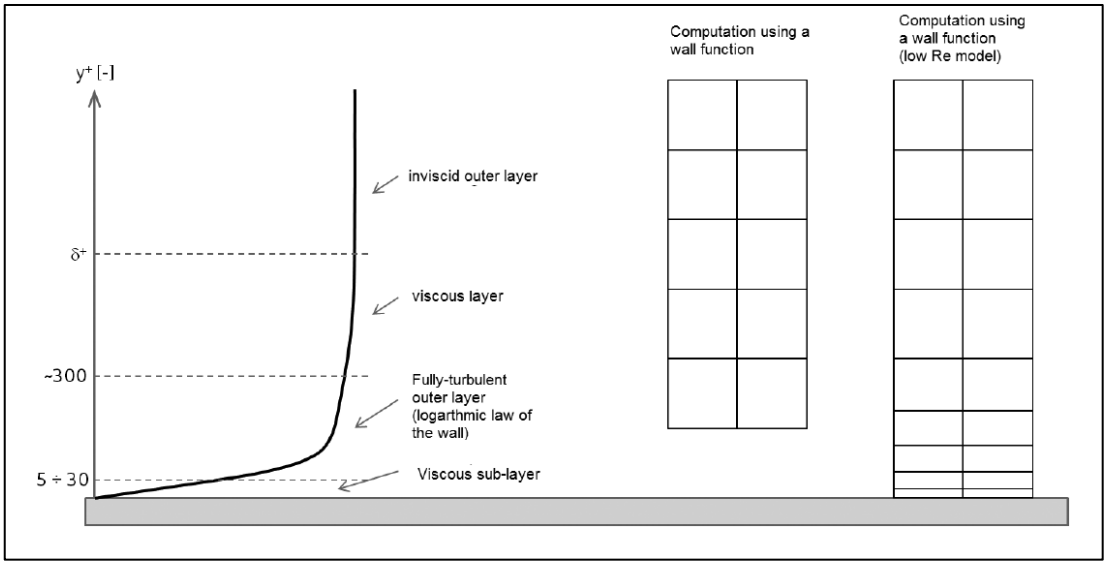

Figure 3.9: Illustration of the near-wall airflow by y^+ by two ways: wall function or low Reynolds model [4]

The velocity profile is fundamentally divided into two regions which are inner and outer as shown in Figure 3.10(a). The inner region starts from the wall surface to about 0.1 δ; While the outer region starts from about 0.1 δ to the free stream. Figure 3.10(b) shows the inner region of the velocity profile which is divided into three layers. Wall functions are used to resolve the inner region ($0 \leq y \leq 0.1\ \delta$; [92]) .

The range of sub-layers in the inner region is defined by a dimensionless parameter [4]:

$$y^+ = y\sqrt{\frac{\tau_w}{\rho\,\nu^2}} \tag{3.31}$$

where y is the vertical distance from the wall, τ_w is the wall shear stress, ρ is the density of the fluid and ν is the kinematic viscosity of the fluid.

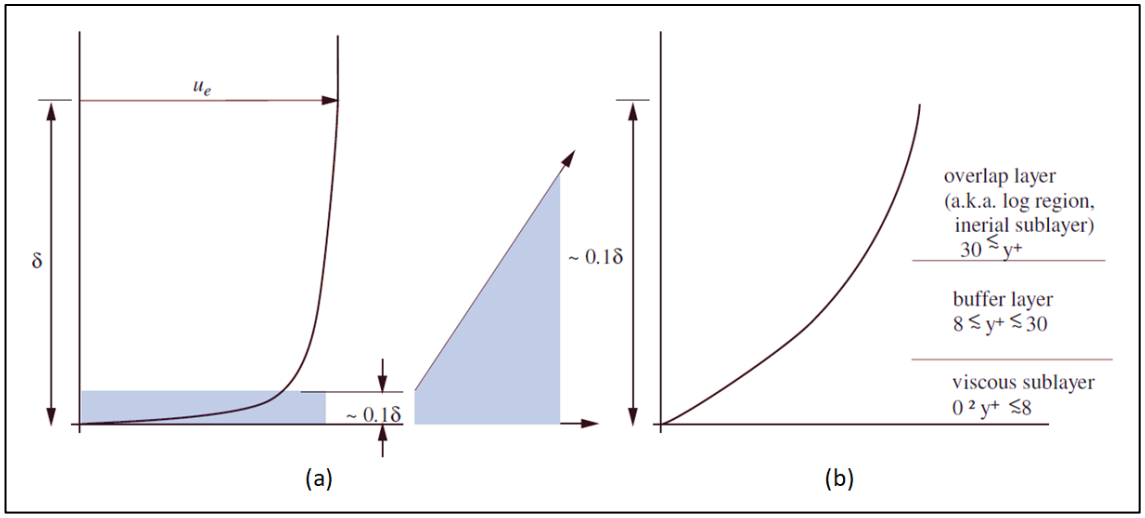

Figure 3.10: Velocity profile in a turbulent boundary layer [92]

3.3.2 Large Eddy Simulation (LES)

RANS approaches employ a single turbulence model to describe all eddies and this complicates the search for widely applicable models. Another approach to calculate the turbulent flows dependent on the larger eddies with a time-dependent simulation. This approach is called Large Eddy Simulation (LES). In general, it is difficult to identify an appropriate turbulence model for a wide range of practical applications. This is largely due to differences in the behaviour of small and large eddies. A continuous transport of energy exists from the free stream to the large eddies at a high Reynolds numbers. Smaller eddies being continuously created from the large eddies. Kinetic energy of the eddies near the wall converts into intermolecular energy and which means small eddies destroy themselves near the wall via energy dissipation. The principal idea of the LES is to ignore the smallest eddies which are the most computationally expensive to resolve filtering of the Navier–Stokes equations therefore Sub-grid scale models are used to include the affect of the smallest eddies on the resolved flow. The following equations are used in LES [66]:

LES continuity equation:

$$\frac{\partial \rho}{\partial t} + div(\rho \bar{\boldsymbol{u}}) = 0 \tag{3.32}$$

The overbar indicates a filtered flow variable.

LES momentum equations:

$$\frac{\partial(\rho\overline{u})}{\partial t} + div(\rho\overline{u}\overline{\mathbf{u}}) = -\frac{\partial\overline{p}}{\partial x} + \mu\, div\big(grad(\overline{u})\big) - \big(div(\rho\overline{u}\overline{\mathbf{u}})\big) - \big(div(\rho\overline{u}\overline{\mathbf{u}})\big) \quad (3.33)$$

$$\frac{\partial(\rho\overline{v})}{\partial t} + div(\rho\overline{v}\overline{\mathbf{u}}) = -\frac{\partial\overline{p}}{\partial y} + \mu\, div\big(grad(\overline{v})\big) - \big(div(\rho\overline{v}\overline{\mathbf{u}})\big) - \big(div(\rho\overline{v}\overline{\mathbf{u}})\big) \quad (3.34)$$

$$\frac{\partial(\rho\overline{w})}{\partial t} + div(\rho\overline{w}\overline{\mathbf{u}}) = -\frac{\partial\overline{p}}{\partial z} + \mu\, div\big(grad(\overline{w})\big) - \big(div(\rho\overline{w}\overline{\mathbf{u}})\big) - \big(div(\rho\overline{w}\overline{\mathbf{u}})\big) \quad (3.35)$$

where $\overline{\mathbf{u}}$ is the 3D velocity vector with components (u, v, w), t is time, $\bar{p}$ is the pressure, μ is kinematic viscosity and ρ is the fluid density. τ corresponds to the subgrid-scale stress tensor.

The first terms in the above equations are the rate of change of the filtered x-, y- and z-momentum. Second and fourth terms are the convective and diffusive fluxes of filtered x-, y- and z-momentum. Third terms are the gradients in the x-, y- and z-directions of the filtered pressure field. The last terms are caused by the filtering operation (like the Reynolds stresses in the RANS momentum equations).

The LES with a Wall- Adapting Local Eddy diffusivity (WALE) model was used in the work described in the proceeding chapters of this thesis as in line with Aljure *et al*. [93] due to the drag coefficient are highly improved when using this model.

This corresponds to the sub-grid-scale stress tensor equation which is as follows:

$$\tau = -2\, v_{SGS}\, \bar{S} + (\tau : \mathbf{I})\mathbf{I}/3 \quad (3.36)$$

where v_{SGS} is the subgrid viscosity, $\bar{S}$ is the rate of strain tensor and **I** is the three-dimensional isotropic tensor.

The subgrid-scale viscosity (v_{SGS}) should be modelled to close the formulation. Modelling of turbulence is carried out in this study by using one type of the SGS model which is the Wall Adapting Local Eddy viscosity (WALE) as proposed by Nicoud and Ducros [94].

The WALE model is an appropriate near wall scaling for the eddy viscosity in addition to accounting for the effects of the rotation rates and strain.

$$v_{SGS} = (C_{wale}\, l)^2 \frac{(\bar{V} : \bar{V})^{3/2}}{(\bar{S} : \bar{S})^{5/2} + (\bar{V} : \bar{V})^{5/4}} \tag{3.37}$$

$$\bar{V} = \frac{1}{2}(\nabla(\bar{\mathbf{u}})^2 + \nabla^T(\bar{\mathbf{u}})^2) - \frac{1}{3}(\nabla(\bar{\mathbf{u}})^2 : \mathbf{I})\,\mathbf{I} \tag{3.38}$$

where C_{wale} is the model constant

$$\bar{S} = \frac{1}{2}[\nabla(\bar{\mathbf{u}}) + \nabla^T(\bar{\mathbf{u}})] \tag{3.39}$$

3.4 The blockage ratio

The blockage ratio affects the aerodynamic coefficients of C_D and C_p. It has been suggested it should be less than 7.5% for wind tunnel tests to obtain a high accuracy of aerodynamic measurements [35]. The blockage ratio equation is defined as (*ibid*):

$$B = \frac{A_v}{A_w} \tag{3.40}$$

where A_v is the frontal sectional area of the vehicle model, and A_w is the frontal sectional area of the wind tunnel (computational domain in numerical studies).

The measured results of the blockage ratios higher than 7.5% should be corrected. There are a number of equations to correct the blockage ratio. In general, the following equation is used to correct the drag coefficient for the high blockage ratios [35]:

$$C_{dc} = \mathcal{W}\, C_{dm} \tag{3.41}$$

where C_{dc} is the corrected drag coefficient, C_{dm} is the measured drag coefficient, and $\mathcal{W}$ is the correction factor (a function of the blockage ratio).

Chapter 4 Methods

As stated in previous chapters, the CFD approach will be used for modelling the airflow around a road vehicle throughout the present study. The Navier–Stokes equations are used to describe the motion of fluid flow around the road vehicle. Different types of the flow behaviour, i.e. laminar, transitional and turbulent flow, could exist around the road vehicle, and the Reynolds number is used to recognise the specific type of flow in order to choose the suitable governing equations. It should be notes that the flow separation is mainly responsible for wake formation and that leads to increase in drag coefficient. In this study, it is considered and discussed in the simulations.

4.1 CFD basics

Simulation is widely used in the external aerodynamics of road vehicles, mainly because changing the external design of vehicles by employing numerical methods is less expensive than experimental methods. Furthermore, due to improvements in computational algorithm and speed, simulation provides reliable and fast results for most cases [91]. There are many softwares which can be used for numerical simulations of aerodynamics such as ANSYS-Fluent, CD-adapco, ANSYS-CFX and Open-Foam. Most researchers in field of the aerodynamic of road vehicles have used ANSYS-Fluent for the simulations as mentioned in Chapter 2. Therefore, ANSYS-Fluent was used in the current study to simulate all cases.

The pre-processor (e.g. computational domain and grid generation) and solver (e.g. finite volume based and discretisation to algebraic equations) are the most important stages in the structure of CFD codes. They have a significant influence on the accuracy of the computational results. The procedure of the assessing reliability and accuracy between the computational solution and highly accurate data should be achieved.

The road vehicles operate in a turbulent flow field. Many types of turbulence models are suitable for a variety of engineering applications such as the aerodynamics of road vehicles. Each of these turbulence models has advantages and limitations.

RANS approach has many turbulence models such as k-ε and k-ω turbulence models. The k-ε and RSM are not accurate enough near the wall compared with the k-ω turbulence model. The k-ε turbulence model is not accurate near the wall due to the modelling of the ε equation which is neither accurate nor easy to solve. It is worth mentioning that the k-ε turbulence model and RSM use wall treatment to correct the simulation results near the wall. The RSM turbulence model mathematically is expensive because this type of

turbulence model has six additional equations. Spalart-Allmaras and all types of k–ω models have accurate simulation results near the wall on condition that the mesh is refined enough near the wall surface.

LES is better than RANS in terms of results accuracy when unsteady flow is encountered or the solution of the largest eddies is important. On the other hand, LES is computationally expensive due to its need for a high quality of mesh and very long simulation run times. It is expected that RANS with a k-ε turbulence model will continue to be used.

4.2 Computational models

The Ahmed model is widely used to study the aerodynamic behaviour of road vehicles because it is simple geometry and there are many experimental and numerical studies of this model. Most of the previous studies were based on the study of simple geometries of road vehicle. There are many studies on the reduction of drag coefficient on road vehicles using CFD simulations. However, there are no previous studies focused on improving the drag and lift coefficient and create a balance between them.

Boat-tail was used in the previous studies as an aerodynamic device for the Ahmed model and heavy trucks only. The collapsible wind friction reduction, rear screen device and fairing were used as add-on devices for SUVs. These devices make the road vehicle more streamlined, but these types of aerodynamic devices cause an increase in weight. To avoid overweight and manufacturing costs the spare tyre can be placed on the rear door of the Land Rover Discovery and this will be investigated in the present study. Different shapes and sizes of VGs were used, but there are no VGs as aerofoil geometry.

Convergent-divergent passages can be created by using VGs as aerofoil geometry. This technique can improve the pressure above the car as well as behind it. Roof deflector was used to improve the drag coefficient of the tractor-trailer while diffuser under sedan model was used to increase the pressure behind the car. The two previous aerodynamic modifications can be used to create a new technique, which is ditch as a convergent-divergent nozzle on the roof. Base bleed was used in the previous studies to improve the drag coefficient, but the researchers did not pay attention to the effects of their designs on the visibility and the comfort of the passengers. A new base bleed design can be used to improve the aerodynamic behaviour without any of the disadvantages in previous designs. This will be investigated in the present research.

Two computational models of road vehicles were used in this study. The first model was the Ahmed model and the second model was the Land Rover Discovery 4. The purpose of the Ahmed model study is to refine the mesh parameters, assess grid / turbulence model combinations, in addition to study the effect of the size of the model, flat plate under the body (which was implemented in most experimental models) and slant angle on the drag and lift coefficients. The main computational model in the current study is the Land Rover Discovery 4, where novel techniques for the drag reduction and stability increase would be investigated in full details. Two different sizes of computational domain were used for the Ahmed body and six different sizes of computational domain were used for the Land Rover Discovery 4.

4.3 Methodology

The Ahmed model [13] is widely used to study external aerodynamic of road vehicles because it is simple geometry and free from wheels and all types of accessories such as bumpers, side mirrors and wheelhouses. It can be used to study the main features of the aerodynamic behaviour of a road vehicle.

4.3.1 Numerical model of the Ahmed body

Figure 4.1 illustrates a schematic diagram of the Ahmed model, with its dimensions in millimetres. A 55% scale model of the Ahmed body with a variety of slant angles (10°, 20°, 25°, 30° and 40°) were simulated using a new technique in order to calculate the drag coefficient by using a rounded rectangular flat plate under the Ahmed model in line an experimental study [18]. The dimensions of the plate were $275 \times 196mm^2$ and its thickness was 3mm. The drag force caused by a flat plate was subtracted from the overall force which was obtained from the whole system.

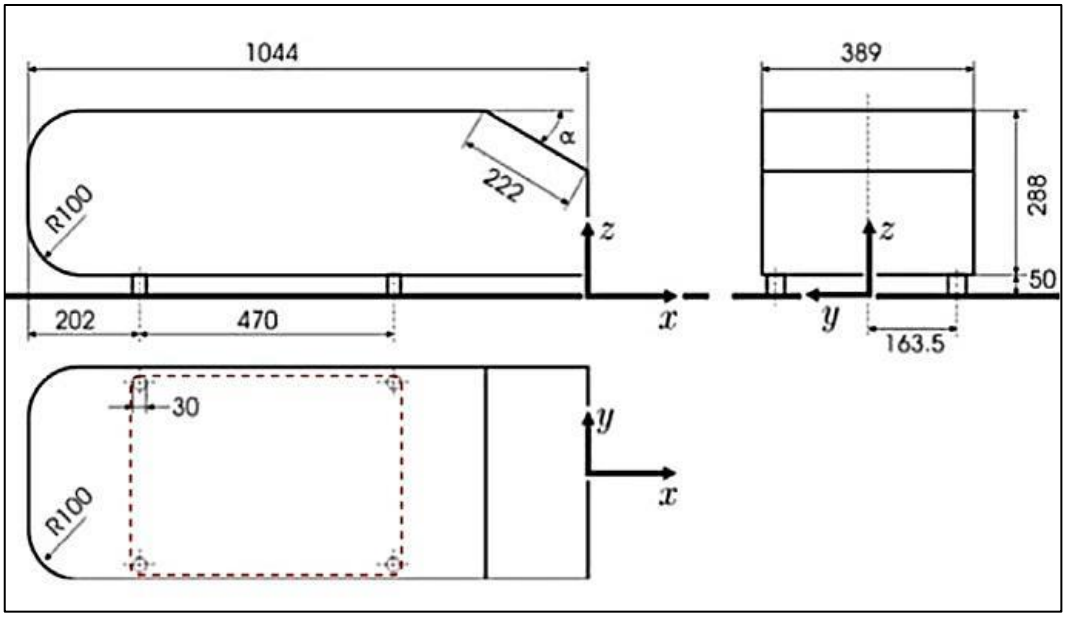

Figure 4.1: The 3-D full scale of the Ahmed model [18]

In addition to the 55% of the Ahmed model, a full-size model was also used to investigate the affect of model size on the results. A closed low speed wind tunnel was used in the experimental studies of Bello-Millán *et al*. [18]. Inlet air velocity ranging from 6.9m/s to 24.5m/s in line with experimental tests. A flat plate was used as a link attached to the underside of the legs of the body and the digital force sensor. The full scale and the 55% scale models of the Ahmed model with and without flat plate under the geometry were used herein. Five slant angles were used in both numerical scale models, i.e. 10°, 20°, 25°, 30° and 40°, to access their affect on the drag and lift coefficients and compared with the experimental study [18] with a slant angle of 25°. The length (*L*), width (*W*) and height (*H*) of the 55% scale model (Figure 4.2) were 0.574m, 0.214m and 0.186m, respectively. The surface roughness was neglected as in the experimental work the model was made from expanded polystyrene using a CNC machine. Figure 4.2 shows the three-dimensional, 55% scale model of the Ahmed body with the rounded flat plate under its legs (in red). A rounded rectangular flat plate was used as a rotating device in the experimental study [18], because it was attached to the main body from the upper side and attached to the digital force sensor from the other side. The dimensions of this plate were $0.275 \times 0.196 m^2$ and its thickness was 0.003m.

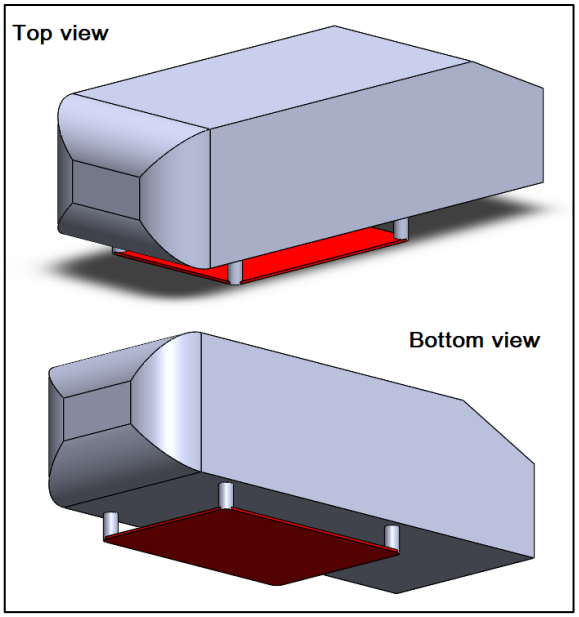

Figure 4.2: The 3-D 55% scale of the Ahmed model

4.3.2 Computational domain of the Ahmed body model

Figure 4.3 shows the experimental set-up which was used by Bello-Millán *et al*. [18]. It consists of a digital camera, continuous laser and force sensor connected to the plate under the Ahmed model which was controlled by a computer. It is clear from this figure that only one visualization showed for the rear side of the Ahmed model. This experimental work [18] was carried out in a closed low speed wind tunnel. The dimensions of this wind tunnel were 4m × 1m × 1m. The symmetry plane for the laser flow illustration was situated in the middle of the test section to reduce the side wall effects. Uniform inlet velocity ranged between 6.9m/s to 24.5m/s in the experimental study and the turbulence intensity was reported to be less than 1.0%.

For the numerical simulations in this work, a rectangular cuboid was used as a computational domain as a replica of the wind tunnel, as shown in Figure 4.4. The length, width and height of the computational domain were 4m, 1m and 1m, respectively, ($1m^2$ as a frontal cross-sectional area). The Ahmed model was located at 2.58 L downstream from the inlet section and at 3.386 L upstream from the outlet boundary, totalling an extension of 6.966 L, to allow full development of the flow downstream. A no-slip boundary condition was prescribed on the ground, roof and tunnel walls, while null pressure was imposed at the outlet wall. The blockage ratio in the experimental test was about 3% for the Ahmed scale model with zero yaw angle and it was the same for the

numerical simulation. Half of the rectangular computational domain was used in the simulation of this work to reduce the calculation time as the whole system can be regarded as symmetric.

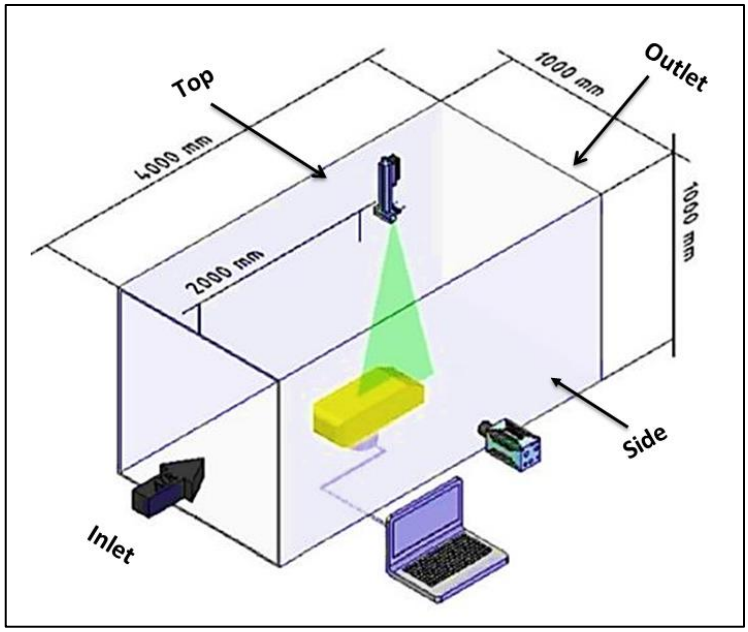

Figure 4.3: The experimental setup with all dimensions of the wind tunnel and devices [18]

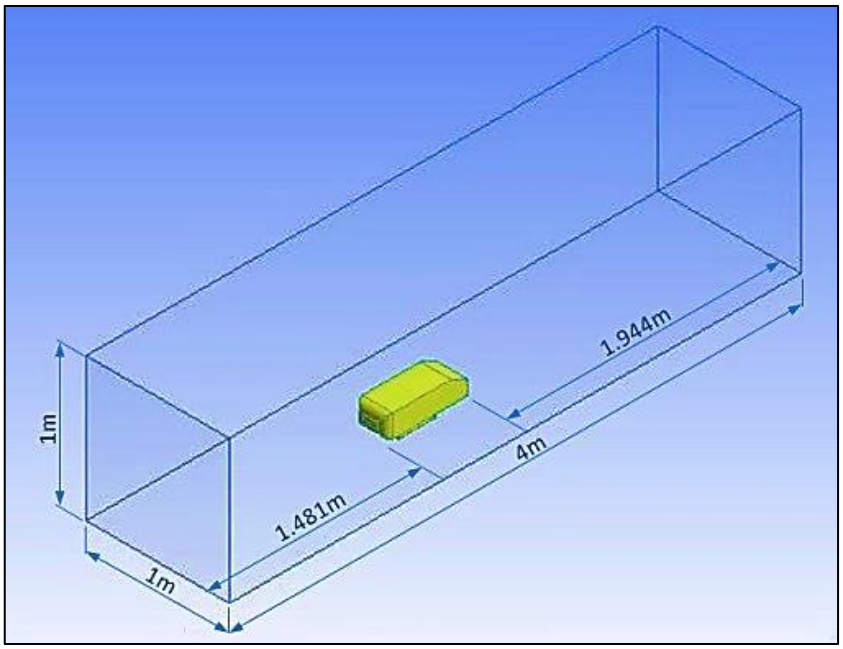

Figure 4.4: The computational domain and the 55% scale of the Ahmed model with all dimensions

4.3.3 Mesh and numerical set-up of the Ahmed model

The mesh quality is a crucial factor in obtaining accurate results in the numerical study. ANSYS Meshing (version 17.1) was used to create a mesh within the computational domain. Analysis of the mesh was investigated to get the optimum mesh. Most researchers prefer the hexahedral mesh, especially for simple geometries, but when the quality cannot be maintained (for example: orthogonal quality, skewness and aspect ratio are poor) then it is better to switch to a tetrahedral mesh. Tetrahedral mesh is a very good choice for complex geometries because the mesh cells may have any shape. This type of mesh is the most flexible type regarding geometries but it requires more mesh density than structured grid [95]. Increasing the mesh density means increasing of accurate results but that leads to an increase in simulation time. Therefore, the mesh density within the computational domain should be high enough to capture all flow features. It is better to improve the mesh quality before creating the prism layers around the surfaces of the geometry.

To control the mesh growth, especially near the surfaces of the vehicle, an inner box (which called the volumetric control region) was used. A Volumetric Control Region (VCR) with a tetrahedral mesh near the geometry is usually needed in the computational domain to improve the overall mesh quality [91, 96]. Three VCRs were used around the Ahmed model to control the mesh cell sizes. Figures 4.5 and 4.6 show three VCRs around the Ahmed model with all symbols and dimensions. All dimensions of the VCRs used in this work were as recommended by Ahmad *et al*. [96] and using scale factor technique to achieve the suitable sizes for the Ahmed model. The VCR1 length was set to be 25% of the computational domain length, increasing to 37.5% for the VCR2 and increasing to 50% for the VCR3. It is clear that VCRs have divided the global area into four zones. More attention was paid to mesh refinement behind the Ahmed model due to the amount of expected vortices.

Table 4.1 illustrates all the dimensions and parameters of the computational domain as well as the total number of meshes for the Ahmed model with a 25° slant angle. The dimensions and parameters of full scale and the 55% scale model of the Ahmed body are shown in this table with the blockage ratio (the ratio of the frontal cross-sectional area of geometry to the inlet cross sectional area of computational domain) for each model. *H*, *W* and *L* symbolize the height, width and length respectively, which were used with the computational domain and all VCRs. The subscript of *H*, *W* and *L* symbolizes the height, width and length respectively. This table enables an analysis of the difference between

the models depending on their scale and type of support (with or without a plate under the legs).

The first inflation layer around the car model and the growth rate of the inflation layers are very important to know how the airflow behaves near the surfaces of the car. The concept of y^+ wall function is a dimensionless quantity represents the distance from the wall measured in terms of viscous lengths. For the road vehicle steady state simulation, y^+ is between 30 and 300 by using the realizable k-ε turbulence model in line with Lanfrit [91].

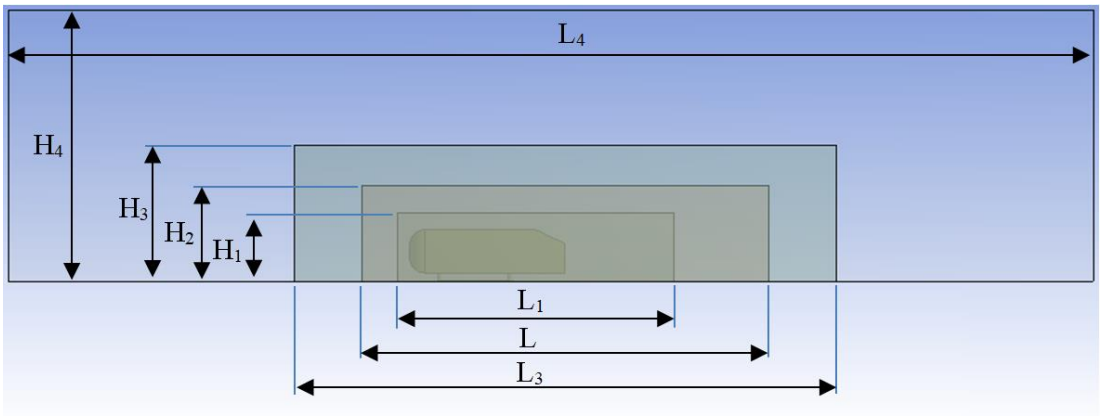

Figure 4.5: The side view of the Ahmed model in the computational domain with three VCRs

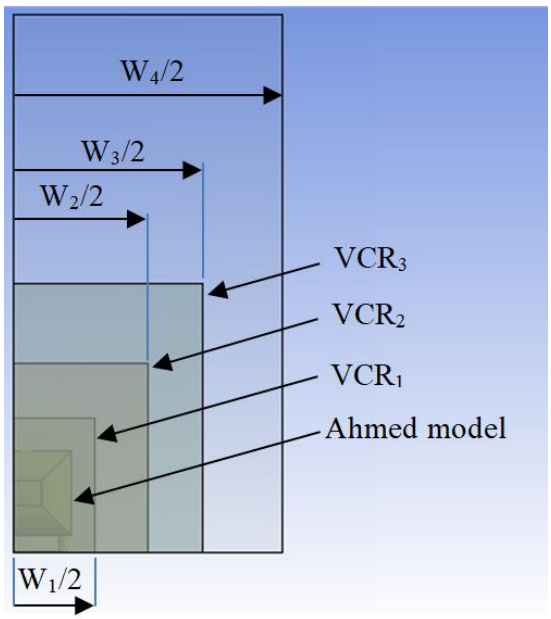

Figure 4.6: The front view of the Ahmed model in the computational domain with three VCRs

		Ahmed model (55% scale)			Ahmed model (full scale)
		Without flat plate	With flat plate	With long flat plate	Without flat plate
No. of cells		4,152,869	4,458,161	4,576,583	4,297,802
External volume (m)	H_4	1	1	1	1.813
	W_4	1	1	1	1.813
	L_4	4	4	4	7.274
Volumetric Control Region (VCR) No. 3 (m)	H_3	0.5	0.5	0.5	0.91
	W_3	0.7	0.7	0.7	1.28
	L_3	2	2	2	3.64
VCR No. 2 (m)	H_2	0.35	0.35	0.35	0.64
	W_2	0.5	0.5	0.5	0.91
	L_2	1.5	1.5	1.5	2.74
VCR No. 1 (m)	H_1	0.25	0.25	0.25	0.455
	W_1	0.3	0.3	0.3	0.546
	L_1	1.02	1.02	1.02	1.86
Offset (m)	O_H	0.814	0.814	0.814	1.48
	O_W	0.286	0.286	0.286	0.52
	O_L	1.481	1.481	1.481	2.692
Blockage ratio (%)		3.479	3.538	3.538	3.5

Table 4-1: Dimensions and parameters of the computational domain and mesh (for the Ahmed model with 25° of the slant angle)

For more accurate results, especially near surfaces, 5 to 10 inflation (prismatic) layers were used following an analysis of the optimum number of prismatic layers for this case. In this work five meshes were used for the Ahmed model with a 25° slant angle as shown in Table 4.3; 4.15×10^6 Finite Volume (FV) for the 55% scale model; 4.3×10^6 FV for the full scale model; 4.46×10^6 FV for the 55% scale model with a standard flat plate under the body; 13.92×10^6 FV for the 55% scale model with a standard flat plate under the body and 4.58×10^6 FV for the 55% scale model with long plate under the body. In

addition to the previous meshes, there are also four different meshes used for the Ahmed model with 10°, 20°, 30° and 40° slant angles.

The prism layers for the *k–ε* turbulence model were grown using a first aspect ratio of 5 and a growth rate of 20%. The optimal number of the prism layers for the *k–ε* turbulence model was 5. This technique provides a smooth transition to the tetrahedral cells. The prism layers for the SST turbulence model were grown using a first layer height of 0.145mm and a growth rate of 20%. The optimal number of the prism layers for the SST turbulence model was 10 to cover all viscous sub-layer. y^+ in these simulations of the Ahmed model by using SST and LES was between about 0.3 and 5 as shown in Figure 4.11.

The optimum mesh for this case using realizable *k-ε* is shown in Figure 4.9 while for SST and LES turbulence models this is shown in Figure 4.10. The range of the mesh cells for half of the computational domain in this study was between 5×10^5 and 15×10^6. A wide range of the total number of mesh cells was used to check the grid dependency.

All boundary conditions in the simulation were similar to those used in the experimental methods in order to ensure a satisfactory comparison between results (Table 4.2). A range of inlet velocities between 6.9m/s and 76.8m/s were used in the current study. Stationary walls with no slip were used for the top and the side walls of the computational domain as in the experimental study. Figures 4.7 and 4.8 show the salient parameters regarding the Ahmed model for this particular computational domain.

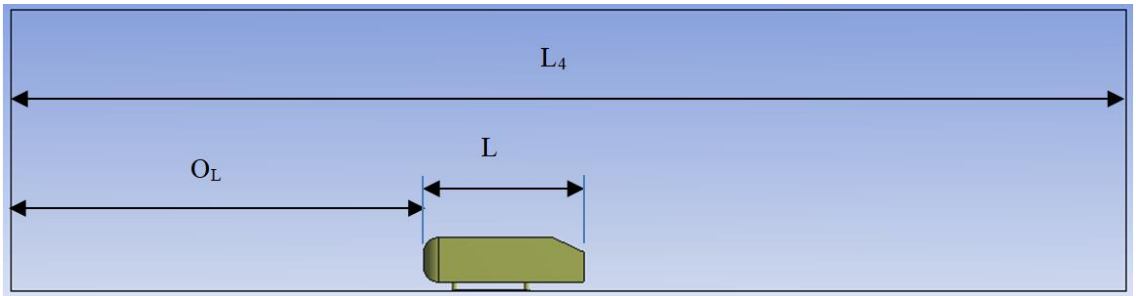

Figure 4.7: The side view of the Ahmed model in the computational domain

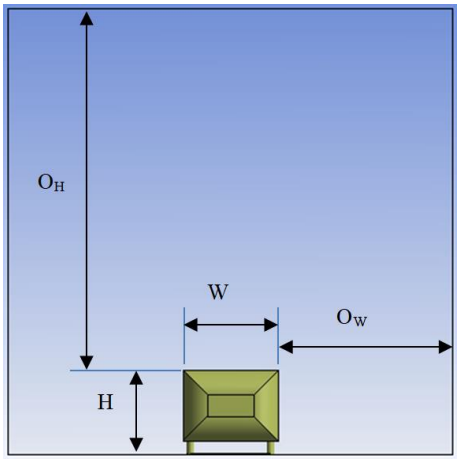

Figure 4.8: The front view of the Ahmed model in the computational domain

Model	Inlet	Outlet	Side	Symmetry	Ground	Top	Body
k-ε	U_∞ (6.9 – 76.35m/s)	Pressure (zero)	No-slip	Symmetry	No-slip	No-slip	No-slip
SST	U_∞ (6.9 and 10.2m/s)	Pressure (zero)	No-slip	Symmetry	No-slip	No-slip	No-slip
LES	U_∞ (6.9 and 10.2m/s)	Pressure (zero)	No-slip	Symmetry	No-slip	No-slip	No-slip

Table 4-2: Boundary conditions used in the numerical simulations of the Ahmed model

Model		**Number of cells**		
		Realizable *k-ε*	SST	LES
Without flat plate	Full scale	4.3×10^6		
	55% scale	4.15×10^6		
With standard flat plate under the model	55% scale	4.46×10^6	13.92×10^6	13.92×10^6
With long flat plate under the model	55% scale	4.58×10^6		

Table 4-3: Number of cells for different meshes of the Ahmed model with a 25° slant angle

The different Reynolds-Averaged Navier-Stokes (RANS) models (realizable *k–ε* and Shear Stress Transport *k-ω*), and LES turbulence models were used in the current study and their results were discussed in detail. A realizable *k–ε* turbulence model has been

widely used for RANS simulations of the external aerodynamics, especially for vehicles as it provides merit results in a reasonable computational time [3, 9].

The second-order upwind scheme was applied for turbulent kinetic energy, the momentum and turbulent dissipation rate. The second-order option was applied for the pressure in terms of spatial discretization. The first-order discretization can be acceptable in the case when the fluid flow is aligned with the mesh such as laminar fluid flow in a rectangular channel modelled with a quadrilateral mesh. However, first-order discretization can lead to an increase in the numerical discretisation error if the fluid flow is not aligned with the mesh. The second-order discretisation can provide more accurate results than first-order in the case of the flow is never aligned with the mesh (i.e. triangular and tetrahedral meshes).

The relaxation factor was 0.25. Three turbulence models were used for the Ahmed model: Realizable k–ε, Shear Stress Transport k-ω (SST) and Large Eddy Simulation (LES). These turbulence models have been widely used for the external aerodynamics of road vehicles by previous researchers (e.g. Levin and Rigdal [9] used the realizable k–ε turbulence model; Gilkeson *et al*. [32] used realizable k–ε and SST k-ω turbulence models; Serre *et al*. [24] used LES turbulence model).

Non-wall function (k-ω) method is sufficiently accurate near the wall surface with low Reynolds number [97]. The near-wall region does not need to be resolved in most high Reynolds number flows because the wall function (k-ε) method substantially saves computational resources. Resolving the flow within the viscous sub layer (y^+ less than 30) for high Reynolds number flows is not a practical choice because a large number of cells must be allocated in this region [91]. Non-equilibrium wall functions can be used to overcome the recognized disadvantages of traditional wall-functions. This option (non-equilibrium wall functions) is of great benefit to the prediction of road vehicle aerodynamics [91].

The fundamental idea of the LES turbulence model is to ignore the smallest eddies by filtering of the Navier–Stokes equations. Resolving small eddies are considered to be computationally very expensive. Therefore, Sub-grid scale (SGS) model is used to include the effect of the smallest eddies on the resolved flow. There are different SGS models to include the effect of the smallest eddies [93, 94, 98, 99, 100]: Smagorinsky-Lilly model; the singular values subgrid model (SIGMA); the Wall-Adapting Local-Eddy viscosity (WALE); the WALE model within a variational multiscale framework (VMS); and a model that uses the invariants (Q and R) of the filtered strain tensor to model eddy viscosity (QR). A Wall-Adapting Local Eddy-Viscosity (WALE) model was used for the

LES in this study as suggested by many researchers [93, 94]. The time step size used in the LES simulation was 0.0001s, each LES simulation used approximately 20,000 time steps covering 2 seconds of flow. Maximum iterations per time step of 20 was used. A convergent stable solution being found after some 380,000 iterations.

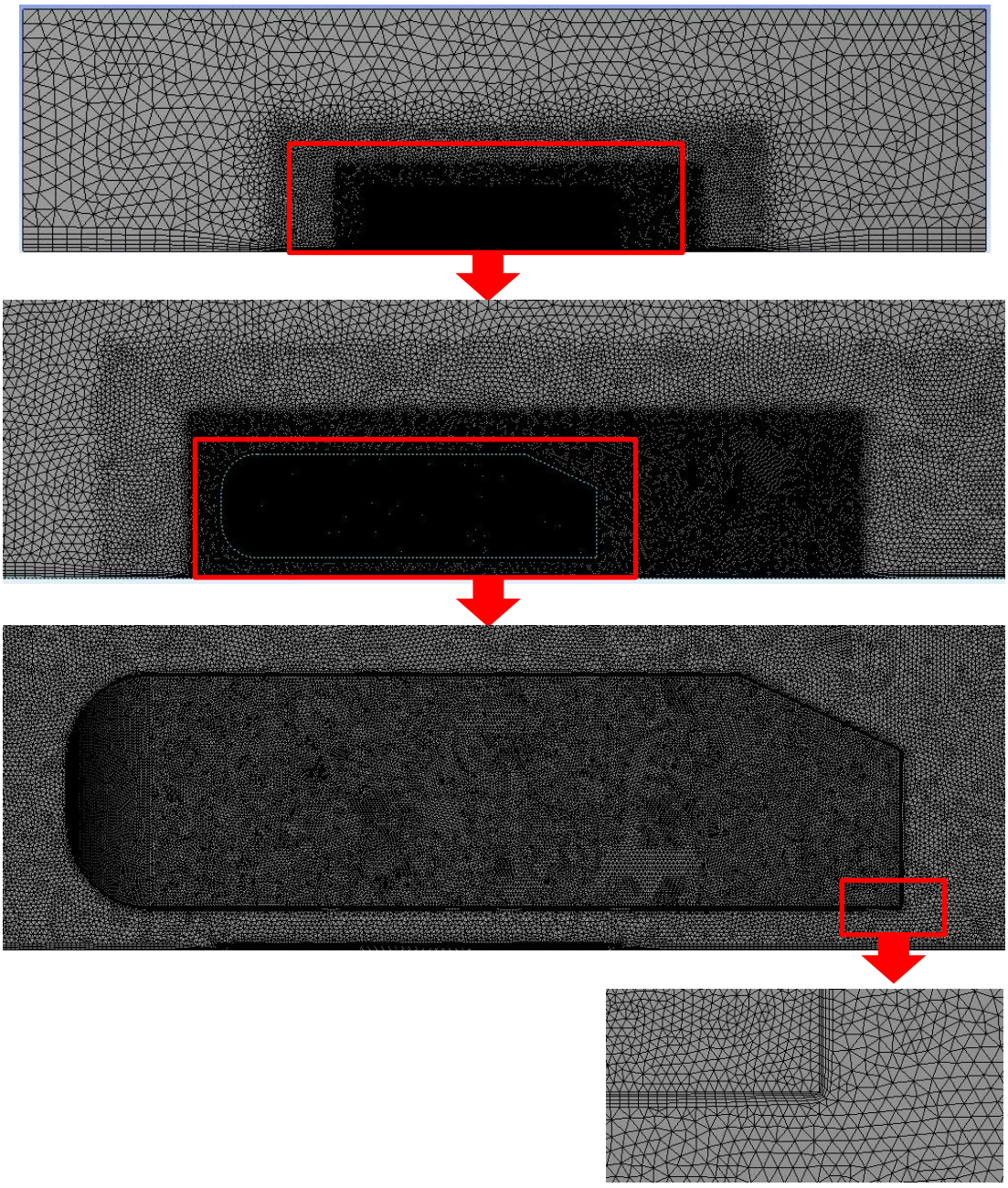

Figure 4.9: Mesh with three VCRs and five inflation layers around the Ahmed model

The time step size is the magnitude of Δt. Observing the number of iterations FLUENT needs to converge at each time step is a good way to choose the suitable time step size.

The time step size of 0.0001s was used as recommended by most previous studies of aerodynamics of the road vehicles [17, 23]. The ideal time step size would be one which yields convergence within 15-20 maximum iterations per time step.

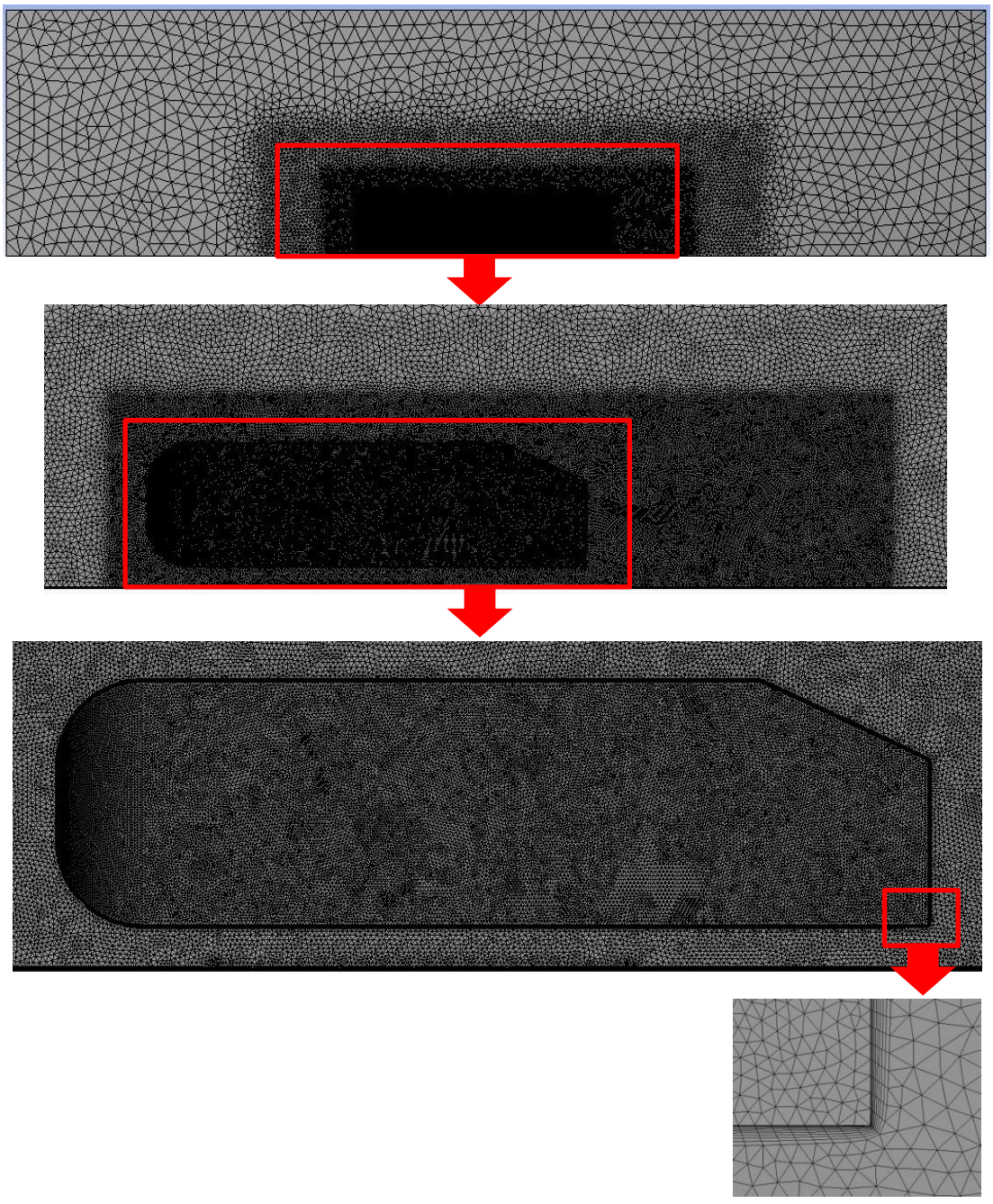

Figure 4.10: Mesh with three VCRs and ten inflation layers around the Ahmed model

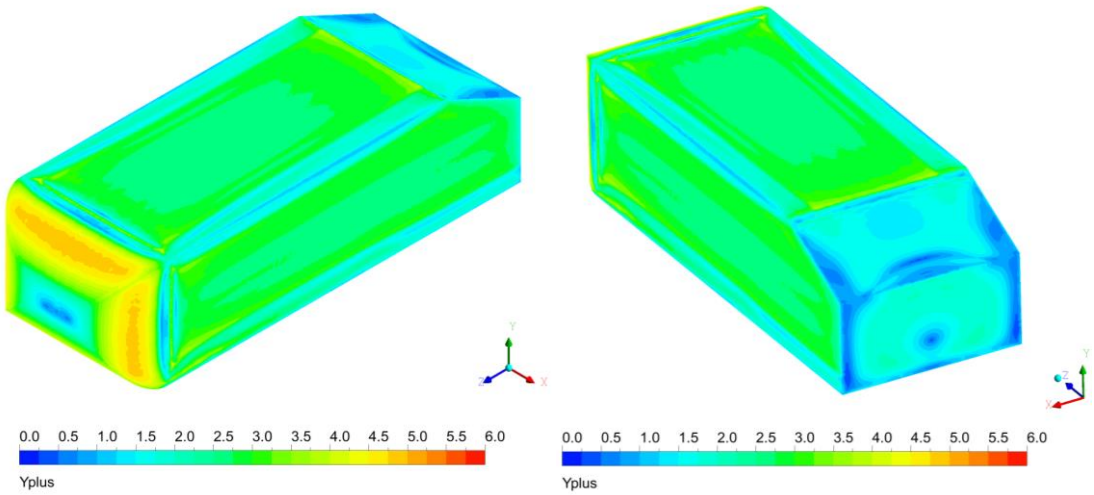

Figure 4.11: y^+ on the Ahmed model surface

4.3.4 Ahmed model verification

The normal numerical simulation is to start with a coarse mesh for the case and gradually refine mesh until the changes observed in the numerical results are smaller than an acceptable error. Grid dependency was obtained by checking a wide range of mesh elements, as shown in Figure 4.12. The optimum mesh cell numbers for the half computational domain and the Ahmed model were chosen between 4.5×10^6 and 5×10^6. The pressure coefficient and velocity of air on a point at wake zone were tested to check the convergence of numerical simulations, as shown in Figures 4.13 and 4.14. Obviously convergence was obtained at about iteration of 400.

The validation was achieved by comparing the present study's results for the drag coefficient and streamlines around the Ahmed model with widely cited experimental studies [13, 18, 28, 29]. Furthermore, a comparison of the present study's results for the drag coefficient with those reported by Serre *et al*. [24] was verified through.

Figure 4.15 shows the drag coefficient (C_D) as a function of the Reynolds number (Re) for the present numerical study (RANS and LES), the experimental results of Bello-Millán *et al.*[18], Thacker *et al.* [29], Ahmed *et al*. [13] and Meile *et al*. [28]. In general, the C_D decreases with an increase in Reynolds number. The results of Bello-Millán *et al*. [18] for the drag coefficient as a function of the Reynolds number were in agreement with the experimental results of Thacker *et al*. [29] who used the full scale Ahmed body as shown in Figure 4.15. It is interesting to note that the two studies used two different

ranges of Reynolds number and the wind tunnel, the scale of Ahmed bodies and the experimental setup of these two studies used were not similar.

The results from the study of Bello-Millán *et al*. [18] had a similar trend to those of Ahmed *et al*. [13] and Meile *et al*. [28] but with higher values. In the present study, we have been using a similar set-up to that of Bello-Millán *et al*. [18] but with 55% of the full scale and two types of turbulence models having been used, RANS and LES, as shown in Figure 4.15. A wide range of Reynolds numbers was used in RANS (between 2.7×10^5 and 3×10^6) but only two Reynolds numbers were used in the LES simulations due to the high computational cost. From Figure 4.15 it can be seen that the trend of RANS results is similar to that of experiments by Bello-Millán *et al*. [18] but underestimates values of C_D because the RANS approach can only provide time averaged mean values for the velocity field. However, the LES simulation results agree well with these experimental results [18].

Table 4.4 shows the drag coefficient (C_D) of the Ahmed model (slant angle of 25°) for the present numerical results (*k-ε*, SST and LES) compared with the numerical simulations detailed in the reference [24]. It can be observed that realizable *k-ε*, SST and LES simulation results agree well with the highly accurate numerical solutions [24].

Highly accurate numerical solutions				**This work**		
DES-SST	LES-NWR	LES-NWM	LES-SVV	LES	SST	*k-ε*
0.343	0.346	0.317	0.431	0.425	0.391	0.338

Table 4-4: C_D of the Ahmed model (slant angle of 25°) for the present numerical results (*k-ε*, SST and LES) as compared with highly accurate numerical solutions [24]

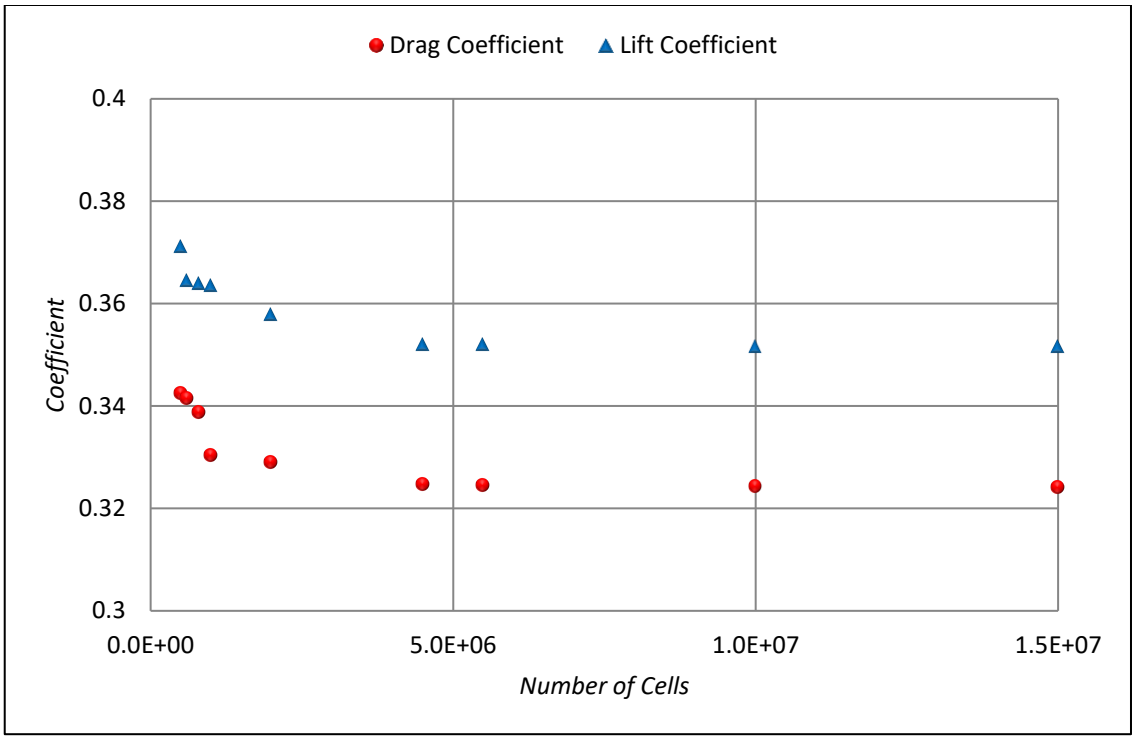

Figure 4.12: Grid-independence

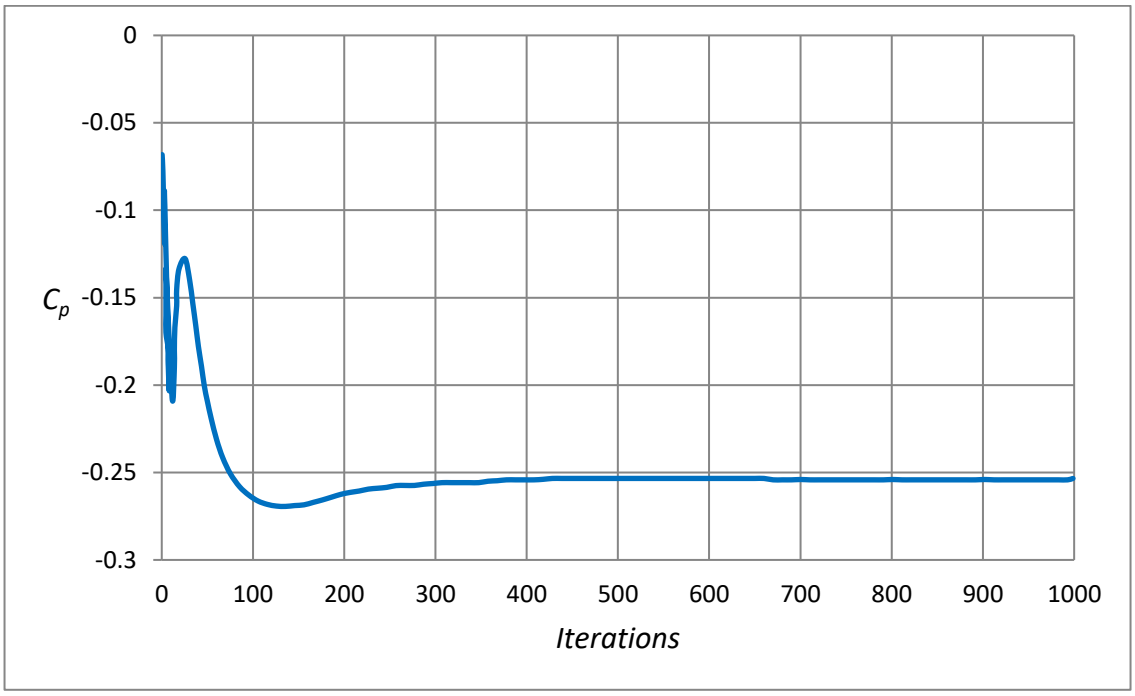

Figure 4.13: Convergence history of the pressure coefficient on a point at wake zone

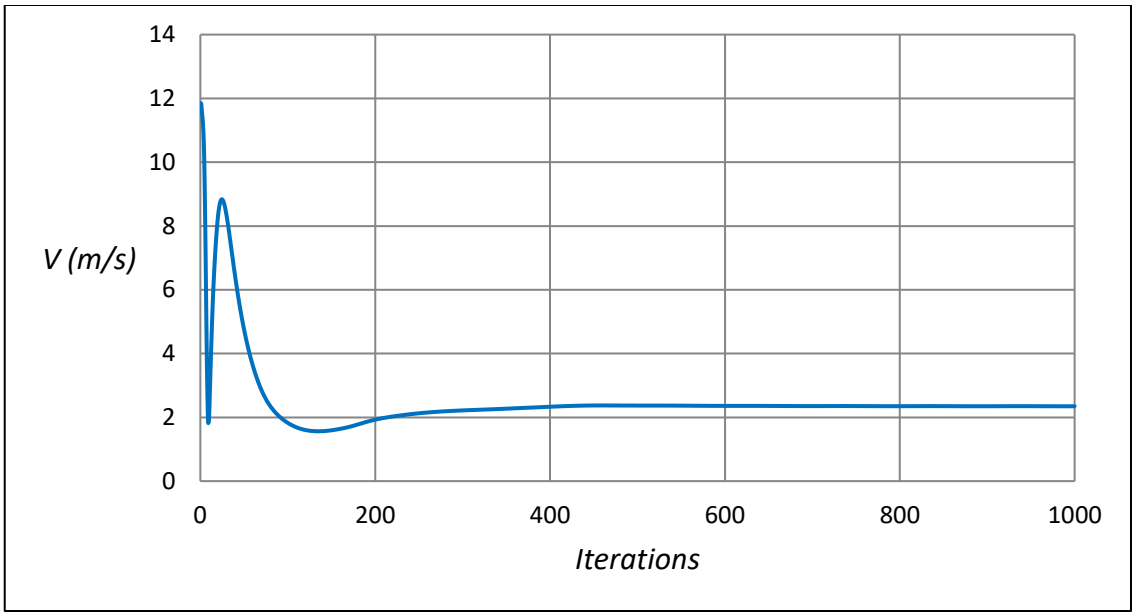

Figure 4.14: Convergence history of velocity magnitude on a point at wake zone

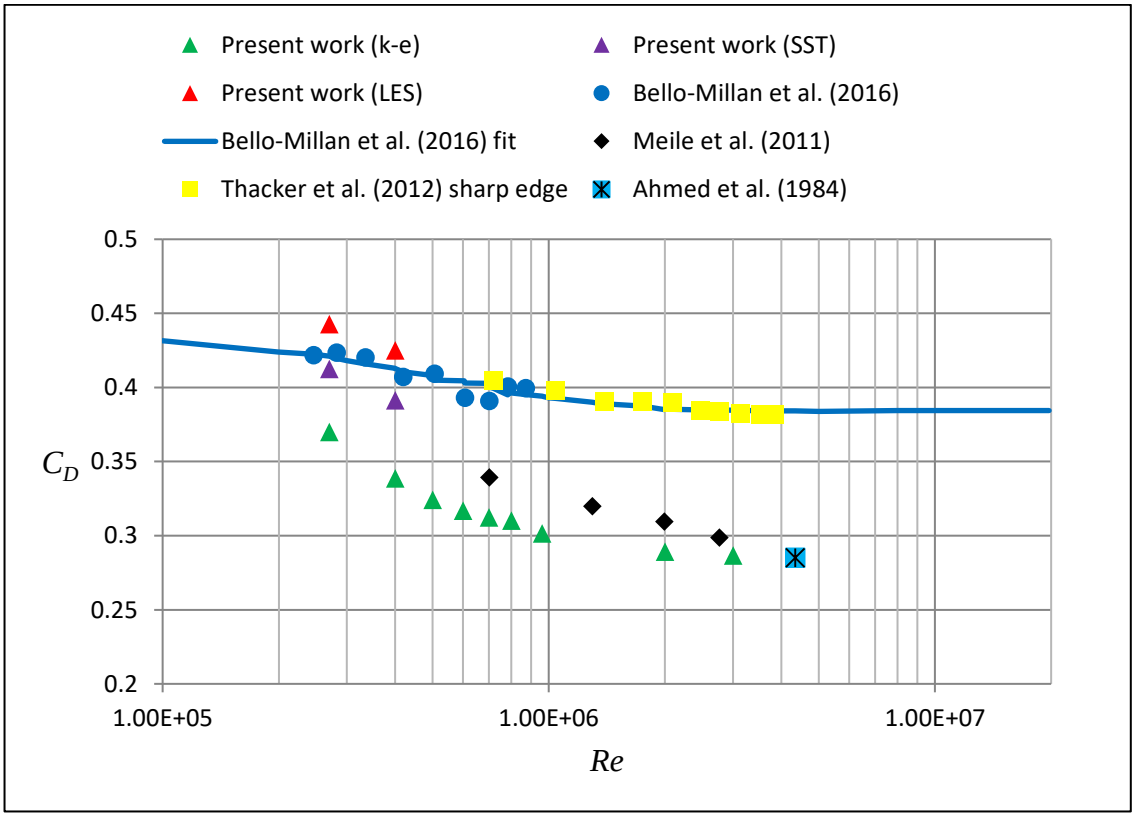

Figure 4.15: C_D as a function of a *Re* for the present numerical results (RANS and LES) as compared with other authors' experimental results

Smoke production was used in the experimental work by Bello-Millán *et al*. [18] in order to obtain flow visualizations. A Ni–Cr wire in the inlet of the wind tunnel and at the symmetry plane with a 0.12mm diameter. All flow visualizations were shown at the laser plane which was perpendicular to the camera's field of view, i.e. at zero yaw angle. The experimental smoke visualizations were carried out at the front and rear sections only with Reynolds number of 6.96×10^5 and zero yaw angle. Flow visualization was used in the experimental study in two regions to investigate how the air flow enters and passes through to the case-study and also to study the separation that occurs near the slant angle. The first region was in the front part of the Ahmed model and the second was at the rear of the model, as shown in Figures 4.16(a) and 4.17(a) respectively.

A two-dimensional smoke plane was illuminated by stable laser light and a digital high-speed camera was used to record the streamlines. Figure 4.16(a) shows the streamlines in the front part of the Ahmed body using smoke visualizations as reported by Bello-Millán *et al*. [18]. It was observed that the streamlines near the surfaces of the Ahmed body were not sufficiently clear. This experimental visualization test was carried out at only one speed with a Reynolds number of about 6.96×10^5. The airflow in the experimental tests was attached to the surfaces of the Ahmed body in the front part, as shown in Figure 4.16(a). The streamlined flow in the front section of the Ahmed model can be clearly observed in both RANS (k-ε, SST) and LES numerical simulations from this work are shown in Figure 4.16.

These numerical visualizations were carried out at a Reynolds number of about 6.96×10^5. In general streamlines of k-ε, SST and LES were similar but the streamline in realizable k-ε was less sensitive to vortices near the separation flow in the slanted surface. Streamlines were much clearer in the LES methodology as compared to that of RANS, presumably due to the fact that RANS can only provide time averaged mean values for the velocity field. The SST turbulence model result is more appropriate than the k-ε model as shown in Figure 4.17. In general, k-ε turbulence model predicts well far from the wall and k-ω turbulence model predicts well near wall. SST turbulence model is a combination of k-ε and k-ω to achieve the best result [66].

The number of inflation layers and their thicknesses has a significant effect on the results of the SST model as this model does not use treatment wall function. The numerical streamlines of RANS (realizable k-ε and SST) and LES agreed very well with the experimental visualization in the front section of the Ahmed model.

The detaching of airflow from the Ahmed model at the rear section was not clear in the experimental visualization, as shown in Figure 4.17(a). The streamline in experimental

tests in the wake region is unclear due to the low velocity in this area. The smoke mainly goes to the high velocity regions, especially after a long distance from the smoke injection nozzle. This problem can be rectified by using a set of nozzles. As it can be observed in Figure 4.17(b), the streamline at the rear section of the Ahmed model using realizable *k*-*ε* simulation clearly shows that the separation starts from the end of the slanted surface. While by using the SST model, the separation of airflow starts from the edge between the roof and the slanting surface, as shown in Figure 4.17(c).

By using the SST model, two vortices were near the slanting surfaces. The smaller was over the slanting surface and the larger vortex was behind the slanting surface. This means more drag force because vortices consume power. This turbulence model (SST) was more accurate than the *k*-*ε* model because the *k*-*ε* model uses wall treatment but on the other hand needs a very good mesh quality. Most properties of airflow vary near the wall, especially at the rear section of the road vehicle. Figure 4.17(d) shows the streamlines in the rear section of the Ahmed model using LES. The air flow separation starts from the beginning of the slanting surface (similar to the SST model) and there was a large vortex above the slanting surface area. This means that there could be a greater drag force against the movement of the vehicle as compared to the realizable *k*-*ε* simulation.

LES is an approach that solves the issue of large-scale fluctuating motions and uses sub-grid scale turbulence models for small scale motion. This approach is supposed to be more accurate than RANS but more time is needed to complete an effective simulation. By comparing the flow at the rear section of the Ahmed model using RANS (*k*-*ε*, SST) and LES approaches it can be seen that the location of the separation bubble is different depending on the turbulence model (Figure 4.17); this means that the wake flow when using the LES and SST approaches starts earlier than when using the *k*-*ε* approach. The air discharge above the Ahmed model was higher than the underbody discharge as the cross-sectional area of flow and the upper surface of this model are greater than the lower surface because of the slanting surface in the rear upper part. All these contribute to a lower pressure zone and create a large recirculation region above the slanting surface. The drag coefficients of the *k*-*ε*, SST and LES approaches were also calculated and compared with experimental data.

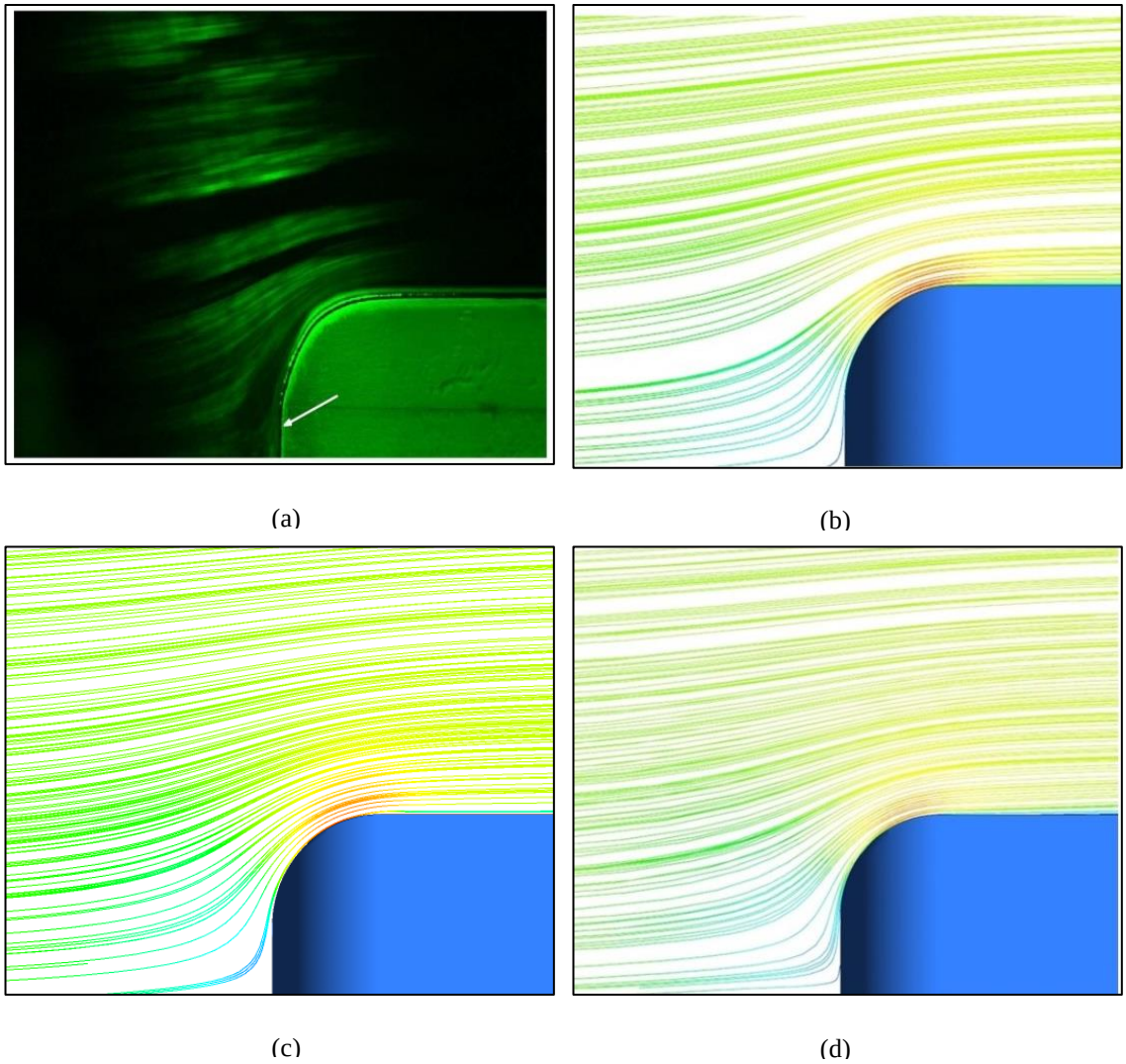

Figure 4.16: Flow visualization of the experimental and numerical results of the 55% scale model of the Ahmed body for the front section (a) experimental result [18], (b) numerical result of realizable *k*-*ε* model, (c) numerical result of SST model, and (d) numerical result of LES model

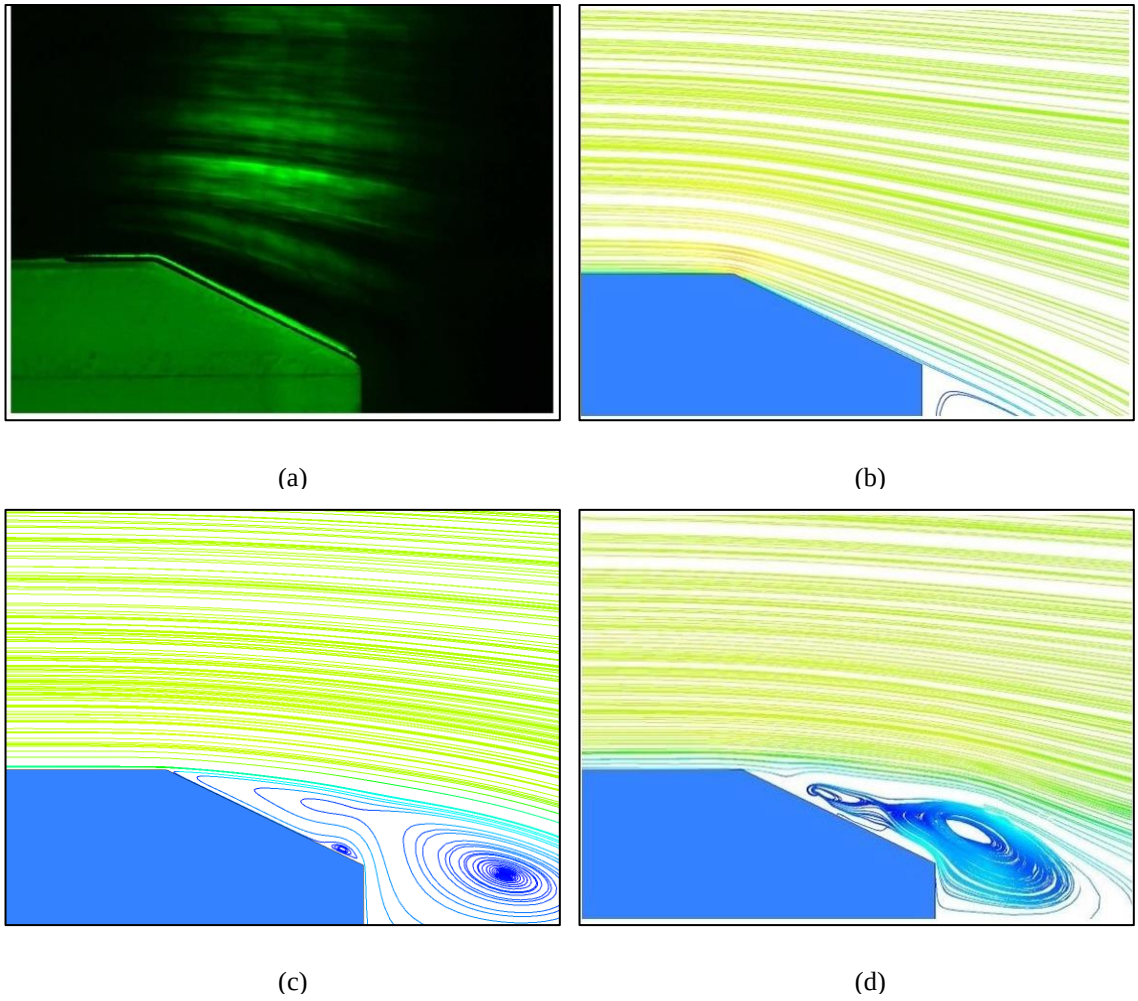

Figure 4.17: Flow visualization of the experimental and numerical results of the 55% scale model of the Ahmed body for the rear section (a) experimental result [18], (b) numerical result of realizable *k-ε* model, (c) numerical result of SST model, and (d) numerical result of LES model

4.3.5 Streamline around the Ahmed model

The effects of the flat plate which was used in the experimental tests to fix the vehicle model onto the load-cell were not studied by Bello-Millán *et al*. [18]. Only the drag force of the flat plate was calculated in order to subtract from the drag of whole case-study (Ahmed model and flat plate). The Reynolds Averaged Navier-Stokes equations (RANS) approach is usually used for predicting turbulent flows which is solved for time averaged solutions. However, there are some cases where this approach is not suitable and the alternative approach of Large Eddy Simulation (LES) can be used.

The overall behaviour of the airflow around the Ahmed body model can be better identified by using the streamline plots on the symmetry plane, as shown in Figures 4.18, 4.19, 4.20, 4.21 and 4.22. These results were obtained at an inlet velocity of 18m/s using realizable *k-ε*, SST and LES turbulence models. These figures clearly show that the wake region is dominated by the upper large vortex formed by the separation of the upper flow. Low speed regions can be located in the base wake. The velocity of the air changes within the computational domain and as expected the high velocity of the air was in the model edges, especially in the upper part of this model; between these areas there was a moderate velocity region with a little separation flow near the upper front curved surface. According to Bernoulli's equation in regions with high velocities the pressure is low and separation might occur.

Figure 4.18 shows the airflow around the Ahmed model without a flat plate. There were two main vortices behind this model; the vortex in the upper part was larger than the vortex in the bottom part because the discharge of air above this model was higher than that in the underbody. Using a flat plate below the model, as shown in Figures 4.19, 4.20 and 4.21, results in an increase in the size of the vortex in the upper part and a decrease in the lower part. Using a long flat plate in the underbody, as shown in Figure 4.22, facilitates the development of a boundary layer away from the model.

By comparing the streamline around the Ahmed model with an inlet air velocity of 18m/s obtained from realizable *k-ε* model (Figure 4.19) and the SST (Figure 4.20) simulations, it is clear that the overall results were almost similar except in the rear section, where the results of *k-ε* show the separation of airflow at the end of the slanting surface whereas the SST results show that at the start of the slanting surface. There were two main vortices in the *k-ε* model which were behind the Ahmed model between the end slanting surface edge and the end underbody edge; while, there were three main vortices in the SST model.

The largest vortex was behind the end slanting surface edge, as shown in Figure 4.20. The second vortex was near the underbody edge at the end of this vehicle model. The last vortex was over the slanting surface and the core of it near the end of this surface. The results of the LES approach were almost similar to the SST model except some streamlines especially above the roof because SST can only give a time averaged mean value for the airflow velocity. The LES was more accurate in this case because it depends on the real and not a mean velocity. The total drag will be reduced by a decrease in the magnitude and size of the wake behind the vehicles. To obtain the minimum drag a variety of slant angles were used. The intensity of the air flow also affects the total drag force.

Table 4.5 shows the drag and lift coefficients from the present study for the Ahmed model with different types of flat plate using the RANS approach. As can be seen there is a little effect the flat plate under the Ahmed model on the drag coefficient. However, the lift coefficient values are influenced by the type and size of the plate as the overall behaviour of the flow and the direction of the force compounds will be affected. Table 4.6 shows the drag coefficient using RANS and LES at 18m/s inlet velocity for the Ahmed model with a flat plate. The inlet velocity of 18m/s was used in the present numerical simulations as in experimental work of Bello-Millán *et al*. [18] to compare the results.

The drag coefficient using LES was higher than RANS because the LES approach solves large-scale fluctuating motions and uses sub-grid scale turbulence models for small scale motion, while RANS uses mean velocity. Lift coefficients for all cases using RANS and LES were very close to each other, especially with the Ahmed model without a plate as can be observed in Table 4.7. The LES approach can more accurately model the eddies behind the geometry of the car which is more important for the drag calculations rather than lift. Using the flat plate below the model obstructs the underbody airflow starting from the leading edge of the flat plate.

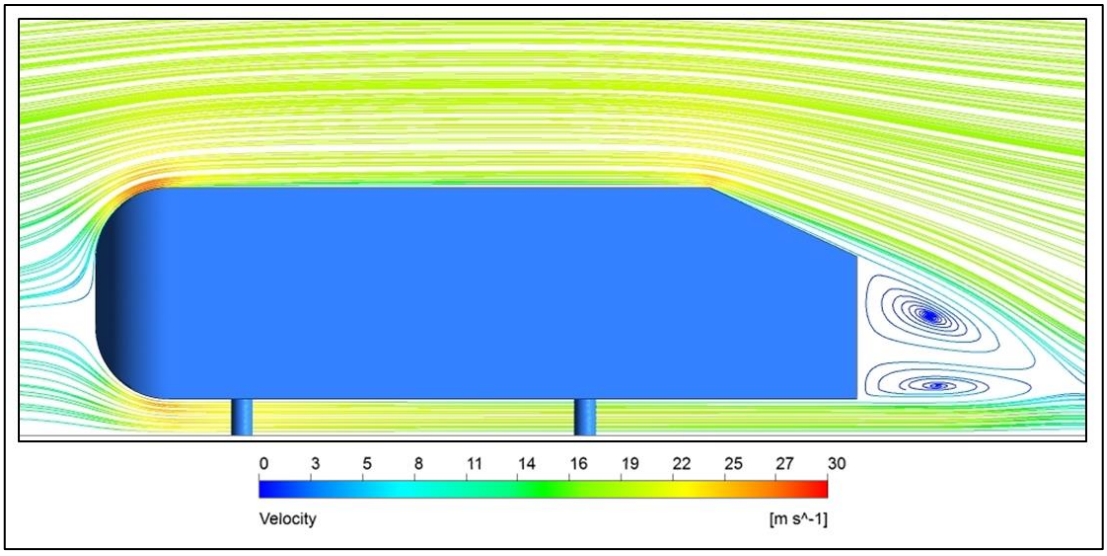

Figure 4.18: Streamline around the Ahmed model using realizable *k-ε* turbulence model and 18m/s of inlet air velocity

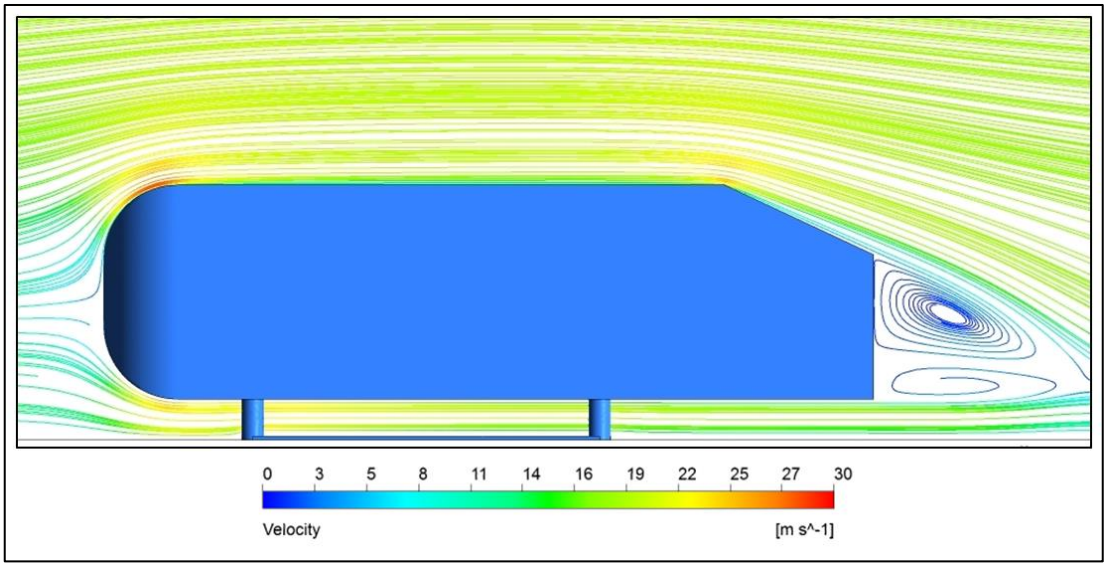

Figure 4.19: Streamline around the Ahmed model which is supported on the flat plate using realizable *k-ε* turbulence model and 18m/s of inlet air velocity

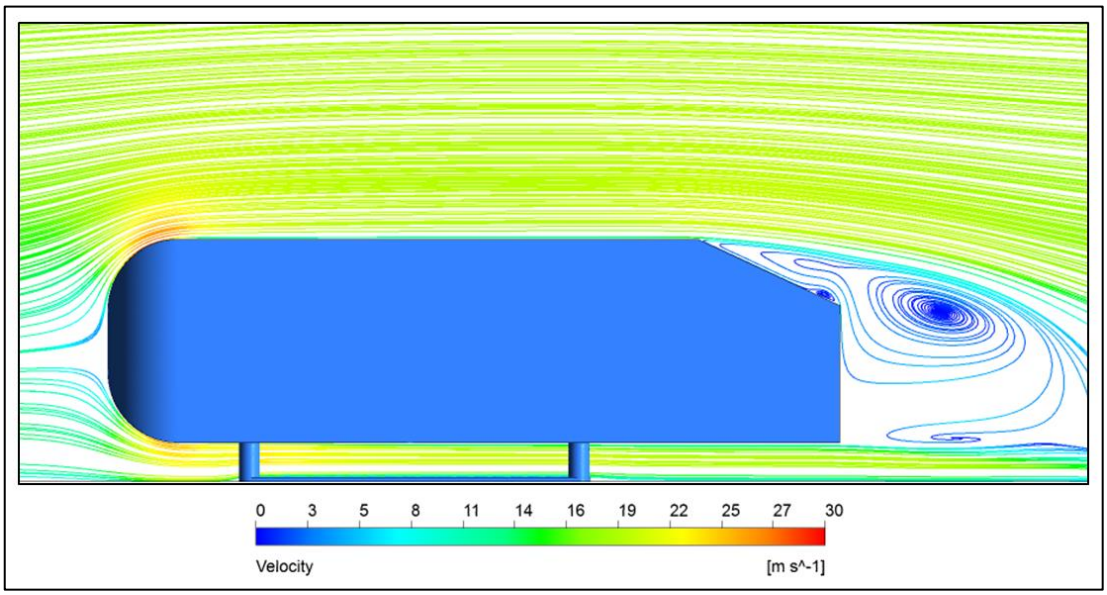

Figure 4.20: Streamline around the Ahmed model which is supported on the flat plate using SST turbulence model and 18m/s of inlet air velocity

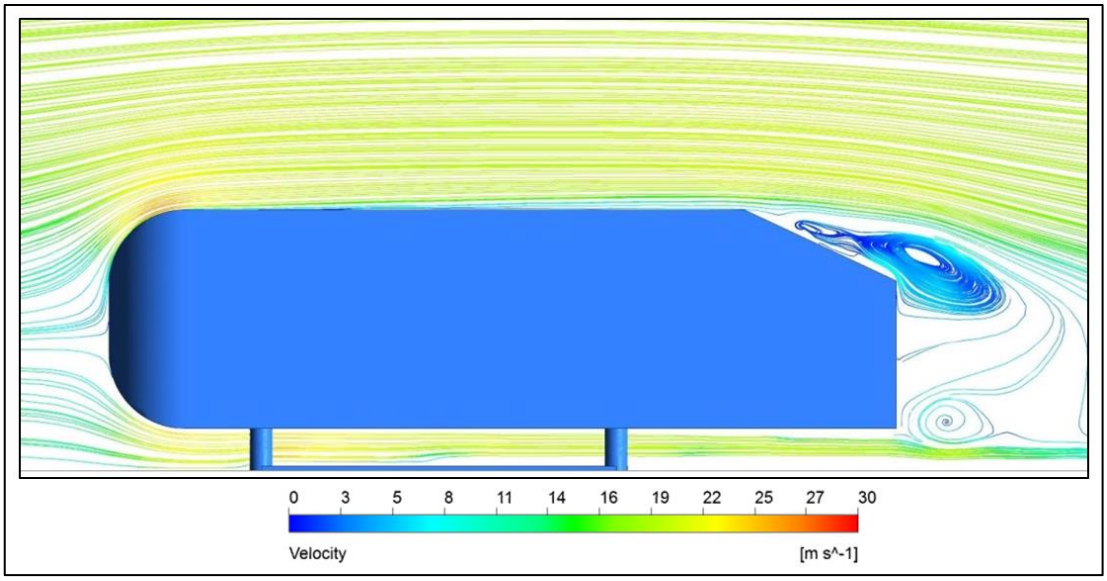

Figure 4.21: Streamline around the Ahmed model which is supported on the flat plate using LES turbulence model and 18m/s of inlet air velocity

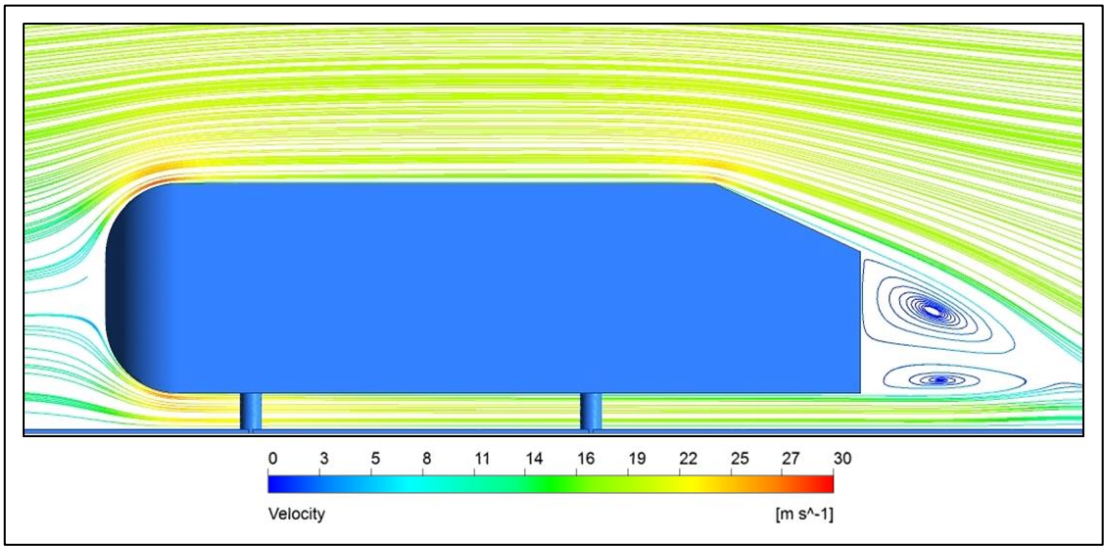

Figure 4.22: Streamline around the Ahmed model which is supported on the long flat plate using realizable *k*-ε turbulence model and 18m/s of inlet air velocity

	Ahmed model without plate	Ahmed model with standard plate	Ahmed model with long plate	Ahmed model with round long plate
C_D	0.3227	0.3247	0.3369	0.3225
C_L	0.2285	0.3846	0.6403	0.3465

Table 4-5: C_D and C_L of the present numerical results (RANS) for the Ahmed model with different cases of the flat plate

	System	Ahmed model	Plate
LES	0.4318	0.4226	0.0092
RANS	0.3391	0.3247	0.0144

Table 4-6: C_D of the present numerical results for the Ahmed model, flat plate and whole system using two turbulence models and 18m/s of inlet air velocity

	System	Ahmed model	Plate
LES	0.8732	0.3766	0.4966
RANS	0.8173	0.3835	0.4338

Table 4-7: C_L of the present numerical results for the Ahmed model, flat plate and whole system using two turbulence models and 18m/s of inlet air velocity

In the work described in this thesis the streamline at the rear part of the Ahmed model was clearly shown but our findings shows the separation flow predicted by the LES approach starts earlier than that of the RANS method. This means the LES approach predicts more drag forces because it solves large-scale fluctuating motions and uses sub-grid scale turbulence models for small scale motion. Numerical simulation can predict a very thin layer of a recirculation bubble, especially when using the LES approach. In general, all results of the turbulence models used in the Ahmed model study agree well with the experimental data. RANS approach has been widely used for aerodynamics simulations of road vehicles because this approach provides good results in a reasonable computational time. Therefore, the RANS approach will be used to simulate the Land Rover Discovery 4 in the next chapter.

4.3.6 Affect of slant angle

The length and size of the wake is the main factor that influences the drag coefficient. The wake is affected by the slant angle as it works to guide the airflow [29]. Figure 4.23 shows the drag coefficient of five cases for the 55% scale of the Ahmed model at the inlet velocity of 18m/s using RANS for different slant angles of 10°, 20°, 25°, 30° and 40°. The drag coefficient starts with the lowest value at the slant angle of 10° then increases till 30° to a maximum drag followed by a slight decrease of 40°. The lowest drag coefficient was achieved with a slant angle of 10° as shown in Figure 4.23 because this case results in a lower circulation flow over the slant surface. For the slant angle of 30° the long wake and large vortex result in a high drag coefficient. The wake was significantly larger and the low speed region behind the vehicle was also greater than that of other cases. Figure 4.24 shows the lift coefficient for the five cases. The best case for the lift coefficient was achieved for the 40° slant angle because for this angle the pressure above the slant surface was higher than other cases. Comparing the results of drag and lift coefficients for different slant angles, 10° slant angle results showed the best performance for the Ahmed body because it has a minimum drag coefficient and accepted lift coefficient.

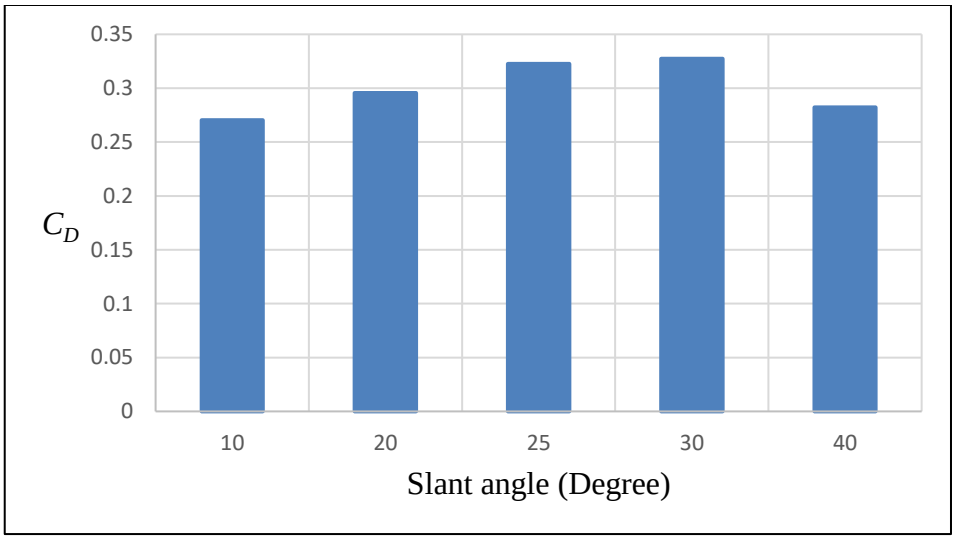

Figure 4.23: C_D as a function of the slant angle of the present numerical results for the Ahmed model using RANS and 18m/s of inlet air velocity.

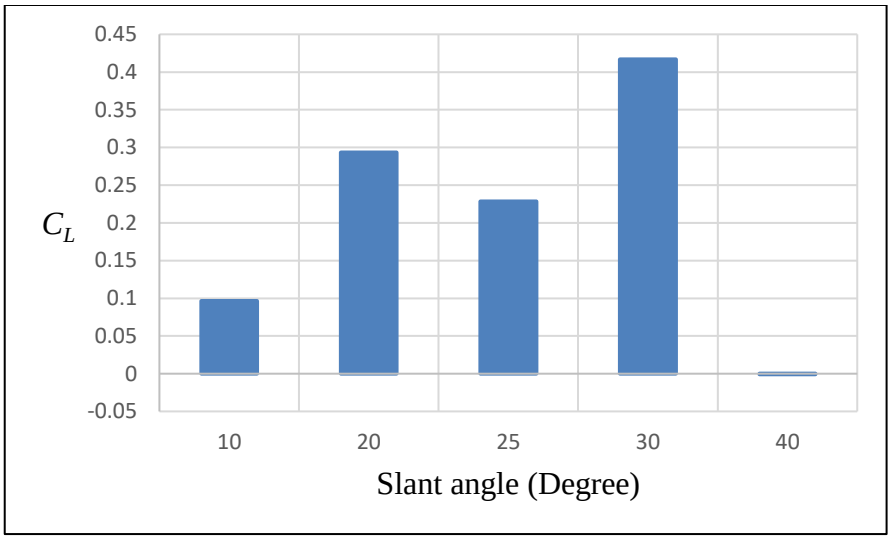

Figure 4.24: C_L as a function of the slant angle of the present numerical results for the Ahmed model using RANS and 18m/s of inlet air velocity.

The study of the effect of the slant angle on the drag and lift coefficients shows that there are three critical cases of slant angle in the Ahmed body model at 10°, 30° and 40°. The Ahmed body with 10° and 40° of the slant angle were the best cases regarding drag coefficients and lift and the worst case was with 30° of slant angle where both coefficients increase to their maximum. The drag coefficient of the full-scale model of the Ahmed body model is found to be less than that of the 55% scale model because of an increase in the friction in small model scales.

4.3.7 Effect of scale model

Table 4.8 illustrates the drag and lift coefficients of the Ahmed model for two different scales models and four different case-studies (with or without plate). Both RANS and LES turbulence models were used in the current study. The number of cells in each case together with the number of cores used are shown in the table in addition to the convergence time in hours. The maximum number of cores in the computer used throughout this work was 16 as mentioned in Table 4.8. High performance computer was used in some cases with 128 cores. It is clear that the LES method is significantly computationally more expensive than RANS, but the results were more accurate for the drag coefficient.

The drag coefficient of the Ahmed model using the RANS approach at the inlet velocity of 18m/s for the full-scale model was less than the case of the 55% scale model as there was an increase in friction for the 55% scale model. On the other hand, the lift coefficient

of the full-scale model was higher than that of the 55% scale model because the resultant pressure and shear forces can be split into the drag and lift forces.

	55% scale model				Full scale
	Without plate	With standard flat plate		With long flat plate	Without plate
Turbulence model	RANS	RANS	LES	RANS	RANS
No. of cells	4,152,869	4,458,161	13,920,537	4,576,583	4,297,802
C_D	0.3227	0.3247	0.4226	0.3226	0.31
C_L	0.3929	0.3815	0.3766	0.3465	0.3949
No. of cores	16	16	16	16	16
Iterations to convergence	700	750	380,000	750	700
Convergence time (h)	32	33	950	33	35

Table 4-8: C_D and C_L of five different cases of the Ahmed model with inlet velocity of 18m/s

4.4 Land Rover Discovery (4-SDV6 GS) domain

The popularity of this type of road vehicle has grown rapidly in recent years due to their practicality and multi-purpose use. The Land Rover Discovery is a medium-size luxury British SUV. Five generations of this SUV have been introduced; with the first production of this vehicle being 1989. The fourth generation (the so-called Land Rover Discovery 4) used in this work, launched in 2009 and was marketed in North America as the LR4. The fifth generation of this SUV was launched in 2017.

4.4.1 Numerical model of the Land Rover Discovery (4-SDV6 GS)

In this work, the Land Rover Discovery (4-SDV6 GS) was used as a benchmark model. The computational model of the Land Rover Discovery 4 was prepared in SolidWorks software. The principal dimensions being: overall length of 4.835m, overall height of 1.887m, width of 1.915m, and a wheelbase of 2.510m [14, 15]. Figure 4.25 illustrates the

three-dimensional full-sized baseline external design of the Land Rover Discovery 4 with coordinating directions. The total frontal projected area of this model is 3.011m^2.

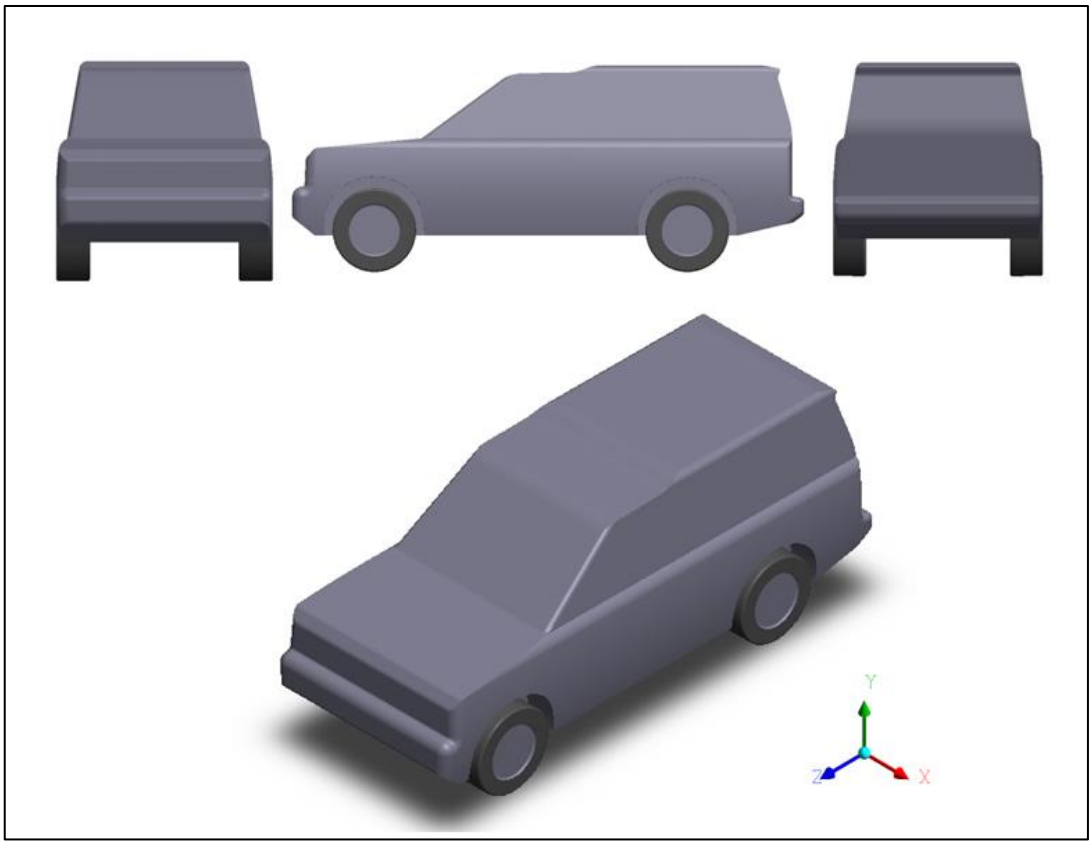

Figure 4.25: Benchmark 4-SDV6 GS

There were some differences between the real model of the Land Rover Discovery 4 and the geometrical model in the simulation. A real car contains side mirrors, rotating wheels, a set of complex geometry parts under the car, while for the simulation model used in this work was simplified. All wheels on the simulation model were stationary, similar to the model tested in the wind tunnel. A flat surface was used for the geometrical model to simplify the mesh. All simulations were conducted without side mirrors; Table 4.9 details the principal assumptions.

	Car models		
	Real	Experimental	Numerical
Rotating wheels	Yes	No	No
Flat under body surface	No	No	Yes
Side mirrors	Yes	Yes	No
Same material for all parts of the car	No	No	Yes
Constant centre of mass	No	Yes	Yes
Car engine takes some air from the front of the vehicle	Yes	No	No
Exhaust gases are injected behind the car	Yes	No	No
The distance between the road and the chassis of the car is constant	No	Yes	Yes

Table 4-9: The assumptions for real, experimental and numerical models

4.4.2 The computational domain of the Land Rover Discovery 4

The numerical simulations conducted for the Land Rover Discovery 4 used a rectangular duct as a computational domain similar to the wind tunnel (Figure 4.26). The MIRA wind tunnel was used to calculate the drag and lift coefficients [15, 101]. The aerodynamic drag force consists of two forces which are viscous and pressure forces. Viscous forces depend on the vehicle surface roughness and the total vehicle surface area. The viscous component of the drag force is variable depending on the total surface area of the car model. Pressure force depends on the pressure difference between the front and the back sections of the Land Rover Discovery 4. Wherefore, the length of the computational domain has a significant influence on the drag force.

Six different sizes of computational domain were investigated to illustrate the affect of the computational domain size. The word case-study in this section was used to describe the size of the computational domain. One of these sizes (case-study 1) has exactly the same dimensions as the MIRA wind tunnel [15, 101]. The distance from the domain's inlet to the front of the car, from the domain's outlet to the rear of the car, from the domain's top to the car roof and from the domain's side to the side of the car was variable to study the influence of these dimensions on the results. The dimensions of the baseline

model of the Land Rover Discovery were as follows: 4.835 m length, 1.915 m width, 1.887 m height [14].

To reduce the calculation time, half of the computational domain and the geometry of the car were used as the system can be regarded as symmetric. The blockage ratio in the numerical simulations was approximately between 2.4 and 9% for the Land Rover Discovery model depending on the computational domain size. The MIRA wind tunnel has a 9% blockage ratio for the full scale model of the Land Rover Discovery [15, 101] and this can cause a wall boundary layer effect. To avoid possible wall boundary layer effects, the cross-sectional area of the computational domain was set larger than in the MIRA wind tunnel. No-slip boundary condition was prescribed on the ground, roof and side walls, while null pressure was imposed at the outlet wall. A wide range of inlet velocities were used for all types of computational domain.

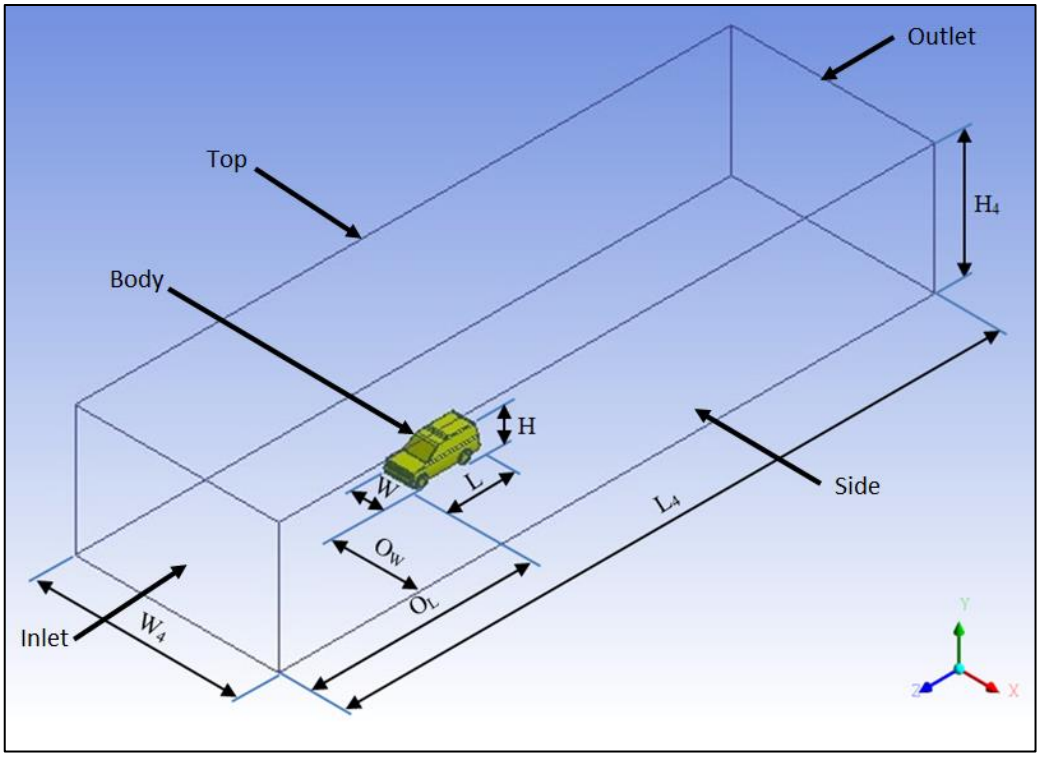

Figure 4.26: The computational domain and the full scale of the Land Rover Discovery (4-SDV6 GS)

4.4.3 Mesh and numerical set-up of the Land Rover Discovery 4

The meshing of the computational domain is a very crucial step in pre-processing. ANSYS Meshing (version 16.0 and 17.1) was used for the mesh generation with varying

levels of refinement. Optimization of mesh parameters was carried out by analysis of the mesh data. Unstructured tetrahedral cells were used throughout the global domain to cope with the geometrical complexity of the Land Rover Discovery model.

In order to generate the refined mesh to represent the model car geometry accurately, the computational domain was divided into two zones. A refined zone, referred to as Volumetric Control Regions (VCRs) with a tetrahedral mesh near the geometry were used around the vehicle to improve the overall mesh quality [91]. Three VCRs were used around the Land Rover Discovery model to control the mesh cell sizes. Figures 4.27 and 4.28 show three VCRs around the full-scale model of the Land Rover Discovery with all symbols and dimensions. The rest of the computational domain is called the global mesh.

The VCRs divide the computational domain into four zones. More attention was paid to mesh refinement behind the Land Rover Discovery model due to separation airflow and vortices. All tyres of the vehicle were stationary similar to the experimental model. The VCR1 was used around all parts of the vehicle, including tyres to accomplish a mesh refinement. Five inflation layers using first aspect ratio of 5 and the growth rate was 1.2 were used around the tyres to capture all fluid properties [91].

Table 4.10 illustrates all the dimensions and parameters of all the sizes of computational domain with VCRs for the baseline model of the Land Rover Discovery 4. The dimensions and parameters of the full-scale model of this SUV are shown in this table with the blockage ratio (the ratio of the frontal cross-sectional area of the vehicle to the front cross-sectional area of the computational domain) for baseline and modified models. *H, W* and *L* symbolize the height, width and length respectively, which were used with the computational domain and all VCRs. The subscript of *H, W* and *L* symbolizes the height, width and length respectively. The subscript of 1, 2, 3 and 4 (Figures 4.27, 4.28 and 4.29) symbolizes the first VCR, second VCR, third VCR and computational domain respectively. This table enables an analysis of the difference between the computational domain case-studies depending on their dimensions. Figures 4.29 and 4.30 show some parameters regarding the Land Rover Discovery model and the computational domain. The number of elements in the computational domain can affect the result of the computational analysis. The range of the mesh cells for half of computational domain in this study was between 8×10^6 and 16×10^6. A wide range of the total number of grids was checked to find the optimal mesh.

Inflation layers with prismatic cells were used to provide an accurate estimation of the velocity profiles near the surfaces of this vehicle as recommended by Lanfrit [91]. The prismatic growth rate for each layer was 1.2. Different mesh types and sizes were

investigated. Five to ten inflation (prismatic) layers were used for the baseline model with different techniques to reach the optimal mesh. The optimum mesh for the Land Rover Discovery model using realizable *k-ε* is shown in Figure 4.32. Three VCRs with five inflation layers were adopted for realizable *k-ε* simulations. Using first aspect ratio of 5 and the growth rate was 1.2, as recommended by Lanfrit [91]. Figure 4.31 shows half vehicle model surface mesh. The cell size near a sharp edge was smaller than the cell on the flat surface.

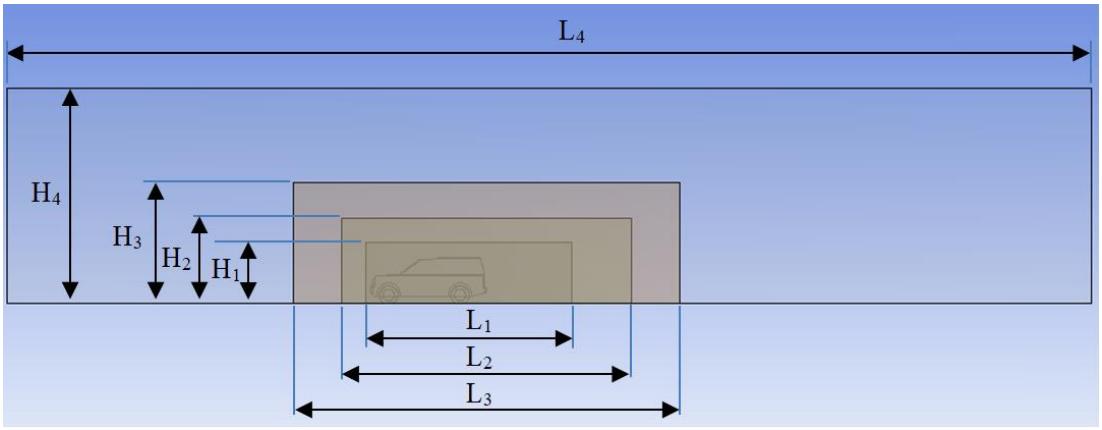

Figure 4.27: The side view of the Land Rover Discovery model in the computational domain with three VCRs

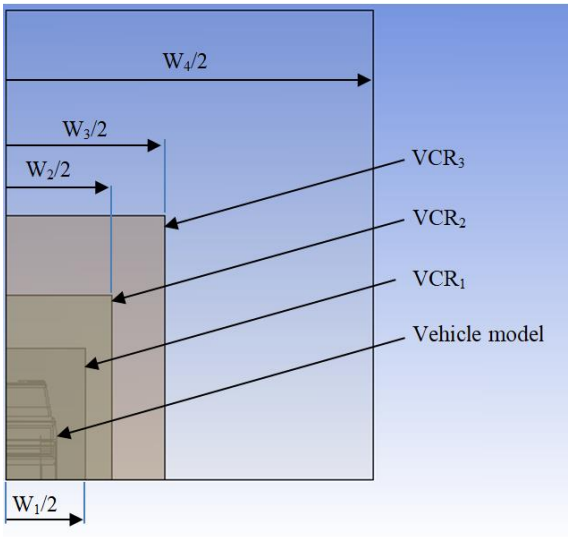

Figure 4.28: The front view of the Land Rover Discovery model in the half computational domain with three VCRs

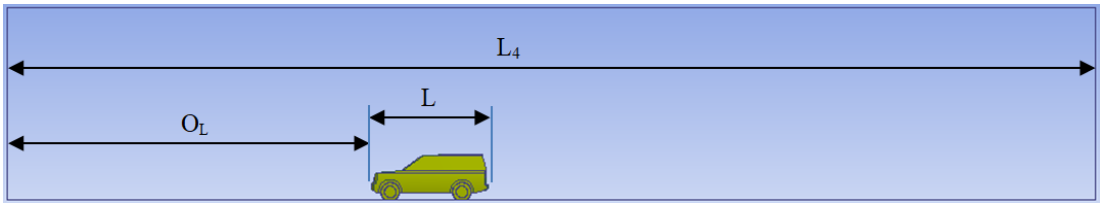

Figure 4.29: The side view of the Land Rover Discovery model in the computational domain

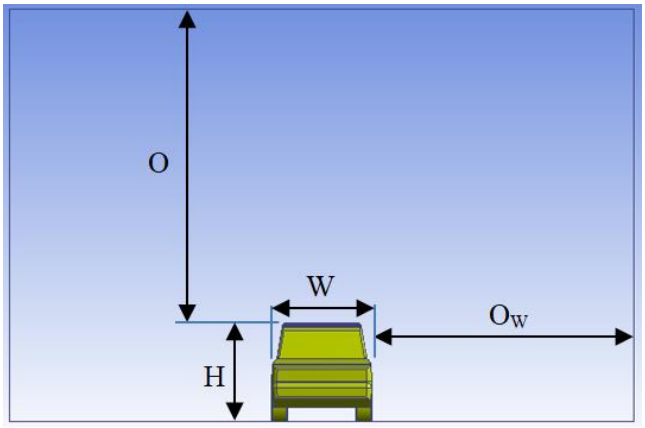

Figure 4.30: The front view of the Land Rover Discovery model in the computational domain

The inflation layers for the non-wall function turbulence models were grown using a first layer height of 0.145mm and a growth rate of 20%. Two mesh techniques were used for the Land Rover Discovery model using standard k-ω and Shear Stress Transport (SST) k-ω turbulence models, as shown in Figures 4.33 and 4.34. The y^+ value is an important parameter for all turbulence models where calculations are started from the viscous sub-layer. y^+ for the Land Rover Discovery model using first layer height was between 2 and 10 depending on its location relative to the surface of the vehicle.

		Case-study 1	Case-study 2	Case-study 3	Case-study 4	Case-study 5	Case-study 6
No. of cells		8,267,824	15,769,536	13,847,822	13,915,265	13,414,019	13,092,359
External volume (m)	H_4	4.4	7.887	7.887	9.887	7.887	8.887
	W_4	7.907	9.415	9.915	11.915	11.915	13.915
	L_4	15	20.835	24.835	29.835	30.835	40.835
VCR_3 (m)	H_3	3.4	5	5	5	5	5
	W_3	5	6	6	6	6	6
	L_3	11.5	16	16	16	16	16
VCR_2 (m)	H_2	2.8	3.5	3.5	3.5	3.5	3.5
	W_2	4	4	4	4	4	4
	L_2	9	12	12	12	12	12
VCR_1 (m)	H_1	2.2	2.5	2.5	2.5	2.5	2.5
	W_1	3	3	3	3	3	3
	L_1	6.5	8.5	8.5	8.5	8.5	8.5
Offset (m)	O_H	2.513	6	6	8	6	7
	O_W	2.996	3.75	4	5	5	6
	O_L	4	6	8	10	10	15
Vehicle (m)	H	1.887	1.887	1.887	1.887	1.887	1.887
	W	1.915	1.915	1.915	1.915	1.915	1.915
	L	4.835	4.835	4.835	4.835	4.835	4.835
Mass flow rate (kg/s)		591.386	1,263.35	1,330.442	2,004.241	1,598.812	2,103.923
Blockage ratio (%)		9.025	4.055	3.85	2.556	3.204	2.435

Table 4-10: Dimensions and parameters of the computational domain and VCRs (for all sizes of the computational domain)

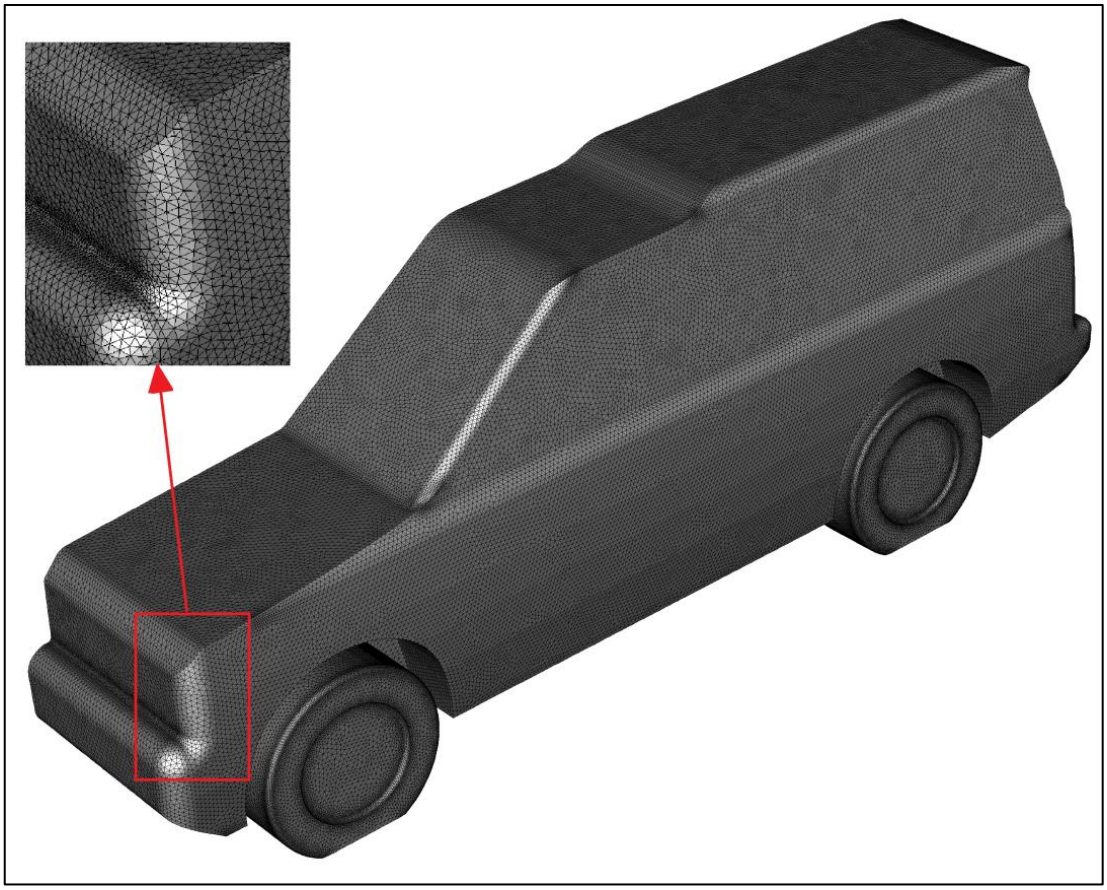

Figure 4.31: Half Land Rover Discovery model surface mesh

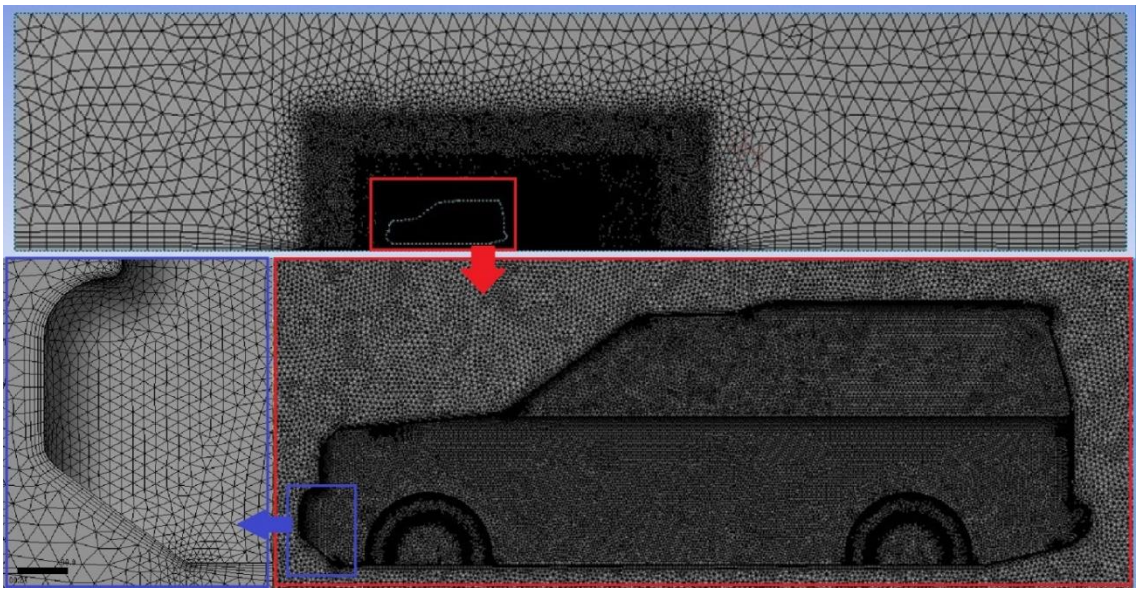

Figure 4.32: Mesh with three VCRs and five inflation layers around the Land Rover Discovery model and over the road (using first aspect ratio)

All boundary conditions used in the numerical simulations should be as close as possible to those used in the experimental method [15, 101], see Table 4.11 for details. Only boundary conditions in the numerical simulations have been chosen according to the experimental available data, see Figure 4.26 for details. A range of inlet velocities between 100km/h and 140km/h were used in this study. Stationary walls with no slip were used for the top and the side walls of the computational domain as in the experimental study. All the wheels of the car were stationary, similar to the model tested in the wind tunnel. The under-body surface was flat to simplify the geometry as well as the mesh.

Model	Inlet	Outlet	Side	Symmetry	Ground	Top	Body
Experimental study	U_∞ (100km/h)	Pressure (zero Pa)	No-slip	-	No-slip	No-slip	No-slip
Numerical study	U_∞ (100km/h - 140km/h)	Pressure (zero Pa)	No-slip	Symmetry	No-slip	No-slip	No-slip

Table 4-11: Boundary conditions used in the numerical simulations of the Ahmed body model

The second-order upwind method was applied for the momentum, turbulent kinetic energy, and turbulent dissipation rate. The second order approach was applied for the pressure in terms of spatial discretization. The upwind scheme uses the values of upstream to evaluate the property on the boundaries of the cell (each cell within computational domain) and then use them to compute the value at the centre of the cell. The main difference between the first and the second order discretisation is basically the number of points used for the computation (one upstream point for the first order and two for the second order). On the other hand, first order scheme is easy to converge while second order scheme is more difficult to converge but it is more accurate than first order scheme. Some researchers have used a first order scheme until reaching some convergence then changed to a second order scheme.

The relaxation factor was 0.25. Four turbulence models were used in the present study: Realizable k–ε, standard k-ω, Shear Stress Transport k-ω (SST) and a Reynolds Stress Model (RSM). These models have been widely applied for the aerodynamic behaviour of cars by previous researchers and would result in reasonable computational time (e.g. Guo *et al.* [33], Hu and Wong [58] used the standard k-ε turbulence model; Levin and Rigdal [9] used the realizable k–ε turbulence model; and Krishnani [3] used the standard k-ε and realizable k–ε turbulence models).

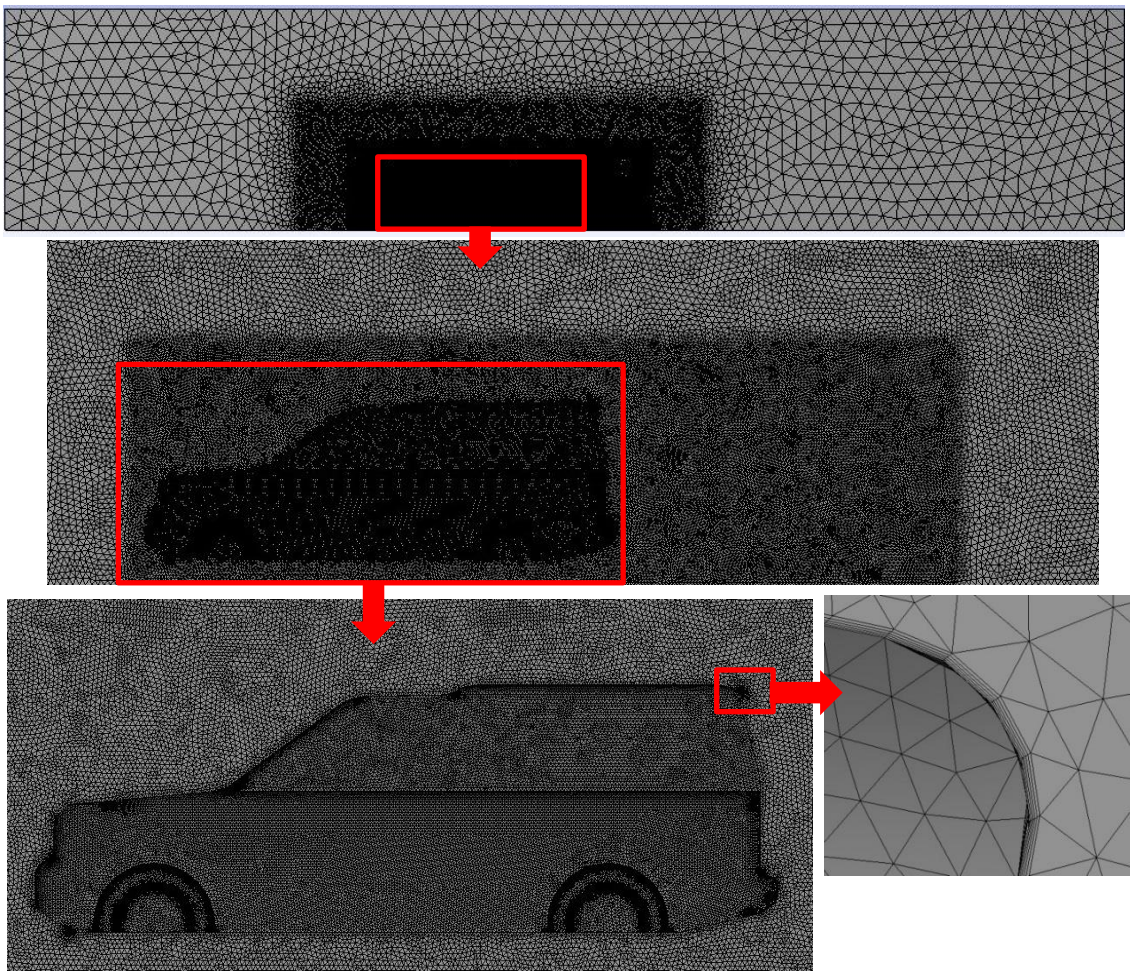

Figure 4.33: Mesh with three VCRs and five inflation layers around the Land Rover Discovery model and over the road (using first layer height)

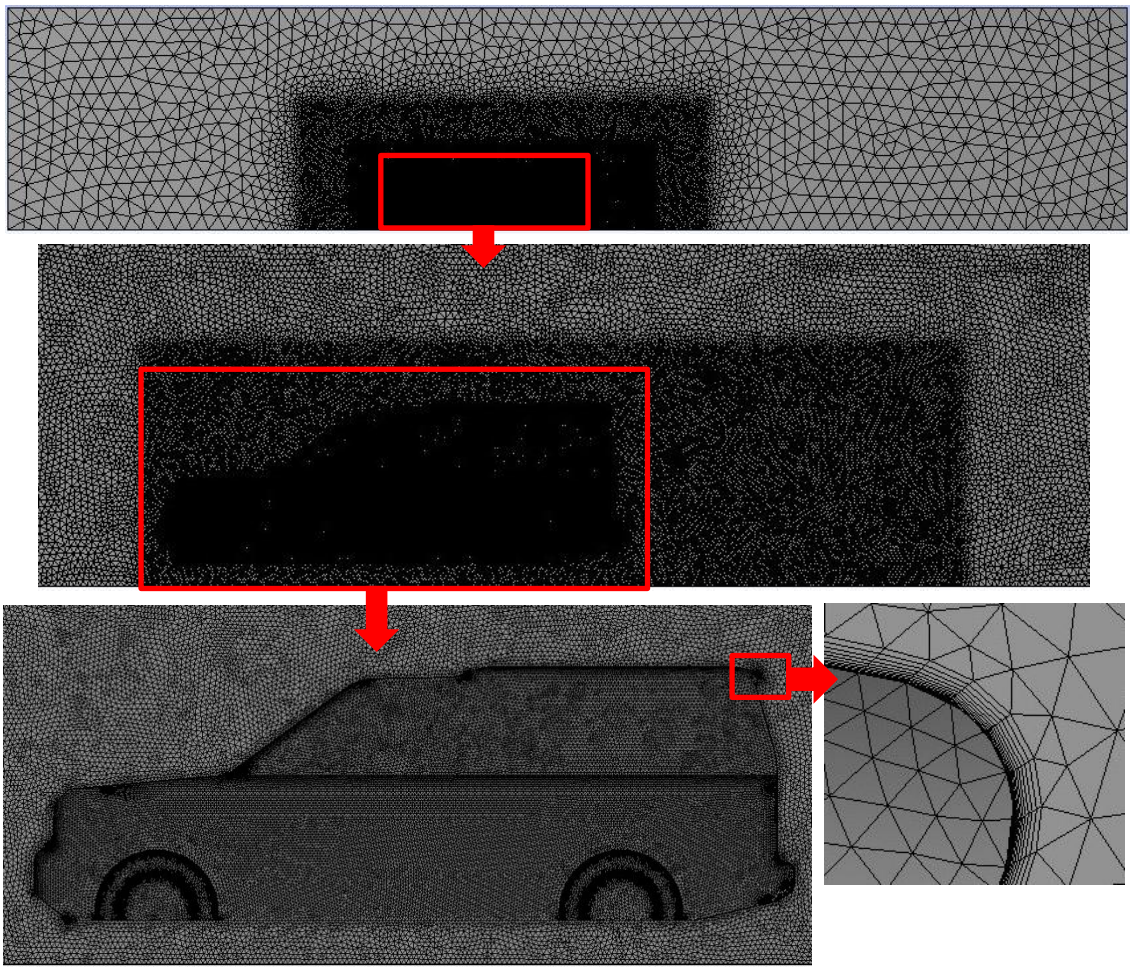

Figure 4.34: Mesh with three VCRs and ten inflation layers around the Land Rover Discovery model and over the road (using first layer height)

4.5 Modified models

Three types of add-on devices were used in this work to reduce the drag coefficient and to increase the stability of the Land Rover Discovery 4 on the road. Boat-tail on the back door of the vehicle, including a spare tyre on the back door of the vehicle acting as a fairing and vortex generators (VGs) on the end of the car roof were used as add-on devices in this work. Two types of modifications were also used for the same previous purposes. The modifications were a convergent-divergent ditch on the car roof and non-straight base bleed.

4.5.1 Boat-tail

Boat-tail was used in some previous studies as an aerodynamic device of tractor-trailer to reduce the drag coefficient [43, 51, 53]. This device can be used for SUV with inclined

plates instead of vertical plates in heavy vehicles. Figure 4.35 shows multi views of the boat-tail on the back door of the vehicle that were used in the Land Rover Discovery model as an aerodynamic device to improve the aerodynamic behaviour. Different dimensions and angles were used for this device to investigate the best aerodynamic design (Table 4.12).

As mentioned earlier in the study of the Ahmed model, the lowest drag coefficient was achieved with a slant angle of 10°. Therefore, the angle of the boat-tail between 8° and 14° was tested to achieve the optimal design. To keep the overall length of this vehicle less than 5 m, L_{bt} between 0.24 and 0.25 was investigated. Other dimensions were selected depending on the external design of this vehicle such as the width. Figure 4.35 shows all dimensions of this device; the red colour represents boat-tail. The overall length of this model was 4.965 m and meaning this model was longer than the benchmark by 0.13 m.

Case	Φ_{bt} (°)	L_{bt} (m)
1	8	0.24
2	10	0.24
3	12	0.24
4	14	0.24
5	16	0.24
6	18	0.24
7	14	0.245
8	14	0.25
9	14	0.244
10	14	0.246
11	14	0.243
12	14	0.247

Table 4-12: 12 different cases of the boat-tail model

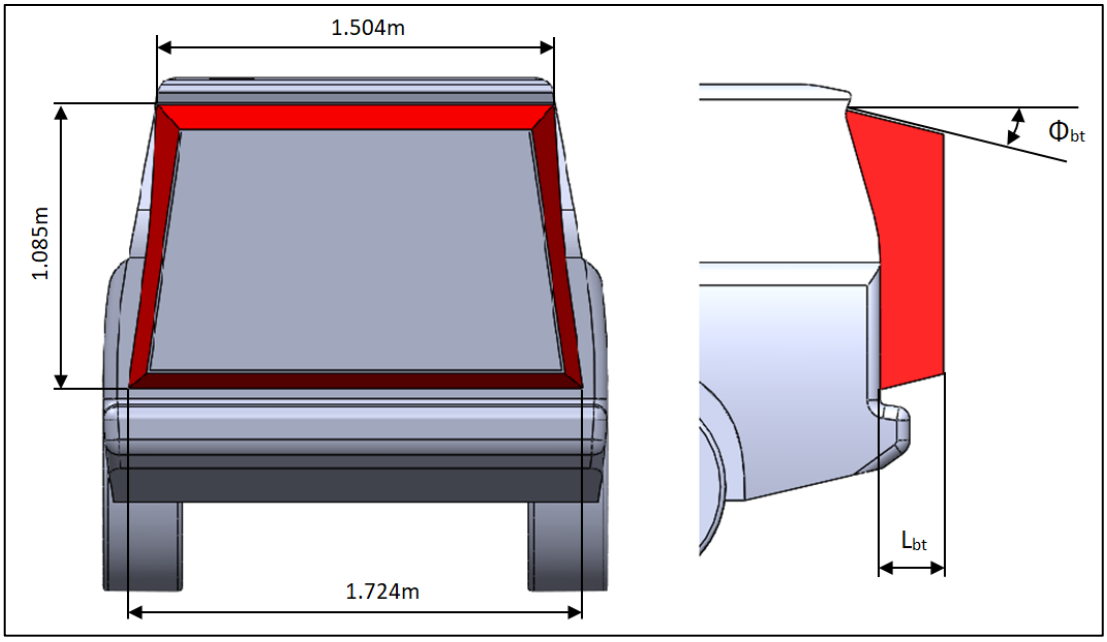

Figure 4.35: The boat-tail model of the Land Rover Discovery with all dimensions

4.5.2 Spare tyre

Leuschen and Cooper [51] tested different add-on aerodynamic components on a Class-8 tractor-trailer. Some of these aerodynamic devices can be used for SUV with suitable modifications such as inflatable boat-tail. Putting a rear screen on the back door of the SUV was used by Rohatgi [65] as an aerodynamic device to reduce the drag coefficient. Rear fairing was used by Rohatgi [65] as an attached device to improve the drag coefficient. All the previous techniques work to cover some wake area. Therefore, putting a spare tyre on the back door of the Land Rover Discovery was proposed in the current study as a fairing for the same purpose. The aerodynamic behaviour can be improved by using fairing especially at the rear section.

The dimensions and position of the tyre are very important to achieve the best design regarding the drag and lift coefficients. Figure 4.36 shows multi views of the model with spare tyre. The same dimensions of the standard tyre of the Land Rover Discovery 4 were used to avoid extra costs. Multi-positions were investigated to obtain the optimal aerodynamic position (Table 4.13). The position of the spare tyre was investigated from the upper surface of the rear bumper until 55mm above the first position to avoid any affect on the visibility of the passengers. Figure 4.37 shows the parameterized position of the spare tyre. The overall length of this model was 5.035 m meaning the model was

longer than the benchmark by 0.2 m and longer than the boat-tail model by 0.07 m. This model can provide more storage space in the boot.

Case	L_{st} (m)
1	1.075
2	1.080
3	1.085
4	1.090
5	1.095
6	1.100
7	1.105
8	1.110
9	1.115
10	1.120
11	1.125
12	1.130

Table 4-13: Twelve different cases of the spare tyre model

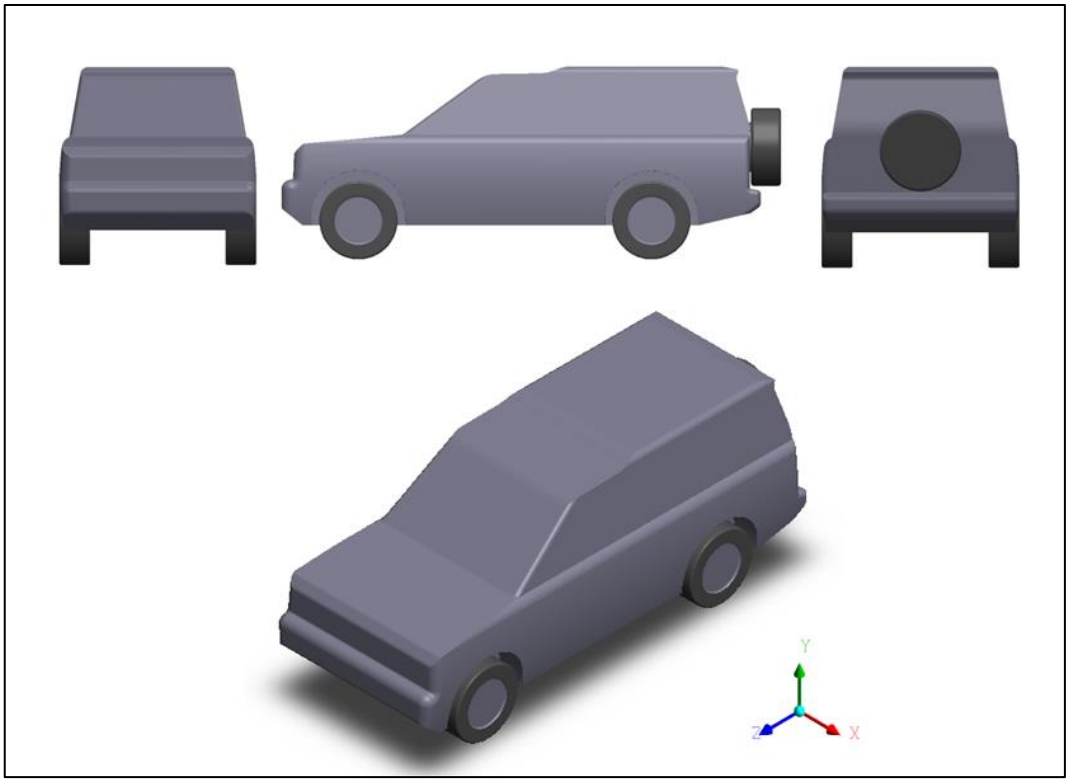

Figure 4.36: The spare tyre model of the Land Rover Discovery 4

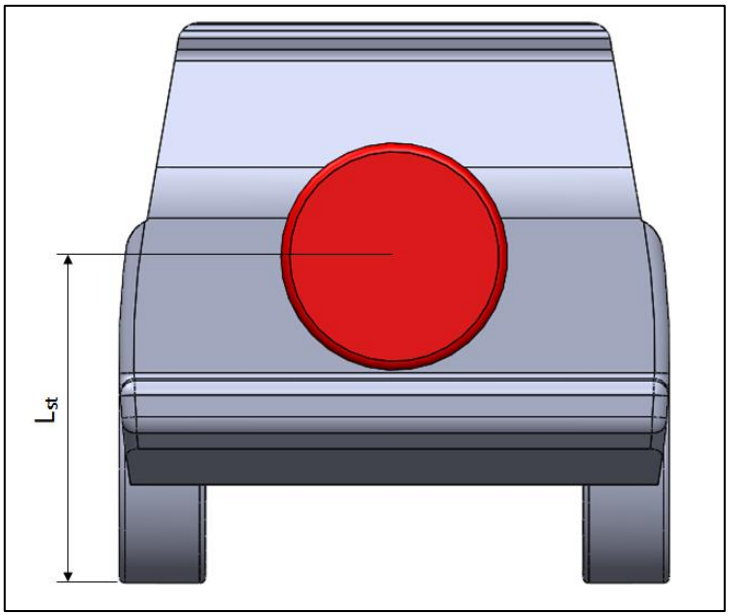

Figure 4.37: The position of the spare tyre model for the Land Rover Discovery 4

4.5.3 Vortex generators

Leuschen and Cooper [51] used Vortex Generators (VGs) on a Class-8 tractor-trailer to create different passages between these VGs. Koike *et al*. [57] used VGs on a saloon car to reduce drag coefficient. Different shapes and sizes of VGs were used by previous researchers, but there were no VGs as aerofoil geometry. Convergent-divergent passages can be created by using VGs as aerofoil geometry. This technique can improve the pressure above the end roof of the car as well as behind it. Therefore, VGs as aerofoil geometry at the end roof of the Land Rover Discovery were investigated in this work to improve the aerodynamic behaviour.

Thirteen diffuser fins at the end of the roof of the Land Rover Discovery 4 formed twelve convergent-divergent air passages, in addition to the two on both sides. These VGs were placed near the separation regions with the main objective of providing controlled flow separation thereby improve the aerodynamic behaviour. This type of add-on device is widely used, especially in tractor-trailers and sports cars. In the present study, the new shape and dimensions were investigated in addition to their location. Twelve different cases were investigated (Table 4.14) to achieve the lowest possible drag and lift coefficients.

Koike *et al*. [57] tested three different heights of VGs (15, 20 and 25mm) for a sedan car. While Leuschen and Cooper [51] used 60mm as a constant height of VGs for a Class-8 tractor-trailer. In the current study, four different heights (30, 40, 50, 60mm) were investigated for the Land Rover Discovery 4 (Table 4.14). The position of the VGs was investigated for a similar range to the study performed by Koike *et al*. [57].

Figure 4.38 shows the VGs at the end of the roof on the Land Rover Discovery 4. Figure 4.39 showing salient dimensions of the VGs. The overall length of this model was similar to the benchmark, but the overall height was higher by 0.05m. All VGs in Figures 4.38 and 4.39 are indicated in red for illustrative purposes. The total frontal projected area of this model was 3.036m^2.

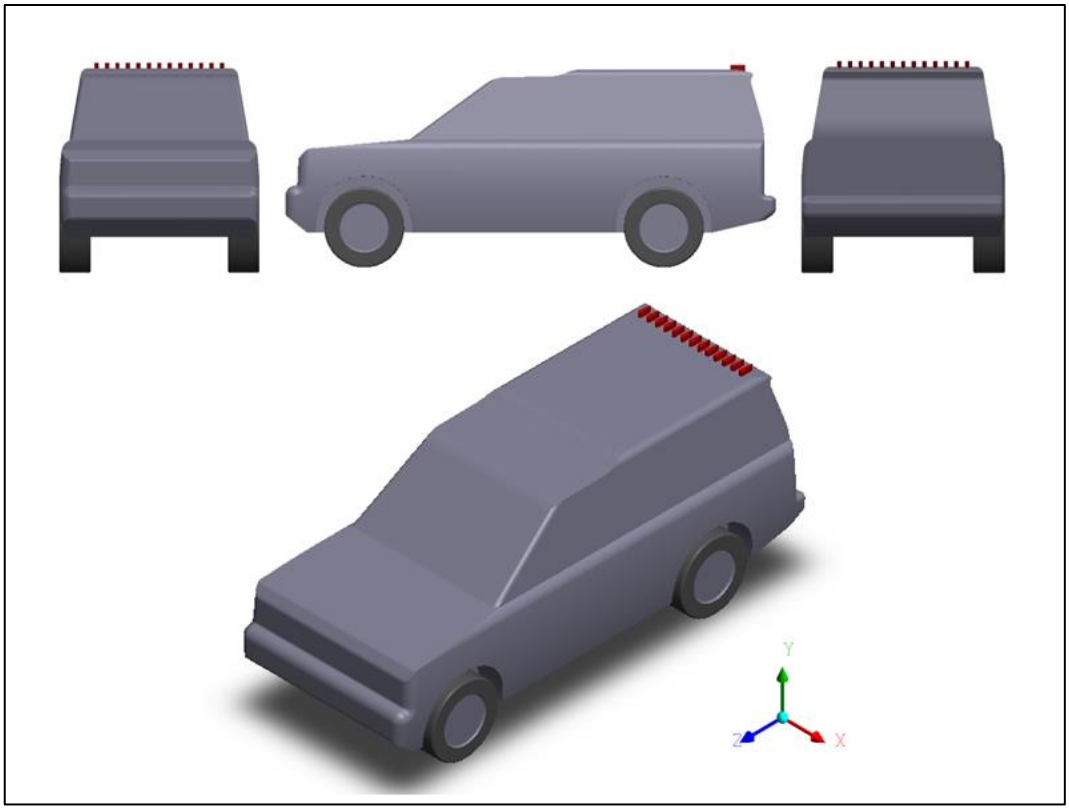

Figure 4.38: The vortex generators model of the Land Rover Discovery 4

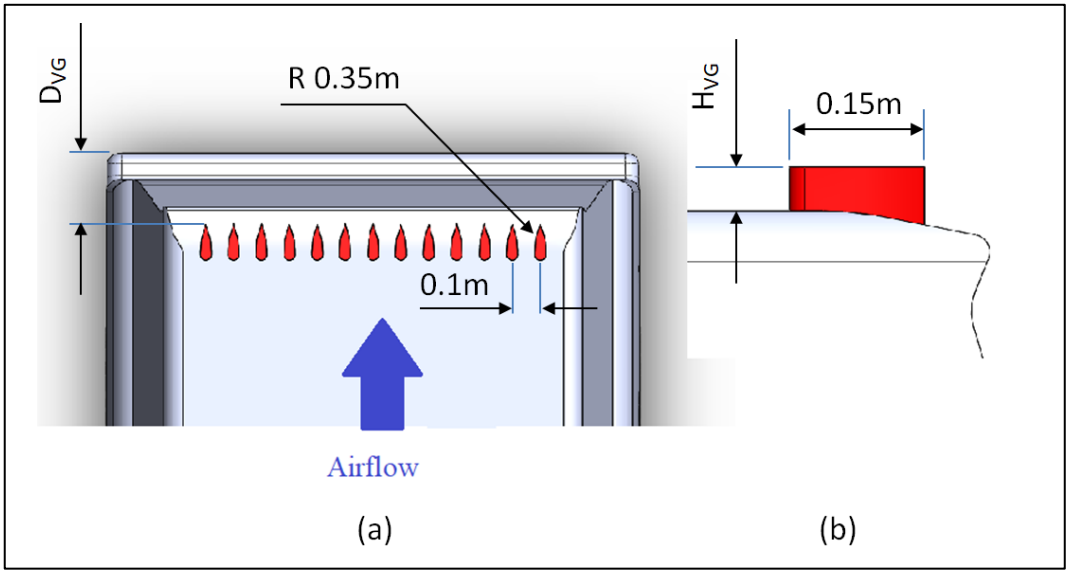

Figure 4.39: The optimal VGs model for the Land Rover Discovery with all dimensions. (a) Top view; (b) Side view

Case	D_{VG} (m)	H_{VG} (m)
1	0.25	0.03
2	0.25	0.04
3	0.25	0.05
4	0.25	0.06
5	0.3	0.03
6	0.3	0.04
7	0.3	0.05
8	0.3	0.06
9	0.35	0.03
10	0.35	0.04
11	0.35	0.05
12	0.35	0.06

Table 4-14: Twelve different cases of the VGs model

4.5.4 Roof ditch

Roof deflector used on a Class-8 tractor-trailer by Leuschen and Cooper [51] to guide the air over the roof. Kang *et al*. [59] used a diffuser device under the rear bumper to reduce air resistance. Roof deflector was used to improve the drag coefficient of the tractor-trailer while diffuser under sedan model was used to increase the pressure behind the car. The two previous aerodynamic modifications were employed in this work to create a new convergent-divergent ditch on the roof.

The roof modification was used to investigate possible in the aerodynamic behaviour specially to increase the pressure above this vehicle. Other authors have not studied this type of modification, convergent-divergent ditch on the roof of the car. This aerodynamic drag reduction technique is shown in Figure 4.40.

The depth of the ditch was 50mm to avoid any adverse effects on passenger comfort. To decrease the number of simulations a constant width (0.5m) for the convergent-divergent ditch in the middle of the roof was used. Different inlet and outlet dimensions for the

ditch were then investigated. The dimensions of the inlet and the outlet of the ditch were chosen depending on the manufacturing limitations.

Eighteen different cases were investigated (Table 4.15) thereby obtain an optimum aerodynamic design of the ditch. The inlet of the roof modification was set between 0.8312m and 0.8326m decreasing to 0.5m, with the outlet varying between 1.1 m and 1.2m with a depth of 50mm (Figure 4.41). The overall length, width and height of this model are similar to the benchmark model though the total frontal projected area used in the drag coefficient calculations, was 2.986m^2 which is less than the projected frontal area of the benchmark model.

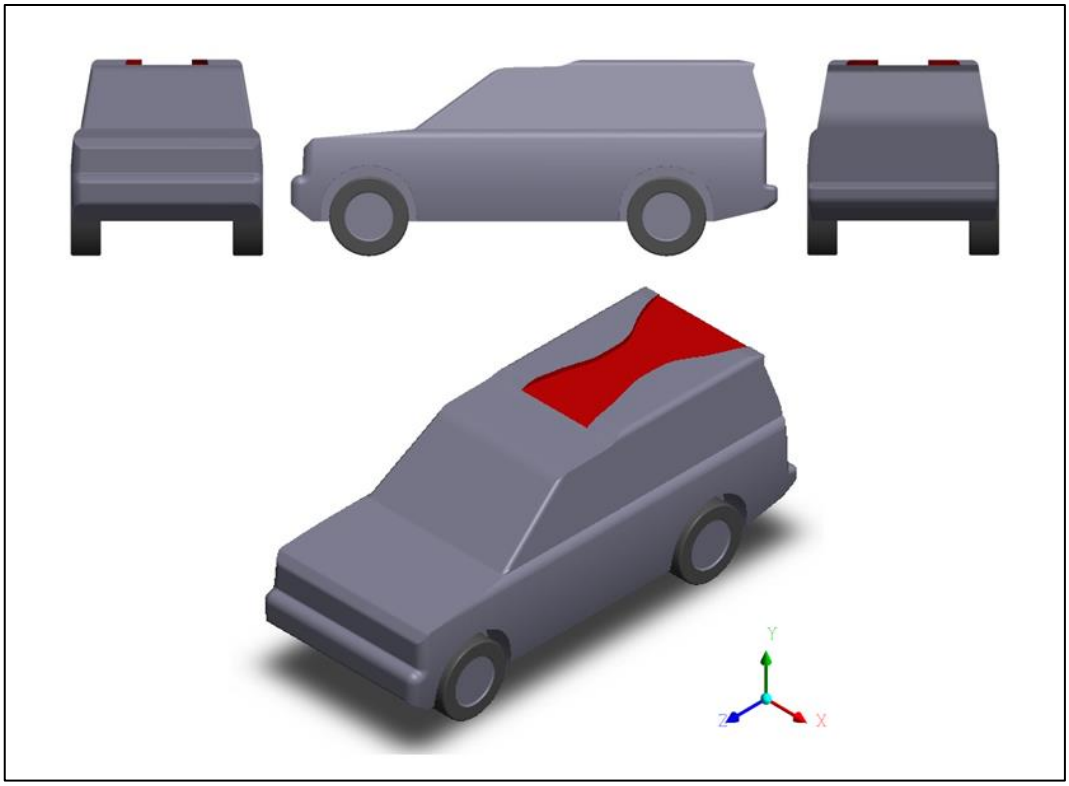

Figure 4.40: Ditch on the roof of the Land Rover Discovery 4

Case	D_{in} (m)	D_{out} (m)
1	0.832	1.1
2	0.832	1.2
3	0.832	1.15
4	0.832	1.18
5	0.832	1.181
6	0.832	1.182
7	0.832	1.183
8	0.832	1.184
9	0.832	1.1835
10	0.832	1.1834
11	0.832	1.1836
12	0.8322	1.1834
13	0.8324	1.1834
14	0.8326	1.1834
15	0.8318	1.1834
16	0.8316	1.1834
17	0.8314	1.1834
18	0.8312	1.1834

Table 4-15: Eighteen different cases of the ditch model

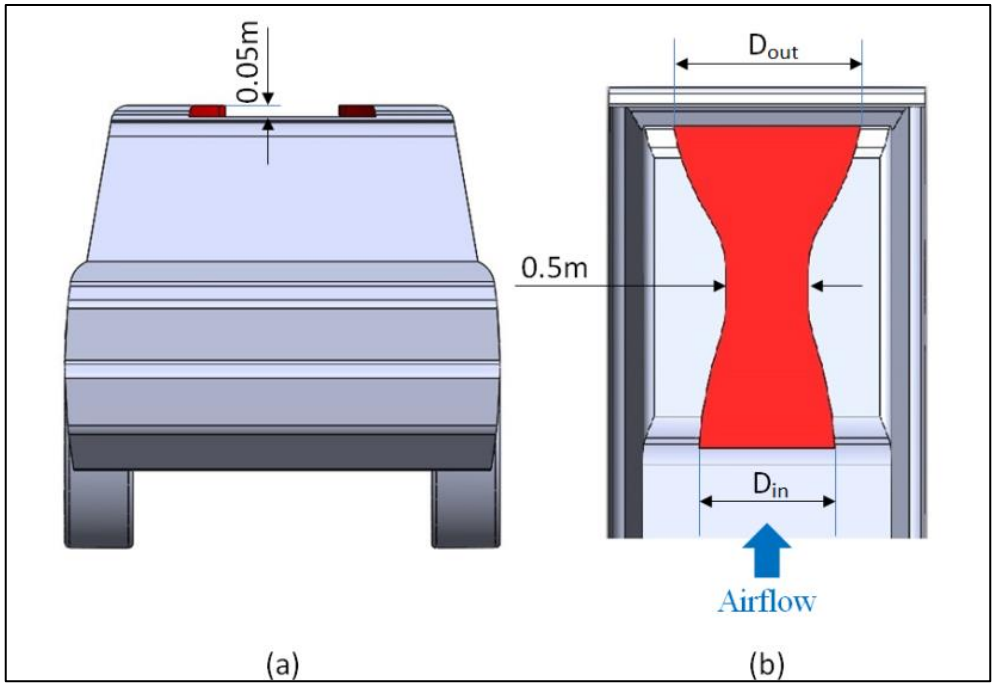

Figure 4.41: The ditch model for the Land Rover Discovery 4 with dimensions (a) Front view; (b) Top view

4.5.5 Base bleed

A base bleed system of the two converging ditch tubes was used by Sivaraj and Raj [61] to decrease air resistance. Brown *et al*. [48] used a straight base bleed for the SUV to reduce the drag coefficient. These modifications affect the comfort and visibility of the passengers. Therefore, the new design of base bleed was investigated in this work. The cross-sectional area and the path of a base bleed design were changed along the length of the car as not to adversely effect the capacity and comfort of the car.

Figure 4.42 shows the base bleed used in this work. This technique leads to a reduction in the drag aerodynamics and vortices behind the car in addition to cooling the engine and other facilities. Base bleed has three different cross-sectional areas. The first cross sectional area was at the front of the vehicle and has the same dimensions as the grill. The second cross sectional area was in the middle having the same dimensions of the gear box space. The final cross-sectional area was at the rear of this vehicle with a range of different dimensions depending on the space between the spare tyre underbody and cargo box.

The cross-sectional area and the path of the base bleed changed along the length of the car to avoid adverse effects on capacity and comfort. Sixteen different cases were

investigated (Table 4.16) to achieve an optimum design. The cross-sectional area of the optimal design of the base bleed was chosen as below: at inlet 0.2277m^2 then 0.0998m^2 in the middle of the car and 0.0599m^2 at the outlet. The total frontal projected area of baseline on this model was 3.011m^2. It should be noted that in reality the suggested base bleed would go through the engine, gear box, drive shaft and axle. In the current study, the existence of the base bleed was simulated as part of a proof of concept study with little detail about the aforementioned components. Figure 4.43 shows dimensions of the base bleed for the Land Rover Discovery 4.

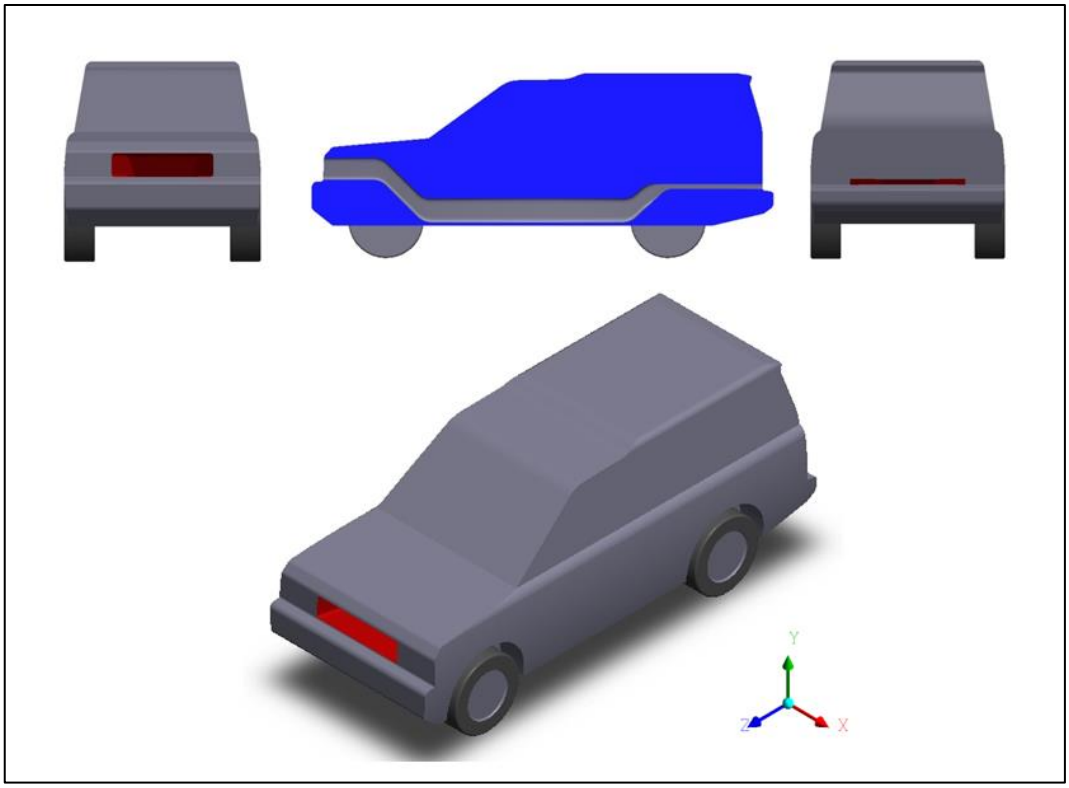

Figure 4.42: Base bleed for the Land Rover Discovery (4-SDV6 GS)

Case	D_{out} (m)	H_{out} (m)
1	1	0.04
2	1	0.05
3	1	0.06
4	1	0.07
5	1.1	0.04
6	1.1	0.05
7	1.1	0.06
8	1.1	0.07
9	1.2	0.04
10	1.2	0.05
11	1.2	0.06
12	1.2	0.07
13	1.3	0.04
14	1.3	0.05
15	1.3	0.06
16	1.3	0.07

Table 4-16: Sixteen different cases of the base bleed model

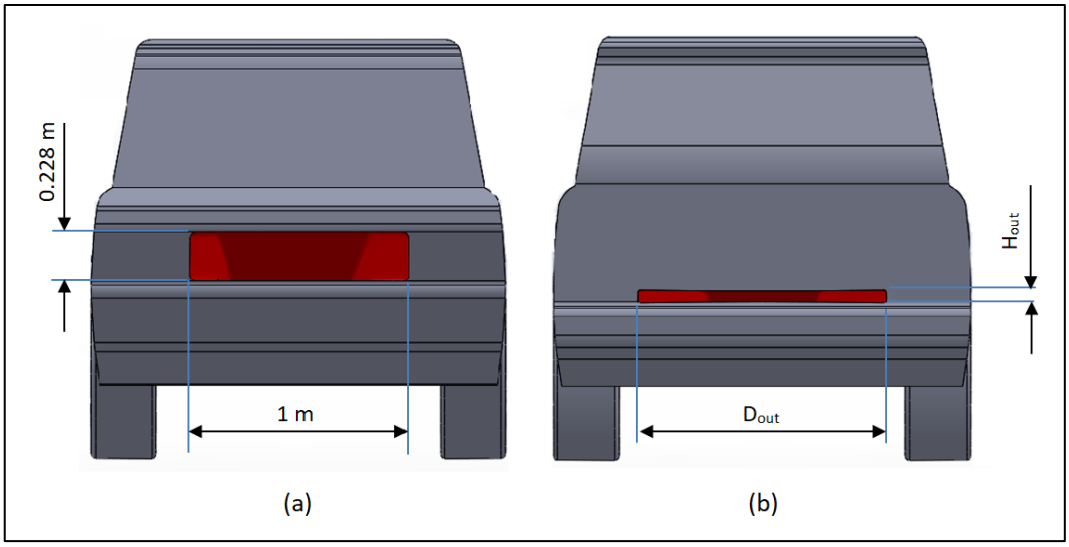

Figure 4.43: The dimensions of the base bleed for the Land Rover Discovery (a) Dimensions of inlet section; (b) Dimensions of outlet section

4.6 Modified models meshes

The computational domain of all modified models was divided into multi zones. Three VCRs were used to control the mesh cell's size (Figure 4.44). Unstructured tetrahedral cells were used for all modified models to cope with the geometrical complexity of the main body and the so-called add-on devices. First aspect ratio of 5 was used for all modified models of the Land Rover Discovery 4, as recommended by Lanfrit [91].

The growth rate was 1.2 for all modified models (*ibid*). Five Inflation layers with prismatic cells were used around all modified models (Figure 4.45) and at the road surface (Figure 4.44) to provide an accurate estimation of flow properties near the surfaces of the vehicle and road. The range of the mesh cells for half of computational domain of modified models was between 13×10^6 and 14×10^6. The optimum mesh for all modified models of the Land Rover Discovery 4 using first aspect ratio of 5 is shown in Figure 4.46. y^+ for all modified models used an aspect ratio less than 300 depending on its location relative to the surface of the vehicle as shown in Figure 4.47.

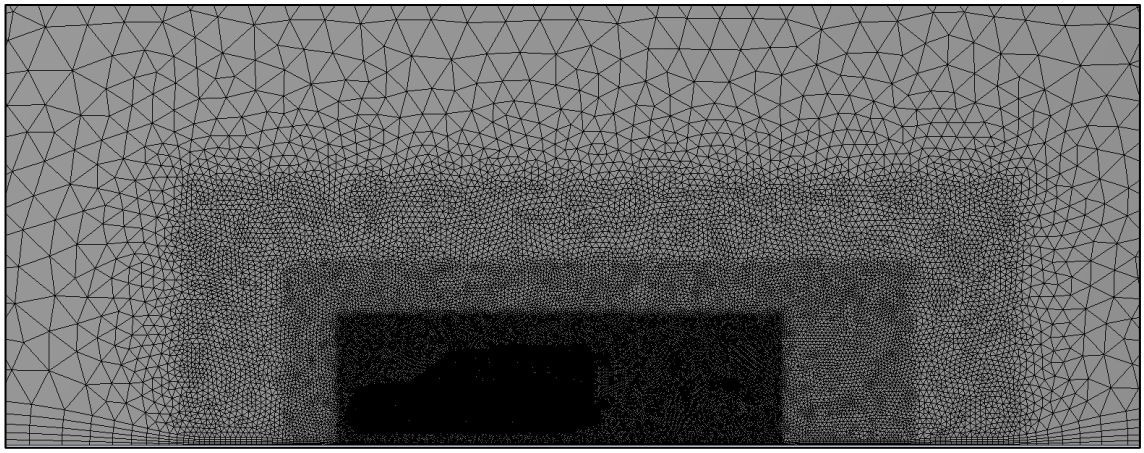

Figure 4.44: Mesh with three VCRs and five inflation layers around the vehicle model and over the road using first aspect ratio

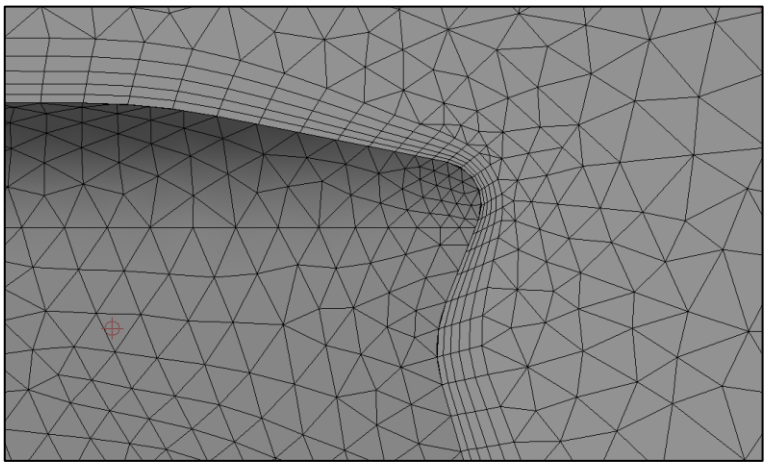

Figure 4.45: Five inflation layers around the vehicle model (this close-up at the end of the roof of the Land Rover Discovery 4)

(a)

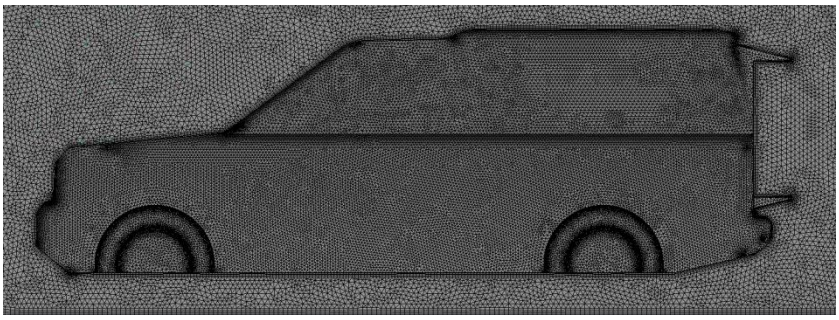

(b)

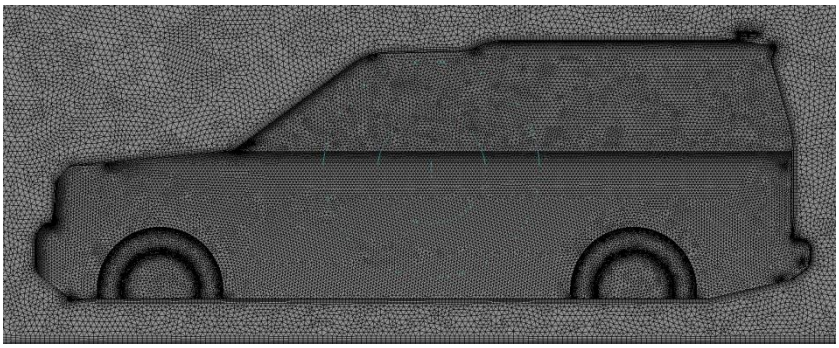

(c)

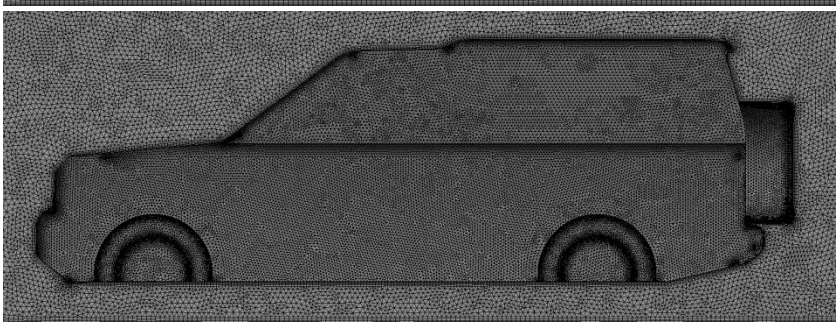

(d)

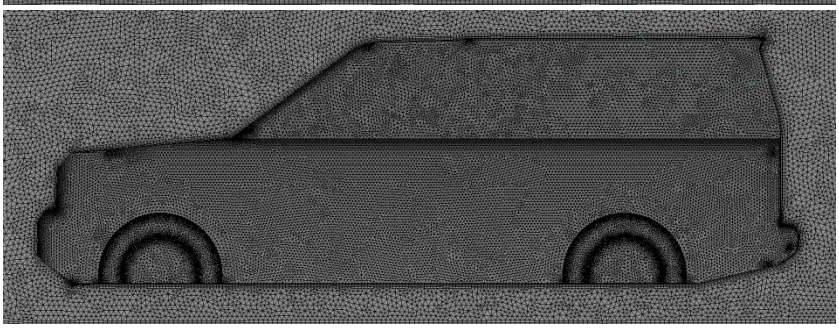

(e)

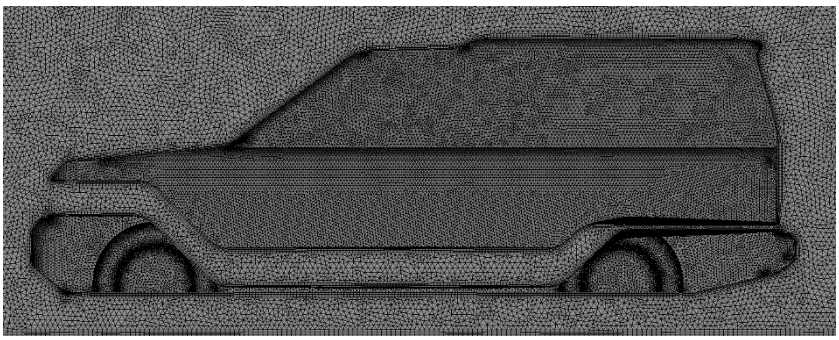

Figure 4.46: Mesh around the modified models of the Land Rover Discovery 4 (a) Boat-tail; (b) VGs; (c) Spare tyre; (d) Ditch on the Roof; (e) Base bleed

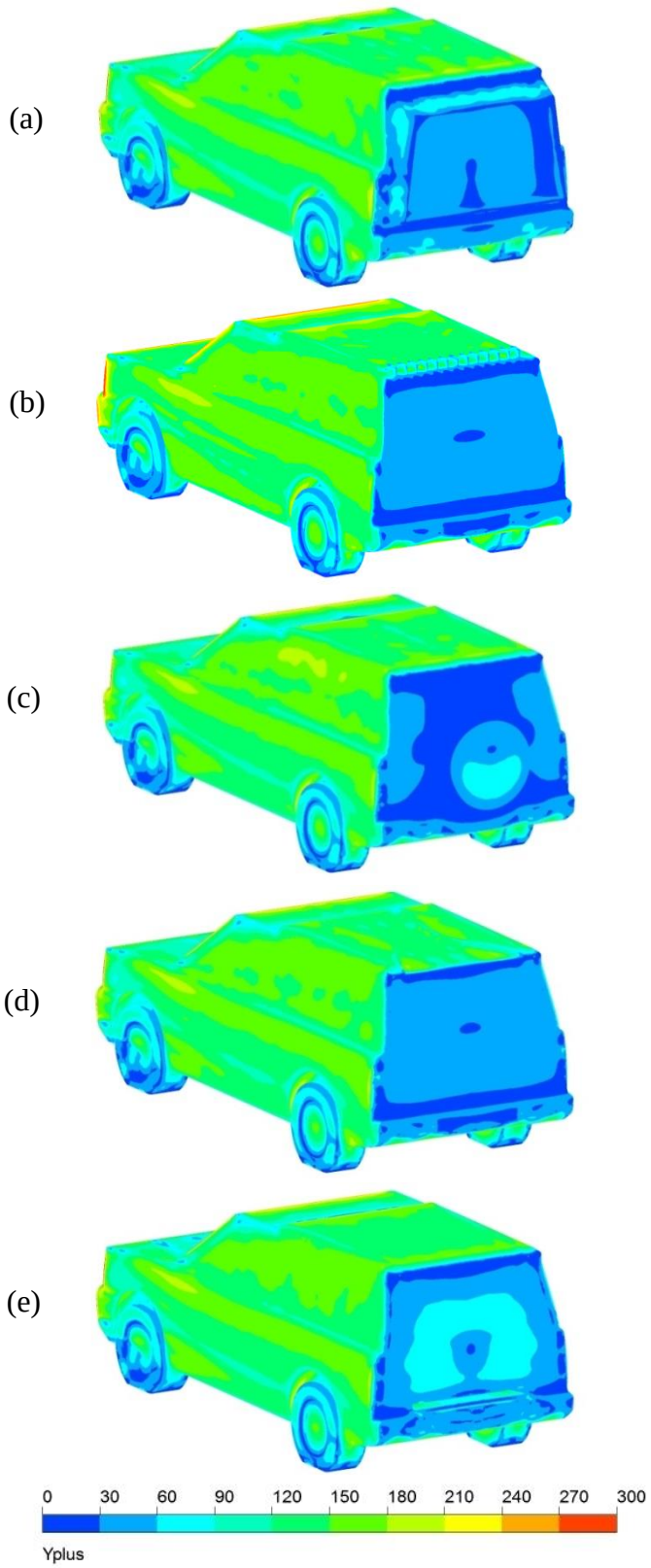

Figure 4.47: y^+ on the modified models surface (a) Boat-tail; (b) VGs; (c) Spare tyre; (d) Ditch on the Roof; (e) Base bleed

4.7 Summary

A wide range of the inlet air velocity was used to study the effect of Reynolds number on the drag coefficient. Increasing in Reynolds number leads to decrease in the drag coefficient. The drag coefficient decreases with increasing Reynolds number in all cases using both RANS and LES approaches.

No attention has been paid to the effect of the flat plate under the Ahmed model on the measurements which was the biggest problem in the aerodynamics of vehicles. The flat plate under the Ahmed body causes a change in the velocity distribution underbody and affects the lift force and this should be taken into account for aerodynamic study of the Ahmed body. This leads to air swirls behind the vehicle and the separation flow was produced by the slant angle in the rear part of this model. The total drag force depends on the size and magnitude of the wake behind the vehicles.

Chapter 5 Results

The results of the numerical simulations of the baseline (benchmark) model of the Land Rover Discovery 4 and all modified models are described in this chapter. The effect of the computational domain and mesh refinement on the aerodynamic behaviour of the benchmark model is presented first. To reduce computational effort, half of computational domain and geometry were used as the system is regarded as symmetric in these simulations. Six different sizes of computational domain were used to study the effect of it on the aerodynamic behaviour. The software used in this study was ANSYS Fluent (version 17.1) and the simulations were specified as pressure based with different turbulence models. Four types of turbulence models were investigated (realizable k-ε, standard k-ω, Shear -Stress Transport k-ω and Reynolds Stress Model) in order to access the most appropriate.

5.1 Grid dependency

The optimal number of cells was obtained by the sensitivity analysis. Figure 5.1 shows a grid dependency analysis for a standard computational domain (Case 6, see section 4.2.3., Table 4.10 for details) using the realizable k-ε turbulence model. It can be seen that the number of mesh influences the drag coefficient calculation until about 13 million cells for half of the computational domain and geometry, beyond which no significant mesh dependency is observable. The number of mesh cells for these simulations was therefore chosen between 13 and 15 million.

Turbulent models were investigated using the numerically calculated by comparing forces acting on the body of the car and the velocity around the body. The pressure coefficient and velocity of air on a point behind the Land Rover Discovery 4 were tested to access the convergence (Figures 5.2 and 5.3). The velocity of this point was varied as a pulse until 200 iterations, beyond which no vary velocity can be observed. This procedure was carried out to check the influence of the iteration number on the results. Figure 5.4 shows convergence equations (continuity, velocities in three dimensions, k and epsilon) for the baseline using a realizable k-ε model. After 700 iterations, the solution of these equations no longer changes. All residuals of velocities (x, y and z) decreased to less than 10^{-6} while k and epsilon residuals decreased to less than 5×10^{-4}. Continuity residual decreased to less than 5×10^{-3}.

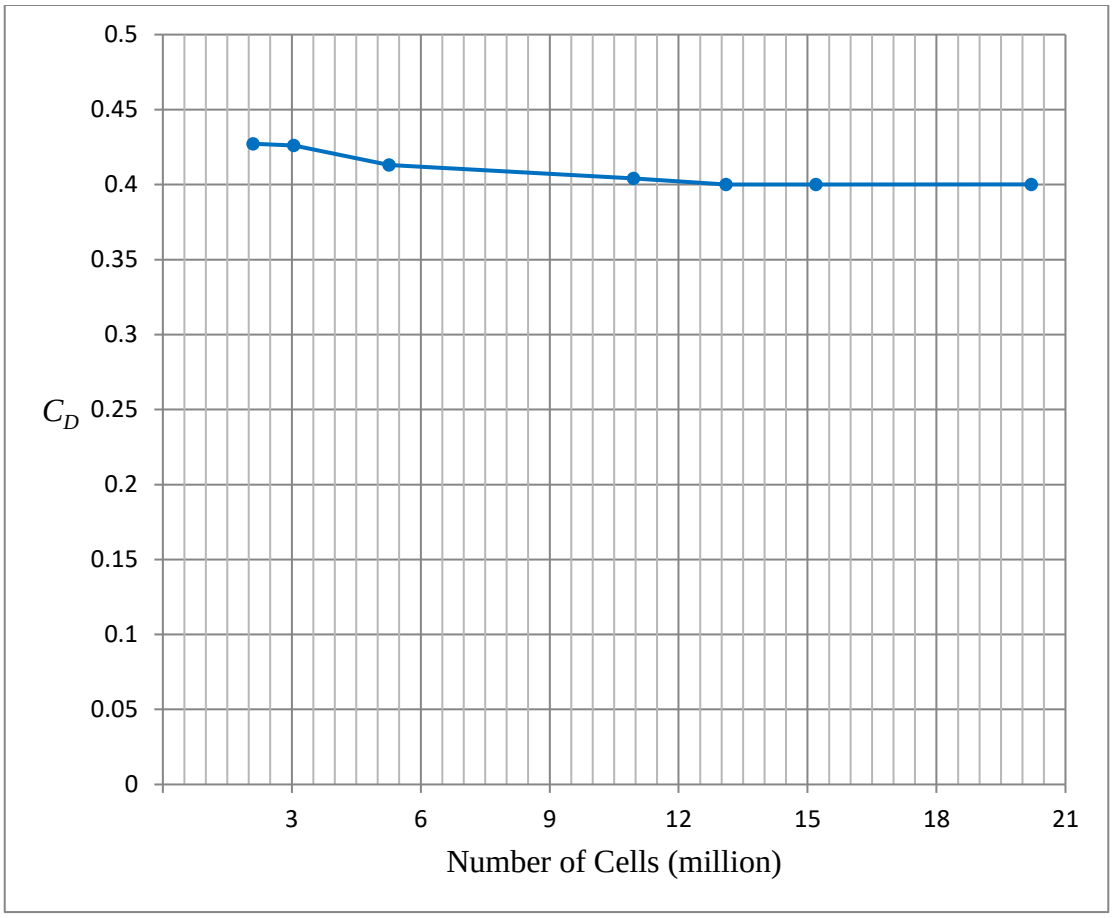

Figure 5.1: Grid dependency for the realizable *k*-*ε* model

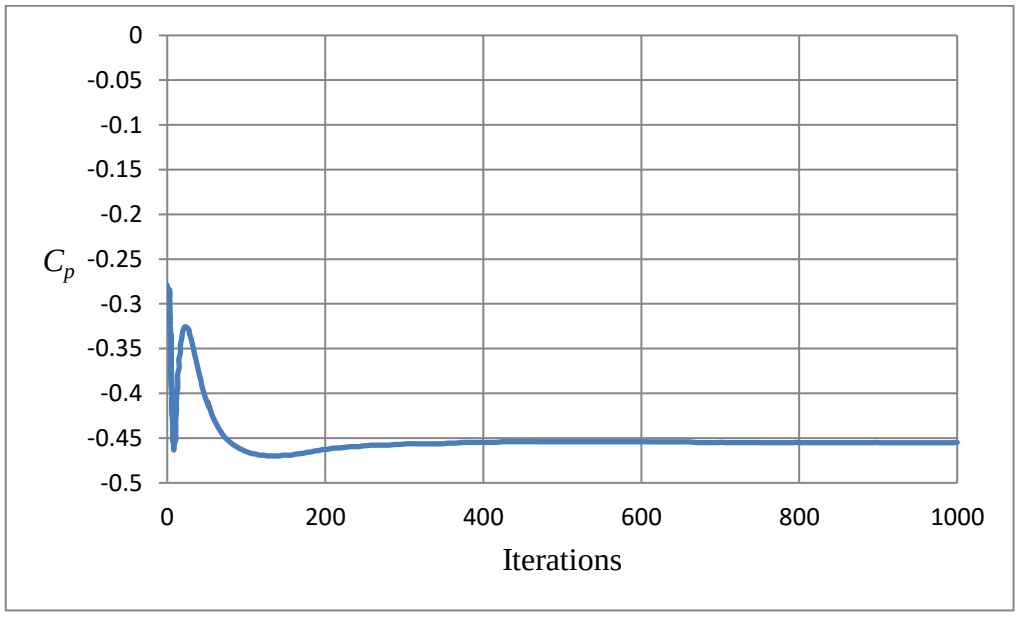

Figure 5.2: Convergence history of the pressure coefficient on a point at wake zone

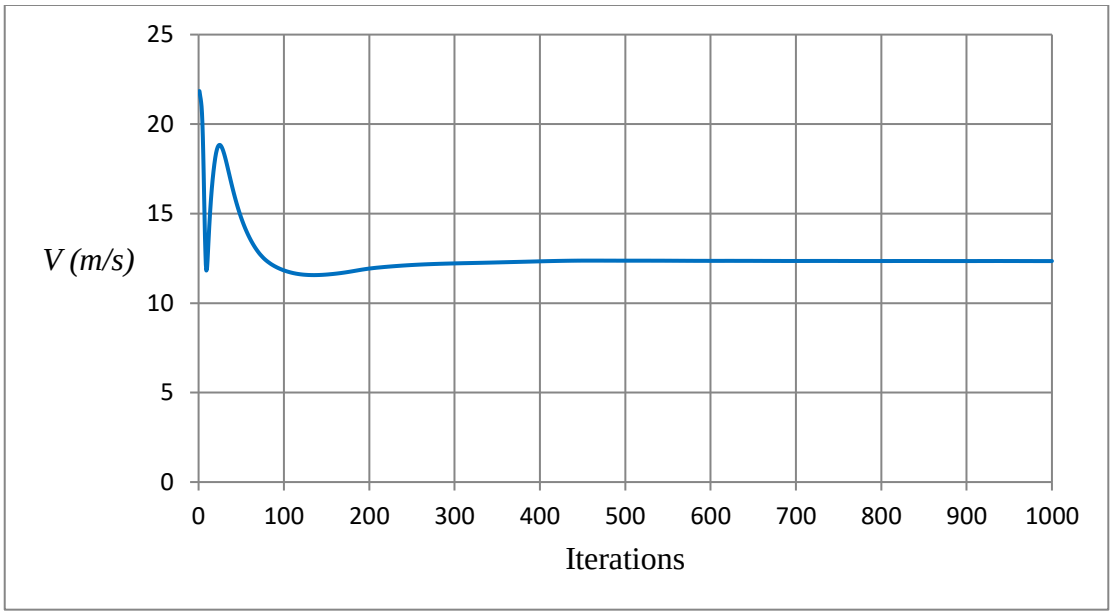

Figure 5.3: Convergence history of velocity magnitude on a point at wake zone

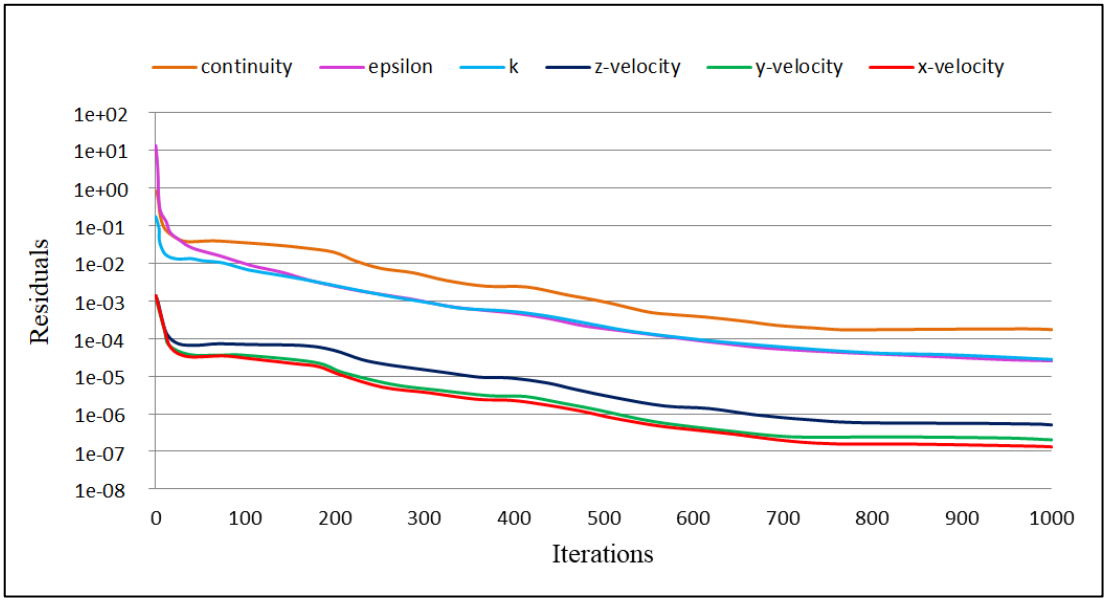

Figure 5.4: Residuals of equations

5.2 Validation of CFD analysis

Numerical simulations were performed on the benchmark using the same dimensions and boundary conditions of the wind tunnel which was experimental investigation [15, 101]. The drag coefficient obtained from modelling of the baseline model was compared with the experimental data [14, 15] as shown in Table 5.1.

Table 5.1 shows the experimental and numerical drag coefficients of the baseline model of the Land Rover Discovery (4-SDV6 GS) using four types of turbulence models. All these results were obtained at an inlet velocity of 27.7m/s (100km/h) and with the test section area of 15m (length) × 7.9m (width) × 4.4m (height). All types of turbulence models provided good agreement with the experimental data as shown in Table 5.1, but the result of the realizable k–ε was the closest. The minimum percentage error was 7 for the realizable k–ε and the maximum was 8.75 for the Shear Stress Transport k-ω. The y^+ value is an important parameter for the SST turbulence model because this type of turbulence model does not use wall treatment. The y^+ for the Land Rover Discovery 4 was high (between 2 and 10) because the complexity of this geometric shape and this could make the % error for SST to be higher than other models. However, for Ahmed body where the shape was less complex, more accurate y^+ was achieved, which led to a less % error.

	Experimental data	**ANSYS Fluent results**			
		Realizable k–ε	Standard k-ω	SST k-ω	Reynolds Stress Model
C_D	0.4	0.428	0.431	0.435	0.371
Percentage Error (%)		7	7.75	8.75	7.25

Table 5-1: Validation of numerical results

Figure 5.5 shows the drag coefficient for the baseline model of the Land Rover Discovery 4 using four types of turbulence model. The drag coefficients obtained from all turbulence models were close to the experimental data, which was 0.4, but the result of realizable k–ε was relatively closer to the experimental data. As can be seen from Figure 5.5 the calculated drag coefficient did not vary much after 400 iterations for all turbulence models.

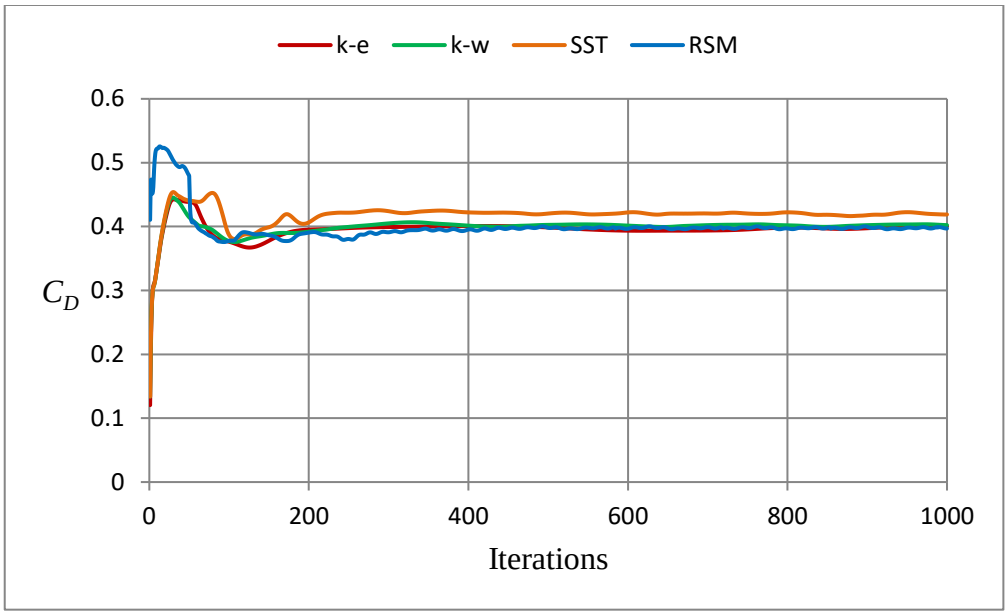

Figure 5.5: C_D for the benchmark model of the Land Rover Discovery 4 using four types of turbulence model

5.3 Effect of the computational domain size

The total drag force consists of the viscous and pressure forces. Viscous forces depend on the total surface area of the car body in addition to the surface roughness while pressure force depends on the pressure difference between the front and the back of the body. Figure 5.6 shows the drag force and its components for the Land Rover Discovery 4 using six different sizes of computational domain. Obviously, the viscous component of the drag force was almost constant for all sizes of computational domain because it depends on the total surface area of the car model, which was constant. The pressure component of the drag force decreases with increasing of computational domain dimensions especially the distance in front and behind the car. There is little difference between the drag force for Cases 4 and 6. The computational domain in Case-study 6 (see Table 4.10 for details) was used as the standard size in this study.

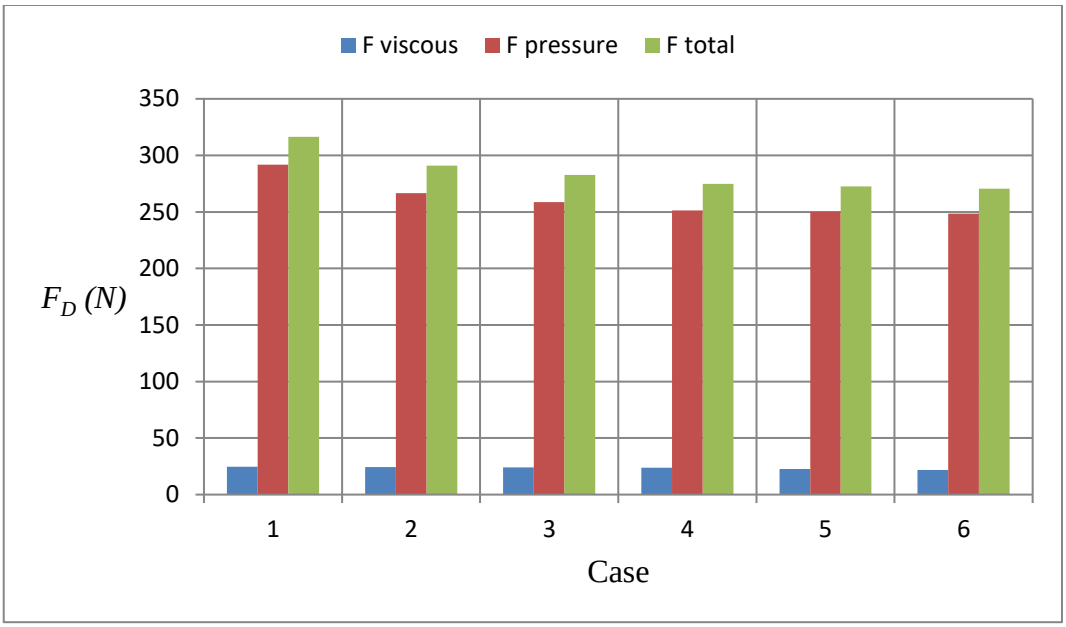

Figure 5.6: The drag force and its components for the baseline model using six different sizes of computational domain

The MIRA wind tunnel had a 9% blockage ratio for a full-scale model. Six different types of test section area were used in this work to evaluate the affect of the test section area on the aerodynamic behaviour (Table 4.10). One of these (Case-study 1) was exactly MIRA wind tunnel dimensions. Figure 5.7 shows the mass flow rate at an inlet velocity of 27.7m/s (100km/h) inside each type of these computational domains. The mass flow rate increases with decreasing of blockage ratio as shown in Figure 5.8.

Case 1 (MIRA wind tunnel) had a lowest mass flow rate, which was 591.38 kg/s because of the low cross-sectional area (17.38m^2). This means, Case 1 had the highest blockage ratio (9.025%). Cases 2 and 3 had the same height with a little difference in width and the blockage ratios were 4.05% (1263.35kg/s) and 3.85% (1330kg/s) respectively. Cases 4 and 6 had the closest blockage ratios, which were 2.55% (2004.24kg/s) and 2.43% (2103.92kg/s) respectively. Case 5 had the same dimensions as Case 4 except for the height, which was 7.887m instead of 9.887m (in Case 4).

The blockage ratio of Case 5 was 3.2% (1598.81kg/s). The car model inside the computational domain causes blocking of the air flow. The average velocity of air in the instant closeness of the car model was increased, especially at a small cross-sectional area of the computational domain (high blockage ratio). As a result, the drag and lift coefficients were influenced by the blockage ratio as shown in Tables 5.2 and 5.3. Figure 5.9 shows the drag coefficient for a wide range of blockage ratio as in Table 5.2. It is

better to use the lowest blockage ratio to avoid the blockage effect, especially with numerical investigation because no expensive equipment is needed. Figure 5.9 shows the drag coefficient for a wide range of blockage ratios.

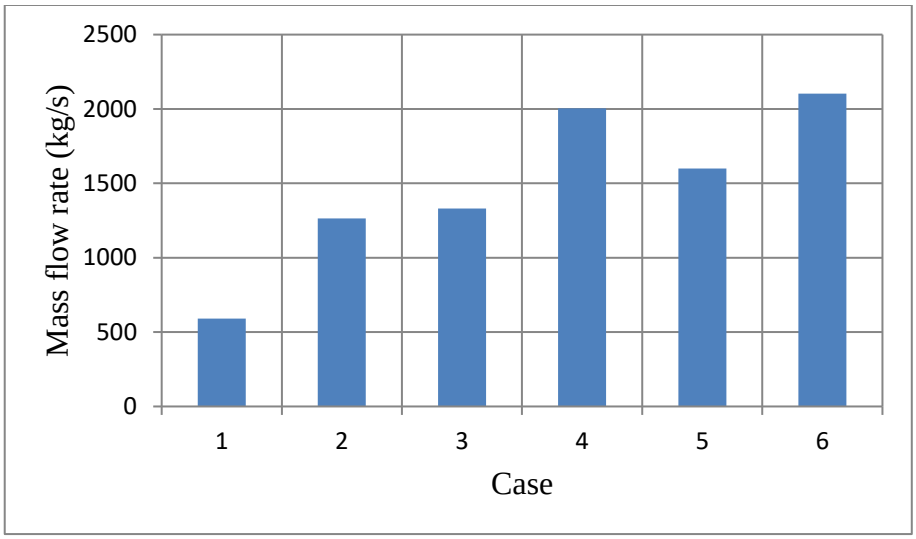

Figure 5.7: Mass flow rate at an inlet velocity of 100km/h for six different computational domains

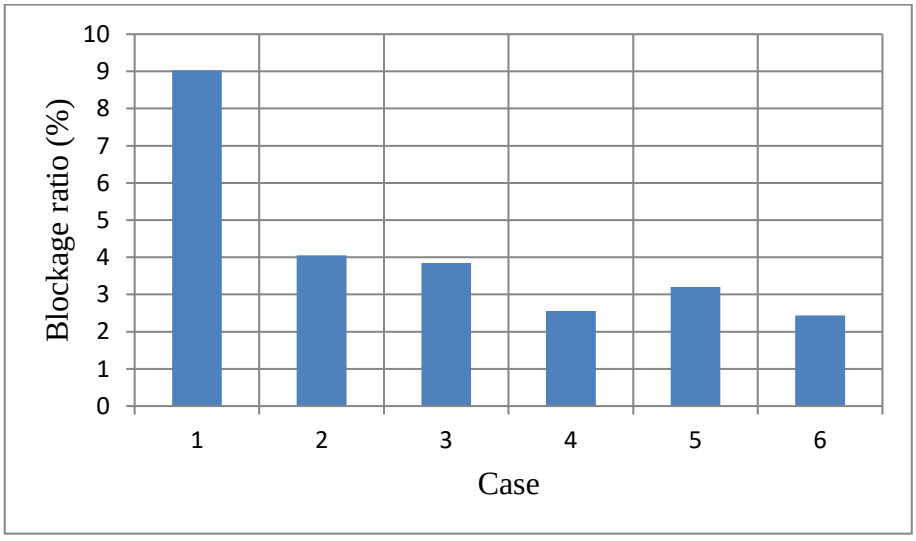

Figure 5.8: Blockage ratio for six different types of computational domains

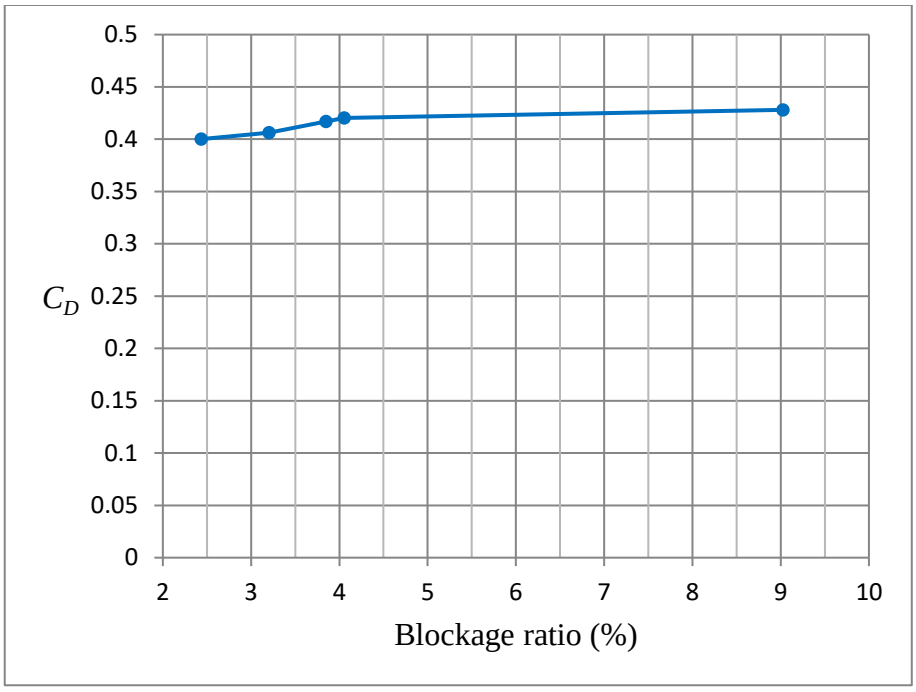

Figure 5.9: C_D for a wide range of blockage ratios

	Blockage ratio (%)				
	2.435	3.204	3.85	4.055	9.025
C_D	0.4001	0.4062	0.417	0.4202	0.4281

Table 5-2: C_D for different blockage ratios

	Blockage ratio (%)				
	2.435	3.204	3.85	4.055	9.025
C_L	0.031	0.025	0.0212	0.02	0.015

Table 5-3: C_L for different blockage ratios

The dimensions of the computational domain had a clear affect on the drag and lift coefficients as shown in Figures 5.10 and 5.11. Six different sizes of computational domain were used to study the affect of size on the aerodynamic behaviour. One of these sizes was the same dimensions as the MIRA wind tunnel (Case 1). These results are summarized in Figures 5.10 and 5.11 using the realizable k–ε model with three different

inlet velocities of air which were 27.7m/s (100km/h), 33.3m/s (120km/h) and 38.8m/s (140km/h) respectively. Figure 5.10 shows the drag coefficient for the benchmark model with six different sizes of computational domain compared with experimental results.

The maximum velocity of air in the small computational domain (the MIRA wind tunnel, Case 1) was higher than in the large computational domain (Case 6) as shown in Figure 5.12. Therefore, the drag coefficient reduces by increasing the inlet velocity of air for small sizes of computational domain. Whilst the larger sizes of computational domain were less influenced by the inlet velocity of air.

Table 5.4 shows the drag coefficient for all computational domains with three different velocities of oncoming air. In general, the lift coefficient is affected by the inlet air velocity and by the size of the computational domain. Figure 5.11 compare computations of the lift coefficient for the benchmark model for using the aforementioned six different sizes of computational domain with an experimental lift coefficient. It is clear that the numerical results using Case 6 of the computational domain were exactly the same results as the experimental data. Figure 5.12 shows the velocity distribution along the symmetry plane at 100km/h of inlet velocity of air using realizable k–ε turbulence model for two different sizes of the computational domain.

Velocity (km/h)	C_D						
	Case 1	Case 2	Case 3	Case 4	Case 5	Case 6	Exp.
100	0.4281	0.4202	0.417	0.4112	0.4062	0.4001	0.4
120	0.4182	0.4145	0.4117	0.4088	0.4039	0.3999	-
140	0.4084	0.4087	0.4063	0.4044	0.4015	0.3997	-

Table 5-4: C_D of the baseline model of the Land Rover Discovery 4 for six different sizes of computational domain and one experimental data

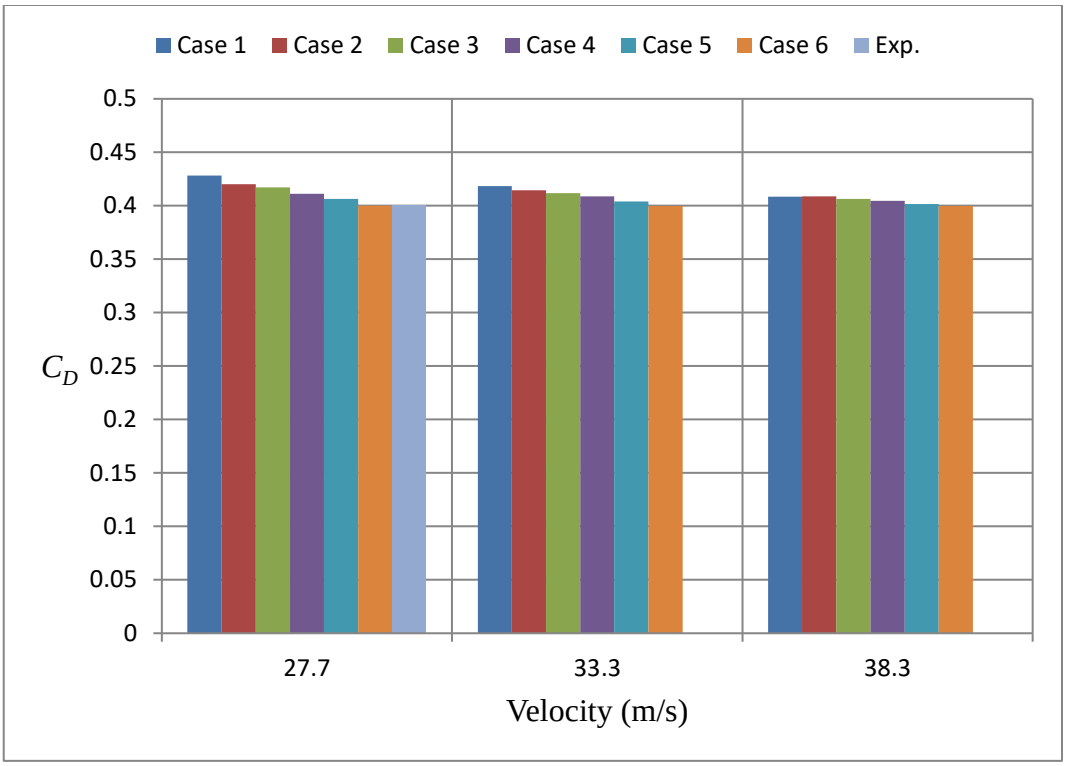

Figure 5.10: C_D for the baseline model of the Land Rover Discovery 4 for the present numerical results using six different sizes of computational domain compared with experimental C_D

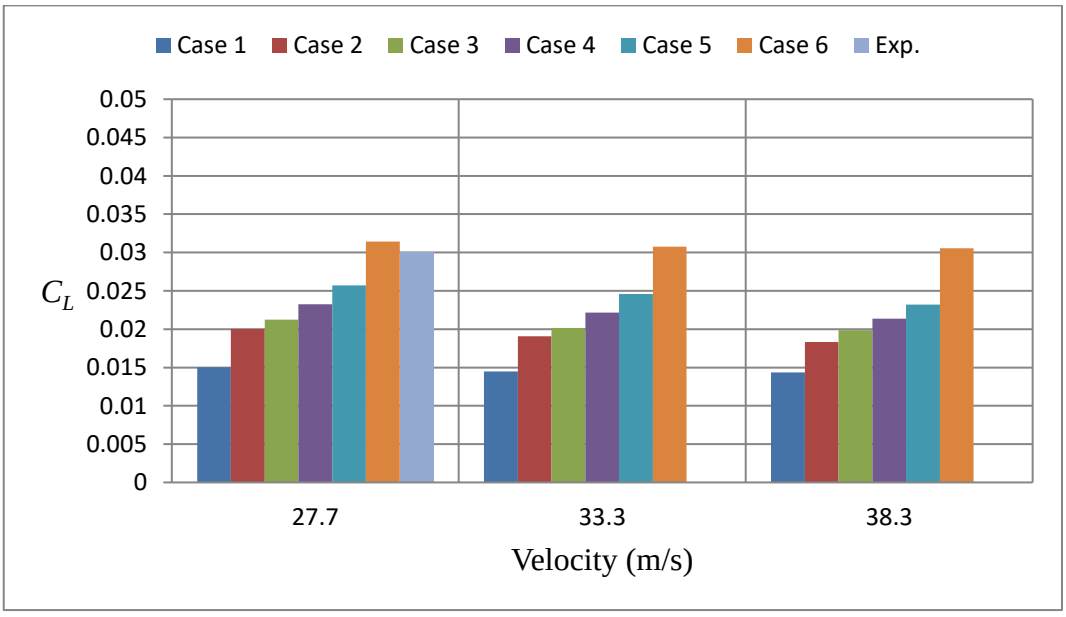

Figure 5.11: C_L for the baseline model of the Land Rover Discovery 4 for the present numerical results using six different sizes of computational domain compared with experimental C_L

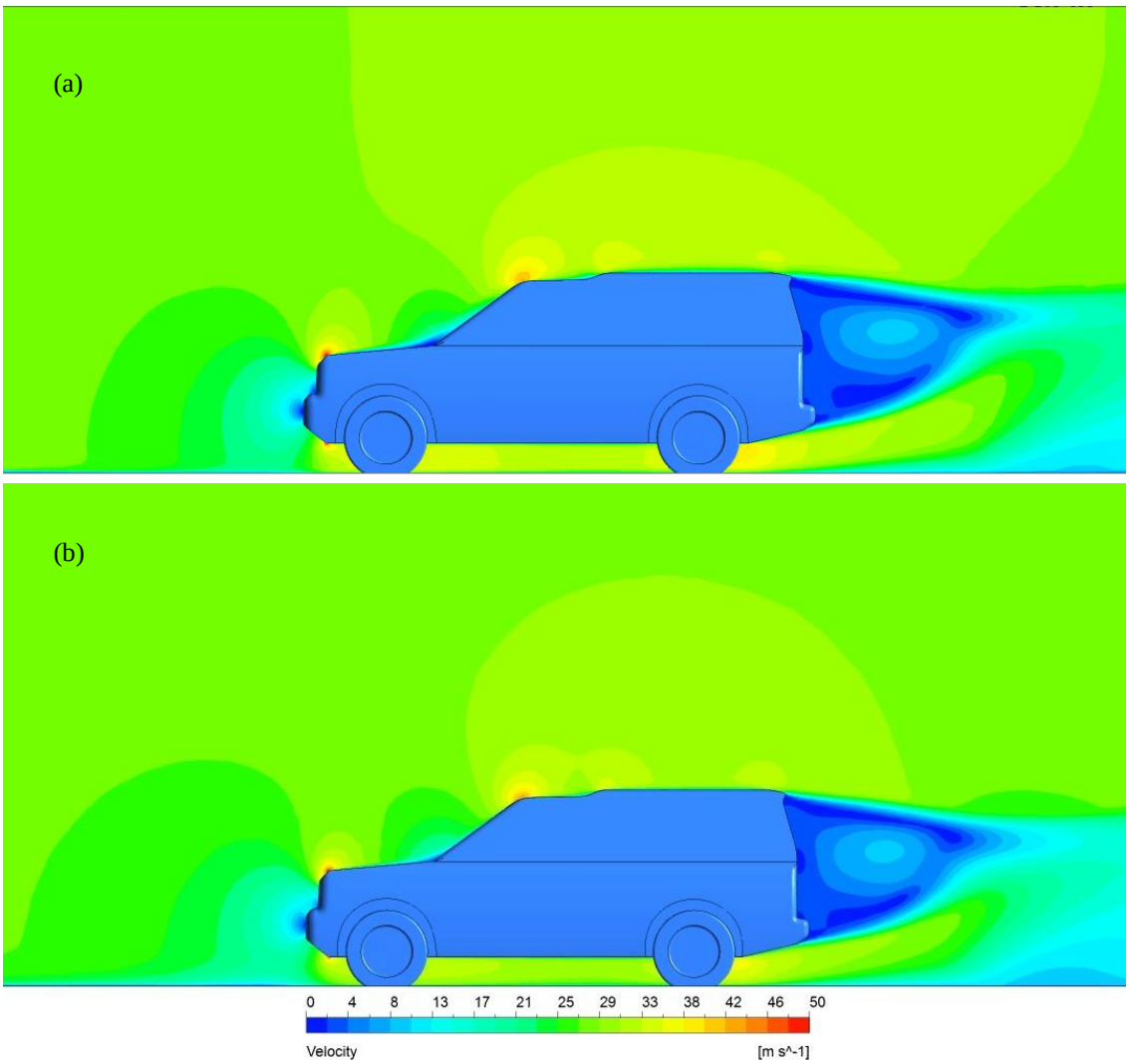

Figure 5.12: Velocity distribution along the symmetry plane at 100km/h of the inlet velocity of air using the Realizable k–ε model (a) Case 1 (the MIRA wind tunnel); (b) Case 6 (Standard computational domain in this study)

5.4 Land Rover Discovery model modifications

Five aerodynamics novel techniques were used in the present study to reduce the drag coefficient and to increase the stability of the Land Rover Discovery 4 on the road. These were boat-tail on the back door of the vehicle, VGs on the end of the vehicle roof, putting a spare tyre on the back door of the vehicle, a convergent-divergent ditch on the vehicle roof and non-straight base bleed. Boat-tail was used in some previous studies for tractor-trailer to reduce the drag coefficient. It can be used for SUV with suitable modifications. Boat-tail for tractor-trailer has perpendicular side plates while it has inclined side plates for SUV.

In this section the results of the so-called add-on devices and modifications to the Land Rover Discovery 4 are presented. Five different types of aerodynamic devices and modifications were used to study the effect on aerodynamic performance. The pressure and velocity of air behind the benchmark model of the Land Rover Discovery 4 decreased significantly due to sharp edges at the rear section of this vehicle. Therefore, mainly external modifications were used at the rear of the vehicle.

All techniques used for the benchmark model were used for all modified models with the realizable *k-ε* turbulence model used to study any resulting changes in the aerodynamics. In most high Reynolds number flows (e.g. external aerodynamics of road vehicles), flow near vehicle surface does not need to be resolved because the wall function method substantially provides sufficient precision whence reduces the time of simulations. Therefore, this turbulence model (realizable *k-ε*) was used for all the seventy modified models.

5.4.1 Boat-tail model

Results for different designs of the boat-tail investigated are shown in Table 5.5.

Case	Φ_{bt} (°)	L_{bt} (m)	C_D	C_L
1	8	0.24	0.3769	-0.0449
2	10	0.24	0.3769	-0.0447
3	12	0.24	0.3769	-0.0447
4	14	0.24	0.3769	-0.0447
5	16	0.24	0.3773	-0.0446
6	18	0.24	0.3813	-0.0446
7	14	0.245	0.3768	-0.0447
8	14	0.25	0.3768	-0.0445
9	**14**	**0.244**	**0.3768**	**-0.0448**
10	14	0.246	0.3768	-0.0447
11	14	0.243	0.3769	-0.0448
12	14	0.247	0.3769	-0.0446

Table 5-5: C_D and C_L for 12 different cases of the boat-tail model

All designs of the boat-tail had acceptable C_L and they were better than baseline model. Four designs from Table 5.4 (case: 7, 8, 9, 10) had the same minimum C_D (0.3768) but different C_L. Case number 9 had the maximum downforce in these four cases. Therefore, case number 9 was the optimal design regarding C_D and C_L. It is worth to mention that case number one had the best C_L but C_D was more than case 9. A reduction of 5.8% was achieved by using the design in case number 9.

5.4.2 Spare tyre model

Results for different positions of the spare tyre are shown in Table 5.6.

Case	L_{st} (m)	C_D	C_L
1	**1.075**	**0.3724**	**-0.1024**
2	1.080	0.3725	-0.1025
3	1.085	0.3727	-0.1025
4	1.090	0.3728	-0.1026
5	1.095	0.3729	-0.1028
6	1.100	0.3731	-0.1029
7	1.105	0.3733	-0.1032
8	1.110	0.3734	-0.1035
9	1.115	0.3736	-0.1037
10	1.120	0.3738	-0.1040
11	1.125	0.3740	-0.1045
12	1.130	0.3743	-0.1047

Table 5-6: C_D and C_L for 12 different cases of the spare tyre model

All positions of the spare tyre produced very similar C_L and each of these cases displayed greater downforce than the benchmark. The optimal position of the spare tyre model was achieved by case number one (Table 5.5). A reduction in the drag coefficient of 6.9% was accomplished by using the spare tyre design this case.

5.4.3 Vortex generators model

Twelve different cases of VGs were investigated are shown in Table 5.7.

Case	D_{VG} (m)	H_{VG} (m)	C_D	C_L
1	0.25	0.03	0.3941	-0.1305
2	0.25	0.04	0.393	-0.1305
3	0.25	0.05	0.3901	-0.1307
4	0.25	0.06	0.3902	-0.1309
5	0.3	0.03	0.3897	-0.131
6	0.3	0.04	0.3841	-0.1311
7	**0.3**	**0.05**	**0.3836**	**-0.1312**
8	0.3	0.06	0.3839	-0.1312
9	0.35	0.03	0.3935	-0.1323
10	0.35	0.04	0.3922	-0.1325
11	0.35	0.05	0.3899	-0.1332
12	0.35	0.06	0.3901	-0.1333

Table 5-7: C_D and C_L for 12 different cases of the VGs model

All cases of the VGs were achieved high downforce and reduced the C_D. The optimal design of the VGs model was achieved in case number seven as shown in Table 5.7. A reduction in the C_D of 4.1% was accomplished by using the optimal design of the VGs.

5.4.4 Roof ditch model

Eighteen different designs of the convergent-divergent ditch on the roof of the car were investigated each of these detailed in Table 5.8.

Case	D_{in} (m)	D_{out} (m)	C_D	C_L
1	0.832	1.1	0.3971	-0.1753
2	0.832	1.2	0.3969	-0.1754
3	0.832	1.15	0.3969	-0.1756
4	0.832	1.18	0.3966	-0.1757
5	0.832	1.181	0.3966	-0.1758
6	0.832	1.182	0.3966	-0.176
7	0.832	1.183	0.3965	-0.1762
8	0.832	1.184	0.3965	-0.1761
9	0.832	1.1835	0.3962	-0.1764
10	0.832	1.1834	0.3962	-0.1763
11	0.832	1.1836	0.3962	-0.1764
12	**0.8322**	**1.1834**	**0.3961**	**-0.1765**
13	0.8324	1.1834	0.3963	-0.1764
14	0.8326	1.1834	0.3964	-0.1765
15	0.8318	1.1834	0.3963	-0.1764
16	0.8316	1.1834	0.3965	-0.1762
17	0.8314	1.1834	0.3965	-0.1761
18	0.8312	1.1834	0.3965	-0.1761

Table 5-8: C_D and C_L for 18 different cases of the roof ditch model

The best downforce was achieved by using the roof ditch as shown in Table 5.8. The optimal design of the roof ditch was accomplished in case number twelve (Table 5.7). This aerodynamic device has reduced the drag coefficient by 0.975%. These results demonstrate that the roof ditch increase vehicle stability, whilst modestly affecting the air resistance.

5.4.5 Base bleed model

Sixteen new designs of the base bleed were investigated. Table 5.9 shows ANSYS-Fluent drag and lift coefficient calculations for each of these designs.

Case	D_{out} (m)	H_{out} (m)	C_D	C_L
1	1	0.04	0.3988	-0.0802
2	1	0.05	0.3859	-0.0819
3	1	0.06	0.3858	-0.0818
4	1	0.07	0.3856	-0.0818
5	1.1	0.04	0.3815	-0.0801
6	1.1	0.05	0.3725	-0.0823
7	1.1	0.06	0.3724	-0.0822
8	1.1	0.07	0.3721	-0.082
9	1.2	0.04	0.3804	-0.0823
10	1.2	0.05	0.3716	-0.0825
11	1.2	0.06	0.3715	-0.0821
12	**1.2**	**0.07**	**0.3714**	**-0.082**
13	1.3	0.04	0.3804	-0.0823
14	1.3	0.05	0.3717	-0.0825
15	1.3	0.06	0.3716	-0.0821
16	1.3	0.07	0.3714	-0.082

Table 5-9: C_D and C_L for 16 different cases of the base bleed model

The minimum drag coefficient was achieved by using the base bleed in case number twelve (Table 5.9). This aerodynamic modification reduced the drag coefficient by 7.15%.

5.5 Land Rover Discovery velocity profile

The streamlines around the baseline of the Land Rover Discovery 4 for different turbulence models (realizable k-ε, standard k-ω, Shear Stress Transport k-ω and Reynolds Stress Model) and inlet air velocity of 28m/s is shown in Figures 5.13 and 5.14.

5.5.1 Velocity profile around the benchmark model

Figure 5.13 shows the streamline around the baseline model with tyres and solid geometry car body while Figure 5.14 shows the close up streamline around the baseline model without tyres and using a hollow body for further illustration. The benchmark model displayed vortices behind the car because the design was not streamlined. Two vortices behind the vehicle were generated by the flow from the roof edge and the underbody as shown in side view. The air leaves the body surface of the vehicle between reverse and forward flow and this phenomenon is called separation. The pressure gradient of air was positive on the back side of the vehicle. The reduction of the air velocity in this area was due to viscosity of air and the positive pressure gradient. The minimum velocity was zero and the maximum was 55m/s. In general, the overall aerodynamic behaviour of realizable k-ε, Shear -Stress Transport k-ω and Reynolds Stress Model evaluated similar flow fields as shown in Figures 5.13(a), 5.13(c), 5.13(d), 5.14(a), 5.14(c) and 5.14(d). However, the upper vortices of the RSM were lower than the other turbulence models investigated. Furthermore, the streamlines from the standard k-ω model was slightly different, the bottom vortices were closer to the rear door as shown in Figures 5.13(b) and 5.14(b).

Figure 5.15 shows the velocity vectors around the baseline of the benchmark using four types of turbulence models (realizable k-ε, standard k-ω, Shear -Stress Transport k-ω and Reynolds Stress Model) for an initial inlet air velocity of 28m/s. The maximum velocity vectors were in the front of the bonnet and the front of the roof for all types of turbulence models investigated; while the minimum velocity vector was behind the car. The length of the wake zone was about 2 m and the velocity of air under the car body was about 34m/s. The velocity vector on the front windscreen was moderate. Six separations occur around this model, which were at the front of the bonnet, front of the roof, curvature of the roof, end of the roof, under the front bumper and under the rear bumper. Figure 5.16 shows the velocity vectors behind the baseline of the benchmark using the aforementioned four turbulence models. Figure 5.16 shows the directions of the speed clearly behind the car where the least speed was at the rear door of the car.

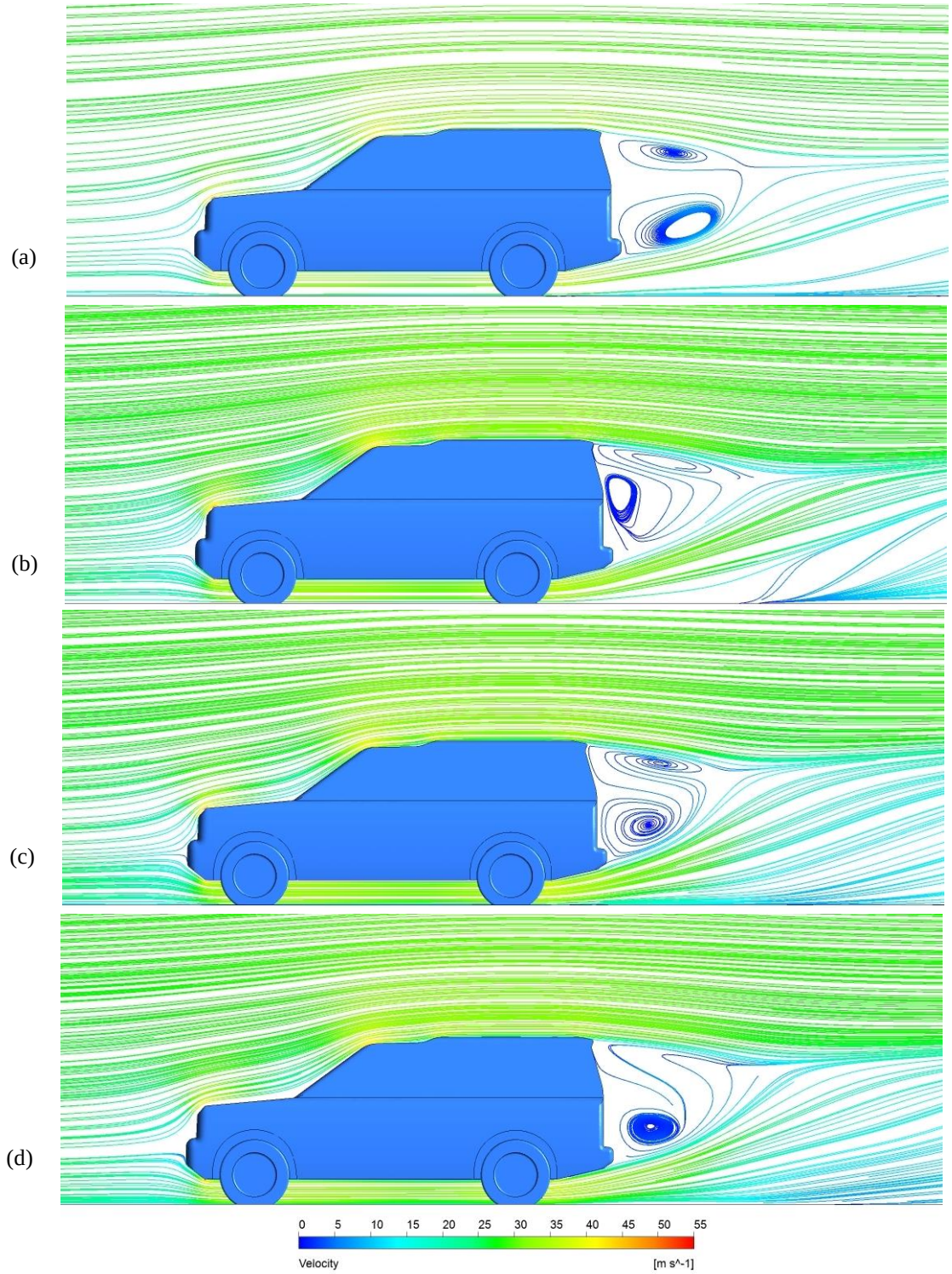

Figure 5.13: Streamline around the baseline of the Land Rover Discovery 4 using four types of turbulence models (a) Realizable k-ε, (b) Standard k-ω, (c) Shear Stress Transport k-ω and (d) Reynolds Stress Model

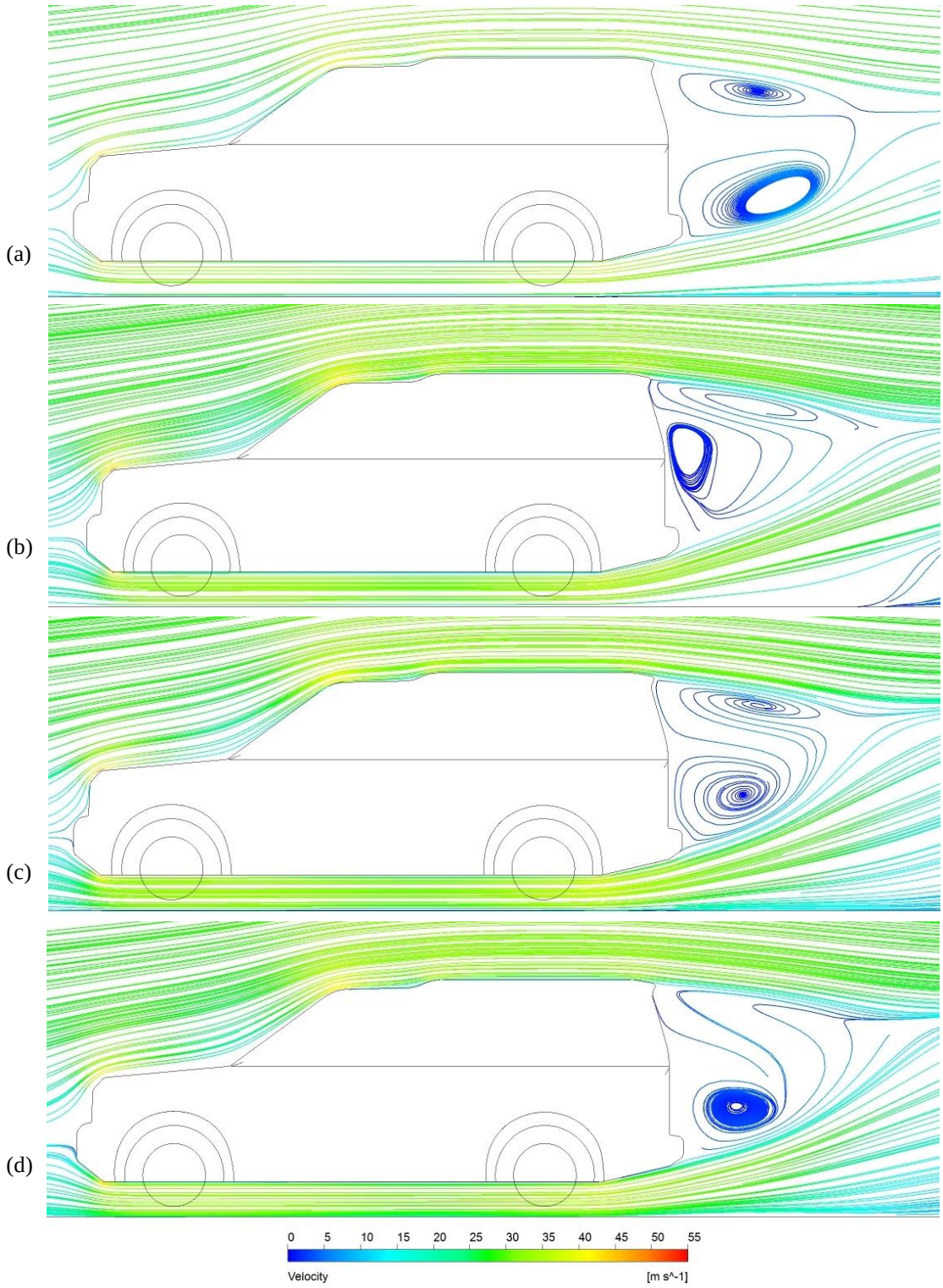

Figure 5.14: Close-up streamlines around the baseline of the Land Rover Discovery 4 using four types of turbulence models (a) Realizable k-ε, (b) Standard k-ω, (c) Shear Stress Transport k-ω and (d) Reynolds Stress Model

(a)

(b)

(c)

(d)

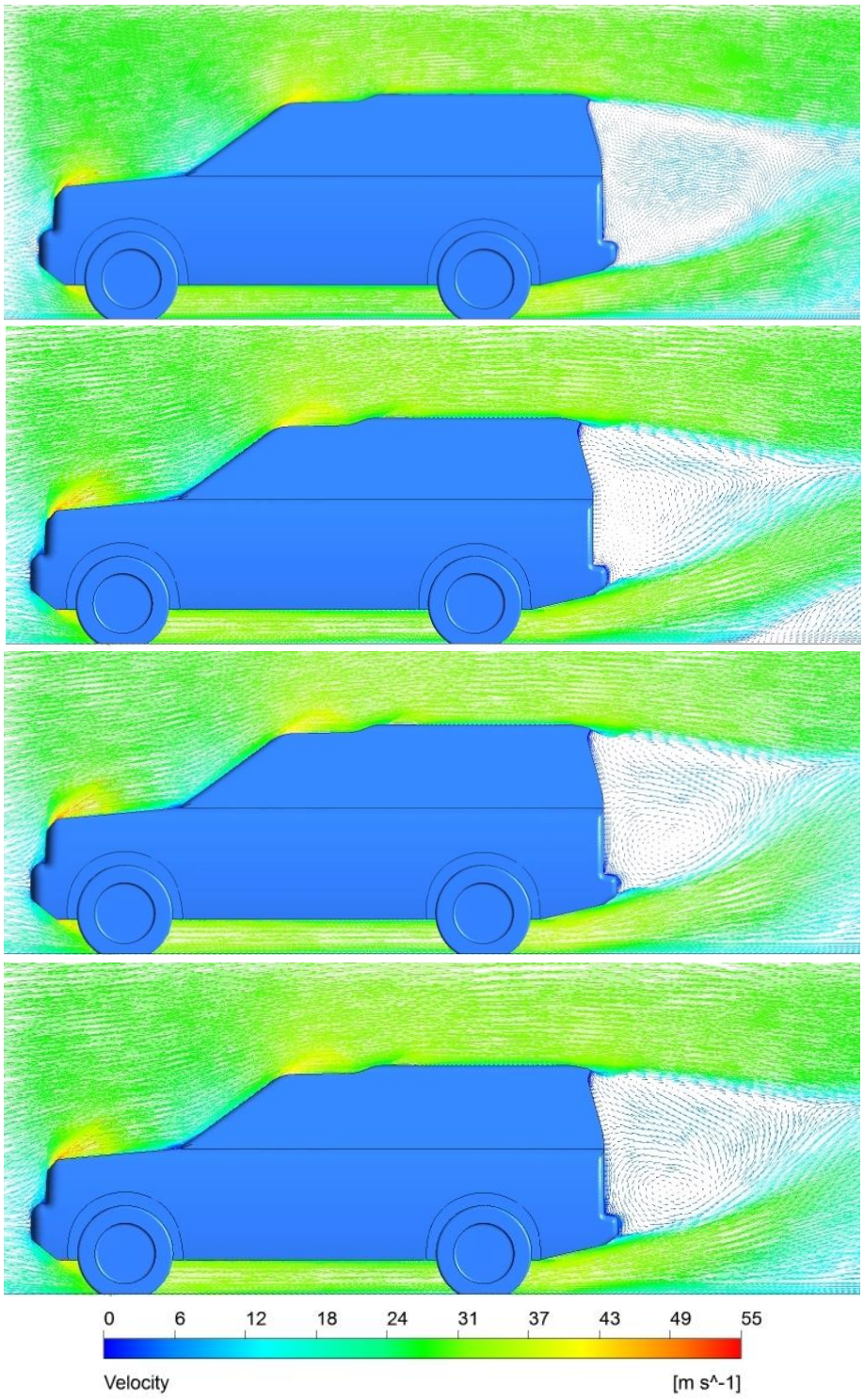

Figure 5.15: Velocity vectors around the baseline of the Land Rover Discovery 4 using four types of turbulence models (a) Realizable k-ε, (b) Standard k-ω, (c) Shear Stress Transport k-ω and (d) Reynolds Stress Model

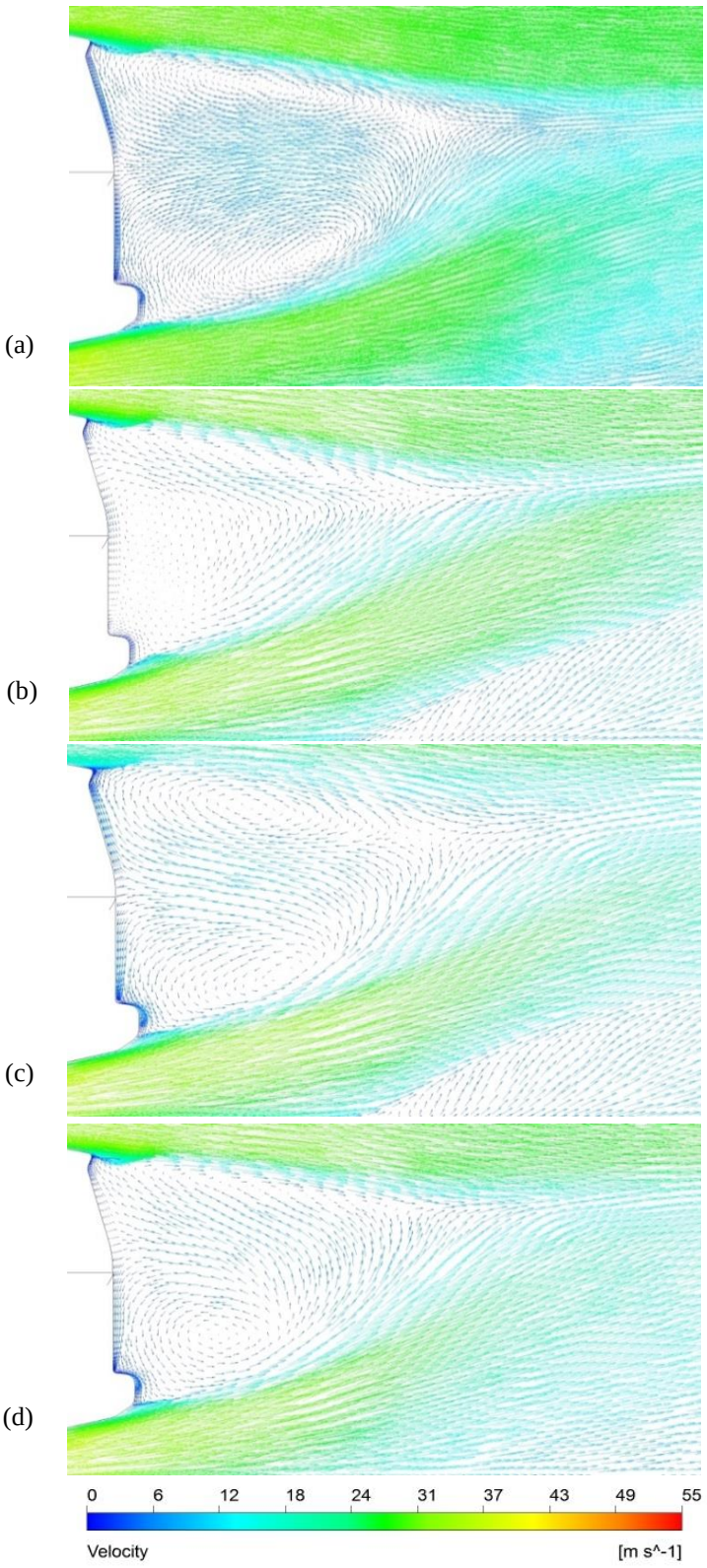

Figure 5.16: Velocity vectors behind the baseline of the Land Rover Discovery 4 using four types of turbulence models (a) Realizable *k*-*ε*, (b) Standard *k*-*ω*, (c) Shear Stress Transport *k*-*ω* and (d) Reynolds Stress Model

5.5.2 Velocity profile around the modified models

Figures 5.17 and 5.18 show the streamlines around the Land Rover Discovery 4 with different aerodynamic devices and modifications in addition to the baseline model. The inlet air velocity of 28m/s was used in the numerical simulations in line with experimental tests. In general, two straight spanwise vortices were generated by the flow from the roof edge and the underbody. Vortices behind the SUV were evident due to a low pressure zone. The vortices were non-uniform because of the low pressure behind this model. Vortices are generated near the rear bumper of the vehicle and after separation of flow at the end of the roof.

Vortices behind the benchmark model were reduced by adding so-called aerodynamic devices and modifications. Figure 5.17 shows the streamline around multiple case-studies with tyres and main car body modelled as solid geometries. While Figure 5.18 shows streamlines around these case-studies without tyres and using a hollow body for further illustration. The minimum velocity was zero and the maximum was 55m/s. Vortices behind the car and high velocity at the front of the bonnet and the roof were evident in these simulations (Figures 5.17 and 5.18) the latter being attributed to the reduction cross-sectional area of the computational domain. The velocity increases with decreasing the cross-sectional area whilst maintaining a constant flow rate. By adding the boat-tail to the rear of the car, swirling flow was significantly reduced as shown in Figures 5.17(b) and 5.18(b). This is a consequence of the air being directed through the plates of the boat-tail. This is quite similar to the fairing, but it is actually different because it is hollow. The boat-tail used in this work consist of four plates connected together as shown in Figure 4.35, page 126. The vortex in the upper part changes its shape as a result of the sloping plate at the top as shown in Figure 5.18(b).

A spare tyre on the rear door of the car resulted in a reduction in vortices but the vortex at the top slightly increased near the rear windscreen as shown in Figures 5.17(c) and 5.18(c). This modification resulted in more regular than other types by filling some of wake regions in addition to filling part of the low pressure area resulting in more streamlined wake. VGs were used to control the flow separation of air in order which improved the aerodynamic behaviour as shown in Figures 5.17(d) and 5.18(d). In general, the vortex in the upper part decreased while it increased in the lower part. Figures 5.17(e) and 5.18(e) show the streamlines around the Land Rover Discovery 4 with roof modification. This modification increased the pressure at the end of the roof. Here the vortices near the rear windscreen were significantly reduced due to increased pressure. The general behaviour of this modification was quite similar to the vortex generators.

The base bleed model showed a decrease in pressure at the front of the vehicle with increased pressure it behind. Air from the base bleed outlet moved down due the pressure being higher behind the rear bumper. The vortex size near the end of the roof increased because the pressure at the base bleed exit was relatively high compared to the pressure near the end of the roof. The maximum velocity of air with base bleed was less than that of the benchmark model because of the reduction in airflow over the vehicle as shown in Figures 5.17(f) and 5.18(f). It should be noted that the base bleed was suitably designed adversely affect the vehicle capacity and comfort.

Boat-tail and spare tyre models have achieved more streamlines than other models because these techniques have filled some wake area. Therefore, low air resistance was predicted for these modifications. In comparison VGs and roof ditch models predicted smaller vortices near the roof of the vehicle because these devices increased the pressure ergo increased the velocity of the near flow field.

Figure 5.19 shows the velocity filed around the Land Rover Discovery 4 with a prescribed inlet velocity of 28m/s; being evaluated on the model symmetry plane for each of the case-studies (baseline and modified models). The primary feature is the shear layers arising at the upper and lower rear edges. Reversed airflow being evident behind the SUV as shown in Figures 5.19 and 5.20 which were surrounded by the two shear layers. The predicted length of wake zone for all case-studies was about 2 m and the velocity of the air underbody was more than 33m/s depending on the devices and modifications. The air velocity underbody of the base bleed model was less than other models because some air passed through the base bleed device.

Figures 5.19(b) and 5.20(b) show the wake profile predictions with a prescribed inlet speed of 28m/s for the boat-tail case-study. A low velocity vector can be seen above the upper plate and at the edges. The size and length of the wake was smaller than the baseline model. Figures 5.19(c) and 5.20(c) show the velocity field for the spare tyre case-study. The flow here appears more homogenous than other case-studies. A low-velocity vector near the rear surface of the spare tyre is predicted.

The velocity distribution behind the SUV with a spare tyre was the best between all modified models. The main objective in adding vortex generators was attempt to delay the flow separation thereby could improve the aerodynamic behaviour as demonstrated in Figures 5.19(d) and 5.20(d). The wake for this device was the shortest because of greater changes in the direction of the flow. By modifying the roof, the velocity vector distribution on the upper boundary of the wake increased and the height of the wake was greater than all the other case-studies as demonstrated in Figures 5.19(e) and 5.20(e).

Simulated streamlines obtained from adding base bleed are shown in Figure 5.19(f). The velocity decreased behind the car whilst the pressure increased because of flow through the device. The velocity field displayed a more uniform distribution than the benchmark case, as was the length of the wake. The velocity field near the bonnet was also more uniform than the benchmark model. The velocity at the front of the car decreased because of the air flow through the device. In general, the aerodynamic flow around the SUV model with this modification is more homogeneous than the benchmark model. The maximum reversed velocity of air in the wake region was between 4 and 8m/s depending on the case-study.

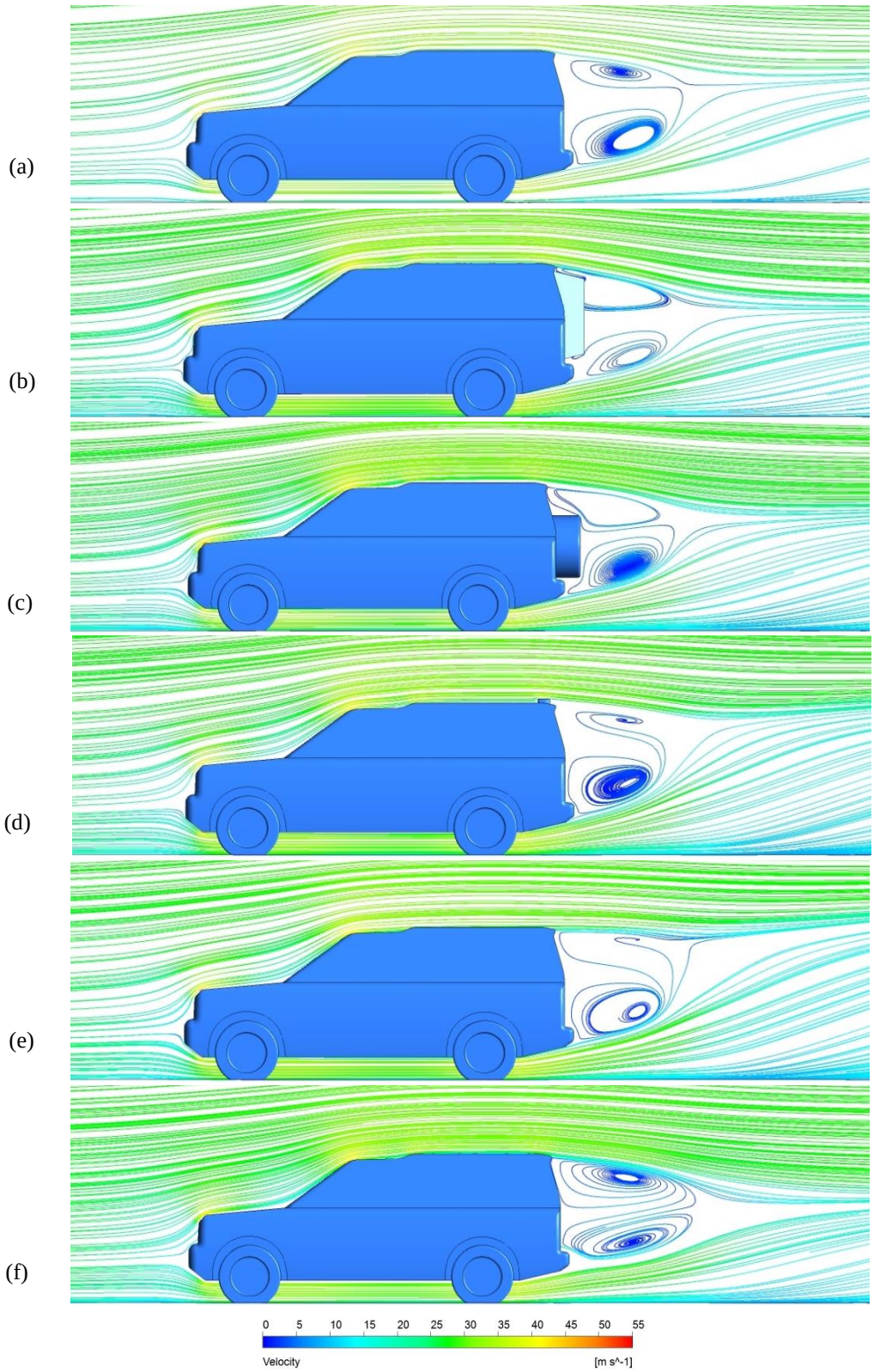

Figure 5.17: Streamline around the Land Rover Discovery 4 with different case-studies (a) Baseline model, (b) Boat-tail, (c) Spare tyre, (d) VGs, (e) Ditch on the roof and (f) Base bleed

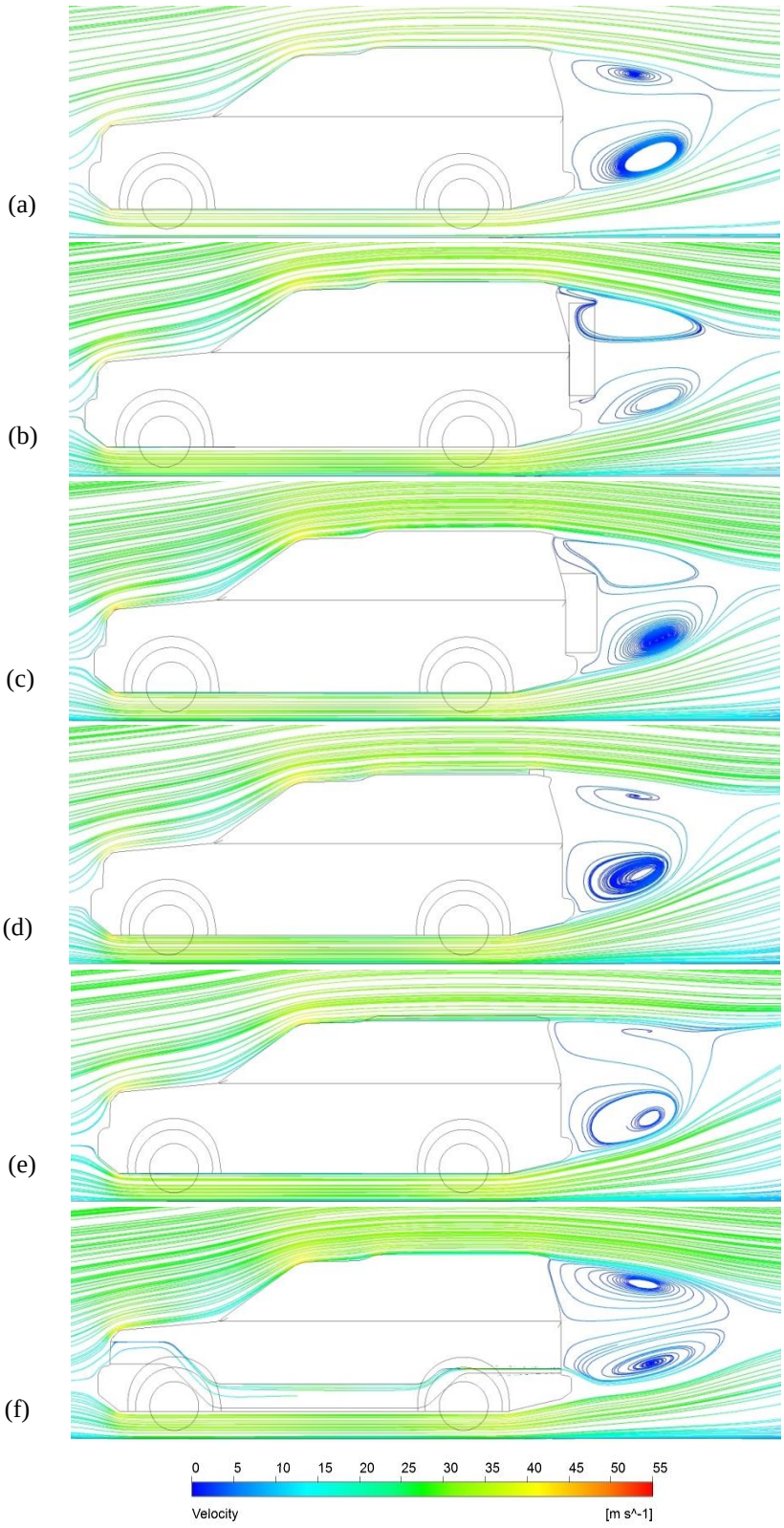

Figure 5.18: Close-up streamline around the Land Rover Discovery 4 with different case-studies (a) Baseline model, (b) Boat-tail, (c) Spare tyre, (d) VGs, (e) Ditch on the roof and (f) Base bleed

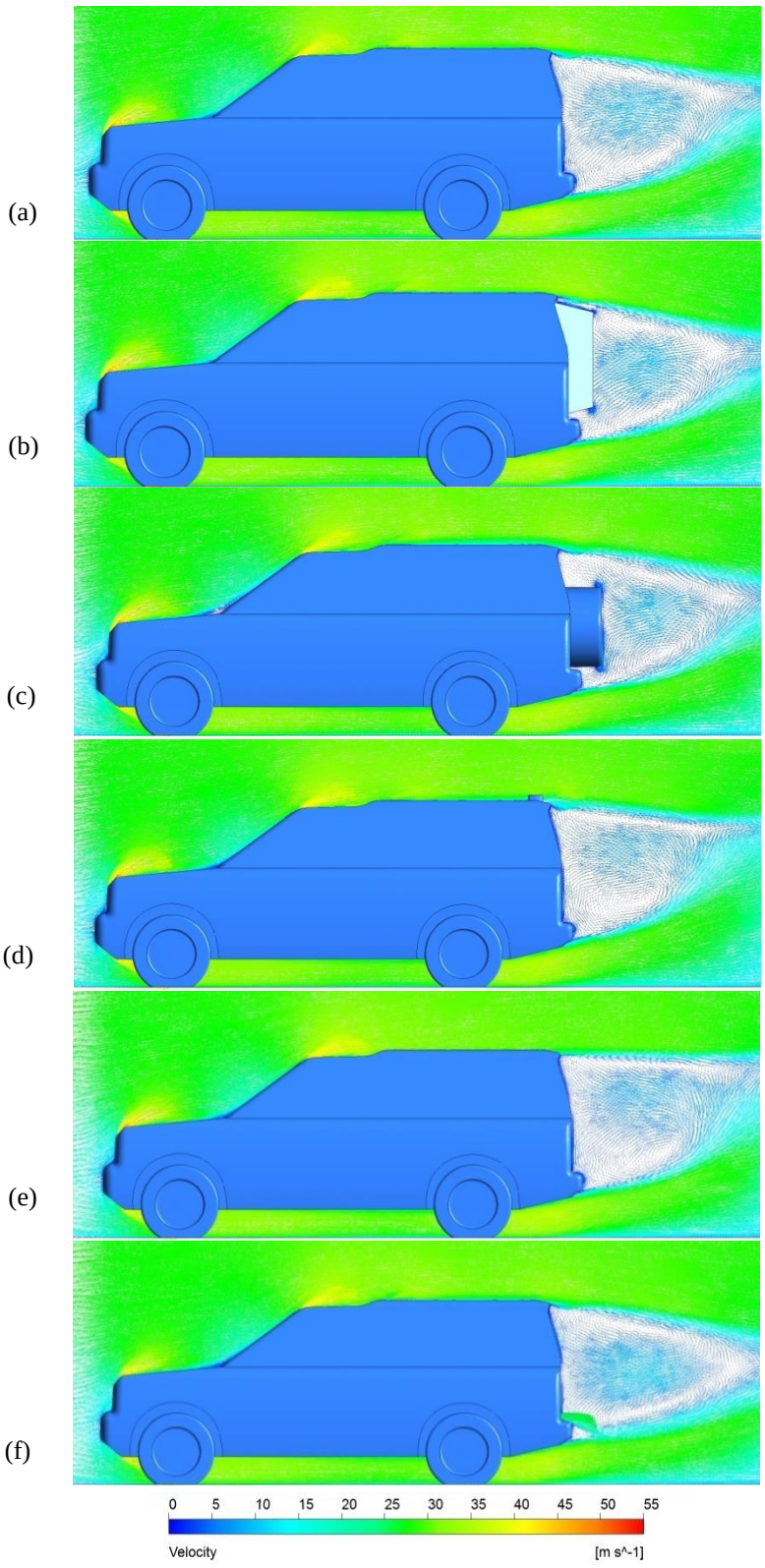

Figure 5.19: Velocity vector around the Land Rover Discovery 4 with different case-studies (a) Baseline model, (b) Boat-tail, (c) Spare tyre, (d) VGs, (e) Ditch on the roof and (f) Base bleed

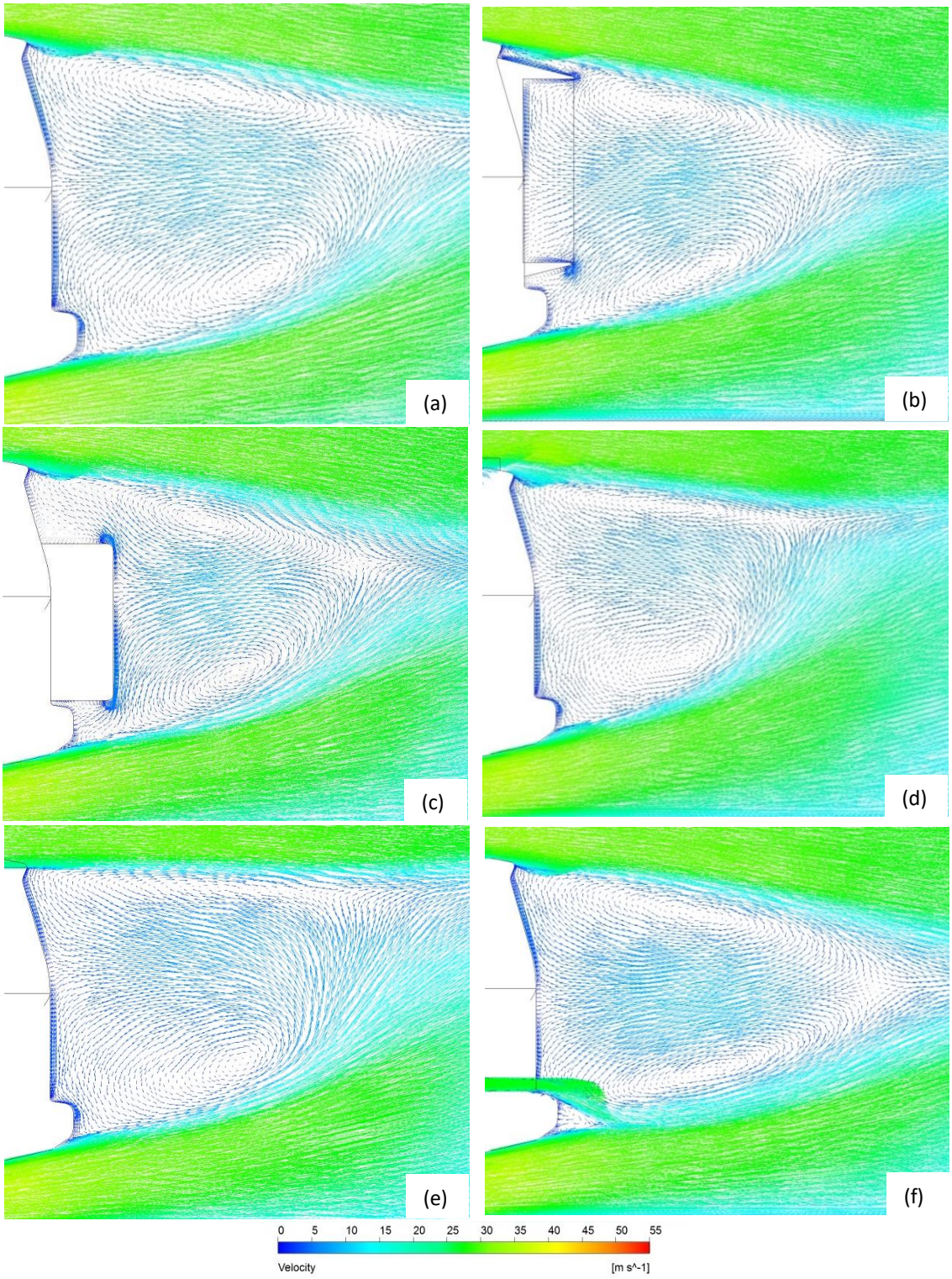

Figure 5.20: Velocity vector behind the Land Rover Discovery 4 with different case-studies (a) Baseline model, (b) Boat-tail, (c) Spare tyre, (d) VGs, (e) Ditch on the roof and (f) Base bleed

5.6 Pressure distributions

The dimensionless pressure coefficient (C_p) is used to express the pressure values in all figures of the pressure contours. Different scales of pressure coefficient were used in this section to highlight all variations in pressure contours. A range between -2 and 1 was used for Figures 5.21, 5.22, 5.28 and 5.29. For the back view in Figures 5.23 and 5.30, a range between -2 and 0.2 was used. A range of pressure coefficient between -1.5 and 0 was used for bottom view, as shown in Figures 5.24 and 5.31. A range between -2 and 0.5 was used for the top view, as shown in Figures 5.25 and 5.32.

5.6.1 Benchmark pressure distributions

Figure 5.21 shows contours of pressure distribution along the symmetry plane for the benchmark model with a prescribed inlet velocity of 28m/s. Four types of turbulence models were used: realizable k-ε, standard k-ω, Shear Stress Transport k-ω and Reynolds Stress Model to produce the results shown in Figures 5.21-5.25. In general, similar results were obtained independent of turbulence model used. A slightly lower pressure being evident in the case of the SST k-ω model behind the car was evident when compared to the other turbulence models. Pressure being predicted in front of the car, especially at the front bumper, headlights and grill, thereby demonstrating more air resistance. The pressure above this model indicates good stability despite there being some low-pressure zones, especially at the front of the bonnet and the front of the car roof. Increasing of down force can lead to increased friction between tyres of the vehicle and road; this results in better road grip and higher stability.

Figure 5.22 shows the pressure distribution on the front surfaces of the benchmark model for the aforementioned turbulence models. Here the pressure on the front bumper, front grill and headlights was similar for all types of turbulence models. However, the pressure distribution on the front windscreen was slightly higher when using the SST and standard k-ω turbulence models when compared with the realizable k-ε and Reynolds Stress Model. Two separation flows at the upper front section at the edge of the bonnet and at the front of the car roof are shown in Figures 5.21 and 5.22. The separation flow occurs at the edges where the cross-sectional area changes. Clearly Figure 5.22 shows three low-pressure zones at the front corner of the car, a pillar and the front tyre. Flow separation predicted at the edge between the front bumper and the underbody (Figure 5.21).

Pressure distribution predictions on the back surfaces of the benchmark model for the four types of turbulence models: realizable k-ε, standard k-ω, SST k-ω and RSM are shown in Figure 5.23. Maximum pressure being predicted in the middle of the back door.

Figure 5.23(c) shows the pressure distribution behind the vehicle using the SST k-ω turbulence model was slightly lower than other turbulence models as shown in. Conversely the distribution of the pressure behind the car using Reynolds Stress Model was higher than the realizable k-ε and standard k-ω predictions (Figure 5.23).

Figure 5.24 shows close up bottom view of the pressure distribution on the surface of the benchmark model of turbulence models i.e.: realizable k-ε, standard k-ω, SST k-ω and RSM). Similarity between these results being evident. There was a slight difference in the pressure distribution in the middle of the underbody, especially with SST turbulence model. Figure 5.25 shows close up top view of the pressure distribution on the surface of the benchmark model. Low-pressure occurs on the roof increasing gradually until a maximum is realized. Therefore, the pressure was high in this area. Pressure of the RSM was slightly higher than other turbulence model.

Figures 5.26 and 5.27 show the pressure coefficient calculations for the benchmark model on the symmetry plane using the realizable k-ε turbulence model. The red line represents the pressure coefficient above the car while the blue line represents C_p on the underbody. The vertical axis detailing the pressure coefficient and the horizontal axis the vehicle length in the z-direction the rear to the front bumper. As expected the highest pressure coefficient was predicted at the front bumper which decreased significantly at the front edge of the bonnet and then rises to 0.6 at the front windscreen. The pressure coefficient drops at the roof as a result of increased air speed. This quantity also increases due to the curvature of the roof. The pressure coefficient was stable over the lower part of the car (underbody) except for a decrease at the edge between the front bumper and the underbody. A second drop being evident at a rear section of the car between the underbody and the diffuser. Figure 5.27 shows the pressure coefficient evaluated on the symmetry plane of the benchmark model for four different types of turbulence models. All the pressure coefficients from these models were similar over the front section of the car but were varied over the rear. All turbulence models provided similar results though slight differences were observed when the SST model was employed.

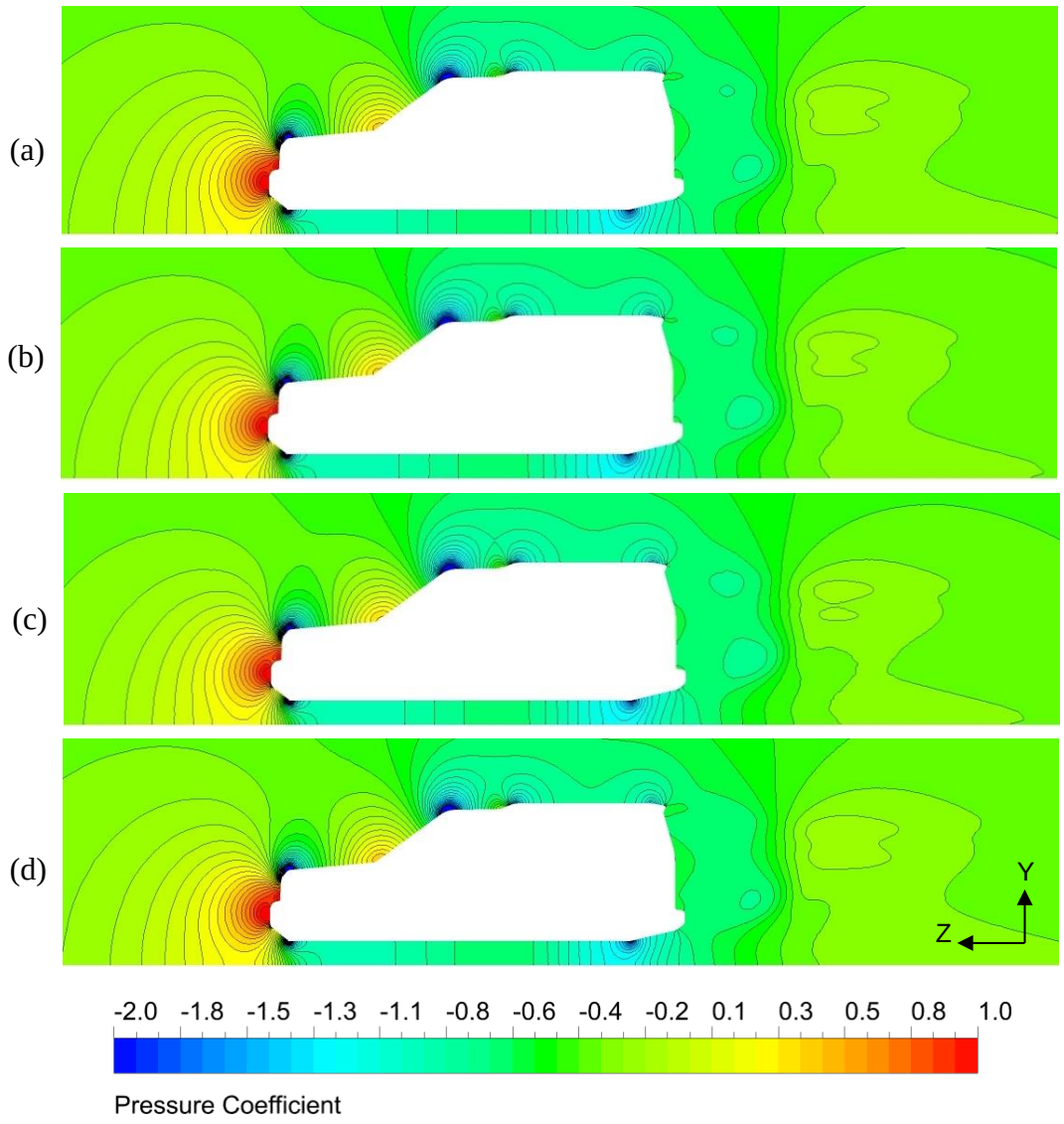

Figure 5.21: Surface pressure distribution on the symmetry plane for the baseline model of the Land Rover Discovery 4 using four types of turbulence models (a) Realizable k-ε (b) Standard k-ω (c) SST k-ω (d) Reynolds Stress Model

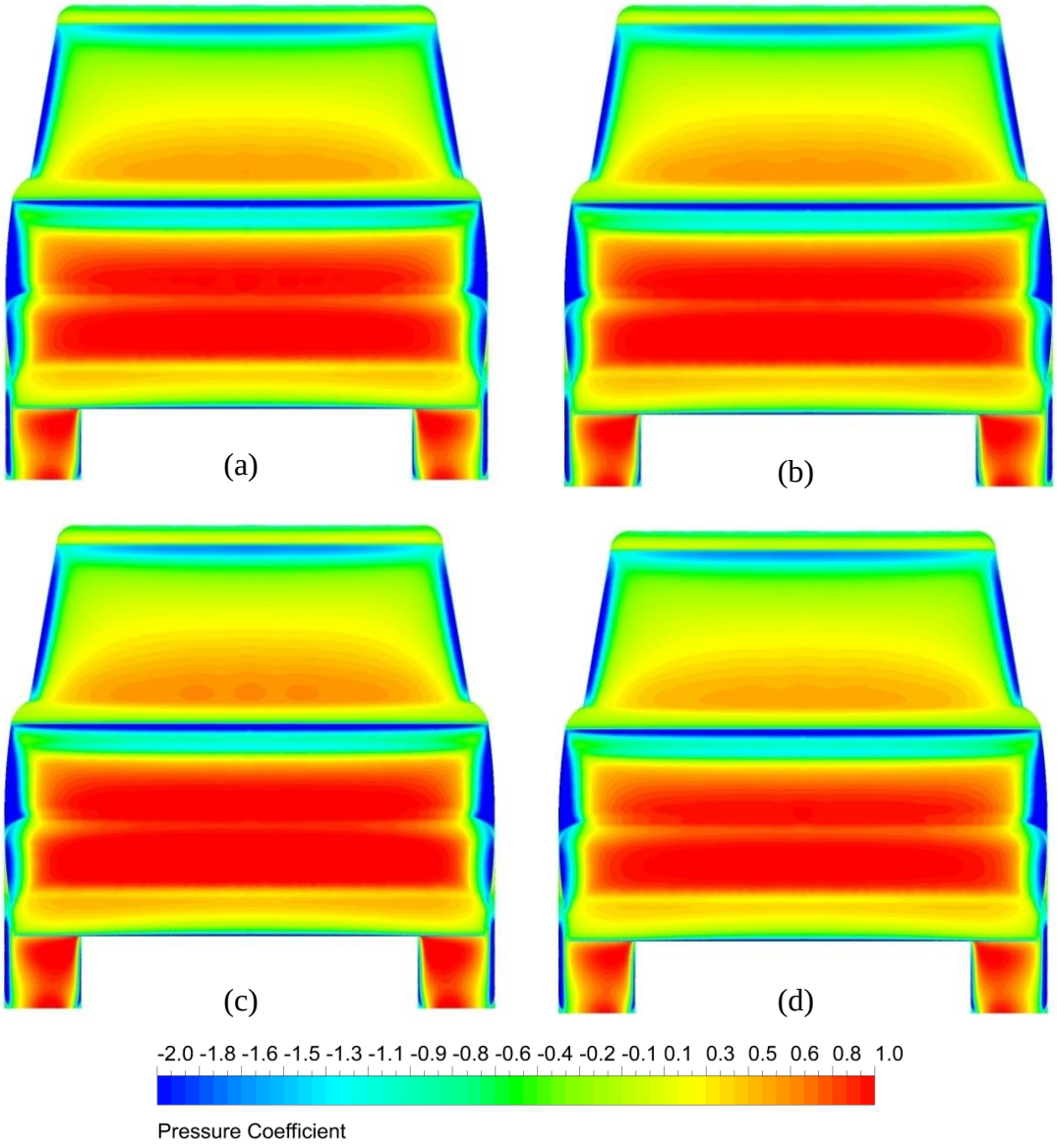

Figure 5.22: Surface pressure distribution on the baseline model of the Land Rover Discovery 4 (front view) using four types of turbulence models (a) Realizable k-ε (b) Standard k-ω (c) SST k-ω (d) Reynolds Stress Model

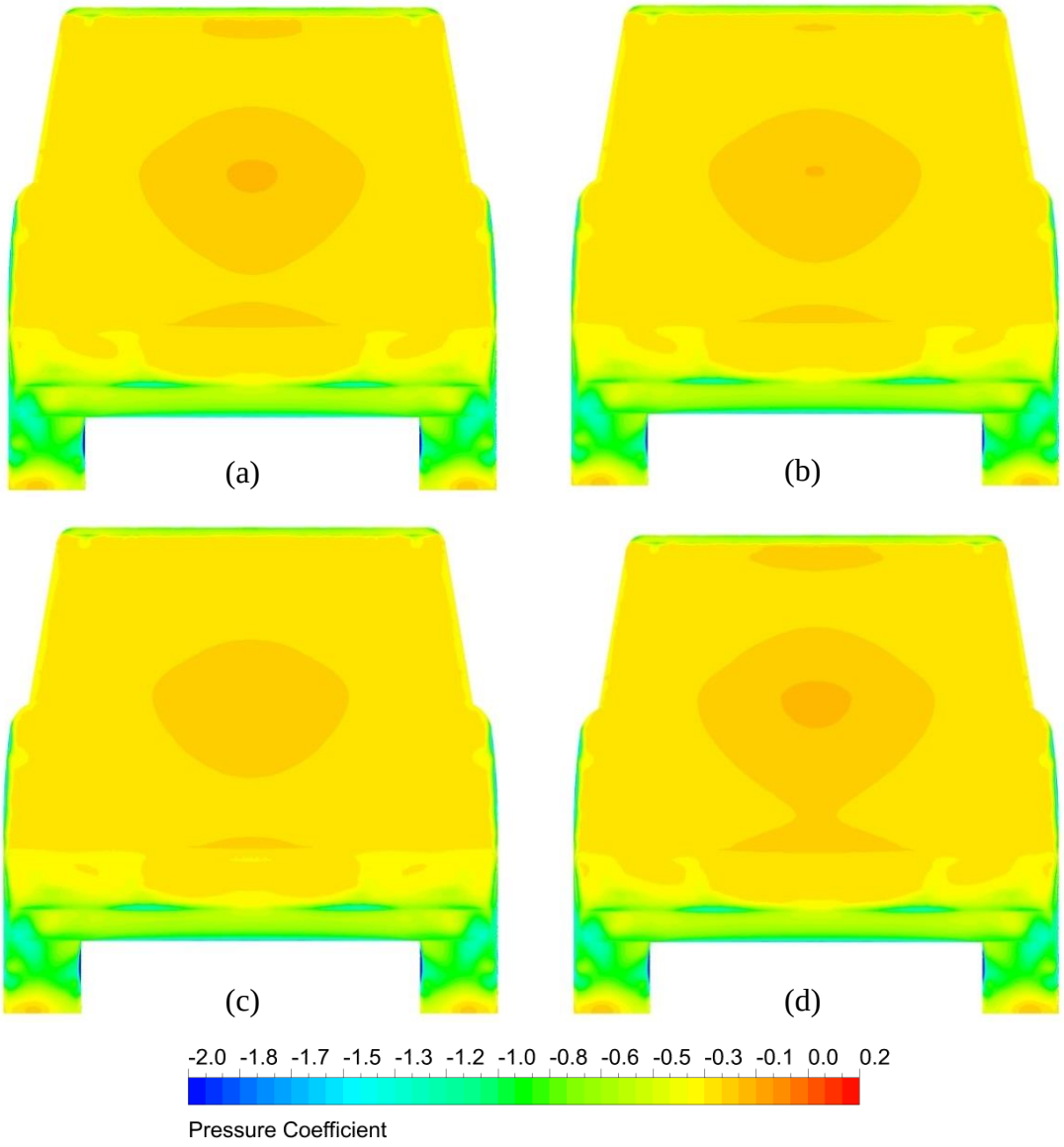

Figure 5.23: Surface pressure distribution on the baseline model of the Land Rover Discovery 4 (back view) using four types of turbulence models (a) Realizable k-ε (b) Standard k-ω (c) SST k-ω (d) Reynolds Stress Model

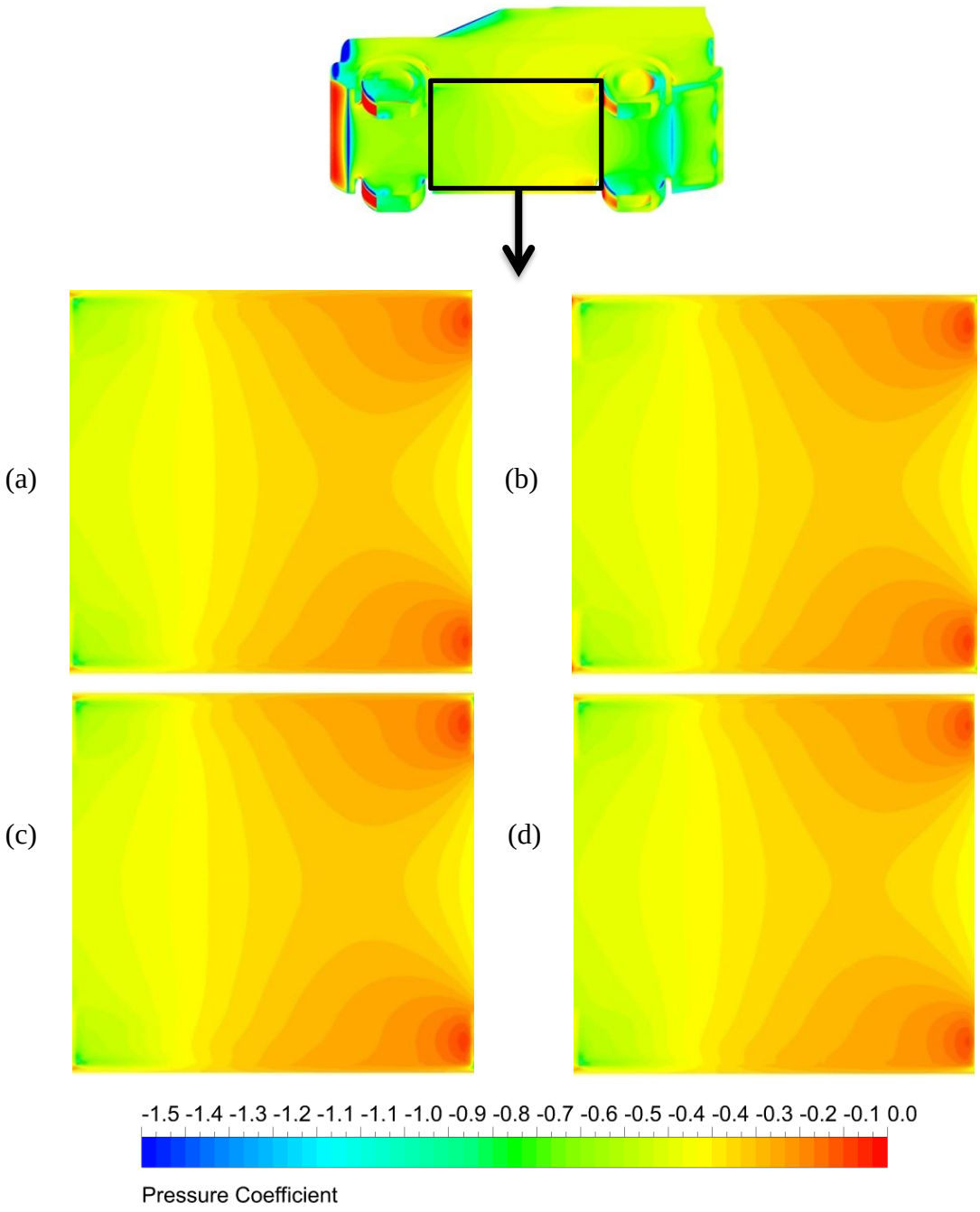

Figure 5.24: Surface pressure distribution on the underbody of the baseline model of the Land Rover Discovery 4 (bottom view) using four types of turbulence models (a) Realizable k-ε (b) Standard k-ω (c) SST k-ω (d) Reynolds Stress Model

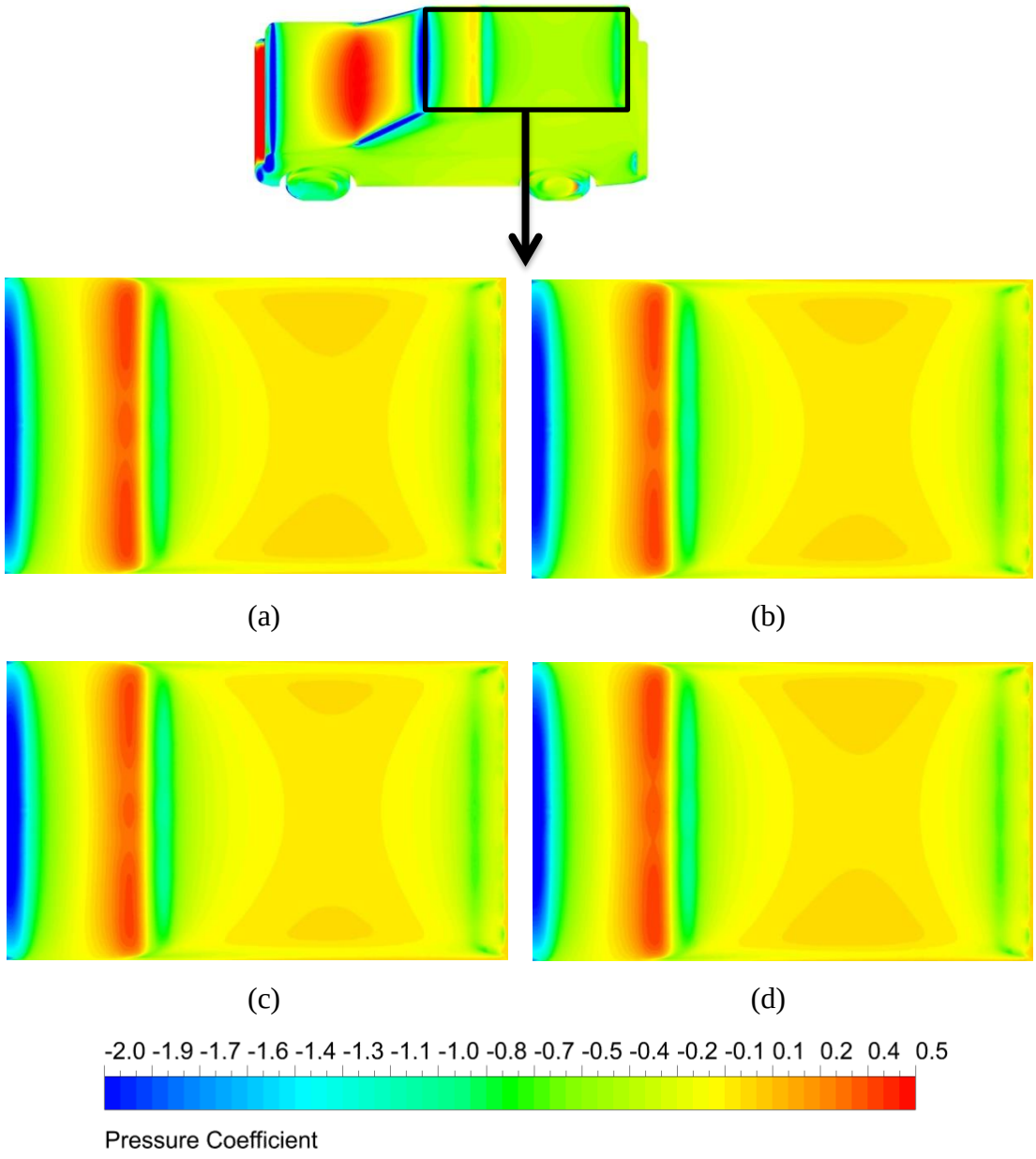

Figure 5.25: Surface pressure distribution on the roof of the baseline model of the Land Rover Discovery 4 (top view) using four types of turbulence models (a) Realizable k-ε (b) Standard k-ω (c) SST k-ω (d) Reynolds Stress Model

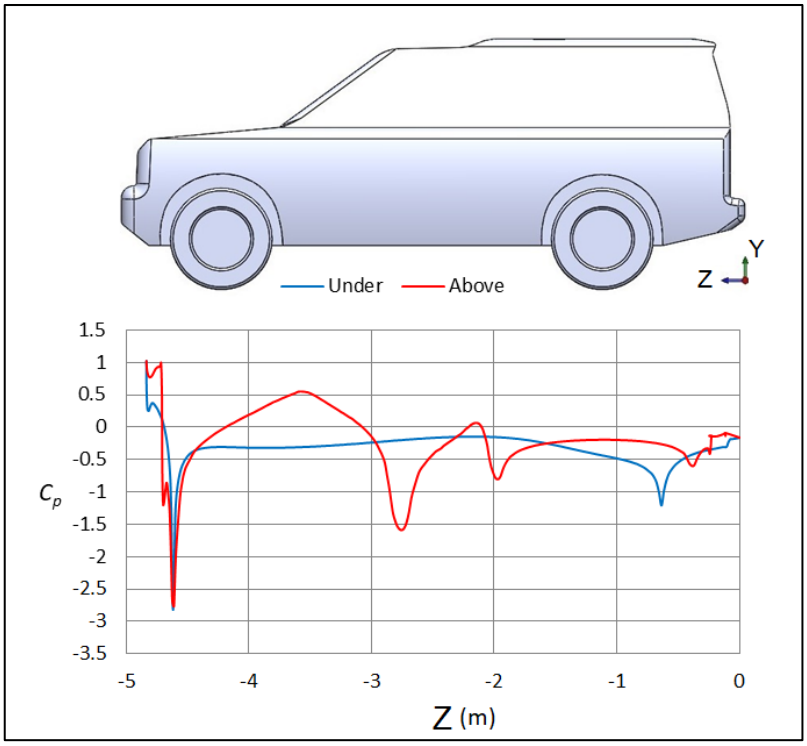

Figure 5.26: Pressure coefficient (C_p) of the baseline model of the Land Rover Discovery on the symmetry plane using the Realizable *k-ε* model

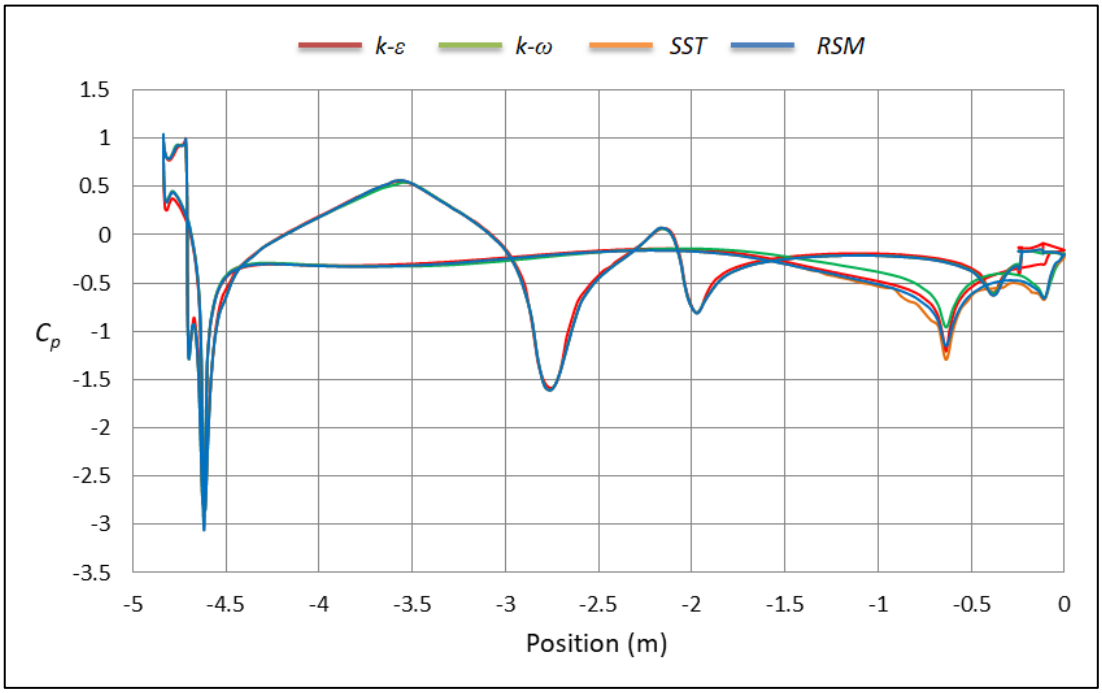

Figure 5.27: Pressure coefficient (C_p) of the baseline model of the Land Rover Discovery on the symmetry plane using four types of turbulence model (Realizable *k-ε*, Standard *k-ω*, SST *k-ω* and RSM)

5.6.2 Modified models pressure distributions

Figure 5.28 shows contours of pressure distribution on a symmetry plane for each of different case-studies: baseline, boat-tail, VGs, spare tyre, roof ditch and base bleed for a prescribed inlet velocity of 28m/s. Figure 5.28(a) shows the distribution of pressure along the symmetry plane of the baseline model. The highest pressure observed at the front of the car. There was a clear effect of the pressure starting from a distance of approximately 5m in front of the car as a result of the reaction resulting from the collision of air at the front of the car. This is one of the important reasons for putting enough space between the air inlet and the front of the car in numerical and experimental studies. There being low pressure at the front of the bonnet and the leading edge of the roof of the car. The pressure behind the vehicle was negative though increased gradually and at distance of about 2 m behind the car became positive. The pressure behind the car increased further for a relative long distance, hence confirming the importance of the size of the wind tunnel experimental studies and computational domains used throughout this work.

Adding the boat-tail reveals an increase in pressure behind the car (Figure 5.28-b). On the other hand, the pressure at the front decreased slightly. Vortex generators have little impact on the pressure behind the car but increased it near the end of the roof as detailed in Figure 5.28(c). While by adding a spare tyre to the back door of this SUV, increased the pressure for quite distance behind the car as shown in Figure 5.28(d).

Figure 5.28(e) shows the ditch on the roof of the car, also generated vortices. As expected the ditch generated more pressure than the vortex generator above the car but less behind the car. The roof ditch was along the length of the vehicle roof, but VGs were at the end of the roof. By adding base bleed modification, the pressure on the front of the car decreased significantly and the pressure behind the car increased more than other modified models. On the other hand, the base bleed reduced the low pressure at the front edge of the bonnet, which increased stability, especially the front wheels.

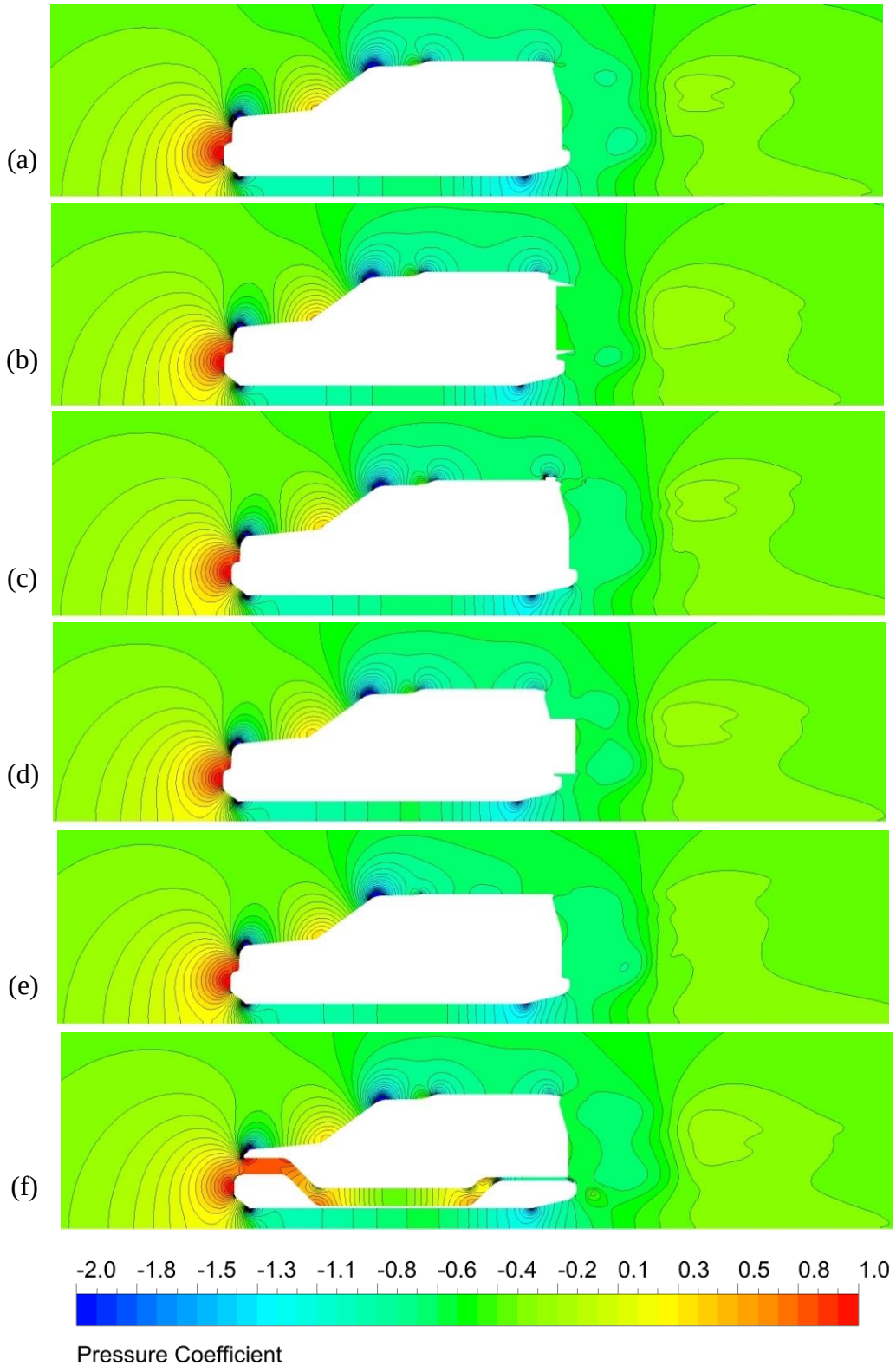

Figure 5.28: Surface pressure distribution on the symmetry plane with different case-studies (a) baseline model (b) boat-tail model (c) VGs model (d) spare tyre model (e) ditch model (f) base bleed model

Figures 5.29, 5.30, 5.31 and 5.32 show the pressure distribution on each of the salient body surfaces of the models. High pressure was predicted at the front of the vehicle, especially the front bumper, headlights and the front of the car, hence increased air resistance. However, adding some add-on devices and modifications was reduced (Figure 5.29), especially by using base bleed. In general, all models had low pressure in front of the bonnet, A-pillars, side lights and the front of the roof. Less pressure being predicted at the front of the vehicle with a boat-tail when compared to the benchmark model, especially the front grill and lower part of the front windscreen as detailed in Figure 5.29(b).

Vortex generators at the end of the roof produced less pressure on the front bumper, headlights and grill when compared the benchmark model. On the other hand, a further resistance resulted from the VGs since they increased the frontal area as shown in Figure 5.29(c). The spare tyre on the back door produced less pressure on the front bumper, grill, headlights and the low part of the front windscreen when compared with the benchmark model. The pressure near the leading edge of the bonnet and front of the roof was higher than the benchmark model. Therefore, the stability of this model was better than the baseline model, especially for the front tyres.

Figure 5.29(e) shows the pressure distribution over the roof ditch model. This modified model produced a frontal area less than the benchmark model, leading to a reduction in drag. In general, less pressure was generated than the benchmark model except on the front roof and bonnet. Adding base bleed resulted in a reduction in pressure at the front part of the vehicle. It was the best modified models regarding the pressure in front part and resulting in the greatest increase in pressure of all the modifications investigated. This model predicted moderate pressure in front of the bonnet and roof. Therefore, this model resulted in greater stability of the front tyres when compared to all other models.

Figure 5.30 shows the pressure distribution on salient back surfaces of the Land Rover Discovery 4 for each of the aforementioned case-studies. Most pressure variations were occurred at the back of the vehicle as demonstrated in Figure 5.30. Most of these pressures behind the vehicle were negative resulting in a decrease in resistance. Two low-pressure areas behind the model were evident, these being near the end of the roof and lower part of the rear bumper. The boat-tail increased the pressure especially inside as shown in Figure 5.30(b). The VGs at the end of the vehicle roof increased the pressure behind on the back door though low-pressure areas are also evident in Figure 5.30(c).

Increasing the pressure behind the Land Rover Discovery 4 was achieved by placing the spare tyre on the back door. This led to increased pressure in most areas behind this model

as detailed in Figure 5.30(d); the maximum pressure occurring the upper part of the spare tyre. The pressure distribution on this model was homogeneous. Figure 5.30(e) shows the pressure distribution on the back door for the roof ditch model. This led to increase the pressure behind the vehicle especially near the edge between the roof and the back door. The base bleed revealed an increased pressure was increased significantly as shown in Figure 5.30(f).

Figure 5.31 shows surface pressure distribution on the underbody of the Land Rover Discovery for multiple case-studies (baseline, boat-tail, VGs, spare tyre, ditch on the roof and base bleed). It is clear that the baseline model had the highest pressure in this section. All modified models revealed similar negative pressure profiles over this part of the vehicle.

Figure 5.32 shows the surface pressure distributions on the roof of the Land Rover Discovery 4 for each of the case-studies with a prescribed inlet velocity of 28m/s. The boat-tail increased the surface area as shown in Figure 5.32(b). The overall aerodynamics behaviour of this modified model was similar to the benchmark model. However, the increased area resulted in increased pressure above the vehicle. Placing VGs at the end of the roof results in pressure an increase especially in front of them. On the other hand, small region of low-pressure area appears near the rear of these devices.

Figure 5.32(d) shows calculations of the pressure distribution on the top surfaces of the spare tyre model. This modification led to increase the pressure above the car especially at the rear end. The distribution of pressure on the roof of the spare tyre model was homogenous. Inclusion of the ditch as expected increased the pressure over the roof, especially at the end as shown in Figure 5.32(e). This can lead to an increase in the road stability of the vehicle, especially at high speeds. Adding the base bleed increased the pressure above the vehicle as shown in Figure 5.32(f).

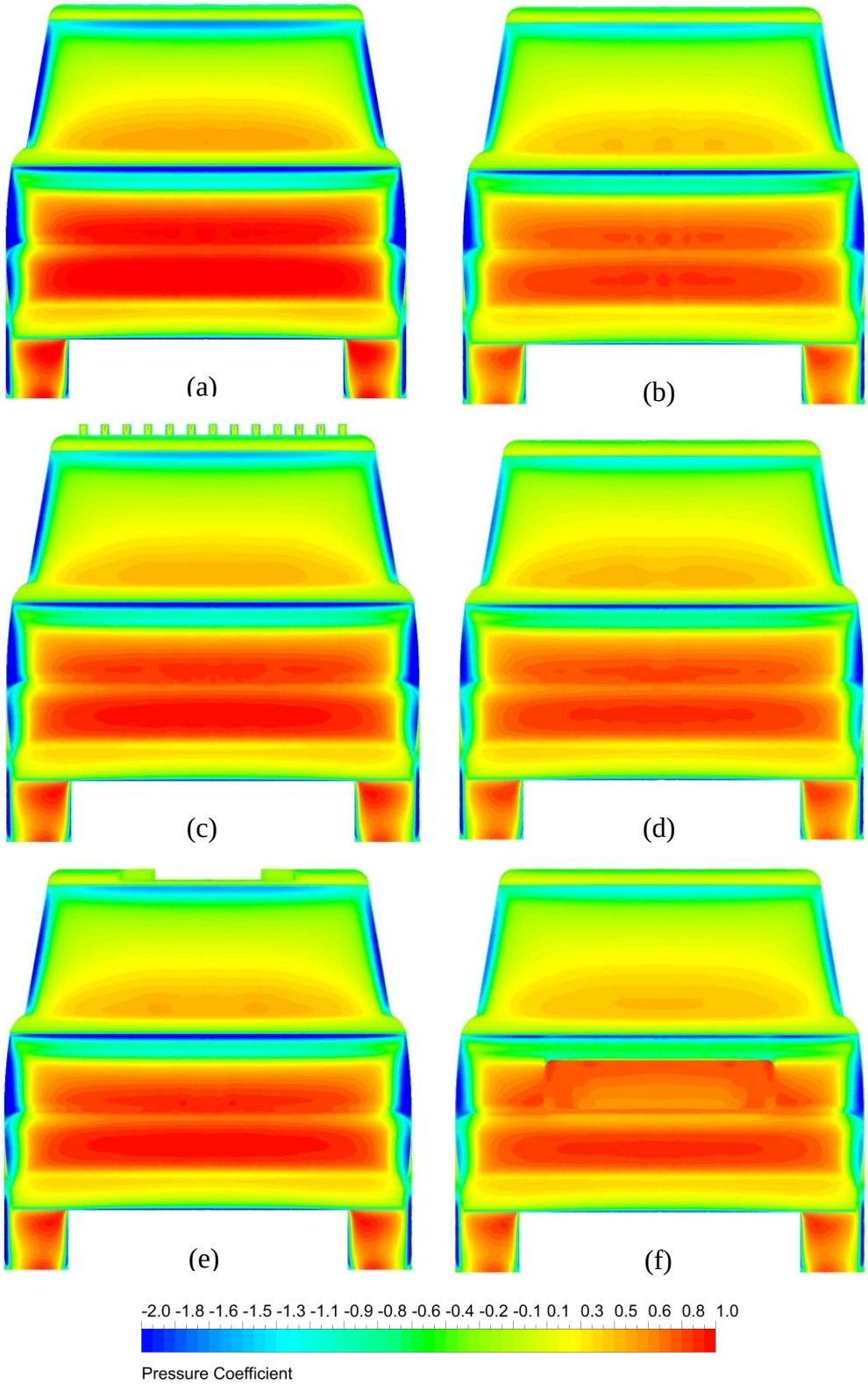

Figure 5.29: Surface pressure distribution on the Land Rover Discovery 4 (front view) with different case-studies (a) baseline model (b) boat-tail model (c) VGs model (d) spare tyre model (e) ditch model (f) base bleed model

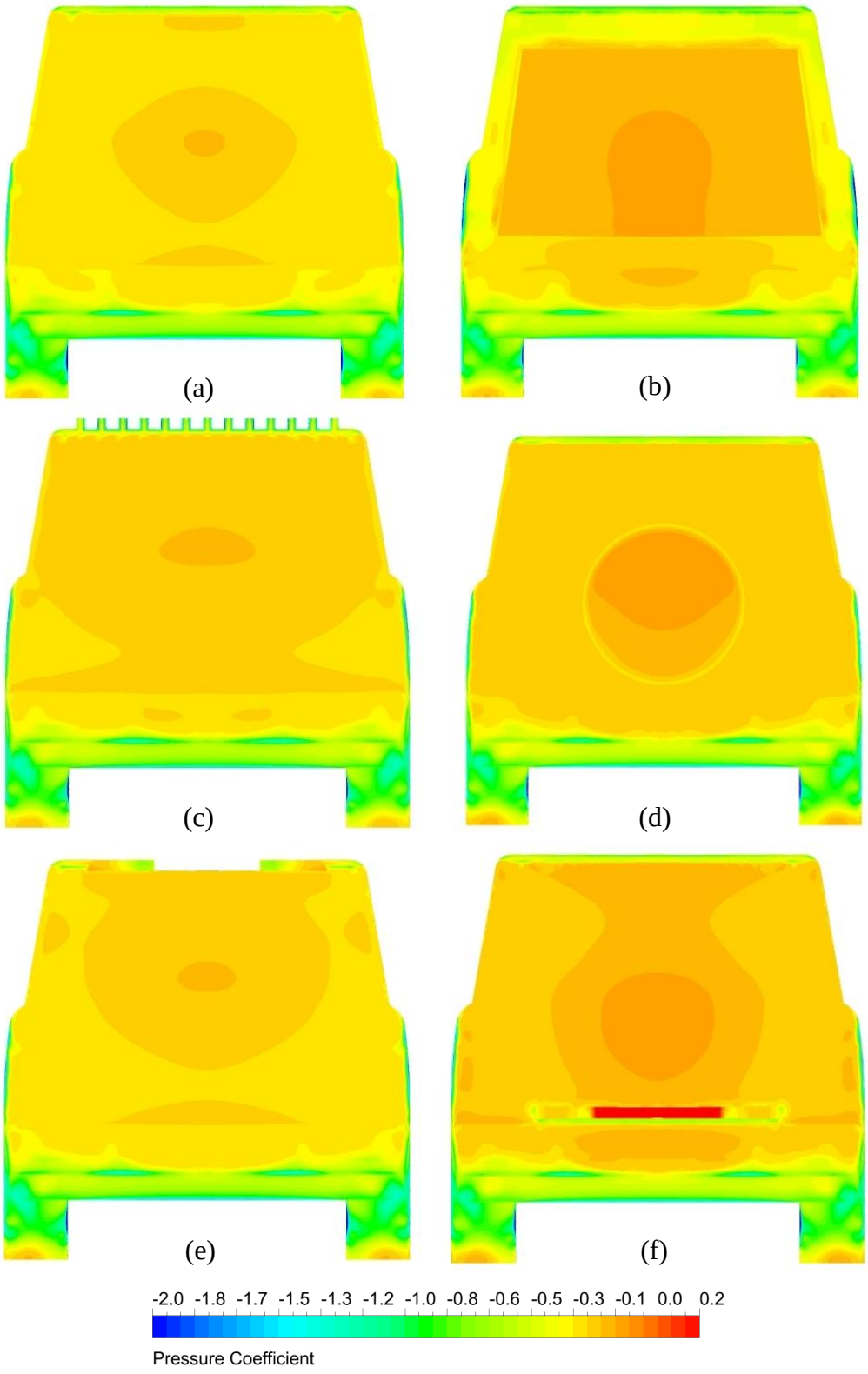

Figure 5.30: Surface pressure distribution on the Land Rover Discovery 4 (back view) with different case-studies (a) baseline model (b) boat-tail model (c) VGs model (d) spare tyre model (e) ditch model (f) base bleed model

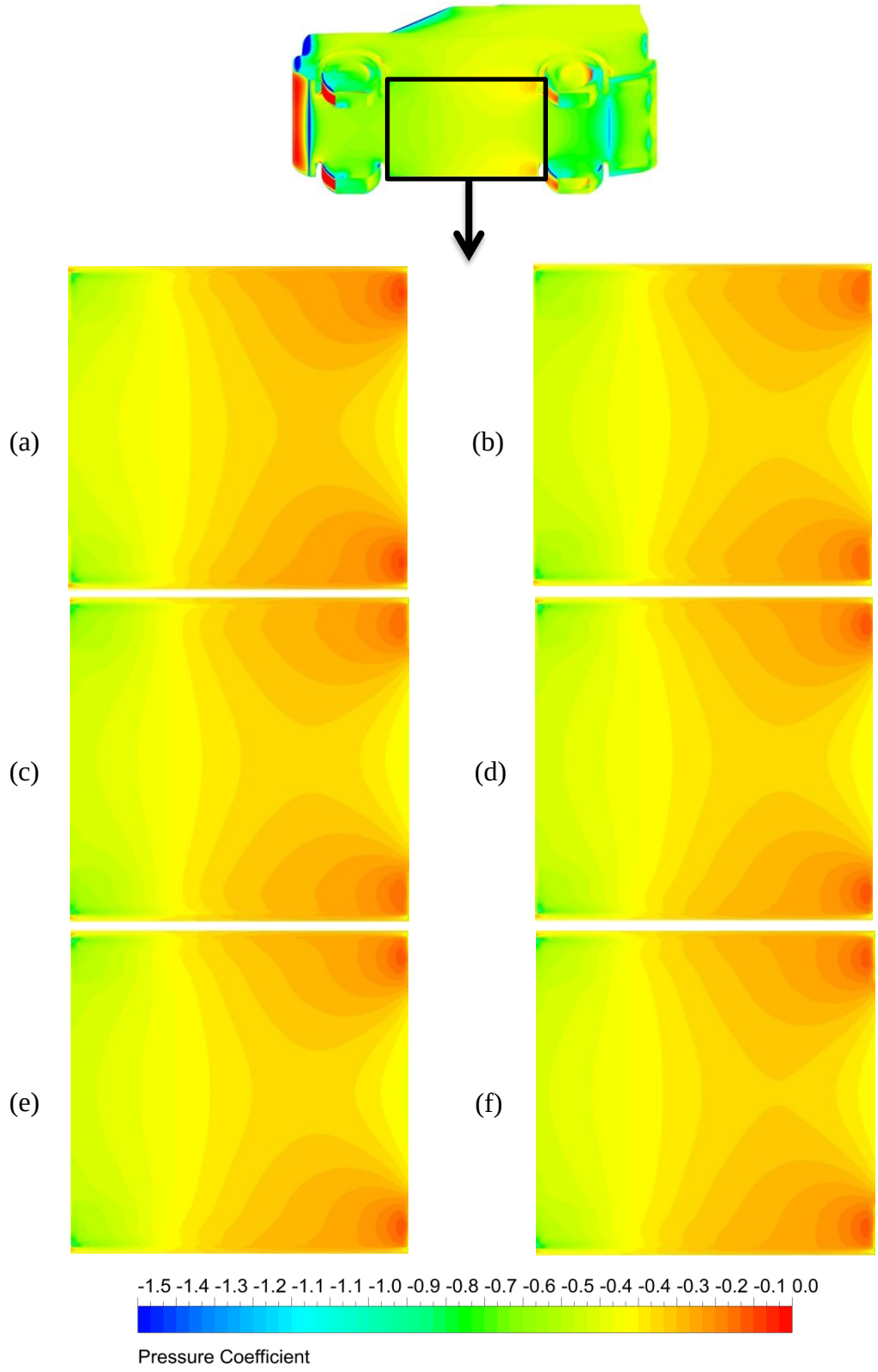

Figure 5.31: Surface pressure distribution on the underbody of the Land Rover Discovery 4 (bottom view) with different case-studies (a) baseline (b) boat-tail (c) VGs (d) spare tyre (e) roof ditch (f) base bleed

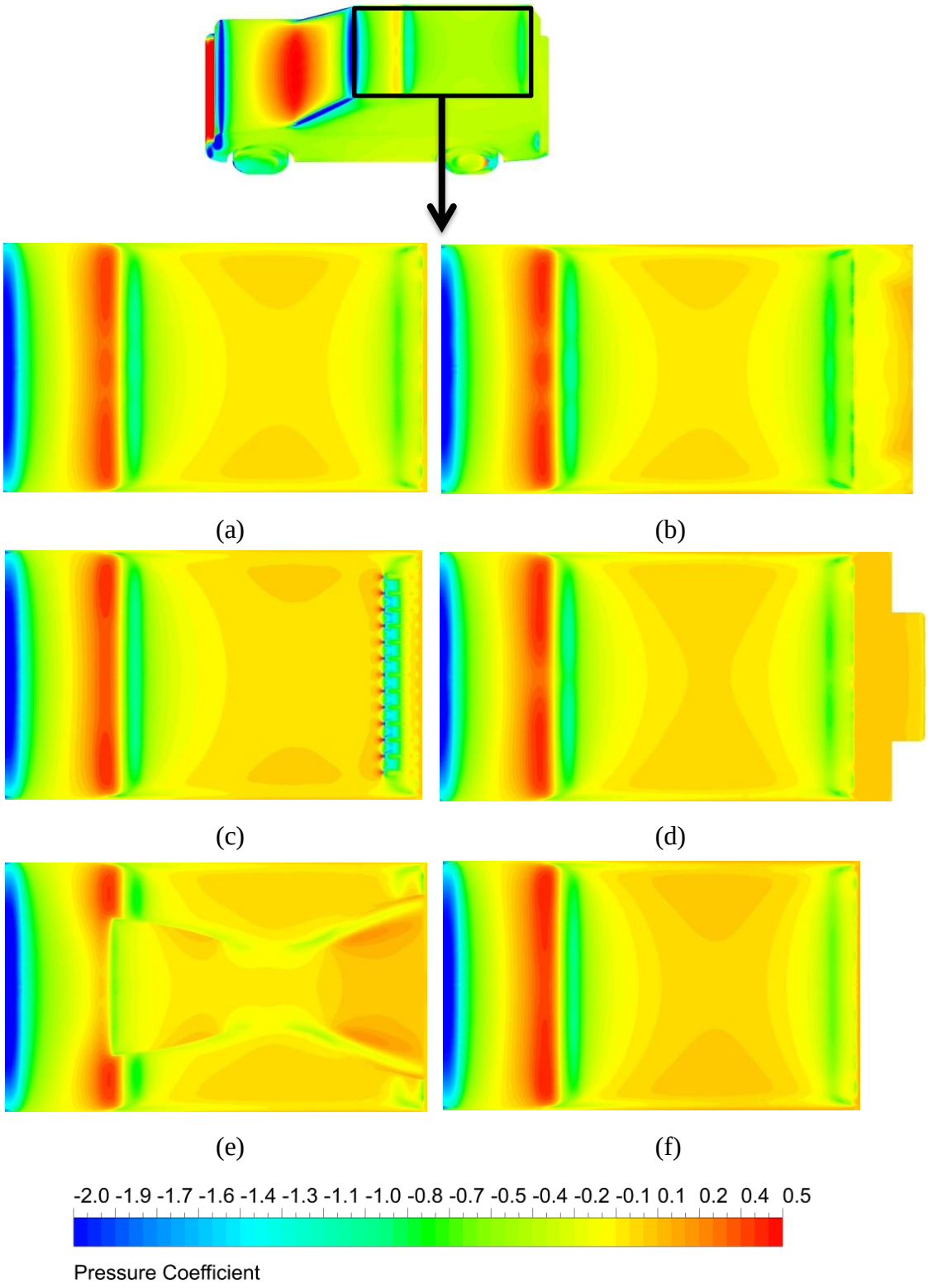

Figure 5.32: Surface pressure distribution on the roof of the Land Rover Discovery 4 (top view) with different case-studies (a) baseline model (b) boat-tail model (c) VGs model (d) spare tyre model (e) ditch model (f) base bleed model

Figure 5.33 shows the pressure coefficient (C_p) computations for each of different case-studies on the symmetry plane using the realizable k-ε turbulence model. The vertical axis represents the pressure coefficient and the horizontal axis represents the vehicle length starting rear bumper and extending -4.835m to the front bumper. The maximum pressure coefficient was one for all case-studies located at the front bumper then decreased significantly at the front edge of the bonnet and then increased again at the front windscreen. The pressure coefficient decreased further at the roof for all models. This resulted in a significant increase in velocity with a relatively high-pressure coefficient evident at spare tyre. This increased at the front curvature of the roof. A ditch on the roof produced a different pressure coefficient above the roof due to the convergent-divergent path resulting in greater stability when compared with the other models. Furthermore, the pressure coefficient decreased due to the speed increase. The pressure coefficient of all models, except the ditch on the roof and vortex generators, decreased at the end of the roof. The pressure coefficient on the roof ditch model did not change at the end of the car roof. There was a significant increase in the pressure coefficient due to the inclusion of the VGs which dropped suddenly then increased again.

In general, the pressure coefficients for all case-study models were similar at the front and middle of the vehicle but were very different at the ends. The pressure coefficient was almost constant in the lower part of the car (underbody) except two regions which were the edge between the front bumper and the underbody in the front section and at the edge between the underbody and the diffuser at the rear section. Figure 5.33 shows that each of the modifications have greater pressure coefficients behind the vehicle when compared with the benchmark. Base bleed model revealed the lowest pressure coefficient in the front of this model. Pressure coefficient above the modified models where higher than in the benchmark model especially for the roof ditch and VGs.

Statistical testing by using ANOVA reveal differences in the pressure distributions on the vehicle surface between all models (benchmark and modified models). Table 5.9 shows the results of the statistical testing by using ANOVA. If the variability between vehicle models was large relative to the variability within vehicle models, data implying that the means of the pressure coefficient from which the data were drawn were significantly different. F statistic is a measure of the variability between treatments divided by a measure of the variability within treatments [102]. The calculated F-value (13.73) was larger than F critical (F from table, 2.22) as shown in Figure 5.34 and that means the variability between treatments (pressure coefficients) was large relative to the variation within treatments, and the null hypothesis of equal means (H_0) was rejected. The test of

one-way ANOVA has confirmed that the pressure distributions on the vehicle surface of benchmark and modified models of the Land Rover Discovery were significantly different. All calculations of this statistical method are shown in Appendix (A).

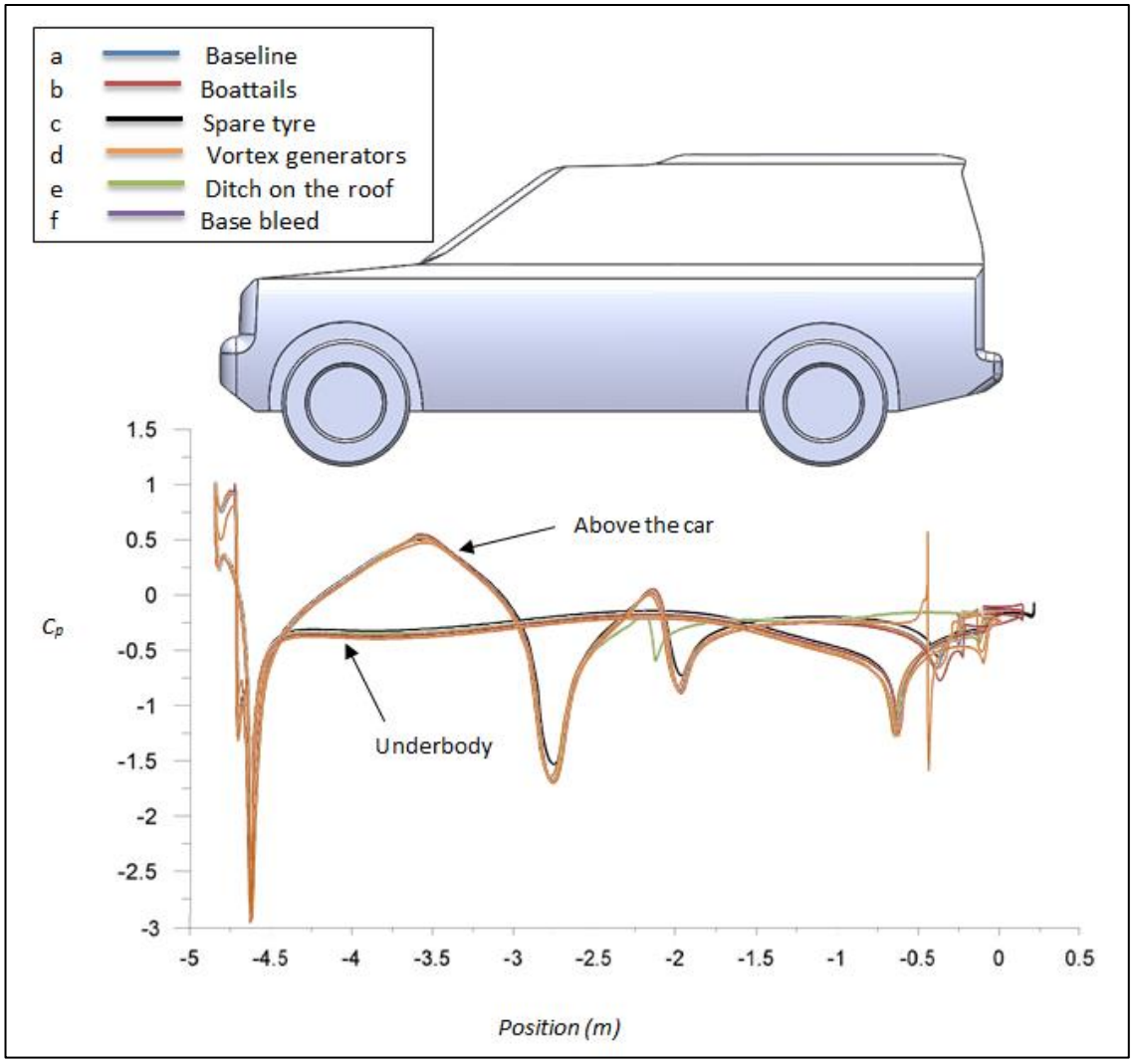

Figure 5.33: Pressure coefficient along the symmetry plane for the Land Rover Discovery with different case-studies (a- baseline model, b- boat-tail, c- spare tyre, d- VGs, e- ditch on the roof and f- base bleed)

Source of Variation (S.O.V)	Sums of Squares (*SS*)	Degrees of Freedom (*df*)	Mean Squares (*MS*)	*F*
Between Treatments	2.755	5	0.551	13.73
Error (or Residual)	39.967	996	0.0401	
Total	42.722	1001		

Table 5-10: The results of the statistical testing by using ANOVA

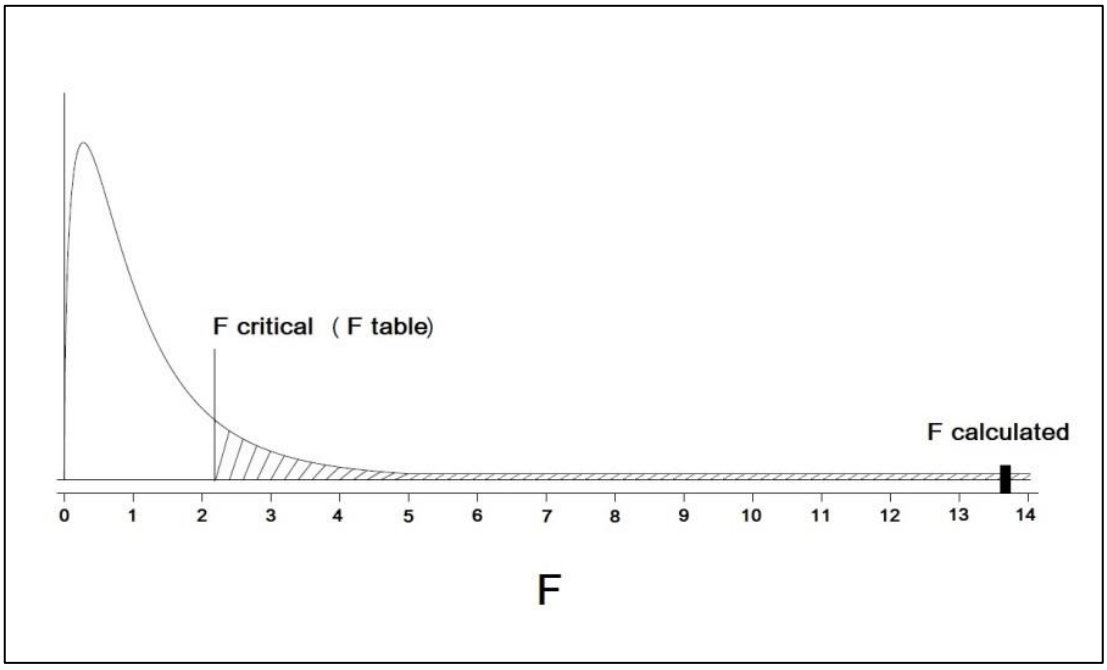

Figure 5.34: *F* critical and *F* calculate

5.7 Drag and lift coefficients

The boat-tail, spare tyre on the back door of the car, vortex generators over the end of the roof of the car, ditch on the roof and base bleed were used to improve the aerodynamic behaviour of Land Rover Discovery 4. The realizable *k-ε* turbulence model was implemented for the simulation. Figure 5.35 and Table 5.10 show the drag coefficient as a function of Reynolds number for five types of modified models in addition to the

benchmark model. The drag coefficient decreases with increasing Reynolds number except the spare tyre model which decreased, until a value of 11.79 million where upon a slight increase is apparent. The best modification for the SUV regarding drag coefficient was base bleed because the minimum drag coefficient over a wide range of Reynolds number (9.7×10^6 to 13.87×10^6). The drag coefficient of the baseline model was about 0.4 which is comparative to 0.371 for the model with base bleed.

Figure 5.36 shows the lift coefficient as a function of Reynolds number for five types of modified models in addition to the benchmark. All modified models produced lift coefficients less than the benchmark model which displayed a positive lift coefficient while all modified models had negative lift coefficient. Negative values of the lift coefficient imply more downforce which, in turn, became more stable. The roof ditch model had the highest downforce because this due to increased pressure above the vehicle. Increasing downforce can lead to increase the rolling resistance at high speed. The base bleed and spare tyre models produced moderate lift coefficients. The lift coefficient for the spare tyre model appeared to be mostly independent of Reynolds number (Figure 5.36).

All the modified models provided better drag and lift coefficients than those in the benchmark model. The best modifications in terms of the highest fuel consumption efficiency and the road stability were achieved by putting the spare tyre on the rear door of the SUV. Though the base bleed and boat-tail render comparable drag coefficients, but the spare tyre is less prohibitive compared to other types of modifications. Moving the spare tyre to the back door of the Land Rover Discovery 4 increased the cargo space and the complex mechanism used to install the spare tyre on the underbody can be replaced with a simple standard mechanism for fixture to the back door. The drag coefficient devalued for the model including the spare tyre was about 0.372 (down from 0.4 in the baseline model) with a lift coefficient of -0.102 (down from 0.03 for the baseline model). It can therefore be postulated that this particular modification will improve the fuel consumption and the stability of the vehicle.

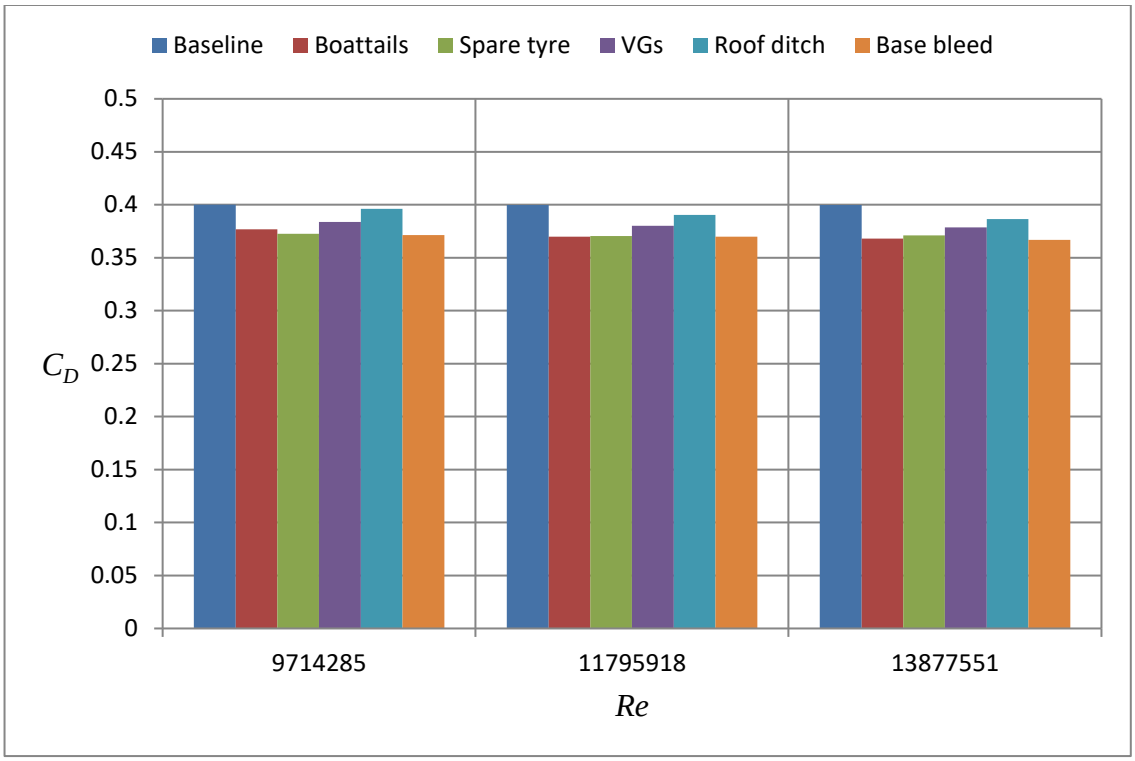

Figure 5.35: Drag coefficient as a function of a Reynolds number for different case-studies of the Land Rover Discovery (a- baseline model, b- boat-tail, c- spare tyre, d- VGs, e- ditch on the roof and f- base bleed).

Re **(× 10^6)**	***C_D***					
	Baseline model	Boat-tail model	VGs model	Spare tyre model	Roof ditch model	Base bleed model
9.71	0.4001	0.3769	0.3836	0.3724	0.3962	0.3714
11.8	0.3999	0.3699	0.3801	0.3704	0.3902	0.3697
13.9	0.3997	0.3679	0.3785	0.3711	0.3864	0.3669

Table 5-11: C_D as a function of a *Re* for different case-studies of the Land Rover Discovery 4

Re **(× 10^6)**	***C_D* reduction (%)**				
	Boat-tail model	VGs model	Spare tyre model	Roof ditch model	Base bleed model
9.71	5.798	4.123	6.923	0.975	7.173
11.8	7.502	4.951	7.377	2.425	7.552
13.9	7.956	5.304	7.155	3.327	8.206

Table 5-12: C_D reduction as a function of a Re for different case-studies of the Land Rover Discovery 4

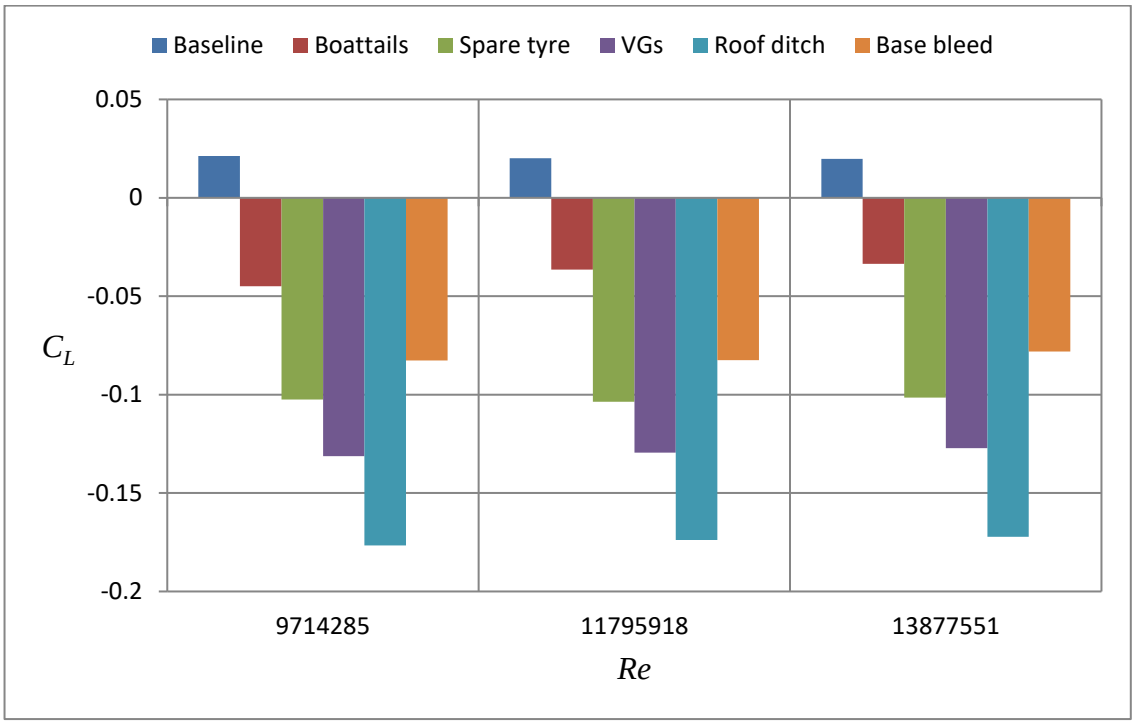

Figure 5.36: Lift coefficient as a function of a Reynolds number for different case-studies of the Land Rover Discovery (a- baseline model, b- boat-tail, c- spare tyre, d- VGs, e- ditch on the roof and f- base bleed).

Chapter 6 Discussion

All types of turbulence models used to simulate the baseline model of the Land Rover Discovery 4 (realizable k–ε, standard k-ω, SST k-ω and RSM) provided good agreement with the experimental data, but the result of the realizable k–ε was the closest. The realizable k–ε turbulence model provides merit results in a reasonable computational time. Therefore, the k-ε turbulence model was used to simulate all modified models of the Land Rover Discovery 4 in the current study. Seventy modified models were tested in the current study using the realizable k–ε turbulence model. Twelve different models for each modification were tested except eighteen for the roof ditch model and sixteen for the base bleeds model in order to achieve the best design for each aerodynamics modification.

The lowest lift coefficient was achieved by using the roof ditch technique due to decreasing in air velocity at the end of the vehicle roof and that leads to increase in the pressure above the vehicle. The same dimensions of the standard tyre of the Land Rover Discovery 4 and simple mechanism to install it were used to avoid extra weight and manufacturing costs. Mechanism of installation of spare tyre under chassis is more expensive and complicated than on the back door. Therefore, using this technique can lead to save a lot of money to the company and passengers. A roof ditch could be added by fixing a foam to the roof of the vehicle, but that leads to increase the frontal area of the vehicle. In general, increasing frontal area means increasing in drag coefficient. A professional designer and special material will be required to add this technique which means more extra money is needed.

6.1 Conventional aerodynamic reduction techniques

To reduce computational time simplified geometries of road vehicles have been employed to evaluate their aerodynamics using CFD. The results obtained were verified using previous numerical studies where possible validated using experimental measurements. Most of these studies focused on evaluation of drag and lift coefficients. However, improving the drag and lift coefficients and creating a balance between them were not studied in the previously so has been investigated throughout this work. However, some of the proposed aerodynamic improvements have drawbacks as they cannot be manufactured. For example, the boat-tail used in the previous studies for the Ahmed model and heavy trucks can lead to an increase the overall weight and length of road vehicles. Some aerodynamic devices used for SUVs (such as the collapsible wind friction

reduction on the back door, rear screen device and fairing) led to a decrease the drag coefficient by decreasing the wake behind the vehicle, but these types of aerodynamic devices cause an increase in the overall weight of road vehicles which lead to an increase of rolling resistance. The spare tyre on the back door can avoid overweighting and will have lower manufacturing costs, considering installation of spare tyre under chassis is more expensive and complicated than on the back door.

Different designs of VGs were used in the previous studies, but VGs as an aerofoil geometry were not studied before. The new design of VGs (similar to the aerofoil) has been shown to create convergent-divergent passages. This improved the pressure above the car and behind it. The frontal area and the total surface area of the VGs model increased leading to an increase in the viscous force, but a decrease in the pressure force.

Since the air flow above the car is higher than under the it modifications above the car are more effective. For instance, a ditch on the roof was shown to increase the pressure above and behind the vehicle. This model had less frontal area than the baseline model. However, adding the material to necessitate the ditch would lead to an increase the frontal area and the overall height of the vehicle.

Different types of base bleed were used in the previous studies to reduce the drag coefficient of road vehicles. However, the previous studies did not pay attention to the effects of their designs on the visibility and the comfort of the passengers. A new design of base bleed was therefore proposed in this work thereby avoiding the disadvantages of previous designs. On the other hand, this aerodynamic modification is expensive and involve extensive vehicle redesign.

6.2 CFD techniques

Flow separation at the rear section of road vehicles is responsible for the wake formation which leads to increased air resistance. Therefore, most modifications suggested throughout this work have aimed improve the aerodynamic behaviour at the rear part of the Land Rover Discovery 4. In general, road vehicles operate in a turbulent flow field and there are a number of turbulence models to cover a wide range of engineering applications.

Available turbulence models have their own advantages and limitations. The RANS approach has a variety of turbulence models (e.g. k-ε, k–ω and RSM turbulence models). Wall functions and non-wall function turbulence models are also available. k-ε and RSM are examples of wall function based models for the simulation results near the wall. The

k–ω turbulence model provides greater detail when the mesh is refined enough near the wall surface because this type of turbulence model does not use wall treatment. In general, LES approach is better than the RANS approach in terms of accuracy, but it has been shown throughout this work to be significantly more computationally than the RANS approaches. In this work, the Ahmed geometry was used as a benchmark model to investigate mesh refinement, assess grid/turbulence model combinations, the affect of model size and the effect of a flat plate located under main geometry. The full and 55% scale models of the Ahmed model were investigated throughout the work described in the previous two chapters of this work.

6.3 Optimization methods

Realizable k–ε, SST and LES turbulence models were used to simulate the Ahmed model. The SST turbulence model was accurate near the wall surface of this model at relatively low Reynolds numbers, but this turbulence model is not a practical choice for high Reynolds number flows because a large number of cells must be allocated near the wall surface. In general, LES is more accurate than RANS but computationally a lot more expensive. The simulate time of Ahmed model using the RANS approach was 27 times faster than that of LES, but does not sacrifice significant accuracy, therefore RANS approach has better justification for the intensive simulation studies in this work.

Computational domain size did affect many of the results detailed in the previous chapter. Therefore, the variety of dimensions of computational domain sizes investigated throughout the CFD aspects of this work. The pressure force increased with decreasing computational domain size. Viscous forces were almost constant for all different sizes of computational domain simulated because of their dependence on the total surface area of the vehicle. No general rules were established for mesh creation. Flexible mesh (tetrahedral) were used for vehicles due to the presence of sharp edges and curved surfaces, but this type of mesh needed a much more density to capture all flow features than a hexdominate analogue. VCRs around the vehicle were therefore used to control cell sizes. It was found that placing a flat plate under the body model (used to install scale model inside the wind tunnel) affect the lift force because this plate causes a change in the velocity distribution. Hence should not be used to calculate the lift coefficient.

6.4 Land Rover Discovery model

The Land Rover Discovery 4 was used as a benchmark model throughout the work described in the previous couple of chapters. The full-scale model of this vehicle was validated using empirical data evident in the literature. The realizable k–ε, standard k-ω, SST k-ω and RSM turbulence models were used in these simulations. All types of turbulence model were in good agreement with experimental data. The realizable k–ε being closest. The k-ε and RSM turbulence models use wall treatment function to correct the simulation results near the surface of the vehicle. The results of RSM were similar to k-ε turbulence model, but RSM computationally was more expensive; it being a six additional equations model. Therefore, the realizable k-ε turbulence model was used to simulate all modified models of the Land Rover Discovery 4 in this work.

It was found that the pressure behind the car significantly changes with distance. The size of the computational domain in the numerical study and the wind tunnel experimental study was shown to be very important. As mentioned in section 5.3 (Figure 5.6, pp. 143) in this work, the pressure force decreases with increasing of computational domain size. Furthermore, the size of the computational domain affects the blockage ratio.

Viscous forces were almost constant for all different sizes of computational domain while pressure force increases with decreasing of the computational domain size. When the blockage ratio increases, C_D increases, but C_L decreases. Six different sizes of computational domain were used in this study; however, only one size was used in the experimental investigation. The MIRA wind tunnel was more suitable for the scaled model than the full-scale model because with the full-scale model of the Land Rover Discovery 4 the blockage ratio was very high. The cross-sectional area of the test is 4.4 m × 7.9 m, maximum wind speed is 40m/s (90mph), with a fan power of 37 kW. The overall length of this wind tunnel is 15m [15, 101].

Pressures were found to be quite high on the front bumper, headlights and front grill of the vehicle, whilst lower pressures were calculated low on the front bonnet, A pillars, side lights and the leading edge of the roof, in comparison with the maximum pressure coefficient at the stagnation point, two vortices behind the benchmark model being evident. Modification to the external design of the vehicle and adding some devices led to smaller vortices behind the vehicle. Five techniques were used to improve the aerodynamic performance reducing drag and increasing stability of the SUV. 71 different CFD models of the Land Rover Discovery 4 were investigated to achieve the best model of this vehicle regarding the drag and lift coefficients. Furthermore, ANOVA statistical

technique was used to evaluate the numerical results of the pressure distributions on the Land Rover Discovery models. A one-way ANOVA of the pressure coefficient numerical results revealed a *F* value (see Appendix A for more details on calculations) larger than the critical *F*, as shown in Table 5.10 and Figure 5.34. The test confirmed that the pressure distributions on the vehicle surface were significantly different. Multiple views of the pressure contours show these differences with the magnitude of the pressure coefficients for all models.

6.5 Modifications and add-ons

The external design of the Land Rover Discovery 4 was shown not to be streamlined leading to the creation of vortices behind this vehicle. These vortices were reduced and become more uniform by modifying the external design or by adding devices. The vortices behind the vehicle were non-uniform because of low pressure near the rear door and bumper after separation of flow at the end of the roof. The vortices behind the vehicle were significantly reduced by adding the boat-tail to the rear of the car with the airflow being direct through the plates the device. Putting the spare tyre on the rear door of the vehicle effectively fills some of wake region, there by streamlining the back of the vehicle.

Vortex generators were placed near the separation edge controlled and delayed the air flow separation, which improved the aerodynamic behaviour. This type of aerodynamic devices clearly affected the drag and lift coefficients because they are placed above the vehicle. The roof ditch has increased the pressure at the end of the roof by decreasing the velocity.

The best aerodynamic modifications in terms of drag coefficient were achieved by using base bleed, the spare tyre on the back door and boat-tail, respectively. The lowest drag coefficient was achieved by using base bleed as it led to a reduction in the drag and the quantity, size and location of vortices behind the vehicle of the reduction in air flow over the top of the vehicle. However, implementation of the of this device requires significant prohibitive re-design of the vehicle. The boat-tail affects the visibility of the passengers as well as increases the overall weight of the vehicle. Surprisingly, movement of the spare tyre to the back of the vehicle produced the most favourable reduction in drag for modest impact on cost and no increase the weight of the vehicle.

The best aerodynamic modifications in terms of lift coefficient were achieved by using roof ditch, VGs and the spare tyre on the back door, respectively. The roof ditch technique

works to decrease the velocity of air at the end of the vehicle roof which leads to an increase in the pressure. However, this technique needs the re-design of the vehicle which means it could be expensive. A roof ditch technique could be added by fixing a foam to the vehicle roof but that leads to the increase of the frontal area of the vehicle. In general, this would increase the frontal area ergo the drag coefficient, VGs also increase the stability of the vehicle, but generates greater drag than the spare tyre. The spare tyre technique has the second lowest simulated drag and lift coefficients. Moreover, movement of the spare tyre to the back door is very easily implemented ergo the less prohibitive of the modifications suggested in the previous two chapters. On the other hand, this increases the overall length of the SUV.

6.6 The effect of lift and drag

All drag coefficients for road vehicles are positive. Reducing the drag coefficient implies reduction in fuel consumption. Whence all researchers and car companies aim to reduce C_D as much as possible. The lift coefficient is more complex to understand because it can be positive or negative. Positive lift coefficient indicates to less stability of vehicles on the road. Negative lift coefficient implies more stability of vehicles on the road, but on the other hand, high negative C_L can lead to an increase in the rolling resistance, which increases fuel consumption. Therefore, the best design of the road vehicle is when the C_D is as low as possible and the C_L is negative but not by a high magnitude. There is no rule to calculate the result of the C_D and C_L because these are dimensionless quantity. Figure 6.1 shows the results of the effect of lift and drag coefficients for all models of the Land Rover Discovery 4. The next equation was used to calculate the combined effect of lift and drag.

$$C_R = \sqrt{C_L^2 + C_D^2} \tag{6.1}$$

It should be noted that Figure 6.1 does not give a complete perception of the best model. For example, boat-tail was the best aerodynamic device for the Land Rover Discovery 4 depending on the results in Figure 6.1. There are some limitations for this type of aerodynamic devices. Adding this part can lead to increase the overall weight of the vehicle and overweight can lead to increase rolling resistance. Roof ditch model has drag coefficient less than the baseline model and with a negative lift coefficient but in this figure, this model has high combined effect of drag and lift. The equation 6.1 does not include other negative aspects such as the visibility effect, overweight and length increase.

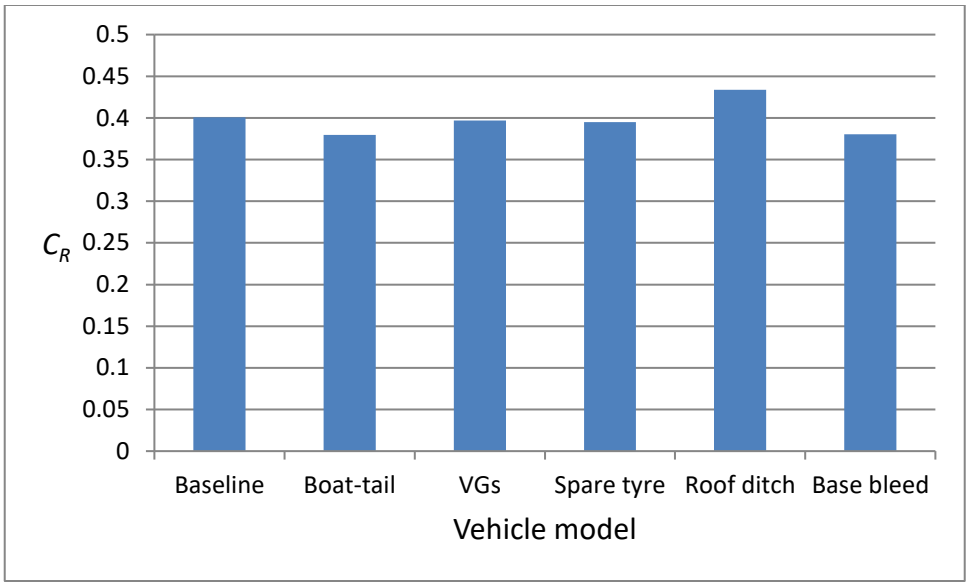

Figure 6.1: The combined effect of lift and drag coefficients for all models of the Land Rover Discovery 4

6.7 Fuel consumption

Reducing drag coefficient of road vehicles can improve acceleration, top speed and fuel economy. Air resistance is reported to be about 50% of the total resistance of the road vehicles at 27.7m/s [4, 7, 8, 9]. The Land Rover Discovery (4-SDV6 GS) consumes fuel about 30.4–36.7 mpg depending on the road conditions [14]. An average of 12,000 miles per year is considered the standard for passenger vehicles. Therefore, the benchmark model consumes about 1486.4 – 1794.5litre per year of fuel depending on the road conditions. Assuming the 50% of power of the road vehicle moving at 27.7m/s (100km/h) is dissipated by the air resistance and the rest is to overcome the rolling resistance, the save in the fuel consumption of modified models the Land Rover Discovery 4 can be estimated. For example, the base bleed model reduced the drag coefficient by about 7%, which means that it can reduce fuel consumption by approximately 3.5%. All data on the fuel consumption saving for different modifications of the Land Rover Discovery 4 in this work are presented in Table 6.1. A fuel (unleaded) price of 131.5p/litre (as of 19 October 2018) was used for the cost analysis [103]. It should be noted that Jaguar Land Rover U.S. sales reached 105,104 units in 2016 and more than 500,000 units worldwide in the same year [14]. Using spare tyre modification (suggested as the optimum modification) could lead to an average 28,325,000 litres (£37,247,375) of fuel saving per year.

Model	Fuel consumption per year (litre)	Fuel saving per year (litre)	Cost saving (Pound)
Baseline	1486.4 – 1794.5	-	-
Boat-tail	1443.2 – 1742.4	43.2 – 52.1	56.81-68.51
VGs	1455.8 – 1757.5	30.6 – 37	40.24-48.65
Spare tyre	1435.1 – 1732.5	51.3 – 62	67.45-81.53
Roof ditch	1479.1 – 1785.6	7.3 – 8.8	9.6-11.57
Base bleed	1433.2 – 1730.3	53.2 – 64.2	69.96-84.42

Table 6-1: The fuel consumption per year for all models of the Land Rover Discovery 4

Chapter 7 Conclusions and recommendations

7.1 Conclusions

The focus of this thesis is to optimize the design modification of the Land Rover Discovery with the aim of reducing the aerodynamic drag and increasing the stability of the car on the road. This was achieved by using computational technique to assess and control the flow behaviour around the Land Rover Discovery. In particular, specific objectives of the thesis as described in section 1.3 were met. The remainder of this section will detail the main scientific conclusions which have been drawn from the work described in this thesis.

- The Ahmed model and the benchmark model of the Land Rover Discovery 4 were investigated to develop and validate the CFD simulations in this study (section 4.1.4 and 5.2).
- The Ahmed model was simulated using three different turbulence models (section 4.1.4) to investigate accuracy and computational time. The numerical drag coefficient as a function of the Reynolds number was in agreement with empirical data of many previous studies. It was found that SST turbulence model was the best for the accuracy and computational time.
- In general, the drag coefficient of the full-scale model is less than the scale model while the lift coefficient of the full-scale model is higher than that of the scale model. The framework developed in the work described throughout this thesis was employed to improve the aerodynamic behaviour by obtaining an external design optimisation of a simplified Land Rover Discovery (4-SDV6 GS) model.
- Mesh refinement (section 4.2.3 and 4.4) and the computational domain size (section 5.3) achieved accurate and repeatable numerical results. It was found that the drag and lift coefficients were influenced by mesh refinement and the computational domain size. The best size required a 123.66m^2 frontal cross-sectional area and a length of 40.835m. This particular computational domain was about 8.4 times the car length. The distance from the inlet to the front of the car and from the outlet to the rear of the car were about 3 times and 4.4 times the car

length, respectively. The distance from top to the car roof was 4.5 times the car height, whilst the domain width was about 6 times the car width.

- Numerical simulations of the Land Rover Discovery 4 using different turbulence models were performed in this work using identical dimensions and boundary conditions to those used experimentally model (section 5.2). The drag and lift coefficients obtained from simulating of the benchmark model compared well with the experimental data. It was found that the realizable k–ε turbulence model was the best regarding the accuracy and computational time for all models of the Land Rover Discovery 4.
- Novel techniques to reduce drag and increase stability for the Land Rover Discovery 4 were implemented (section 4.3, 5.4). A boat-tail on the back door of the vehicle, Vortex Generators (VGs) on the end of the car roof, moving the spare tyre to the back door of the vehicle, a convergent-divergent ditch on the vehicle roof and a specifically designed base bleed were used as investigated. Design optimization techniques being exploited to obtain the best positions for each of the proposed modifications (section 4.3, 5.4).
- Two airflow vortices were generated in all the case-studies principal flow being simulated over the roof edge and from the underbody. The reduction in velocity at the rear part of this vehicle was due to viscous effects and positive pressure gradients. As a result, the maximum pressure was calculated on the front face of the car and the minimum on the back face. Therefore, the modifications proposed reduce the vortices and pressure gradient at the back of the SUV leading to an increase in the pressure behind the car and consequently a reduction in the drag.
- All modified SUVs produced lower drag coefficients than the benchmark model. It was found that the lowest drag coefficient was achieved using the base bleed model, while the lowest lift coefficient was obtained by the model with the ditch on the roof which decreased the velocity of air at the end of the vehicle roof leading an increase in the pressure (C_L for this model was -0.176). However, some modifications are very expensive, such as base bleed because of the need for re-design.

- Analysing the simulation results of different aerodynamic techniques was achieved in order to identify the greatest reduction in drag whilst increasing stability (section 5.7). The most efficient modification was moving the spare tyre on the back door of the Land Rover Discovery 4 acting as a fairing. This model revealed second lowest drag coefficient and lift coefficient whilst being the less prohibitive of the modifications investigated throughout this thesis. This modification could lead to 51.3 – 62litre of fuel saving per year if 12,000 miles per year are covered.

7.2 Future Work

The framework of research described throughout this thesis can be applied to the Land Rover Discovery baseline model with some accessories such as side mirrors and wheels with details. This proposal needs more attention given to the mesh and that means more time to complete the simulations.

The suggested numerical approach for calculating the drag and lift coefficients could be tested for other road vehicles and could be tested for different scales of model to verify its reliability.

Future work is needed to study the aerodynamics of the Land Rover Discovery 4 under crosswind. This study could be for the benchmark model and could be investigated for all modified models herein to verify whether these modifications can still improve aerodynamics under the crosswind.

Future work is needed to investigate the replacement of a normal spare tyre on the back door of the SUV by a spare tyre with a streamlined cover. This modification could lead to reducing the vortices around the spare tyre especially at the rear side corners of the SUV.

Most changes in airflow occur either behind or below the vehicle model. Therefore, future work is needed to investigate the effect of the distance between the chassis of the vehicle and the ground. This could be done in two ways: (i) using the standard conditions herein and (ii) crosswind.

The present study focused on the aerodynamic reduction techniques individually, such as the ditch on the car roof. Some of these techniques can improve the drag coefficient and others can improve the lift coefficient. More work is needed in the future to investigate the combination of these modifications and aerodynamic devices to verify if some combination can provide better overall aerodynamic behaviour.

Appendix (A): Analysis of variance

Analysis of Variance (ANOVA) reveals differences between samples (pressure coefficient in the current study). This test can provide some information to check if the numerical results are statistically significant or not.

Hypotheses of ANOVA:

These are always the same.

H_0: The pressure coefficient means of all vehicle models under consideration were equal.

H_1: The pressure coefficient means were not all equal. (Note: This is different than saying they were all unequal).

The analysis of variance as one-way ANOVA was used because there was just one explanatory variable was needed to check which was pressure coefficient [102].

A large number of the pressure coefficient for each model of vehicle was used. The following Table A1 shows some of these numbers.

	Pressure coefficient						
	Baseline	Boat-tail	VGs	Spare tyre	Roof ditch	Base bleed	
	1	1	1	1	1	1	
	0.9592	0.9636	0.9747	0.9859	0.9668	0.9641	
	0.9371	0.9395	0.9506	0.9638	0.9448	0.9421	
	0.9151	0.9196	0.9275	0.9384	0.9241	0.9205	
	0.8908	0.8952	0.8983	0.9175	0.9021	0.8981	
	0.8667	0.8734	0.8672	0.8922	0.8865	0.8729	
	0.8451	0.8491	0.8451	0.8683	0.8659	0.8543	
	0.8171	0.8272	0.8208	0.8451	0.8451	0.8294	
	.	.	.	.	.	.	
	.	.	.	.	.	.	
	0.6617	0.5339	0.5927	0.6393	0.6311	0.6642	
	0.6651	0.5081	0.5821	0.6393	0.6211	0.6651	
	0.6705	0.5659	0.5707	0.6399	0.6167	0.6707	
Total	89.5952	81.7771	106.5694	86.176	100.9612	87.1799	**T..=552.25**
n	167	167	167	167	167	167	**N=1,002**

Table A1: The pressure coefficient for all models of the Land Rover Discovery 4

The following hypothesis was used:

H_0: $\mu_{\text{Baseline}} = \mu_{\text{Boat-tail}} = \mu_{\text{VGs}} = \mu_{\text{Spare tyre}} = \mu_{\text{Roof ditch}} = \mu_{\text{Base bleed}}$

The number of pressure coefficient for each model was 167 (n=167)

$$N = n_1 + n_2 + n_3 + n_4 + n_5 + n_6 \quad \text{(A.1)}$$

$N = 167 \times 6 = 1{,}002$

$T..$ = The summation of the pressure coefficient for all models = 552.25

$$C.F = \frac{T_{..}^2}{N} = \frac{(556.63)^2}{1002} = 304.381 \quad \text{(A.2)}$$

SS is sum of squares.

SST measures variation of the data around the overall mean.

SSG measures variation of the group means around the overall mean.

SSE measures the variation of each observation around its group mean.

$$SST = \sum_{i=1}^{K}\sum_{j=1}^{n_j} y_{ij}^2 - C.F \quad \text{(A.3)}$$

$SST = 347.103 - 304.381 = 42.722$

$$SSG = \sum_{i=1}^{K} \frac{y_i^2}{n_i} - C.F \quad \text{(A.4)}$$

$$SSG = \left[\frac{(89.6)^2}{167} + \frac{(81.78)^2}{167} + \frac{(106.57)^2}{167} + \frac{(86.18)^2}{167} + \frac{(100.96)^2}{167} + \frac{(87.8)^2}{167}\right] - 304.381$$

$SSG = 2.755$

$SSE = SST - SSG$

$SSE = 42.722 - 2.755 = 39.967$

$df(A) = K - 1 = 6 - 1 = 5$

$df(E) = N - K = 1002 - 6 = 996$

$df(T) = N - 1 = 1002 - 1 = 1001$

$$SST = SSG + SSE \quad \text{(A.5)}$$

MS = Mean Square = SS/df (A.6)

The ANOVA table can now be constructed.

Source of Variation (S.O.V)	**Sums of Squares (*SS*)**	**Degrees of Freedom (*df*)**	**Mean Squares (*MS*)**	**F**
Between Treatments	*SSG*	*df* (*A*) = K-1	$MSA = \frac{SSA}{K-1}$	$Fc = \frac{MSA}{MSE}$
Error (or Residual)	*SSE*	*df* (*E*) = N-K	$MSE = \frac{SSE}{N-K}$	
Total	*SST*	*df* (*T*) = N-1		

Table A2: The ANOVA table

The results of the statistical testing by using ANOVA are shown in the following table:

Source of Variation (S.O.V)	**Sums of Squares (*SS*)**	**Degrees of Freedom (*df*)**	**Mean Squares (*MS*)**	**F**
Between Treatments	2.755	5	0.551	13.73
Error (or Residual)	39.967	996	0.0401	
Total	42.722	1001		

Table A3: The results of the statistical testing by using ANOVA

If the variability between vehicle models was large relative to the variability within vehicle models, then the data suggest that the means of the pressure coefficient from which the data were drawn were significantly different. F statistic is a measure of the variability between treatments divided by a measure of the variability within treatments. F calculated (13.73) was larger than F critical (F from table, 2.22) and that means the variability between treatments (pressure coefficients) was large relative to the variation within treatments, and the null hypothesis of equal means (H_0) was rejected.

References

1. Anderson Jr, J.D., *Fundamentals of aerodynamics*. 5th ed. 2010, New Delhi: Tata McGraw-Hill Education.
2. Obidi, T.Y., *Theory and applications of aerodynamics for ground vehicles*. 2014: Society of Automotive Engineers.
3. Krishnani, P.N., *CFD study of drag reduction of a generic sport utility vehicle*. 2009, American Society of Mechanical Engineers.
4. Schuetz, T., *Aerodynamics of road vehicles*. Vol. Fifth Edition 2016, USA: Society of Automotive Engineers.
5. Reddy Gondipalle, S., *CFD Analysis of the Under Hood of A Car for Packaging Considerations.* 2011.
6. Hilliard, J.C. and G.S. Springer, *Fuel Economy: In Road Vehicles Powered by Spark Ignition Engines*. 2013: Springer Science & Business Media.
7. Heisler, H., *Advanced vehicle technology*. 2nd Edition ed. 2002, Great Britain Butterworth Heinemann Books - Elsevier.
8. Katz, J., *Automotive aerodynamics*. 2016, Chichester, UK;Hoboken, NJ;: John Wiley & Sons.
9. Levin, J. and R. Rigdal, *Aerodynamic analysis of drag reduction devices on the underbody for SAAB 9-3 by using CFD.* Chalmers University of Technology, 2011.
10. Hucho, W.-H., *Aerodynamics of road vehicles: from fluid mechanics to vehicle engineering*. 4th ed. 1998, Warrendale, PA: Society of Automotive Engineers.
11. Hucho, W.-H. and S.R. Ahmed, *Aerodynamics of road vehicles: from fluid mechanics to vehicle engineering*. 1987, London: Butterworths.
12. Lay, W., *Is 50 Miles Per Gallon Possible With Correct Streamlining?, Part 1*. 1933, SAE Technical Paper. 330041, doi:10.4271/330041
13. Ahmed, S.R., G. Ramm, and G. Faltin, *Some salient features of the time-averaged ground vehicle wake*. 1984, SAE Technical Paper.
14. Discovery, L.R. *The official Media Centre for Jaguar Land Rover*. 2012 12 March 2016]; Available from: http://newsroom.jaguarlandrover.com/en-in/land-rover/press-kits/2011/07/d4_2012my_presskit_060711/.
15. Gaylard, A., *Discovery 4 SDV6 GS*. 2017, The Official Centre for Jaguar Land Rover.
16. Han, T., *Computational analysis of three-dimensional turbulent flow around a bluff body in ground proximity.* Momentum, 1989. **510**: p. 3.
17. Minguez, M., R. Pasquetti, and E. Serre, *High-order large-eddy simulation of flow over the "Ahmed body" car model.* Physics of fluids, 2008. **20**(9): p. 095101.
18. Bello-Millán, F., *et al.*, *Experimental study on Ahmed's body drag coefficient for different yaw angles.* Journal of Wind Engineering and Industrial Aerodynamics, 2016. **157**: p. 140-144.
19. Guilmineau, E., *Computational study of flow around a simplified car body.* Journal of wind engineering and industrial aerodynamics, 2008. **96**(6): p. 1207-1217.
20. Conan, B., J. Anthoine, and P. Planquart, *Experimental aerodynamic study of a car-type bluff body.* Experiments in Fluids, 2011. **50**(5): p. 1273-1284.

21. Howard, R. and M. Pourquie, *Large eddy simulation of an Ahmed reference model.* Journal of Turbulence, 2002. **3**(5).
22. Hinterberger, C., M. Garcia-Villalba, and W. Rodi, *Large eddy simulation of flow around the Ahmed body*, in *The aerodynamics of heavy vehicles: trucks, buses, and trains*. 2004, Springer. p. 77-87.
23. KrajnoviÄ, S.a. and L. Davidson, *Flow around a simplified car, part 1: large eddy simulation.* Journal of Fluids Engineering, 2005. **127**(5): p. 907-918.
24. Serre, E., *et al.*, *On simulating the turbulent flow around the Ahmed body: A French–German collaborative evaluation of LES and DES.* Computers & Fluids, 2013. **78**: p. 10-23.
25. Verzicco, R., *et al.*, *Large eddy simulation of a road vehicle with drag-reduction devices.* AIAA journal, 2002. **40**(12): p. 2447-2455.
26. Franck, G., *et al.*, *Numerical simulation of the flow around the Ahmed vehicle model.* Latin American applied research, 2009. **39**(4): p. 295-306.
27. Watkins, S. and G. Vino, *The effect of vehicle spacing on the aerodynamics of a representative car shape.* Journal of wind engineering and industrial aerodynamics, 2008. **96**(6): p. 1232-1239.
28. Meile, W., *et al.*, *Experiments and numerical simulations on the aerodynamics of the Ahmed body.* CFD Letters, 2011. **3**(1): p. 32-39.
29. Thacker, A., *et al.*, *Effects of suppressing the 3D separation on the rear slant on the flow structures around an Ahmed body.* Journal of Wind Engineering and Industrial Aerodynamics, 2012. **107**: p. 237-243.
30. Ortega, J., *et al.*, *Aerodynamic drag reduction of class 8 heavy vehicles: a full-scale wind tunnel study*. 2013, Lawrence Livermore National Laboratory (LLNL), Livermore, CA.
31. Hilmi Safuan, J., *Aerodynamic Study Of Heavy Truck Using CFD Fluent.* 2010.
32. Gilkeson, C., *et al.*, *An experimental and computational study of the aerodynamic and passive ventilation characteristics of small livestock trailers.* Journal of Wind Engineering and Industrial Aerodynamics, 2009. **97**(9-10): p. 415-425.
33. Guo, L., Y.-M. Zhang, and W.-J. Shen, *Simulation Analysis of Aerodynamics Characteristics of Different Two-Dimensional Automobile Shapes.* JCP, 2011. **6**(5): p. 999-1005.
34. Harinaldi, H., *et al.*, *Modification of flow structure over a van model by suction flow control to reduce aerodynamics drag.* Makara Journal of Technology, 2012. **16**(1): p. 15-21.
35. Altinisik, A., E. Kutukceken, and H. Umur, *Experimental and Numerical Aerodynamic Analysis of a Passenger Car: Influence of the Blockage Ratio on Drag Coefficient.* Journal of Fluids Engineering-Transactions of the ASME, 2015. **137**(8): p. 81104.
36. Tsubokura, M., *et al.*, *Large eddy simulation on the unsteady aerodynamic response of a road vehicle in transient crosswinds.* International Journal of Heat and Fluid Flow, 2010. **31**(6): p. 1075-1086.
37. Sealy, M., *et al.*, *Motor coach*. 1996, Google Patents: USA.
38. Roy, S. and P. Srinivasan, *External flow analysis of a truck for drag reduction*. 2000, SAE Technical Paper. 2000-01-3500, https://doi.org/10.4271/2000-01-3500.

39. Amirnordin, S.H., *et al.*, *Numerical analysis on the effects of air flow in the wake of a large vehicle on trailing a passenger car*. Malaysian Technical Universities Conference on Engineering and Technology (MUCET), 2010.
40. Ghani, O.A., *Design optimization of aerodynamic drag at the rear of generic passenger cars using nurbs representation*, in *Mechanical Engineering*. 2013, University of Ontario: UOIT.
41. Hucho, W.-h. and G. Sovran, *Aerodynamics of road vehicles.* Annual review of fluid mechanics, 1993. **25**(1): p. 485-537.
42. Rossitto, G., *et al.*, *Influence of afterbody rounding on the pressure distribution over a fastback vehicle.* Experiments in Fluids, 2016. **57**(3): p. 43.
43. Miralbes, R. *Analysis of Some Aerodynamic Improvements for Semi-Trailer Tankers*. in *Proceedings of the World Congress on Engineering*. 2012.
44. Barbut, D. and E.M. Negrus, *CFD analysis for road vehicles-case study.* INCAS bulletin, 2011. **3**: p. 15-22.
45. Song, K.-S., *et al.*, *Aerodynamic design optimization of rear body shapes of a sedan for drag reduction.* International Journal of Automotive Technology, 2012. **13**(6): p. 905-914.
46. Chaligné, S., R. Turner, and A. Gaylard. *The Aerodynamics Development of the New Land Rover Discovery 5*. in *FKFS Conference*. 2017. Springer.
47. Pitman, J. and A. Gaylard. *An experimental investigation into the flow mechanisms around an SUV in open and closed cooling air conditions*. in *FKFS Conference*. 2017. Springer.
48. Brown, Y.I., S. Windsor, and A. Gaylard, *The effect of base bleed and rear cavities on the drag of an SUV*. 2010, SAE Technical Paper. 2010-01-0512, https://doi.org/10.4271/2010-01-0512.
49. Khalighi, B., K.-H. Chen, and G. Iaccarino, *Unsteady aerodynamic flow investigation around a simplified square-back road vehicle with drag reduction devices.* Journal of fluids engineering, 2012. **134**(6): p. 061101.
50. Du Buisson, J. and J. Erens, *Reduction of Aerodynamic Resistance of Heavy Vehicles and Effect on Fuel Economy*. 1990.
51. Leuschen, J. and K.R. Cooper, *Full-scale wind tunnel tests of production and prototype, second-generation aerodynamic drag-reducing devices for tractor-trailers*. 2006, SAE Technical Paper. 2006-01-3456, https://doi.org/10.4271/2006-01-3456.
52. Van Raemdonck, G.M. and M.J. Van Tooren. *Design of an aerodynamic aid for the underbody of a trailer within a tractor-trailer combination*. in *BBAA VI International Colloquium on Bluff Bodies Aerodynamics & Applications Milano, Italy*. 2008.
53. Salari, K. and J. Ortega, *Aerodynamic Design Criteria for Class 8 Heavy Vehicles Trailer Base Devices to Attain Optimum Performance*. 2010, Lawrence Livermore National Laboratory (LLNL), Livermore, CA.
54. Farkas, S., *Fuel Efficiency in Truck Industry*. Scientific Bulletin of the" Petru Maior" University of Targu Mures, 2010. **7**(2): p. 59.
55. Shukri, I. and A. Akram. *Improvement of aerodynamics characteristic of heavy trucks*. in *3rd International Conference on Trends in Mechanical and Industrial Engineering (ICTMIE'2013) January*. 2013.

56. Chowdhury, H., *et al.*, *A study on aerodynamic drag of a semi-trailer truck.* Procedia Engineering, 2013. **56**: p. 201-205.
57. Koike, M., T. Nagayoshi, and N. Hamamoto, *Research on aerodynamic drag reduction by vortex generators.* Mitsubishi motors technical review, 2004. **16**: p. 11-16.
58. Hu, X. and T. Wong, *A numerical study on rear-spoiler of passenger vehicle.* World Academy of Science, Engineering and Technology, 2011.
59. Kang, S.-O., *et al.*, *Actively translating a rear diffuser device for the aerodynamic drag reduction of a passenger car.* International Journal of Automotive Technology, 2012. **13**(4): p. 583-592.
60. Raju, D.K.M., M. Tech, and G.J. Reddy, *A conceptual design of wind friction reduction attachments to the rear portion of a car for better fuel economy at high speeds.* International Journal of Engineering Science and Technology, 2012. **4**(5): p. 2366-2372.
61. Sivaraj, G. and M.G. Raj, *Optimum Way to Increase the Fuel Efficiency of the Car Using Base Bleed.* International Journal of Modern Engineering Research (IJMER), 2012. **2**(3): p. 1189-1194.
62. Bijlani, B., P.P. Rathod, and A.S. Sorthiya, *Experimental Investigation of Aerodynamic Forces on Sedan, Fastback and Square-Back Car by simulation in CFD" Review Study.* International journal of emerging technology and advanced engineering, 2013. **2**(3): p. 346-349.
63. Dubey, A., S. Chheniya, and A. Jadhav, *Effect of Vortex generators on Aerodynamics of a Car: CFD Analysis.* International Journal of Innovations in Engineering and Technology (IJIET), 2013. **2**(1).
64. Wood, A., *et al.*, *Base pressure and flow-field measurements on a generic SUV model.* SAE International Journal of Passenger Cars-Mechanical Systems, 2015. **8**(2015-01-1546): p. 233-241.
65. Rohatgi, U.S. *Methods of reducing vehicle aerodynamic drag*. in *ASME 2012 Summer Heat Transfer Conference*. 2012.
66. Versteeg, H.K. and W. Malalasekera, *An introduction to computational fluid dynamics: the finite volume method*. 2007: Pearson Education.
67. Faber, T.E., *Fluid Dynamics for Physicists*. First ed. 1995: Cambridge University Press.
68. Schlichting, H. and K. Gersten, *Boundary-layer theory*. 2016: Springer.
69. Reynolds, O., *On the dynamical theory of incompressible viscous fluids and the determination of the criterion.* Philosophical Transactions of the Royal Society of London. A, 1895. **186**: p. 123-164.
70. Massey, B. and J. Ward-Smith, *Mechanics of fluids 8th ed*. 2005, Taylor & Francis e-Library.
71. Wu, Y., *et al.*, *Flow visualization of Mach 3 compression ramp with different upstream boundary layers.* Journal of Visualization, 2015. **18**(4): p. 631-644.
72. Bergman, T.L., *et al.*, *Fundamentals of heat and mass transfer*. 2011: John Wiley & Sons.
73. Frank, M., *Fluid Mechanics* 2017, McGraw-Hill.
74. Bernoulli, D., *Hydrodynamica, sive De viribus et motibus fluidorum commentarii. Opus academicum ab auctore, dum Petropoli ageret, congestum*.

1738: Sumptibus Johannis Reinholdi Dulseckeri; Typis Joh. Henr. Deckeri, typographi Basiliensis.
75. Lamb, H., *Hydrodynamics (6th edn).* Cambridge UniverSity PrCSS, 1932.
76. Falkovich, G., *Fluid Mechanics*. 2011, GB: Cambridge University Press - M.U.A.
77. Hucho, W.-H., *Aerodynamics of road vehicles: from fluid mechanics to vehicle engineering*. 2013: Elsevier.
78. Madenci, E. and I. Guven, *The finite element method and applications in engineering using ANSYS®*. 2015: Springer.
79. Hirsch, C., *Numerical computation of internal and external flows: The fundamentals of computational fluid dynamics*. Vol. 1. 2007, USA: Butterworth-Heinemann.
80. Oberkampf, W.L. and T.G. Trucano, *Verification and validation in computational fluid dynamics.* Progress in Aerospace Sciences, 2002. **38**(3): p. 209-272.
81. Babuska, I. and J.T. Oden, *Verification and validation in computational engineering and science: basic concepts.* Computer Methods in Applied Mechanics and Engineering, 2004. **193**(36): p. 4057-4066.
82. Suard, S., *et al.*, *Verification and validation of a CFD model for simulations of large-scale compartment fires.* Nuclear Engineering and Design, 2011. **241**(9): p. 3645-3657.
83. Groves, C., M. Ilie, and P. Schallhorn. *Comprehensive Approach to Verification and Validation of CFD Simulations Applied to Backward Facing Step-Application of CFD Uncertainty Analysis*. in *51st AIAA Aerospace Sciences Meeting including the New Horizons Forum and Aerospace Exposition*. 2012.
84. Eggenspieler, G., *Turbulence modeling.* ANSYS Inc, 2011.
85. Iaccarino, G., *Predictions of a turbulent separated flow using commercial CFD codes.* Transactions-American Society of Mechanical Engineers Journal of Fluids Engineering, 2001. **123**(4): p. 819-828.
86. Fitzgibbon, W.E. and M.F. Wheeler, *Computational methods in geosciences*. Vol. 33. 1992: SIAM.
87. Hanjalic, K., *Will RANS survive LES? A view of perspectives.* Journal of fluids engineering, 2005. **127**(5): p. 831-839.
88. Notes, I.F., *Introduction to CFD Analysis. Introductory FLUENT Training, ANSYS*. 2006, ANSYS Inc.
89. Almohammadi, K.M., *Optimization of a CFD based design of a straight blade vertical axis wind turbine (SB-VAWT)*. 2014, University of Leeds.
90. Zaki, M., S. Menon, and L.N. Sankar, *Hybrid Reynolds-Average Navier-Stokes and Kinetic Eddy Simulation of External and Internal Flows.* Journal of Aircraft, 2010. **47**(3): p. 805-811.
91. Lanfrit, M., *Best practice guidelines for handling Automotive External Aerodynamics with FLUENT*. Fluent Deutschland GmbH: Germany.
92. Recktenwald, G., *The $k-\in$ Turbulence Model*. 2009, Lecture notes, Mechanical and Materials Engineering Department, Portland State University.
93. Aljure, D.E., *et al.*, *Flow and turbulent structures around simplified car models.* Computers & Fluids, 2014. **96**: p. 122-135.

94. Nicoud, F. and F. Ducros, *Subgrid-scale stress modelling based on the square of the velocity gradient tensor.* Flow, turbulence and Combustion, 1999. **62**(3): p. 183-200.
95. Nakos, D., *High resolution schemes for bluff-body aerodynamics.* MSc Thesis, 2013.
96. Ahmad, N.E., E.F. Abo-Serie, and A. Gaylard, *Mesh optimization for ground vehicle aerodynamics.* CFD Letters, 2010. **2**(1): p. 54-65.
97. Ariff, M., S.M. Salim, and S.C. Cheah. *Wall y+ approach for dealing with turbulent flow over a surface mounted cube: Part 1—Low Reynolds number*. in *Seventh International Conference on CFD in the Minerals and Process Industries*. 2009.
98. Nicoud, F., *et al.*, *Using singular values to build a subgrid-scale model for large eddy simulations.* Physics of Fluids, 2011. **23**(8): p. 085106.
99. Hughes, T.J., L. Mazzei, and K.E. Jansen, *Large eddy simulation and the variational multiscale method.* Computing and visualization in science, 2000. **3**(1-2): p. 47-59.
100. Verstappen, R., *When does eddy viscosity damp subfilter scales sufficiently?* Journal of Scientific Computing, 2011. **49**(1): p. 94.
101. Horiba-MIRA. *MIRA Wind Tunnel*. 2017; Available from: https://www.horiba-mira.com/our-services/full-scale-wind-tunnel-(fswt)
102. Wonnacott, T.H. and R.J. Wonnacott, *Introductory statistics*. 5th ed. 1990: Wiley New York.
103. PetrolPrices, *Average UK Fuel Prices.* 2018. https://www.petrolprices.com/